Tetranuclear $CaMn_3O_4$ and Mn_4O_4 Complexes as Spectroscopic Models of the Oxygen Evolving Complex of Photosystem II

Thesis by

Angela Ann Shiau

In Partial Fulfillment of the Requirements for
the degree of
Doctor of Philosophy

Division of Chemistry and Chemical Engineering
CALIFORNIA INSTITUTE OF TECHNOLOGY
Pasadena, California

2023
(Defended May 5, 2023)

ACKNOWLEDGEMENTS

First, I would like to thank my advisor Prof. Theodor Agapie. Theo, your mentorship over the past six years has been invaluable, and I thank you for always challenging me to do my best, for being patient when my results are no results, and for bringing your creativity in and passion for chemistry to every meeting. I've learned so much!

I would also like to thank my thesis committee: Profs. Ryan Hadt, Harry Gray, and Sarah Reisman. I am very grateful for your support and advice. Harry, thank you especially for your excitement for my science and support for my career. It means a lot!

Since my first day at Caltech, I have been blessed with great lab mates and mentors. Dr. Heui Beom Lee, you are a spectacular mentor and I learned so much from you. Thank you for always being patient and supportive, for cheering me up when I am down, for believing in me even when I do not, and for always bringing such a positive attitude everywhere you go! Your mentorship and friendship over the years means so much to me! I hope you are proud of what I have been able to accomplish!

None of the work in this thesis would have been possible without the help of Dr. Paul Oyala at the Caltech EPR facility. Paul, thank you for being a great collaborator and mentor, especially in the past couple months! Your enthusiasm for, expertise in, and dedication to EPR is very inspiring! I've learned so much about EPR from you and I promise to go to the gym so I can actually lift the transfer line without (as much) assistance (one day).

I would also like to thank all my other mentors in the Agapie group, including previous members Drs. Joshua Buss, Marcus Low, Chris Reed, and Charlie Arnett. Marcus, thank you for always cooking delicious food for all of us at parties, for group camping trips, or even just for fun! Thank you to all members of the cluster subgroup as well: HB, Chris,

Charlie, Anna, Linh, Mike, your feedback always helped me strive to become a better chemist!

Over the last six years I have been lucky to have Meaghan Bruening as a friend. Thank you for surviving all these crazy years in grad school with me! Your unfailing humor and unwavering support have made this experience fun and memorable. Thank you (and Zuri) for helping me overcome my cat allergy and for being the godmother of my cats! Mike He, thank you as well for your friendship and for always being able to make me laugh. I will miss the dinner parties and video game parties dearly! I wish the best of luck to both of you!

Dr. Matt Espinosa, thank you for your help with crystallography and for always giving great advice. Fernando, thanks for being a great box mate, especially for accommodating my monopoly over the real-estate in the glovebox. Gavin, teaching Ch5b with you and Meaghan was a fun and character-building experience. To the rest of the group: thank you for being great colleagues and making my time here fun.

Caltech truly is a great place to do science. I would like to thank the Caltech staff for everything they do behind the scenes to make sure we can run our experiments! Dr. Mike Takase, thank you for answering all my questions and helping with some really tough crystallography. Larry, thank you for spending countless hours helping me mount crystals. Dr. Dave VanderVelde, thank you for keeping the NMRs (especially hg2) running, and Dr. Mona Shahgholi, thank you for running the ESI facility. I would also like to thank our group's admin Margarita Davis for all your hard work supporting us.

To my collaborators Dr. David Marchiori and Prof. R. David Britt at UC Davis for D-band spectroscopy, thank you for your enthusiasm for our collaborative projects. I'm very excited to learn more about EPR at Davis soon! I'd also like to thank Dr. Byung-Kuk Yoo,

Dr. Jens T. Kaiser, and Prof. Doug Rees for the collaboration on the Ca cubane work. Additionally, thank you to Drs. Sheraz Gul, Ruchira Chatterjee, and Junko Yano at the Lawrence Berkeley National Laboratory for XAS spectroscopy.

Before coming to Caltech, I also had a great group of mentors and friends in the Arnold group at UC Berkeley that I must thank for inspiring me to pursue chemistry. Thank you, Dr. Alex Brown, for your friendship over the years and for sharing your unwavering enthusiasm for chemistry. Learning how to do Schlenk and glovebox chemistry along with you made it even more fun! I'm so proud of what you have accomplished at MIT; you're a rockstar! Dr. Nick Settineri, thanks for being an awesome mentor and for your enthusiasm in talking about all the latest movies and TV shows! I'd like to thank Prof. John Arnold for giving me the opportunity to learn synthetic chemistry in your lab! I would not be here today without your guidance and mentorship.

Finally, I would like to thank my friends and family. To Ellen, thank you for being my best friend – thanks for your constant support for more than ten years! Our time exploring restaurants, watching trashy TV, good TV, mediocre TV, and playing video games really helped balance the stress from grad school. It's a shame we won't overlap much at Caltech, but I wish you the best!

To my sister Lily, thank you for always, always being there for me. You've been my biggest cheerleader for as long as I can remember and I'm so grateful to have you as a sister! Good luck with the rest of your graduate career here at Caltech. I believe in you! To my parents, thank you for all your unconditional love and support throughout my entire life, and for always encouraging me to chase my dreams. I couldn't have done any of this without you, and I love you so much!

ABSTRACT

This thesis describes a series of studies focused on tetranuclear model complexes of the Oxygen Evolving Complex (OEC) of Photosystem II (PSII). The OEC is a unique $CaMn_4O_4$ metallocofactor responsible for biological water oxidation, producing the dioxygen in the atmosphere required for aerobic life. Advances in spectroscopic and structural studies have deepened our understanding of the mechanism and S-state intermediates of the OEC, but details regarding the (1) role of Ca^{2+}, (2) location of substrate waters, (3) (electronic) structures of the S-states, and (4) precise mechanism of the O–O bond formation remain debated. It is proposed that synthetic model complexes, due to tunability in aspects such as metal composition, oxidation state, geometry, and ligand environment, can provide important structure-function and structure-property relationships applicable to the OEC. However, due to synthetic challenges, series of complexes suitable for such comparisons remain rare in the literature.

In Chapter 1, a brief introduction to the OEC and recent advances in the characterization of the S-state intermediates is discussed. Relationships between synthetic model complexes and how they influence mechanistic proposals for the biological system are highlighted. While it is clear spin state and cluster geometry are strongly correlated, it is important to also consider the effects of smaller, systematic changes in structure and ligand environment on the spectroscopic properties of multimetallic model complexes.

Chapter 2 presents a magnetometry and spectroscopic study of a series of related $CaMn^{IV}_3O_4$ complexes varying in the symmetry of the cluster core, ligand environment, and protonation state of the bridging oxo groups. These complexes serve as models of the

$CaMn^{IV}_3$ cuboidal subsite, where cluster spin state has been previously proposed to be indicative of cluster geometry. Results from our study show that intact $CaMn^{IV}_3O_4$ cubane structures can possess spin states of S = 3/2, 5/2, and 9/2, with spin state changes attributed to minor distortions within the cluster core and, importantly, from protonation state of bridging oxo moieties. Thus, interpretation of and structural assignments based on the assumption of a S = 9/2 $CaMn^{IV}_3O_4$ subsite must be done cautiously.

Chapter 3 presents a series of $Mn^{III}Mn^{IV}_3$ cuboidal complexes as spectroscopic models of the S_2 state of the OEC. Though not in the same geometric arrangement of Mn ions as in the OEC, these model complexes bear remarkably similar EPR spectroscopic features to the low-spin multiline signal of the S_2 state. Importantly, differences within this series of essentially isostructural complexes emphasize how the electronic structures of tetranuclear Mn complexes are highly sensitive to changes in ligand environment. Specifically, the energy gap between the ground S = 1/2 spin state and higher spin excited states can be tuned based on ligand electronics, resulting in complexes where both high-spin and low-spin features can be observed by EPR spectroscopy.

In Chapter 4, we expand upon our previous series of $Mn^{III}Mn^{IV}_3$ model complexes utilizing a new synthetic approach to access complexes varying in Mn coordination numbers of five and six. Importantly, both proposed structures of the S_2 state contain a five-coordinate Mn^{III} poised for binding an additional aquo or hydroxide ligand in the S_2 to S_3 transition. Results from this study demonstrate that Mn coordination number can significantly affect the spin state and observed spectroscopy of tetramanganese-oxo clusters. The complex featuring a five coordinate Mn^{III} possesses a ground spin state of S_G = 5/2 and reactivity with water

generates a $Mn^{III}Mn^{IV}_3O_4$ complex with all *pseudo*-octahedral Mn centers displaying a $S = 1/2$ ground state.

Chapter 5 details ligand design strategies in accessing higher oxidation state clusters beyond $Mn^{III}Mn^{IV}_3$. The S_3-state is the last observable intermediate prior to O−O bond formation and assigned as $S = 3$. Previous studies from our group demonstrated the first synthetic example corroborating this spin state, concurrent with a change from antiferromagnetic coupling within the cluster core to overall ferromagnetic coupling upon oxidation to the Mn^{IV}_4 oxidation state. Synthetic challenges remain in accessing related, isolable clusters. Utilizing aspects of ligand charge and basicity of a disiloxide ligand, a room temperature stable $Mn^{IV}_4O_4$ cluster was isolated and studied via magnetometry and EPR spectroscopy. Results provide a second example of a Mn^{IV}_4 cluster assigned as $S = 3$.

While unfinished, Appendix 1 presents spectroscopic studies of model $Mn^{III}Mn^{IV}_3$ complexes putatively bound to biologically relevant substrates such as water, hydroxide, methanol, and ammonia. Such chemical alterations and the spectroscopic effects arising from them have been widely studied in the biological system, providing information on the electronic structure of the OEC as well as, importantly, ruling out potential substrate water binding sites. As reactivity with small molecules typically requires an open-coordination site, such studies have been rare in the literature due to the difficulty in accessing lower-coordinate Mn sites within multimetallic Mn clusters. Thus, the ongoing characterization of these reaction products are proposed to be invaluable as benchmarking tools for future mechanistic work.

PUBLISHED CONTENT AND CONTRIBUTIONS

The work described in this thesis is the result of collaborative efforts, as described below.

Lee, H. B.; Shiau, A. A.; Marchiori, D. A., Oyala, P. H., Yoo, B. K., Kaiser, J. T., Rees, D. C., Britt, R. D., Agapie, T. "$CaMn_3^{IV}O_4$ Cubane Models of the Oxygen Evolving Complex: Spin Ground States $S < 9/2$ and the Effect of Oxo Protonation" *Angew. Chem. Int. Ed.*, **2021**, *60*, 17671 – 17696. doi: 10.1002/anie.202105303.

A.A.S. synthesized and characterized complex **4-Ca**, prepared the data, participated in data collection for complex **3-Ca**, and participated in the writing of the manuscript.

Lee, H. B.; Shiau, A. A.; Oyala, P. H.; Marchiori, D. A.; Gul, S.; Chatterjee, R.; Yano, J.; Britt, R. D.; Agapie, T. "Tetranuclear $[Mn^{III}Mn_3^{IV}O_4]$ Complexes as Spectroscopic Models of the S_2 State of the Oxygen Evolving Complex in Photosystem II" *J. Am. Chem. Soc.* **2018**, *140*, 17175 – 17187. doi: 10.1021/jacs.8b09961.

A.A.S. synthesized and characterized complexes **2** and **2-ox**, prepared the data, and participated in the writing of the manuscript.

Shiau, A. A.; Lee, H. B.; Oyala, P. H.; Agapie, T. "$Mn^{IV}{}_4O_4$ Model of of the S_3 Intermediate of the Oxygen-Evolving Complex: Effect of the Dianionic Disiloxide Ligand" *Inorg. Chem.* **2023**, *62*, 1791 – 1796. doi: 10.1021/acs.inorgchem.2c01612.

A.A.S. participated in the conception of the project, synthesized and characterized new complexes, prepared the data, and participated in the writing of the manuscript.

Figures from the following articles were reproduced in part with permission from the American Chemical Society:

"Synthetic Cluster Models of Biological and Heterogeneous Manganese Catalysts for O_2 Evolution" Emily Y. Tsui, Jacob S. Kanady, and Theodor Agapie. *Inorg. Chem.* **2013**, *52,* 13833 – 13848. doi: 10.1021/ic402236f.

"^{55}Mn ENDOR of the S_2-State Multiline EPR Signal of Photosystem II: Implications on the Structure of the Tetranuclear Mn Cluster" Jeffrey M. Peloquin, Kristy A. Campbell, David W. Randall, Marc A. Evanchik, Vincent L. Pecoraro, William H. Armstrong, and R. David Britt. *J. Am. Chem. Soc.* **2000**, *122*, 10926 – 10942. doi: 10.1021/ja002104f.

X-band and Q-band EPR studies reported in this thesis were performed with Dr. Paul H. Oyala at the California Institute of Technology. X-ray crystallographic studies were performed with the assistance of Dr. Michael K. Takase and Mr. Lawrence M. Henling at the California Institute of Technology. SQUID magnetometry studies were performed at the University of California, Los Angeles with the assistance of Dr. Ignacio Martini.

In Chapter 2, the magnetometry data for the bis-oximate clusters, as well as the synthetic procedure for the Y analog, were obtained and analyzed by Dr. Heui Beom Lee. The MicroED structure of cluster **2-Ca** was solved and refined by Dr. Byung-Kuk Yoo, Dr. Jens T. Kaiser, and Prof. Douglas C. Rees. D-band EPR studies were performed and analyzed by Dr. David A. Marchiori and Prof. R. David Britt at the University of California, Davis.

In Chapter 3, the synthesis and characterization of the diamidate supported clusters were developed by Dr. Heui Beom Lee. X-ray spectroscopic studies were performed by Dr. Sheraz Gul, Dr. Ruchira Chatterjee, and Dr. Junko Yano at the Lawrence Berkeley National Laboratory.

In Chapter 4, the synthesis of the incomplete cubane precursor utilized for accessing acetate-free Mn_4O_4 complexes was developed by Dr. Heui Beom Lee. The weakly coordinating anion used in isolation of the reaction product with water was developed by Mr. Tianyi He.

In Chapter 5, the electrochemical characterization of the tris-amidate cluster was performed by Dr. Heui Beom Lee.

In Appendix 1, X-ray crystallographic studies and refinement were performed with the assistance of Dr. Michael K. Takase and Dr. Matthew Espinosa. High-vacuum line experiments were performed with the assistance of Mr. Tianyi He.

TABLE OF CONTENTS

CHAPTER 1

General Introduction to the Oxygen Evolving Complex of Photosystem II and Related Synthetic Model Complexes

One of the most important chemical transformations required for aerobic life is the oxidation of water to dioxygen.[1-3] In nature, this reaction is catalyzed by the Oxygen Evolving Complex (OEC) in Photosystem II (PSII) found in the thylakoid membranes of photosynthetic organisms. In addition to generating the O_2 required for aerobic life, formal equivalents of protons and electrons produced as byproducts of water oxidation are utilized in the synthesis of important biomolecules used in biological carbon fixation. In this chapter, a general introduction to the OEC and some relevant synthetic model complexes will be presented.

1.1) General introduction to the Oxygen Evolving Complex

The mechanism of water oxidation by the OEC can be broadly described by the S-state cycle (Figure 1), in which the metallocofactor is sequentially oxidized in a five-step redox process.[2-4] O_2 is formed and released in the S_4 state and the OEC is recycled to the S_0 state. Each redox event is triggered by photon absorption by PSII, and, remarkably, this behavior has been determined since the 1960s, prior to establishment of OEC metal composition and structure.[5-6]

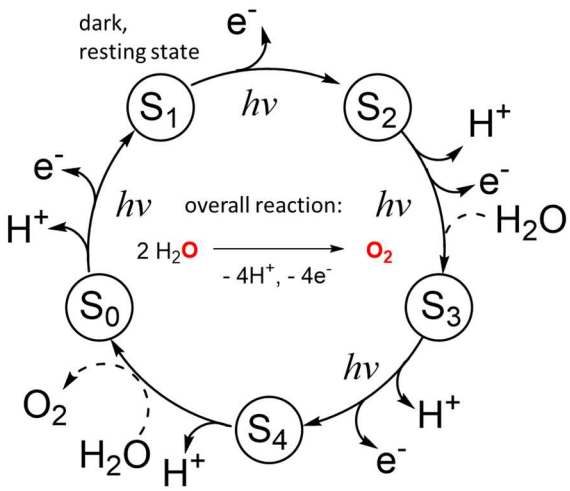

Figure 1. S-state cycle describing the overall mechanism of water oxidation by the OEC. Adapted from Ref 7.

Determination of the structure and metal composition of the OEC has historically been a collaborative effort between the fields of biochemistry, biophysics, spectroscopy, computation, and synthetic coordination chemistry.[2-4, 7-13] Early quantitative electron paramagnetic resonance (EPR) spectroscopy and atomic absorption spectroscopy studies determined the tetramanganese stoichiometry of the OEC.[14-15] Early biochemical studies implicated the presence of Ca in the OEC based on its ability to affect catalytic O_2 production.[16-17]

Developments in the synthesis of multimetallic Mn-oxo complexes provided examples of several cluster geometries of adamantane,[18-22] cuboidal,[23-25] "butterfly,"[26] linear chain,[27-29] and "basket" shapes.[30] The relationship between cluster geometry and spin state of these model complexes influenced interpretations of the EPR and X-ray absorbance spectroscopy data of the OEC, leading to various proposals for the structure and mechanism of the biological system over the years. These results, detailed in several reviews,[11, 31-32] have been instrumental in our understanding of the OEC prior to direct structural characterization.

For example, based on extended X-ray absorption fine structure (EXAFS) data, a "dimer-of-dimers" model was proposed (Figure 2).[33] A separate "trimer/monomer" (or "dangling," "3+1") model was proposed based on EPR experiments.[34-35] While $[Mn^{III}Mn^{IV}O_2]^{3+}$ dinuclear complexes (Figure 2) are not structural models of the OEC, these simplified complexes have greatly guided understanding of exchange interactions in Mn-oxide clusters. In these complexes, the two manganese centers are antiferromagnetically coupled, leading to an overall $S_G = 1/2$, with the magnitude of this coupling interaction typically in the range of $J = -100$ to -400 cm^{-1}. The EPR spectra of these types of complexes are reminiscent of the multiline signal of the S_2 state of the OEC, featuring broad transitions

centered about $g \approx 2$ with ^{55}Mn hyperfine interactions. ENDOR spectra of dinuclear complex $[Mn_2O_2(phen)_4]^{3+}$ were analyzed to assign the ^{55}Mn nuclear spin transitions for both the Mn^{III} and Mn^{IV} centers.[34] The parameters obtained in this analysis were unable to simulate ENDOR spectra of the S_2 state of the OEC. This ruled out proposals of a dimeric structure as the origin of the multiline signal in the S_2 state.

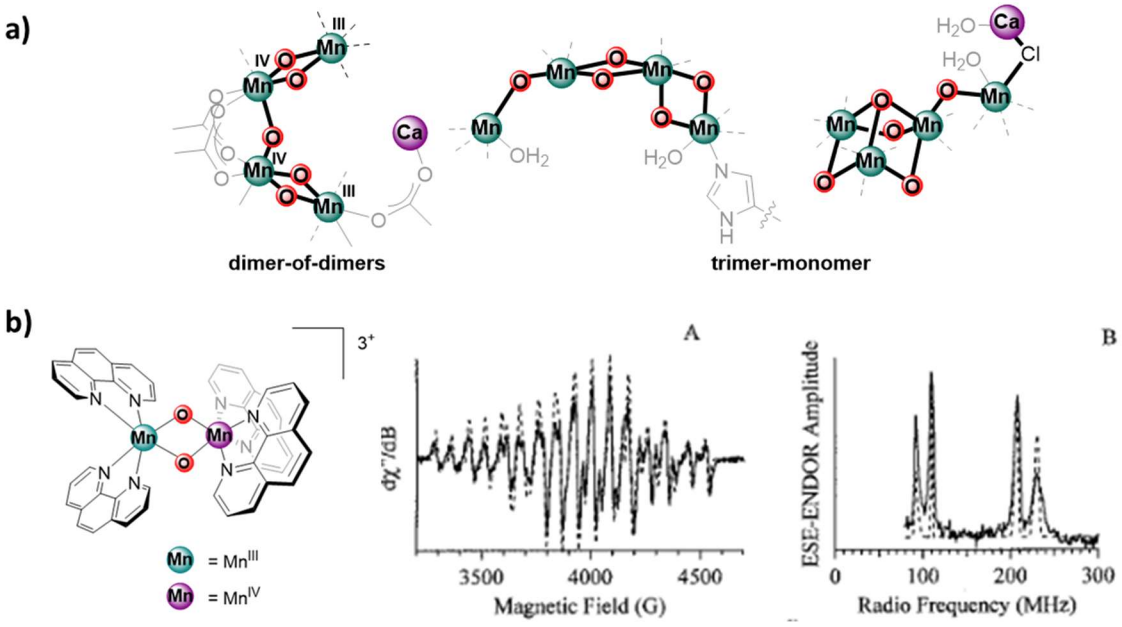

Figure 2. a) Examples of "dimer-of-dimers" and "trimer-monomer" proposals for OEC structure. **b)** CW-EPR and ENDOR of $[Mn_2O_2(phen)_4]^{3+}$. Spectra figures reprinted with permission from Peloquin, J. M.; Campbell, K. A.; Randall, D. W.; Evanchik, M. A.; Pecoraro, V. L.; Armstrong, W. H.; Britt, R. D., ^{55}Mn ENDOR of the S_2-State Multiline EPR Signal of Photosystem II: Implications on the Structure of the Tetranuclear Mn Cluster. *J. Am. Chem. Soc.* **2000,** *122* (44), 10926-10942. Copyright 2000 Americal Chemical Society.

Structural characterization of the OEC was achieved soon after these reports, with structures confirming the 3+1 arrangement of Mn ions, albeit with some concerns regarding spatial resolution and the possibility of radiation damage.[36-38] As revealed by the high resolution, radiation-damage free crystal structure at 1.95 Å resolution of the dark-stable resting state (S_1), the active site of the OEC is a metal-oxo cluster featuring a cuboidal $CaMn_3$ unit bridged to a fourth "dangler" manganese through either an oxo or hydroxo moiety.[39] In

the absence of unambiguous structural data for all S-state intermediates, available structural and spectroscopic studies of lower S_n states heavily influence computational studies and mechanistic proposals.

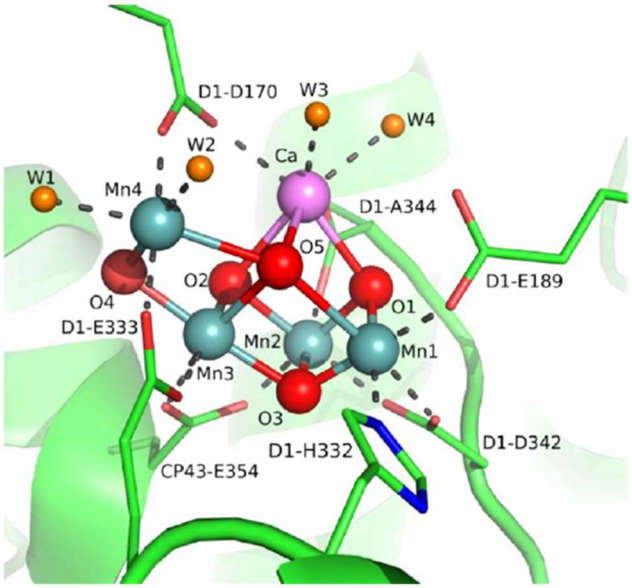

Figure 3. Crystal structure of the OEC at 1.95 Å resolution.[39] Figure reprinted with permission from Tsui, E. Y.; Kanady, J. S.; Agapie, T., Synthetic Cluster Models of Biological and Heterogeneous Manganese Catalysts for O_2 Evolution. *Inorg. Chem.* **2013,** *52* (24), 13833-13848. Copyright 2013 American Chemical Society.

In particular, the two signals observed in the EPR spectrum for the S_2 state[40-46] have been computationally attributed to structural isomers of similar energies, accounting for the observed interconvertibility under relatively mild conditions. In summary, a "closed-cubane" structure gives rise to a ground spin-state of $S_G = 5/2$ from ferromagnetic coupling of Mn^{IV}_3 within the $CaMn_3O_4$ core and antiferromagnetic coupling to the dangler Mn^{III}. In the "open-cubane" structure, the five-coordinate Mn^{III} is within the cuboidal subsite and a different coupling scheme results in an overall $S_G = 1/2$.[40] While this open-closed cubane model is considered a hallmark feature of the OEC, the closed cubane structure for the S_2 state has not yet been observed, discussed *vide infra*.

More recently, X-ray free electron laser (XFEL) techniques have been utilized to characterize S-state intermediates under conditions that limit photo-induced damage.[13, 47-51] As this is still a developing technique, insufficient precise spatial and temporal resolution in the electron-transfer, proton-transfer, and substrate binding hampers the ability to fully understand the mechanism of water oxidation. Nevertheless, direct structural evidence on higher S-state intermediates provides exciting opportunities to structurally characterize the OEC under catalytically relevant conditions. Specifically, recent studies include the S_3 state, the last spectroscopically observable intermediate prior to O_2 formation, showing incorporation of a new atom X in the coordination sphere of Mn(1).[49] This results corroborates the *pseudo*-octahedral coordination environment of all Mn^{IV} centers determined by EPR.[52] Due to the proximity of atom X to solvent exchangeable bridging oxo O(5), this result implicates O(5) and X as the atoms involved in O−O bond formation. Notably, however, in these experiments, the proposed closed-cubane structure is not observed within the level of detection. Clearly, discrepancies between results and interpretations from different techniques remain to be addressed in order to fully understand the OEC.

1.2) Multimetallic model complexes of the OEC

Historically, multimetallic synthetic model complexes have been instrumental in providing examples of possible cluster geometries and their corresponding spin states.[9-10] Since the discovery of the structure of the OEC, synthetic efforts have targeted complexes that mimic the unique geometry of the OEC. Pentametallic metal-oxo clusters that contain a cuboidal subunit and a dangling fifth metal remain incredibly rare, with only a few examples from the Christou, Agapie, Zhang, and Tilley groups (Figure 4).[53-58] As with many multinuclear Mn clusters described above, the self-assembly methods used to synthesize

some of these pentametallic complexes increase the difficulty in development of related complexes.[31, 59] This, in turn, hampers the ability to establish structure-function and structure-property relationships.

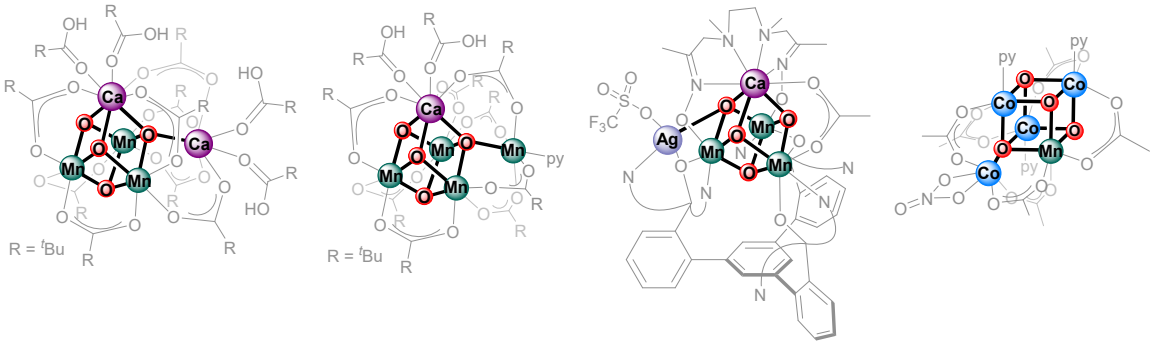

Figure 4. Examples of pentametallic metal-oxo complexes featuring a cubane subunit and a dangling fifth metal.[53-58]

Incomplete model complexes are useful in benchmarking spectroscopic interpretations and mechanistic proposals of different subsites of the OEC.[23-24, 53, 60] Tetranuclear Mn-oxo complexes in appropriate oxidation states reflective of each S_n state (i.e. S_0: $Mn^{III}_3Mn^{IV}$, S_1: $Mn^{III}_2Mn^{IV}_2$, S_2: $Mn^{III}Mn^{IV}_3$, S_3: Mn^{IV}_4) have been recently reviewed as spectroscopic models of the OEC.[7] For higher oxidation state complexes ($Mn^{III}Mn^{IV}_3$, Mn^{IV}_4), clusters of different geometries exhibit different ground spin states. As an example, Mn^{IV}_4 complexes can be classified into three categories: (1) linear-chain complexes exhibiting diamagnetic ground states arising from pairwise antiferromagnetic coupling, (2) adamantane shaped complexes possessing ground states of $S = 6$ from ferromagnetic coupling, and most recently, (3) a cuboidal complex displaying an $S = 3$ ground state, representing the first synthetic example corroborating the $S = 3$ spin state assigned to the S_3 state (Figure 5).[61] It is important to note, however, that the number of these examples is still quite limited, and such generalizations of the relationship between cluster geometry and spin state may not be upheld upon further exploration into the synthesis and spectroscopic

characterization of such complexes. Some specific examples are further described in this thesis.

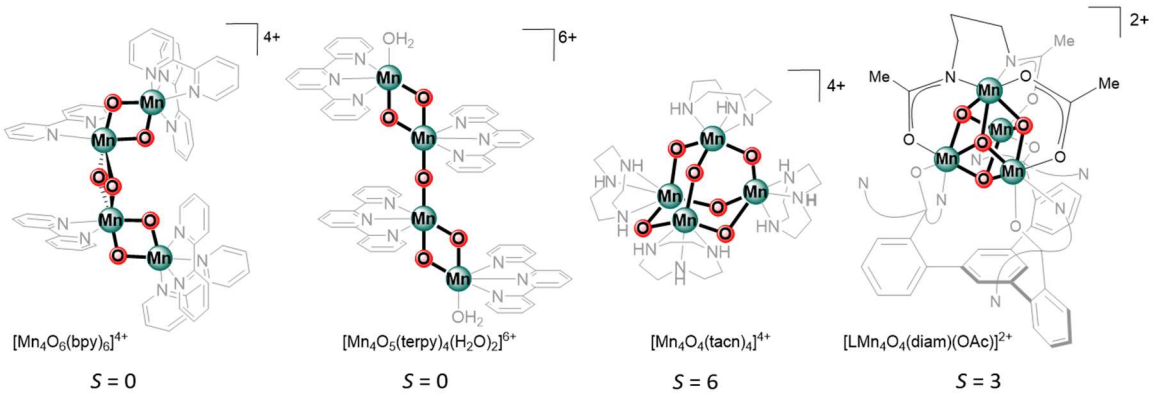

Figure 5. Examples of $Mn^{IV}_4O_x$ complexes of varying geometries and their spin states.

As previously described in the open-closed cubane model, the spin state of the $CaMn^{IV}_3O_4$ cuboidal subsite of the OEC is critical in the spectroscopic interpretation and understanding of the electronic structure of the S-state intermediates. Thus far, only two $Ca_2Mn^{IV}_3O_4$ and $CaMn^{IV}_3O_4$ synthetic complexes have been studied by magnetometry and spectroscopy.[53, 60, 62] Results in Chapter 2 show that additional examples challenge this notion that intact $CaMn^{IV}_3O_4$ cubane cores must have a ferromagnetically coupled trimanganese unit yielding $S = 9/2$.

In the absence of direct and unambiguous structural data for the different intermediates of the OEC, systematic studies that probe structure-function and structure-electronic structure relationships on synthetic complexes of full or partial models provide valuable information for benchmarking against spectroscopic studies of the biological system.

1.3) Electronic structure characterization of multimetallic Mn complexes

As previously described, each S-state intermediate is assigned a characteristic ground spin state(s): S_G (S_0) = 1/2, S_G (S_1) = 0, S_G (S_2) = 1/2 or 5/2, S_G (S_3) = 3.[63] The spin state of the S-state intermediates has often been correlated to conclusions on cluster geometry;[62-63] thus, understanding the magnetic behavior and determination of ground spin state of multimetallic complexes is important.

The energetic ordering of spin states of magnetically coupled transition metal complexes can be described using the Heisenberg-Dirac-van Vleck (HDvV) Hamiltonian (Equation 1), where S_i and S_j are the spins of each metal center and *Jij* are the isotropic exchange coupling constants.[63] Depending on the sign of *J*, the spins can be either aligned to be ferromagnetic ($J_{ij} > 0$) or antiferromagnetic ($J_{ij} < 0$). The magnitude of *J* determines the energetic difference(s) between each possible spin state. Typically, for Mn-oxo complexes, these are the only parameters that need to be considered to account for the magnetic behavior, though other phenomena (i.e., double exchange) may be needed to describe systems such as FeS complexes. Notably, *J* is highly dependent on the distance between metal centers, nature of the bridging ligand(s), and geometric parameters such as bond angles and distances, as demonstrated for a series of dinuclear $Mn^{III}Mn^{IV}O_2$ complexes.[70]

$$\widehat{H} = -2 \sum_{i \neq j}^{i,j \in N} J_{ij} \widehat{S}_i \cdot \widehat{S}_j \qquad (1)$$

Each S-state intermediate is also characterized by distinct EPR spectroscopic signatures. EPR spectroscopy offers a wealth of information pertaining to the electronic structure of multinuclear paramagnetic metal clusters beyond spin state and can be described using the following Hamiltonian (Equation 2). [34, 63-64] In this case, there is the assumption that the exchange interaction represents the largest term of the spin Hamiltonian. The first

term (Zeeman interaction) represents the interaction between the electron spin and external magnetic field (B_0). The second term is the zero-field splitting (ZFS) interaction, in which magnetic interactions between unpaired electrons lifts the degeneracy between magnetic sublevels (for $S > 1/2$). The third term encompasses interactions between the total spin S_T and neighboring magnetic nuclei (i.e., ^{55}Mn, $I = 5/2$), with the hyperfine interactions (A) giving information on spin density/oxidation state. Nuclear Zeeman interactions are typically orders of magnitude smaller than the electronic Zeeman interaction. Nuclear quadrupole interaction (NQI) (for nuclei with $I > 1/2$), represented with the operator P, gives information on the symmetry and magnitudes of electronic charge distribution to a nucleus of interest.

$$\hat{H} = \mu_0 \vec{B}_0 g_{\text{eff}} \hat{S}_T + \hat{S}_T D_{\text{eff}} \hat{S}_T + \sum_j^m \left[\hat{S}_T A_{\text{eff},j} \hat{I}_j + \mu_N g_N \vec{B}_0 \hat{I}_j + \hat{I}_j \hat{P}_j \hat{I}_j \right] \quad (2)$$

Thus, the combination of biochemical and spectroscopic studies on the OEC is powerful not only for inferring cluster geometry, but also for determining local Mn oxidation states, exchange coupling topology of the Mn ions, and details on coordination sphere by probing ligand nuclei (^{13}C, $^{14/15}$N, ^{17}O).[64-69] Furthermore, perturbations to the HS-LS equilibrium and/or line-shape of the multiline signal in the S_2 state of the OEC due to chemical treatment with alcohols, amines, and peroxides have been studied to better understand interactions between the cluster and these analogues for substrate water/hydroxide.[64-66] This area is underexplored for well-defined synthetic tetramanganese complexes, where trends in structural parameters or ligand environment to observable spectroscopic parameters can be established.

1.4) Conclusion

Despite the advances from structural, spectroscopic, biochemical, and coordination chemistry studies described above, aspects of the S-state cycle and mechanism of water oxidation by the OEC remain debated. Development of more accurate synthetic models along with series of complexes amenable for systematic studies probing how the multimetallic nature (cluster geometry, metal identity/oxidation state, nature/protonation state of bridging ligand(s), ligand environment, etc.) affects different aspects of spectroscopy will likely provide exciting new insight into the OEC and its mechanism for water oxidation. In this thesis, models based on the $CaMn^{IV}_3O_4$ cuboidal subunit, models of the $Mn^{III}Mn^{IV}_3O_4$ oxidation state analogous to the S_2 state, and models of the $Mn^{IV}_4O_4$ oxidation state analogous to the S_3 state will be discussed.

1.5) References

(1) Shen, J.-R., The Structure of Photosystem II and the Mechanism of Water Oxidation in Photosynthesis. *Annu. Rev. Plant Biol.* **2015,** *66* (1), 23-48.

(2) Yano, J.; Yachandra, V., Mn_4Ca Cluster in Photosynthesis: Where and How Water is Oxidized to Dioxygen. *Chem. Rev.* **2014,** *114* (8), 4175-4205.

(3) Pantazis, D. A., Missing Pieces in the Puzzle of Biological Water Oxidation. *ACS Catalysis* **2018,** *8* (10), 9477-9507.

(4) Cox, N.; Pantazis, D. A.; Neese, F.; Lubitz, W., Biological Water Oxidation. *Acc. Chem. Res.* **2013,** *46* (7), 1588-1596.

(5) Joliot, P.; Joliot, A., A polarographic method for detection of oxygen production and reduction of Hill reagent by isolated chloroplasts. *Biochim. Biophys. Acta, Bioenerg.* **1968,** *153* (3), 625-634.

(6) Kok, B.; Forbush, B.; McGloin, M., COOPERATION OF CHARGES IN PHOTOSYNTHETIC O2 EVOLUTION–I. A LINEAR FOUR STEP MECHANISM. *Photochem. Photobiol.* **1970,** *11* (6), 457-475.

(7) Lee, H. B.; Oyala, P. H.; Agapie, T., Synthesis, Electronic Structure, and Spectroscopy of Multinuclear Mn Complexes Relevant to the Oxygen Evolving Complex of Photosystem II. In *Oxygen Production and Reduction in Artificial and Natural Systems*, WORLD SCIENTIFIC: 2018; pp 259-283.

(8) Siegbahn, P. E. M., Structures and Energetics for O2 Formation in Photosystem II. *Acc. Chem. Res.* **2009,** *42* (12), 1871-1880.

(9) Paul, S.; Cox, N.; Pantazis, D. A., What Can We Learn from a Biomimetic Model of Nature's Oxygen-Evolving Complex? *Inorg. Chem.* **2017,** *56* (7), 3875-3888.

(10) Paul, S.; Neese, F.; Pantazis, D. A., Structural models of the biological oxygen-evolving complex: achievements, insights, and challenges for biomimicry. *Green Chemistry* **2017,** *19* (10), 2309-2325.

(11) Wieghardt, K., The Active Sites in Manganese-Containing Metalloproteins and Inorganic Model Complexes. *Angewandte Chemie International Edition in English* **1989,** *28* (9), 1153-1172.

(12) Tsui, E. Y.; Kanady, J. S.; Agapie, T., Synthetic Cluster Models of Biological and Heterogeneous Manganese Catalysts for O_2 Evolution. *Inorg. Chem.* **2013,** *52* (24), 13833-13848.

(13) Cox, N.; Pantazis, D. A.; Lubitz, W., Current Understanding of the Mechanism of Water Oxidation in Photosystem II and Its Relation to XFEL Data. *Annu. Rev. Biochem* **2020,** *89* (1), 795-820.

(14) Yocum, C. F.; Yerkes, C. T.; Blankenship, R. E.; Sharp, R. R.; Babcock, G. T., Stoichiometry, inhibitor sensitivity, and organization of manganese associated with photosynthetic oxygen evolution. *Proc. Natl. Acad. Sci. U. S. A.* **1981,** *78* (12), 7507-7511.

(15) Murata, N.; Miyao, M.; Omata, T.; Matsunami, H.; Kuwabara, T., Stoichiometry of components in the photosynthetic oxygen evolution system of Photosystem II particles prepared with Triton X-100 from spinach chloroplasts. *Biochim. Biophys. Acta, Bioenerg.* **1984,** *765* (3), 363-369.

(16) Piccioni, R. G.; Mauzerall, D. C., Increase effected by calcium ion in the rate of oxygen evolution from preparations of Phormidium luridum. *Biochim. Biophys. Acta, Bioenerg.* **1976,** *423* (3), 605-609.
(17) Yocum, C. F., The calcium and chloride requirements of the O_2 evolving complex. *Coord. Chem. Rev.* **2008,** *252* (3), 296-305.
(18) Dubé, C. E.; Mukhopadhyay, S.; Bonitatebus, P. J.; Staples, R. J.; Armstrong, W. H., Tuning Tetranuclear Manganese−Oxo Core Electronic Properties: Adamantane-Shaped Complexes Synthesized by Ligand Exchange. *Inorg. Chem.* **2005,** *44* (14), 5161-5175.
(19) Dubé, C. E.; Sessoli, R.; Hendrich, M. P.; Gatteschi, D.; Armstrong, W. H., A Spin Topological Model for the g = 4.1 S_2 State Photosystem II Water Oxidase Manganese Aggregate. *J. Am. Chem. Soc.* **1999,** *121* (14), 3537-3538.
(20) Dubé, C. E.; Wright, D. W.; Pal, S.; Bonitatebus, P. J.; Armstrong, W. H., Tetranuclear Manganese-Oxo Aggregates Relevant to the Photosynthetic Water Oxidation Center. Crystal Structure, Spectroscopic Properties and Reactivity of Adamantane-Shaped $[Mn_4O_6(bpea)_4]^{4+}$ and the Reduced Mixed-Valence Analog $[Mn_4O_6(bpea)_4]^{3+}$. *J. Am. Chem. Soc.* **1998,** *120* (15), 3704-3716.
(21) Hagen, K. S.; Westmoreland, T. D.; Scott, M. J.; Armstrong, W. H., Structural and electronic consequences of protonation in $\{Mn_4O_6\}^{4+}$ cores: pH dependent properties of oxo-bridged manganese complexes. *J. Am. Chem. Soc.* **1989,** *111* (5), 1907-1909.
(22) Wieghardt, K.; Bossek, U.; Gebert, W., Synthesis of a Tetranuclear Manganese(IV) Cluster with Adamantane Skeleton: $[(C_6H_{15}N_3)_4Mn_4O_6]^{4+}$. *Angewandte Chemie International Edition in English* **1983,** *22* (4), 328-329.
(23) Ruettinger, W. F.; Campana, C.; Dismukes, G. C., Synthesis and Characterization of $Mn_4O_4L_6$ Complexes with Cubane-like Core Structure: A New Class of Models of the Active Site of the Photosynthetic Water Oxidase. *J. Am. Chem. Soc.* **1997,** *119* (28), 6670-6671.
(24) Ruettinger, W. F.; Ho, D. M.; Dismukes, G. C., Protonation and Dehydration Reactions of the $Mn_4O_4L_6$ Cubane and Synthesis and Crystal Structure of the Oxidized Cubane $[Mn_4O_4L_6]^+$: A Model for the Photosynthetic Water Oxidizing Complex. *Inorg. Chem.* **1999,** *38* (6), 1036-1037.
(25) Hendrickson, D. N.; Christou, G.; Schmitt, E. A.; Libby, E.; Bashkin, J. S.; Wang, S.; Tsai, H. L.; Vincent, J. B.; Boyd, P. D. W., Photosynthetic water oxidation center: spin frustration in distorted cubane $Mn^{IV}Mn^{III}_3$ model complexes. *J. Am. Chem. Soc.* **1992,** *114* (7), 2455-2471.
(26) Christou, G.; Vincent, J. B., The molecular 'double-pivot' mechanism for water oxidation. *Biochimica et Biophysica Acta (BBA) - Reviews on Bioenergetics* **1987,** *895* (3), 259-274.
(27) Chen; Collomb, M.-N.; Duboc, C.; Blondin, G.; Rivière, E.; Faller, J. W.; Crabtree, R. H.; Brudvig, G. W., New Linear High-Valent Tetranuclear Manganese-Oxo Cluster Relevant to the Oxygen-Evolving Complex of Photosystem II with Oxo, Hydroxo, and Aqua Coordinated to a Single Mn(IV). *Inorg. Chem.* **2005,** *44* (25), 9567-9573.
(28) Blondin, G.; Davydov, R.; Philouze, C.; Charlot, M.-F.; Styring, t.; Åkermark, B.; Girerd, J.-J.; Boussac, A., Electron paramagnetic resonance study of the

S =1/2 ground state of a radiolysis-generated manganese(III)–trimanganese(IV) form of $[Mn^{IV}_4O_6(bipy)_6]^{4+}$ (bipy = 2,2′ -bipyridine). Comparison with the photosynthetic Oxygen Evolving Complex†. *J. Chem. Soc., Dalton Trans.* **1997,** (21), 4069-4074.

(29) Philouze, C.; Blondin, G.; Girerd, J.-J.; Guilhem, J.; Pascard, C.; Lexa, D., Aqueous Chemistry of High-Valent Manganese. Structure, Magnetic, and Redox Properties of a New Type of Mn-Oxo Cluster, $[Mn_4^{IV}O_4(bpy)_6]^{4+}$: Relevance to the Oxygen Evolving Center in Plants. *J. Am. Chem. Soc.* **1994,** *116* (19), 8557-8565.

(30) Chan, M. K.; Armstrong, W. H., Support for a dimer of di-.mu.-oxo dimers model for the photosystem II manganese aggregate. Synthesis and properties of [(Mn2O2)2(tphpn)2](ClO4)4. *J. Am. Chem. Soc.* **1991,** *113* (13), 5055-5057.

(31) Mukhopadhyay, S.; Mandal, S. K.; Bhaduri, S.; Armstrong, W. H., Manganese Clusters with Relevance to Photosystem II. *Chem. Rev.* **2004,** *104* (9), 3981-4026.

(32) Vrettos, J. S.; Limburg, J.; Brudvig, G. W., Mechanism of photosynthetic water oxidation: combining biophysical studies of photosystem II with inorganic model chemistry. *Biochim. Biophys. Acta, Bioenerg.* **2001,** *1503* (1), 229-245.

(33) Yachandra, V. K.; DeRose, V. J.; Latimer, M. J.; Mukerji, I.; Sauer, K.; Klein, M. P., Where Plants Make Oxygen: a Structural Model for the Photosynthetic Oxygen-Evolving Manganese Cluster. *Science* **1993,** *260* (5108), 675-679.

(34) Peloquin, J. M.; Campbell, K. A.; Randall, D. W.; Evanchik, M. A.; Pecoraro, V. L.; Armstrong, W. H.; Britt, R. D., ^{55}Mn ENDOR of the S_2-State Multiline EPR Signal of Photosystem II: Implications on the Structure of the Tetranuclear Mn Cluster. *J. Am. Chem. Soc.* **2000,** *122* (44), 10926-10942.

(35) Britt, R. D.; Campbell, K. A.; Peloquin, J. M.; Gilchrist, M. L.; Aznar, C. P.; Dicus, M. M.; Robblee, J.; Messinger, J., Recent pulsed EPR studies of the Photosystem II oxygen-evolving complex: implications as to water oxidation mechanisms. *Biochim. Biophys. Acta, Bioenerg.* **2004,** *1655*, 158-171.

(36) Zouni, A.; Witt, H.-T.; Kern, J.; Fromme, P.; Krauss, N.; Saenger, W.; Orth, P., Crystal structure of photosystem II from Synechococcus elongatus at 3.8 Å resolution. *Nature* **2001,** *409* (6821), 739-743.

(37) Kamiya, N.; Shen, J.-R., Crystal structure of oxygen-evolving photosystem II from Thermosynechococcus vulcanus at 3.7-Å resolution. *Proc. Natl. Acad. Sci. U. S. A.* **2003,** *100* (1), 98-103.

(38) Ferreira, K. N.; Iverson, T. M.; Maghlaoui, K.; Barber, J.; Iwata, S., Architecture of the Photosynthetic Oxygen-Evolving Center. *Science* **2004,** *303* (5665), 1831-1838.

(39) Umena, Y.; Kawakami, K.; Shen, J.-R.; Kamiya, N., Crystal structure of oxygen-evolving photosystem II at a resolution of 1.9 Å. *Nature* **2011,** *473*, 55.

(40) Pantazis, D. A.; Ames, W.; Cox, N.; Lubitz, W.; Neese, F., Two Interconvertible Structures that Explain the Spectroscopic Properties of the Oxygen-Evolving Complex of Photosystem II in the S_2 State. *Angew. Chem. Int. Ed.* **2012,** *51* (39), 9935-9940.

(41) Bovi, D.; Narzi, D.; Guidoni, L., The S_2 State of the Oxygen-Evolving Complex of Photosystem II Explored by QM/MM Dynamics: Spin Surfaces and Metastable States Suggest a Reaction Path Towards the S_3 State. *Angew. Chem. Int. Ed.* **2013,** *52* (45), 11744-11749.

(42) Vinyard, D. J.; Khan, S.; Askerka, M.; Batista, V. S.; Brudvig, G. W., Energetics of the S_2 State Spin Isomers of the Oxygen-Evolving Complex of Photosystem II. *J. Phys. Chem. B* **2017,** *121* (5), 1020-1025.

(43) Boussac, A.; Un, S.; Horner, O.; Rutherford, A. W., High-Spin States (S ≥ 5/2) of the Photosystem II Manganese Complex. *Biochemistry* **1998,** *37* (12), 4001-4007.

(44) Horner, O.; Rivière, E.; Blondin, G.; Un, S.; Rutherford, A. W.; Girerd, J.-J.; Boussac, A., SQUID Magnetization Study of the Infrared-Induced Spin Transition in the S2 State of Photosystem II: Spin Value Associated with the g = 4.1 EPR Signal. *J. Am. Chem. Soc.* **1998,** *120* (31), 7924-7928.

(45) Lohmiller, T.; Ames, W.; Lubitz, W.; Cox, N.; Misra, S. K., EPR Spectroscopy and the Electronic Structure of the Oxygen-Evolving Complex of Photosystem II. *Appl. Magn. Reson.* **2013,** *44* (6), 691-720.

(46) Lohmiller, T.; Krewald, V.; Navarro, M. P.; Retegan, M.; Rapatskiy, L.; Nowaczyk, M. M.; Boussac, A.; Neese, F.; Lubitz, W.; Pantazis, D. A.; Cox, N., Structure, ligands and substrate coordination of the oxygen-evolving complex of photosystem II in the S2 state: a combined EPR and DFT study. *PCCP* **2014,** *16* (24), 11877-11892.

(47) Suga, M.; Akita, F.; Sugahara, M.; Kubo, M.; Nakajima, Y.; Nakane, T.; Yamashita, K.; Umena, Y.; Nakabayashi, M.; Yamane, T.; Nakano, T.; Suzuki, M.; Masuda, T.; Inoue, S.; Kimura, T.; Nomura, T.; Yonekura, S.; Yu, L.-J.; Sakamoto, T.; Motomura, T.; Chen, J.-H.; Kato, Y.; Noguchi, T.; Tono, K.; Joti, Y.; Kameshima, T.; Hatsui, T.; Nango, E.; Tanaka, R.; Naitow, H.; Matsuura, Y.; Yamashita, A.; Yamamoto, M.; Nureki, O.; Yabashi, M.; Ishikawa, T.; Iwata, S.; Shen, J.-R., Light-induced structural changes and the site of O=O bond formation in PSII caught by XFEL. *Nature* **2017,** *543*, 131.

(48) Kern, J.; Alonso-Mori, R.; Tran, R.; Hattne, J.; Gildea, R. J.; Echols, N.; Glöckner, C.; Hellmich, J.; Laksmono, H.; Sierra, R. G.; Lassalle-Kaiser, B.; Koroidov, S.; Lampe, A.; Han, G.; Gul, S.; DiFiore, D.; Milathianaki, D.; Fry, A. R.; Miahnahri, A.; Schafer, D. W.; Messerschmidt, M.; Seibert, M. M.; Koglin, J. E.; Sokaras, D.; Weng, T.-C.; Sellberg, J.; Latimer, M. J.; Grosse-Kunstleve, R. W.; Zwart, P. H.; White, W. E.; Glatzel, P.; Adams, P. D.; Bogan, M. J.; Williams, G. J.; Boutet, S.; Messinger, J.; Zouni, A.; Sauter, N. K.; Yachandra, V. K.; Bergmann, U.; Yano, J., Simultaneous Femtosecond X-ray Spectroscopy and Diffraction of Photosystem II at Room Temperature. *Science* **2013,** *340* (6131), 491.

(49) Kern, J.; Chatterjee, R.; Young, I. D.; Fuller, F. D.; Lassalle, L.; Ibrahim, M.; Gul, S.; Fransson, T.; Brewster, A. S.; Alonso-Mori, R.; Hussein, R.; Zhang, M.; Douthit, L.; de Lichtenberg, C.; Cheah, M. H.; Shevela, D.; Wersig, J.; Seuffert, I.; Sokaras, D.; Pastor, E.; Weninger, C.; Kroll, T.; Sierra, R. G.; Aller, P.; Butryn, A.; Orville, A. M.; Liang, M.; Batyuk, A.; Koglin, J. E.; Carbajo, S.; Boutet, S.; Moriarty, N. W.; Holton, J. M.; Dobbek, H.; Adams, P. D.; Bergmann, U.; Sauter, N. K.; Zouni, A.; Messinger, J.; Yano, J.; Yachandra, V. K., Structures of the intermediates of Kok's photosynthetic water oxidation clock. *Nature* **2018,** *563* (7731), 421-425.

(50) Kern, J.; Tran, R.; Alonso-Mori, R.; Koroidov, S.; Echols, N.; Hattne, J.; Ibrahim, M.; Gul, S.; Laksmono, H.; Sierra, R. G.; Gildea, R. J.; Han, G.; Hellmich, J.; Lassalle-Kaiser, B.; Chatterjee, R.; Brewster, A. S.; Stan, C. A.; Glöckner, C.; Lampe, A.; DiFiore, D.; Milathianaki, D.; Fry, A. R.; Seibert, M. M.; Koglin, J. E.;

Gallo, E.; Uhlig, J.; Sokaras, D.; Weng, T.-C.; Zwart, P. H.; Skinner, D. E.; Bogan, M. J.; Messerschmidt, M.; Glatzel, P.; Williams, G. J.; Boutet, S.; Adams, P. D.; Zouni, A.; Messinger, J.; Sauter, N. K.; Bergmann, U.; Yano, J.; Yachandra, V. K., Taking snapshots of photosynthetic water oxidation using femtosecond X-ray diffraction and spectroscopy. *Nature Communications* **2014,** *5*, 4371.

(51) Simon, P. S.; Makita, H.; Bogacz, I.; Fuller, F.; Bhowmick, A.; Hussein, R.; Ibrahim, M.; Zhang, M.; Chatterjee, R.; Cheah, M. H.; Chernev, P.; Doyle, M. D.; Brewster, A. S.; Alonso-Mori, R.; Sauter, N. K.; Bergmann, U.; Dobbek, H.; Zouni, A.; Messinger, J.; Kern, J.; Yachandra, V. K.; Yano, J., Capturing the sequence of events during the water oxidation reaction in photosynthesis using XFELs. *FEBS Lett.* **2023,** *597* (1), 30-37.

(52) Cox, N.; Retegan, M.; Neese, F.; Pantazis, D. A.; Boussac, A.; Lubitz, W., Electronic structure of the oxygen-evolving complex in photosystem II prior to O-O bond formation. *Science* **2014,** *345* (6198), 804.

(53) Mukherjee, S.; Stull, J. A.; Yano, J.; Stamatatos, T. C.; Pringouri, K.; Stich, T. A.; Abboud, K. A.; Britt, R. D.; Yachandra, V. K.; Christou, G., Synthetic model of the asymmetric [Mn_3CaO_4] cubane core of the oxygen-evolving complex of photosystem II. *Proc. Natl. Acad. Sci. U. S. A.* **2012,** *109* (7), 2257.

(54) Kanady, J. S.; Lin, P.-H.; Carsch, K. M.; Nielsen, R. J.; Takase, M. K.; Goddard, W. A.; Agapie, T., Toward Models for the Full Oxygen-Evolving Complex of Photosystem II by Ligand Coordination To Lower the Symmetry of the Mn_3CaO_4 Cubane: Demonstration That Electronic Effects Facilitate Binding of a Fifth Metal. *J. Am. Chem. Soc.* **2014,** *136* (41), 14373-14376.

(55) Zhang, C.; Chen, C.; Dong, H.; Shen, J.-R.; Dau, H.; Zhao, J., A synthetic Mn_4Ca-cluster mimicking the oxygen-evolving center of photosynthesis. *Science* **2015,** *348* (6235), 690.

(56) Chen, C.; Chen, Y.; Yao, R.; Li, Y.; Zhang, C., Artificial Mn_4Ca Clusters with Exchangeable Solvent Molecules Mimicking the Oxygen-Evolving Center in Photosynthesis. *Angew. Chem. Int. Ed.* **2019,** *58* (12), 3939-3942.

(57) Yao, R.; Li, Y.; Chen, Y.; Xu, B.; Chen, C.; Zhang, C., Rare-Earth Elements Can Structurally and Energetically Replace the Calcium in a Synthetic Mn_4CaO_4-Cluster Mimicking the Oxygen-Evolving Center in Photosynthesis. *J. Am. Chem. Soc.* **2021,** *143* (42), 17360-17365.

(58) Nguyen, A. I.; Darago, L. E.; Balcells, D.; Tilley, T. D., Influence of a "Dangling" Co(II) Ion Bound to a [$MnCo_3O_4$] Oxo Cubane. *J. Am. Chem. Soc.* **2018,** *140* (29), 9030-9033.

(59) Chen, C.; Xu, B.; Yao, R.; Chen, Y.; Zhang, C., Synthesizing Mechanism of the Mn_4Ca Cluster Mimicking the Oxygen-Evolving Center in Photosynthesis. *ChemSusChem* **2022,** *15* (6), e202102661.

(60) Kanady, J. S.; Tsui, E. Y.; Day, M. W.; Agapie, T., A Synthetic Model of the Mn_3Ca Subsite of the Oxygen-Evolving Complex in Photosystem II. *Science* **2011,** *333* (6043), 733.

(61) Lee, H. B.; Marchiori, D. A.; Chatterjee, R.; Oyala, P. H.; Yano, J.; Britt, R. D.; Agapie, T., S = 3 Ground State for a Tetranuclear $Mn^{IV}_4O_4$ Complex Mimicking the S_3 State of the Oxygen-Evolving Complex. *J. Am. Chem. Soc.* **2020,** *142* (8), 3753-3761.

(62) Krewald, V.; Neese, F.; Pantazis, D. A., On the Magnetic and Spectroscopic Properties of High-Valent Mn_3CaO_4 Cubanes as Structural Units of Natural and Artificial Water-Oxidizing Catalysts. *J. Am. Chem. Soc.* **2013,** *135* (15), 5726-5739.

(63) Krewald, V.; Retegan, M.; Neese, F.; Lubitz, W.; Pantazis, D. A.; Cox, N., Spin State as a Marker for the Structural Evolution of Nature's Water-Splitting Catalyst. *Inorg. Chem.* **2016,** *55* (2), 488-501.

(64) Oyala, P. H.; Stich, T. A.; Stull, J. A.; Yu, F.; Pecoraro, V. L.; Britt, R. D., Pulse Electron Paramagnetic Resonance Studies of the Interaction of Methanol with the S_2 State of the Mn_4O_5Ca Cluster of Photosystem II. *Biochemistry* **2014,** *53* (50), 7914-7928.

(65) Oyala, P. H.; Stich, T. A.; Debus, R. J.; Britt, R. D., Ammonia Binds to the Dangler Manganese of the Photosystem II Oxygen-Evolving Complex. *J. Am. Chem. Soc.* **2015,** *137* (27), 8829-8837.

(66) Marchiori, D. A.; Oyala, P. H.; Debus, R. J.; Stich, T. A.; Britt, R. D., Structural Effects of Ammonia Binding to the Mn_4CaO_5 Cluster of Photosystem II. *J. Phys. Chem. B* **2018,** *122* (5), 1588-1599.

(67) Rapatskiy, L.; Ames, W. M.; Pérez-Navarro, M.; Savitsky, A.; Griese, J. J.; Weyhermüller, T.; Shafaat, H. S.; Högbom, M.; Neese, F.; Pantazis, D. A.; Cox, N., Characterization of Oxygen Bridged Manganese Model Complexes Using Multifrequency ^{17}O-Hyperfine EPR Spectroscopies and Density Functional Theory. *J. Phys. Chem. B* **2015,** *119* (43), 13904-13921.

(68) Rapatskiy, L.; Cox, N.; Savitsky, A.; Ames, W. M.; Sander, J.; Nowaczyk, M. M.; Rögner, M.; Boussac, A.; Neese, F.; Messinger, J.; Lubitz, W., Detection of the Water-Binding Sites of the Oxygen-Evolving Complex of Photosystem II Using W-Band ^{17}O Electron–Electron Double Resonance-Detected NMR Spectroscopy. *J. Am. Chem. Soc.* **2012,** *134* (40), 16619-16634.

(69) Lohmiller, T.; Krewald, V.; Sedoud, A.; Rutherford, A. W.; Neese, F.; Lubitz, W.; Pantazis, D. A.; Cox, N., The First State in the Catalytic Cycle of the Water-Oxidizing Enzyme: Identification of a Water-Derived μ-Hydroxo Bridge. *J. Am. Chem. Soc.* **2017,** *139* (41), 14412-14424.

CHAPTER 2

$CaMn_3^{IV}O_4$ Cubane Models of the Oxygen Evolving Complex: Spin Ground States S < 9/2 and the Effect of Oxo Protonation

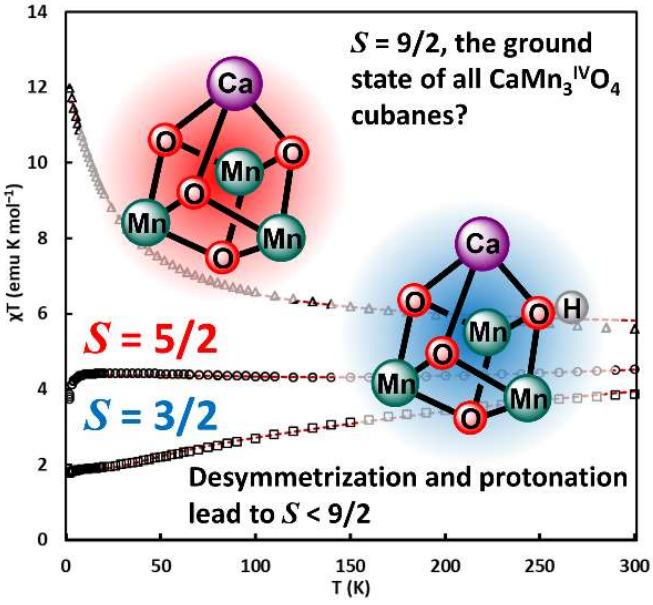

The text for this chapter was reproduced in part from:

Lee, H. B., Shiau, A. A., Marchiori, D. A., Oyala, P. H., Yoo, B. K., Kaiser, J. T., Rees, D. C., Britt, R. D., Agapie, T., *Angew. Chem. Int. Ed.*, **2021**, *60*, 17671 – 17679.

Abstract

The mechanism of biological water oxidation performed by the Oxygen Evolving Complex (OEC) of Photosystem II (PSII) is an important area of study. Current understanding of the magnetic interactions between the Mn ions in the pentametallic $CaMn_4$ core is based on computational results that hypothesize an intact $CaMn^{IV}_3O_xH_n$ (x = 4 – 0, n = 0 – 4) core must be ferromagnetically coupled, giving a $S = 9/2$ ground state. Due to synthetic challenges, few model complexes in the literature have been studied in the context of benchmarking these results. Herein, the synthesis, crystal structure, SQUID magnetometry, and EPR spectroscopy of a desymmetrized $CaMn_3O_4$ cluster is described and compared to a series of related complexes. In this series, magnetic and spectroscopic differences arising from differences in ligand environment and protonation state of a bridging oxo are explored. Results suggest small distortions in metal-oxo bond lengths imposed by ligand rigidity greatly affect the magnetic coupling in the trimanganese unit, in direct contrast to computationally predicted coupling schemes for $CaMn^{IV}_3O_xH_n$ subunits.

2.1) Introduction

Biological water oxidation is performed by the Oxygen Evolving Complex (OEC) of Photosystem II (PSII).[1-3] Structural characterization of the OEC reveals a pentametallic $CaMn_4O_5$ cluster with a unique geometry featuring a cuboidal $CaMn_3O_4$ subsite and a "dangler" Mn center bound to the cluster via a bridging oxo or hydroxo motif.[4-6] Mechanistic studies have been performed in the context of the Joliot-Kok cycle of S_n ($n = 0 – 4$) states. In the absence of direct structural and spectroscopic studies on the elusive S_4 state, mechanistic proposals for O−O bond formation rely heavily on interpretations of lower S_n state intermediates.[7-20]

Each S_n state intermediate adopts a characteristic spin ground state:[21] S_G (S_0) = 1/2,[22] S_G (S_1) = 0,[23] S_G (S_2) = 1/2 or 5/2,[22, 24-26] S_G (S_3) = 3.[12, 27-28] Notably, the spin states of these intermediates are often considered as markers for cluster geometry. The interconversion between the two spin states observed for the S_2 state (S = 1/2 and S = 5/2) has been computationally assigned to structural changes in the $CaMn_4$ core.[10] A key difference in the two structures is the location of the O(5) oxo moiety, with concomitant changes in the magnetic coupling interactions between Mn centers resulting in different S_G. In the "closed-cubane" structure (Figure 1), it is proposed that ferromagnetic coupling within the Mn^{IV}_3 of the $CaMn^{IV}_3O_4$ cuboidal subunit leads to a S = 9/2 spin state. Antiferromagnetic coupling to the dangler Mn^{III} (S = 2) results in an overall S_G = 5/2. In this model, shifting the position of the O(5) ligand to the "open-cubane" structure (Figure 1) to a bridging position between Mn(3) and Mn(4) results in an internal valence redistribution. This $CaMn^{III}Mn^{IV}_2$ subsite is proposed to have S = 1 spin state and antiferromagnetic coupling to the dangler Mn^{IV} (S = 3/2) leads to an overall S_G = 1/2. This structural isomerism model can explain the spin state

interconversion, however, only the open-cubane form has been observed crystallographically under turnover conditions.[6, 29] XFEL (X-ray free electron laser) structural studies of the S_3 state show incorporation of a sixth oxygen O(6) ligand between Mn(1) and Mn(4) in proximity to O(5), a oxo implicated in O–O bond formation.[6] This intermediate is proposed to originate from the open-cubane form of the S_2 state yet is also proposed to have a similar magnetic coupling scheme to the closed-cubane S_2 isomer, featuring all ferromagnetic coupling in the $CaMn^{IV}_3$ subunit ($S = 9/2$). Antiferromagnetic coupling to the dangling Mn^{IV} ($S = 3/2$) leads to the observed $S_G = 3$. Furthermore, XAS studies performed on the high spin form of the S_2 state show differences compared to the low spin form, though calculated Mn-Mn distances also differ from the proposed closed cubane structure.[15]

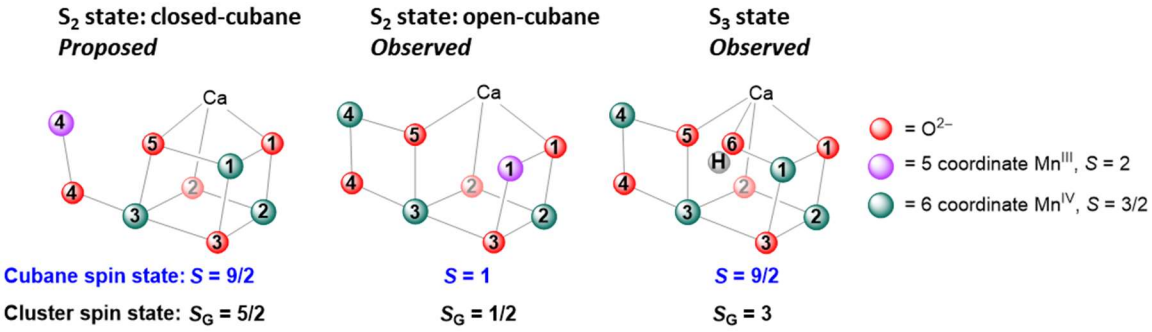

Figure 1. Proposed and observed structures of the $CaMn_4$ core of the OEC in the S_2 and S_3 states. Spin state of the cuboidal subunit highlighted in blue. Antiferromagnetic coupling to dangler Mn(4) leads to observed spin ground state S_G.

An alternative interpretation of the spin state interconversion in the S_2 state is based on the observed pH dependence of this process, where at higher pH, the high spin (HS) form is favored.[20, 30] While atomistic details following deprotonation are unknown, the aquo moiety bound to Mn(4) was hypothesized to be the site of deprotonation, as no pH dependent behavior was observed when NH_3 is bound to Mn(4) at this site.[14, 20, 30] Importantly, structural changes to the OEC through either oxo exchange or (de)protonation can affect the nature and

magnitude of the magnetic exchange coupling *J*, which in turn can affect both S_G and the sign and magnitude of projected ^{55}Mn hyperfine coupling constants.[12, 31] Computationally, one study has proposed that protonation of a bridging oxo O(4) can lead to a high spin state with an open-cubane structure.[20] Overall, discrepancies between different structural, spectroscopic, and computational studies highlight the intricacy of the relationship between geometry, nature of bridging ligands, and electronic structure of tetramanganese clusters.

Multimetallic model complexes of appropriate metal composition, oxidation state, and cluster geometry have been demonstrated to be valuable in benchmarking and influencing mechanistic proposals.[32-37] Access to closer structural mimics of the OEC has been limited by synthetic challenges.[38-39] While representing an incomplete model of the OEC, cuboidal $CaMn^{IV}_3O_4$ complexes can be studied to better understand the magnetic properties of the closed cubane subsite of the S_2 state, as any changes in the magnetic coupling of this unit will ultimately affect the total spin observed following magnetic coupling to the dangler. Asymmetric $Ca_2Mn^{IV}_3O_4$ and *pseudo-C*$_3$ symmetric $CaMn^{IV}_3O_4$ model complexes have been assigned to $S_G = 9/2$ based on computational, magnetometry, and spectroscopic characterization (Figure 2).[38, 40] Building upon these observations, computational studies concluded that the spin ground state of $CaMn^{IV}_3O_4$ complexes and all possible protonation analogs (i.e., $CaMn^{IV}_3O_n(OH)_{(4-n)}$ $(n = 0-4)$) is $S_G = 9/2$.[41] Importantly, however, systematic studies that probe the effects of oxo protonation and structural changes in $CaMn^{IV}_3O_4$ complexes have not been reported.

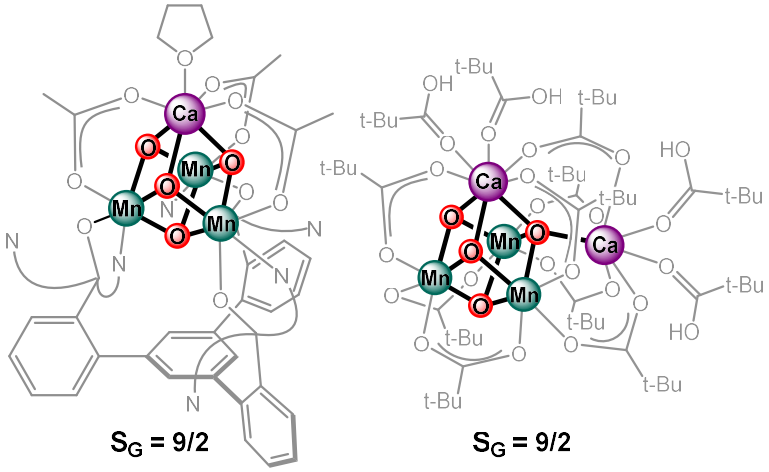

Figure 2. Previously reported complexes featuring $CaMn^{IV}_3O_4$ cores.[38, 40]

Herein, we report the synthesis, crystal structure, MicroED structure, magnetic susceptibility, and EPR spectroscopy of a series of $CaMn^{IV}_3O_4$ complexes varying in symmetry and oxo protonation state. These subtle changes in cluster geometry result in complexes with S_G = 5/2 and S_G = 3/2. Importantly, these complexes maintain intact $CaMn^{IV}_3O_4$ cores, demonstrating that smaller changes such as distortions in symmetry induced by ligand environment and notably protonation state of bridging ligands, can have significant effects in cluster spin state. These studies complement the pH-dependent conversion between the high and low spin forms of the S_2 state, suggesting that protonation states of bridging or terminal oxygen-based ligands in the OEC can be connected to spin state changes.

2.2) Synthesis and crystal structure

The acetate-bridged complex **1-Ca** was used as a precursor for other complexes (Figure 3).[40] Desymmetrization of this *pseudo-C*$_3$ symmetric cluster can be achieved by treatment of **1-Ca** with $H_2N_4O_2$ in a protonolysis reaction, substituting two acetate ligands for a chelating bis-oximate.[42] Since the MicroED structure of **2-Ca** is not of sufficient

quality for detailed discussion of bond lengths, analogous Y complexes were synthesized, and trends will be discussed instead, *vide infra*.

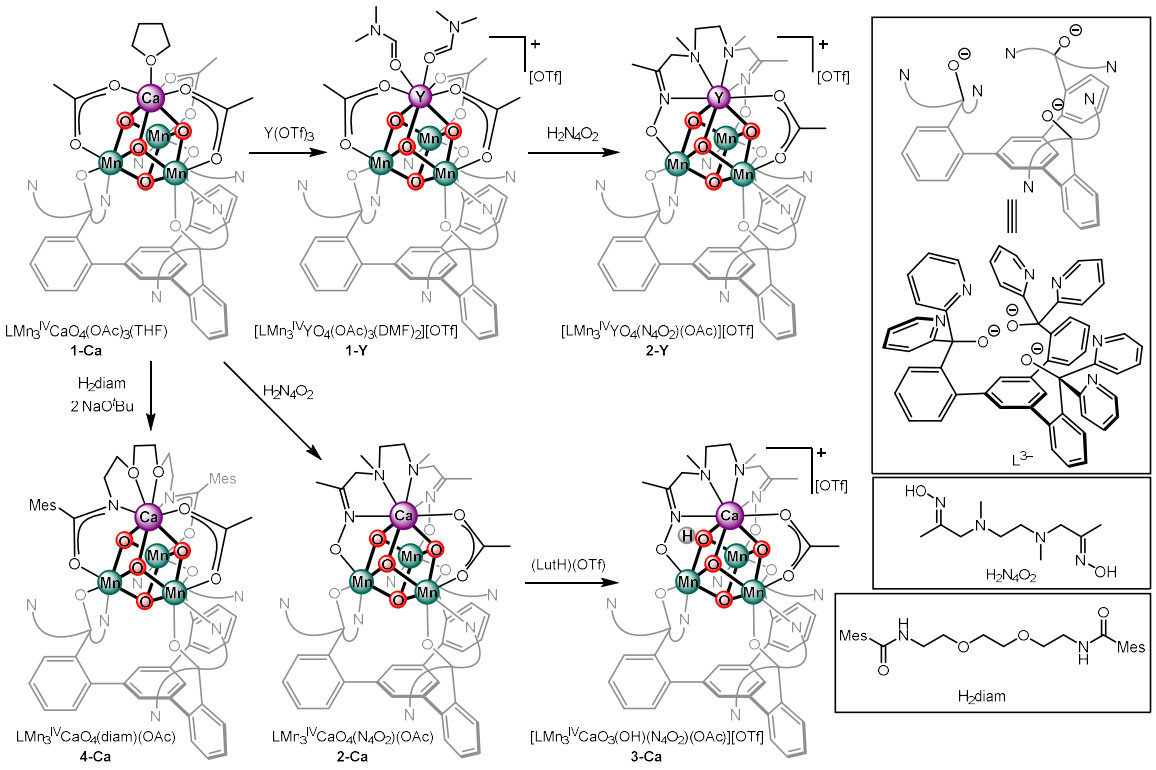

Figure 3. Synthesis of desymmetrized complexes supported by tethered dianionic ligands studied in this work. Complexes **1-Ca**, **2-Ca**, and **3-Ca** are previously reported.[40, 42]

Toward expanding the series of *pseudo-C*$_S$ symmetric $CaMn_3O_4$ clusters, desymmetrization using bulky benzoate ligands was targeted. Starting from an incomplete cuboidal $LMn_3O_4(py)_3(OTf)$ precursor, addition of two equivalents of $M(OBz^{p\text{-}tBu})_2$ (M = Ca, Sr) results in reconstitution of a *pseudo-C*$_3$ symmetric $CaMn_3O_4$ cubane supported by bridging benzoate ligands.[53] This reactivity is reminiscent of the synthesis of heterometallic MFe_3S_4 clusters from a tris-thiolate supported $[Fe_3S_4]^0$ complex reported by Holm and coworkers.[43-46] Increasing steric bulk of these benzoate ligands was hypothesized to allow for control over stoichiometry of these ligands around the cubane core. To enforce steric bulk that points towards the faces of the cubane, *m*-terphenyl benzoates were utilized. Flanking

aryl rings could direct steric bulk towards the other faces of the cubane. Reaction of $LMn_3O_4(py)_3(OTf)$, one equivalent of $Ca(OTf)_2$, and three equivalents of $NaOBz^{Ph2}$ results in the formation of a benzene-soluble species displaying only two paramagnetically shifted peaks in the ^1H NMR spectrum, suggesting the formation of a highly symmetric species (**5-Ca**, Figure 4). The X-ray structure is consistent with the formulation $LCaMn_3O_4(OBz^{Ph2})_3(py)$ (Figure 5). Metalation conditions using fewer than three equivalents of the benzoate, however, only resulted in the isolation of **5-Ca**, as determined by ^1H NMR spectroscopy. Further tuning of ligand sterics may allow for access to the desired *pseudo-C*$_S$ symmetric $CaMn_3O_4$ cuboidal cluster, but control of ligand stoichiometry via tethering bridging ligands appears more promising.

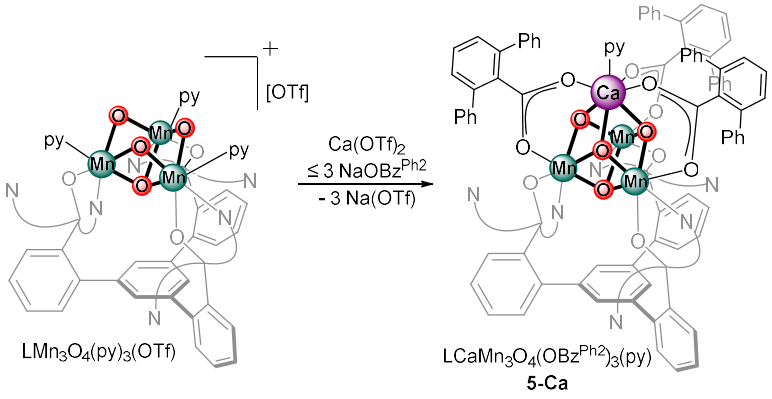

Figure 4. Synthesis of bulky benzoate complex **5-Ca**.

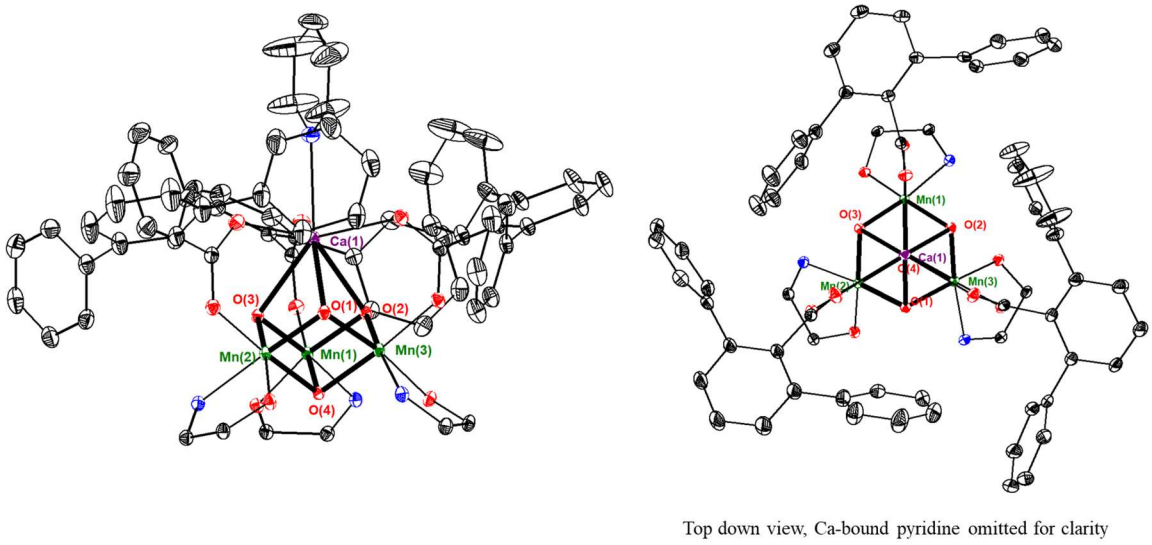

Figure 5. Truncated crystal structure of **5-Ca**. Ca (purple), Mn (green), O (red), N(blue), C (black). Bolded bonds highlight M-oxo bonds. Thermal ellipsoids are plotted at 50% probability.

Toward expanding the series of $CaMn_3O_4$ complexes with chelating ligands of similar basicity to the oximate moieties, an amidate-bridged complex was targeted. Treatment of **1-Ca** with a triethylene glycol derived bis-amide (H_2diam) in the presence of NaO^{t}Bu leads to the formation of **4-Ca**, successfully demonstrating a second *pseudo-C*$_S$ symmetric $CaMn^{IV}_3O_4$ cuboidal complex. The crystal structure of **4-Ca** is consistent with the $LCaMn_3O_4$(diam)(OAc) formulation in which two acetate moieties of **1-Ca** are replaced by the chelating bis-amidate moiety (Figure 6).

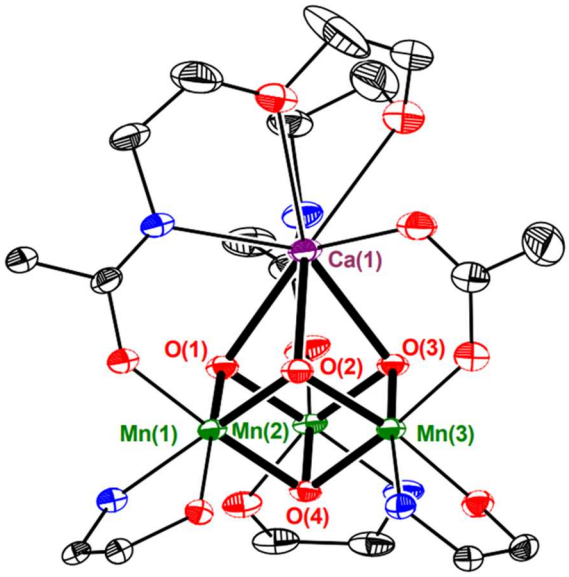

Figure 6. Truncated crystal structure of **4-Ca**. Ca (purple), Mn (green), O (red), N(blue), C (black). Bolded bonds highlight M-oxo bonds. Thermal ellipsoids are plotted at 50% probability.

To explore the effects of oxo protonation state, the $CaMn_3O_4$ core of **2-Ca** can be further desymmetrized via treatment with 2,6-lutidinium triflate, which results in the protonation of a unique oxo in between the oximate moieties to afford a complex with a $CaMn_3O_3(OH)$ core (**3-Ca**).[42] Unfortunately, analogous reactivity with **1-Ca**, **4-Ca**, and **5-Ca** resulted in intractable mixtures. Overall, **1-Ca(Y)**, **2-Ca(Y)**, **3-Ca**, **4-Ca**, and **5-Ca** represent a unique series of complexes mimicking the cuboidal substructure of the OEC in which cluster symmetry, heterometal identity, bridging ligand, and oxo protonation state is systematically varied.

Metal-oxo distances were compared across this series to understand the effect of chelating ligands and oxo protonation on structure. Interestingly, comparisons between complexes **1-Ca** and **4-Ca** reveal that the high flexibility of the diamidate ligand in **4-Ca** does not induce major structural changes in the metal-oxo core (Table 1). Within each complex **1-Ca**, **4-Ca**, or **5-Ca**, Ca-oxo, Mn-Mn, and M-O(4) distances are all similar to each

other, with the other six Mn-oxo bond distances around the *pseudo*-C_3 axis limited to a small range between 1.83 and 1.87 Å. Notably, the oximate-bridged complexes (**2-Ca**, **2-Y**, and previously reported compound **2-Gd**) do not possess this high symmetry within the metal-oxo core. The structure of **2-Y** was used as a surrogate for that of **2-Ca** for structural comparisons because precise structural metrics could not be reliably obtained from the MicroED structure of **2-Ca**. This comparison is reasonable because the structural parameters of **2-Y** and **2-Gd** are very similar to each other, with Mn-oxo distances within 0.01 Å, implying that general structural trends are observable.[47] In **2-Y**, the Y-O(1) distance is significantly shorter by 0.1 Å than the other two Y-oxo distances. Notably, O(1) is the unique oxo located between the two oximate donors, suggesting that the metal-oxo core has been both structurally and electronically desymmetrized. Another observable trend, albeit of a smaller magnitude, is that the Mn-oxo distances *trans* to the Mn-oximate bonds are slightly elongated compared to the Mn-oxo distances *trans* to the Mn-acetate/amidate bonds. Similarly, Mn-Mn distances in **2-Y** also distort in a manner that is consistent with a *pseudo*-C_S symmetry with the mirror plane containing the Y(1)−O(1) vector and bisecting the Mn(1)−Mn(2) vector. On the basis that the three-fold symmetry of **1-Y**(**Gd**) is broken upon substitution of two acetates with the bridging oximate N_4O_2, a similar structural distortion is expected in **2-Ca**, away from the *pseudo*-C_3 symmetry of **1-Ca**. The structure of **3-Ca** is also consistent with a *pseudo*-C_S symmetry, with Mn-(μ^3-OH) distances that are slightly elongated by roughly 0.1 Å in comparison to the corresponding Mn-(μ^3-O) distances in **1-Ca**.[42] Overall, distinct structural changes are observed depending on the nature of the bridging ligands and the protonation state of bridging oxos; these relatively small structural

changes across the series have a significant influence in the electronic structure of the $CaMn_3^{IV}O_4$ core.

Table 1. Metal-oxo distances (Å) in selected complexes. Bold distances for emphasis.

	1-Ca[40]	**2-Y**[48]	**2-Gd**[47]	**3-Ca**[42]	**4-Ca**	**5-Ca**
Ca/Y-O(1)	2.431(2)	**2.308(2)**	**2.319(5)**	2.401(5)	2.450(3)	2.438(1)
Ca/Y-O(2)	2.391(2)	2.396(2)	2.443(4)	2.513(5)	2.412(2)	2.428(1)
Ca/Y-O(3)	2.430(2)	2.422(3)	2.445(4)	2.468(5)	2.398(3)	2.433(2)
Mn(1)-O(1)	1.864(2)	1.863(3)	1.853(5)	**1.926(5)**	1.861(3)	1.867(2)
Mn(1)-O(2)	1.837(3)	1.882(2)	1.885(5)	1.842(6)	1.835(3)	1.829(2)
Mn(1)-O(4)	1.912(2)	**1.941(3)**	**1.945(4)**	1.945(5)	1.921(2)	1.915(2)
Mn(2)-O(1)	1.833(2)	1.875(3)	1.871(5)	1.943(5)	1.829(3)	1.832(2)
Mn(2)-O(3)	1.863(3)	1.849(2)	1.853(5)	1.811(5)	1.885(3)	1.869(1)
Mn(2)-O(4)	1.907(2)	**1.946(3)**	**1.946(4)**	1.958(5)	1.919(2)	1.915(2)
Mn(3)-O(2)	1.869(2)	1.836(3)	1.844(4)	1.830(5)	1.870(3)	1.870(2)
Mn(3)-O(3)	1.828(2)	1.869(3)	1.857(4)	1.863(5)	1.838(3)	1.835(2)
Mn(3)-O(4)	1.913(3)	1.906(2)	1.895(5)	1.893(5)	1.913(3)	1.915(2)
Mn(1)-Mn(2)	2.833(1)	**2.882(1)**	**2.870(1)**	**2.968(2)**	2.833(1)	2.8276(6)
Mn(1)-Mn(3)	2.830(1)	2.836(1)	2.837(2)	2.828(2)	2.818(1)	2.8259(6)
Mn(2)-Mn(3)	2.839(1)	2.840(1)	2.837(2)	2.841(2)	2.838(1)	2.8604(5)

2.3) Magnetometry

To gain insight into the magnetic exchange coupling between the Mn centers of $CaMn^{IV}_3O_4$ complexes, magnetic susceptibility studies were performed on this series of clusters. In a threefold-symmetric Mn^{IV}_3 system, all J values are expected to be the same. Lowering the symmetry to a *pseudo*-C_S symmetric Mn^{IV}_3 core, the exchange coupling can be described using an isotropic spin exchange Hamiltonian with two distinct magnetic interactions, with a unique $J' = J_{12}$ and $J = J_{13} = J_{23}$ (Equation 1).[49] Defining $S' = S_1 + S_2$ and $S_T = S' + S_3$, application of the vector coupling model gives rise to twelve $|S_T, S'\rangle$ states for $S_1 = S_2 = S_3 = 3/2$ in a Mn^{IV}_3 system (Figure 7). While the relative energies of these twelve states is dependent on both the signs and magnitudes of J and J', the ground state can be predicted based on the ratio of J/J' (Figure 8).[38, 41]

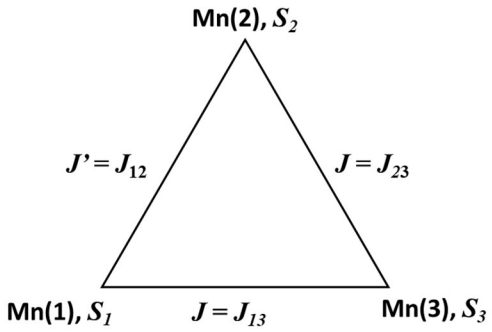

$S_T = S_{12} + S_3, S_{12} + S_3 - 1, \ldots, |S_{12} - S_3|$
$S_{12} = S_1 + S_2, S_1 + S_2 - 1, \ldots, 1/2$ or 0

For $S_i = 3/2$ (Mn^{IV}):

$S_{12} = 3$	$S_T = 9/2, 7/2, 5/2, 3/2$
$S_{12} = 2$	$S_T = 7/2, 5/2, 3/2, 1/2$
$S_{12} = 1$	$S_T = 5/2, 3/2, 1/2$
$S_{12} = 0$	$S_T = 1/2$

Figure 7. Vector coupling model gives rise to twelve $|S_T, S'\rangle$ states for a Mn^{IV}_3 system.

$$\hat{H} = -2J(S_1S_3 + S_2S_3) - 2J'S_1S_2 \qquad (1)$$

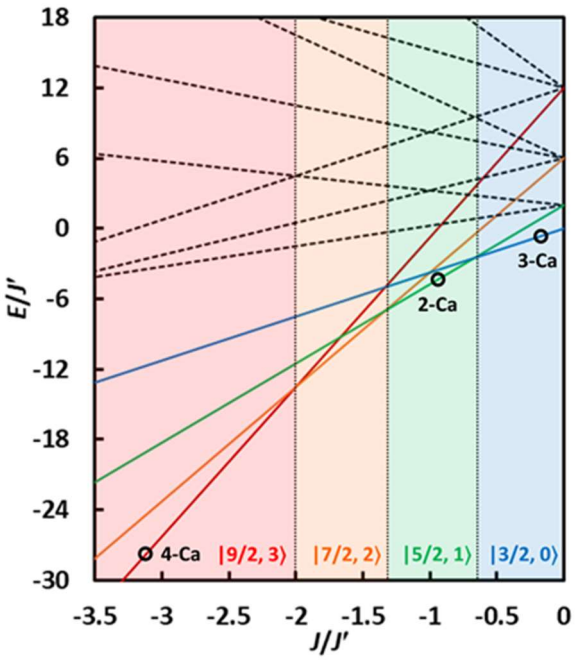

Figure 8. Relative energies E/J' of the $|S_T, S'\rangle$ states as a function of J/J' (for $J' < 0$). Each colored region represents a different spin ground state. Experimental points shown as black circles.

Although complex **1-Ca** is *pseudo*-C_3 symmetric, its magnetic susceptibility data was found to be better modeled using a *pseudo*-C_S symmetric coupling scheme utilizing $J = 3.5$ cm^{-1} and $J' = -1.8$ cm^{-1}.[40] In the series **2-Ca**~**4-Ca**, complex **4-Ca** has the most similar structural parameters within the cluster core to that of **1-Ca** and was studied via SQUID

magnetometry. The magnetic susceptibility data for **4-Ca** shows a χT value of 5.60 emu·K·mol^{-1} at 300 K, indicative of antiferromagnetic coupling. Upon cooling, the χT value increases to reach a maximum of 11.98 emu·K·mol^{-1} at 2 K, in good agreement with a S_G = 9/2 (g = 2) system (12.375 emu·K·mol^{-1}). This data can be modeled with a *pseudo-*C_S symmetric coupling scheme, yielding parameters J = 5.0 cm^{-1}, J' = −1.6 cm^{-1}, g = 1.97. The calculated energy level diagram using these values indicates small energy gaps between the |9/2, 3⟩ ground state and the |7/2, 2⟩ first excited state (5.5 cm^{-1}) as well as between the ground state and the |5/2, 1⟩ second excited state (8.8 cm^{-1}). The sharp decrease in χT from its maximum value upon increasing temperature corroborates these calculated small energy separations. The J/J' ratio of −3.125 is within the expected range for S_G = 9/2 and is directly comparable to the ratio of −3.75 obtained for the asymmetric $Ca_2Mn^{IV}{}_3O_4$ complex reported by Christou and coworkers (Figure 8). The reduced magnetization data for **4-Ca** shows little deviation from the ideal Brillouin function for S_G = 9/2, indicating the presence of a small zero field splitting value (D = −0.1 cm^{-1}, determined by EPR).

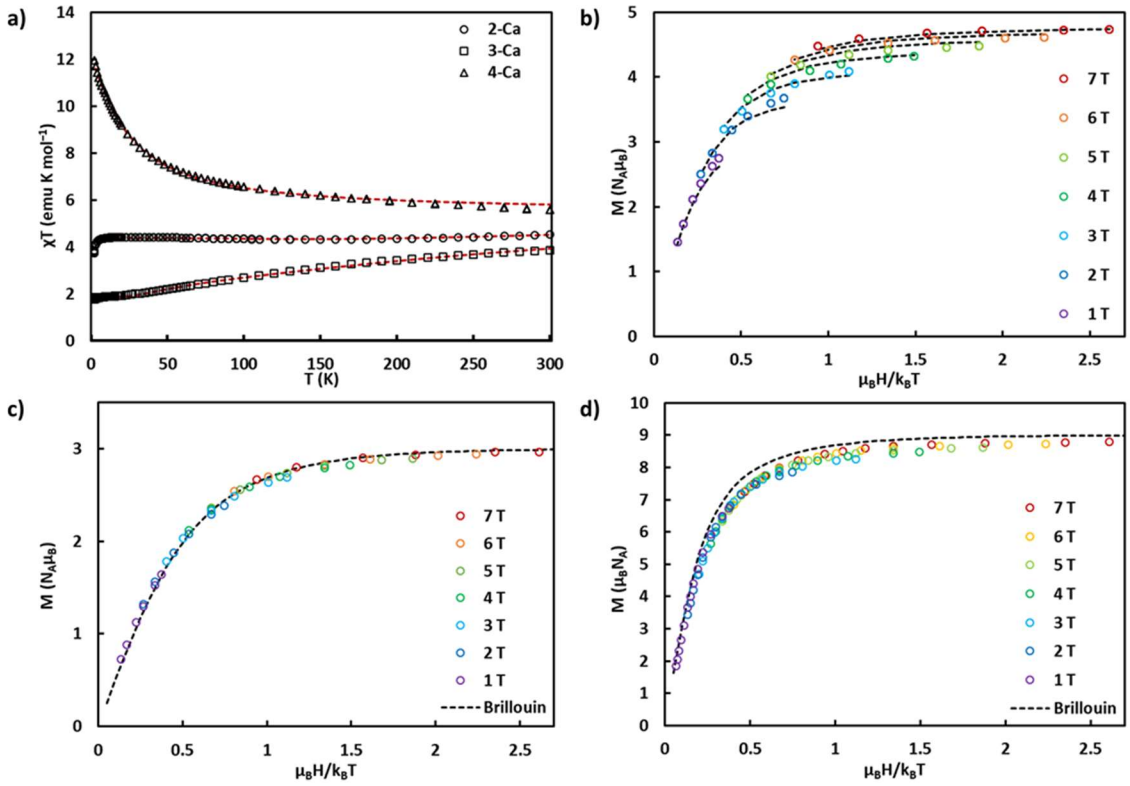

Figure 9. a) χT vs. T plot of complexes **2-Ca**, **3-Ca**, and **4-Ca** with corresponding fits to the data. **b)–d)** Reduced magnetization plot of **2-Ca**, **3-Ca**, and **4-Ca**, respectively. See text for fit parameters.

Complexes **2-Ca** and **3-Ca** were also studied via SQUID magnetometry (Figure 9). Importantly, both complexes do not display S_G = 9/2, deviating from computational predictions for $CaMn^{IV}_3O_4H_x$ (x = 0 – 4) cuboidal complexes. Magnetic susceptibility data for **2-Ca** can be fit as S_G = 5/2 (g = 1.99, J = 250 ± 50 cm^{-1}, J' = −280 ± 50 cm^{-1}), with a narrower range of the J/J' ratio between −0.90 and −0.93.

Interestingly, upon selective protonation of the bridging oxo between the two oximate moieties to form complex **3-Ca**, a change in the ground spin state is observed. Magnetic susceptibility data for **3-Ca** shows a χT value of 3.856 at 300 K and this decreases monotonically with temperature to reach a value of 1.886 at 10 K, in good agreement with the expected value of 1.875 for S_G = 3/2 (g = 2). This data can be simulated using the

parameters $J = 11\ cm^{-1}$, $J' = -55\ cm^{-1}$, $g = 2.0$, with a J/J' ratio of −0.2. Together, complexes **2-Ca** and **3-Ca** demonstrate intact $CaMn^{IV}_3O_4$ cuboidal complexes need not necessarily have a $S_G = 9/2$.

2.4) EPR spectroscopy

These desymmetrized complexes were studied by EPR spectroscopy. While not amenable for a simple qualitative analysis ($D < h\nu$ at X-band), the spectrum of **4-Ca** suggests a $S_G = 9/2$ with multiple overlapping transitions from the five Kramers doublets and is reminiscent of the spectrum of the $Ca_2Mn_3O_4$ complex with an $S_G = 9/2$ ground state (Figure 10).[38] The ZFS parameters of **4-Ca** were obtained by simultaneously fitting spectra obtained at X- and D-band (130 GHz). At higher microwave frequencies, the electron Zeeman term that splits the energy levels of a spin system in an applied magnetic field may be appreciably larger than that of the ZFS parameter. This is the case for **4-Ca** at 130 GHz, where $h\nu >> D$. In such cases, the resulting EPR spectrum is centered around the g value that defines the total spin system. The width of the spectrum is determined by D, while the spacing of the EPR transitions is determined by E/D. The D-band electron-spin echo EPR spectrum of **4-Ca** (Figure 11) displays approximately nine transitions centered about $g = 1.99$ and spans approximately 1.5 T. The transitions that appear at magnetic fields lower than 4.67 T ($g = 1.99$) are evenly spaced by approximately 200 mT, while those at fields higher than 4.67 T are unevenly spaced. This is consistent with a small, negative ZFS parameter that is axial ($D = -0.1\ cm^{-1}$, $E/D = 0.11$).

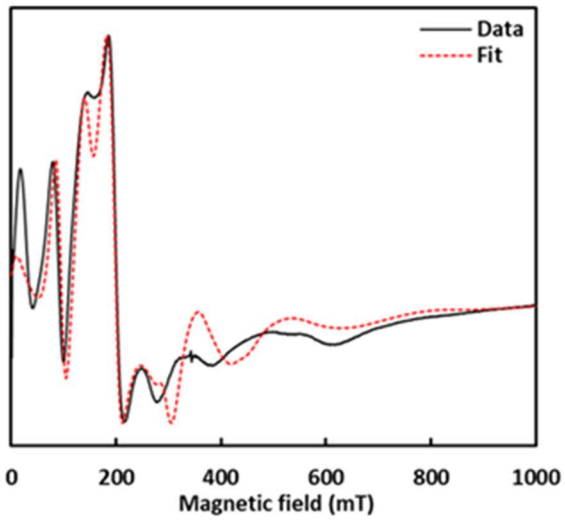

Figure 10. X-band CW EPR spectrum of **4-Ca** collected at T = 5 K (black traces) and simulation (dashed red traces). Simulation parameters: $S = 9/2$, $g = 1.99$, $D = -0.1$ cm^{-1}, $E/D = 0.11$. Acquisition parameters: frequency = 9.6371 MHz, power = 8 mW, conversion time = 82 ms, modulation amplitude = 4 G.

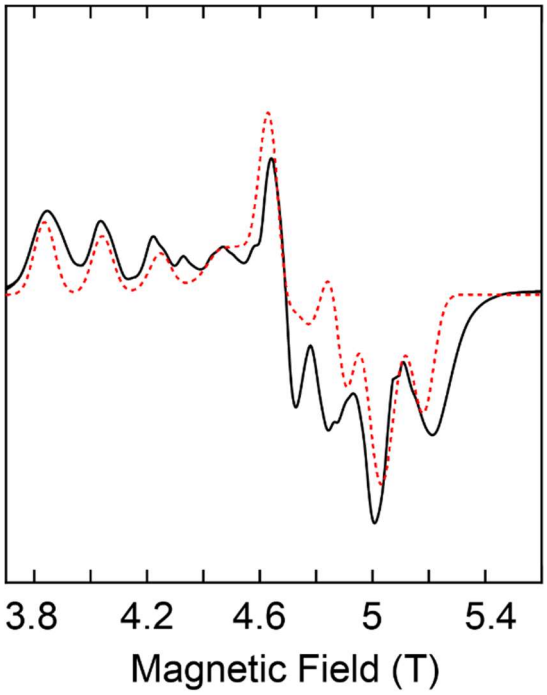

Figure 11. Pseudomodulated (derivative-like) D-band frozen solution EPR spectrum of **4-Ca** collected at 7 K (black trace) and corresponding simulation (red trace). Simulation parameters: $S = 9/2$, $g = 1.99$, $D = 0.1$ cm^{-1}, $E/D = 0.11$.

In comparison, the X-band CW EPR spectra of complexes **2-Ca** and **3-Ca** can be qualitatively explained using rhombograms (Figure 12). For half-integer spin states $S > 1/2$ and in the regime where $D \gg h\nu$ (~ 0.3 cm^{-1} at X-band), peak positions are primarily determined by the E/D ratio, where E and D represent the transverse and axial components of the zero-field splitting parameter, respectively. Overall, EPR spectroscopic studies of **2-Ca~4-Ca** are consistent with the electronic structure and spin ground state description obtained from magnetic susceptibility studies.

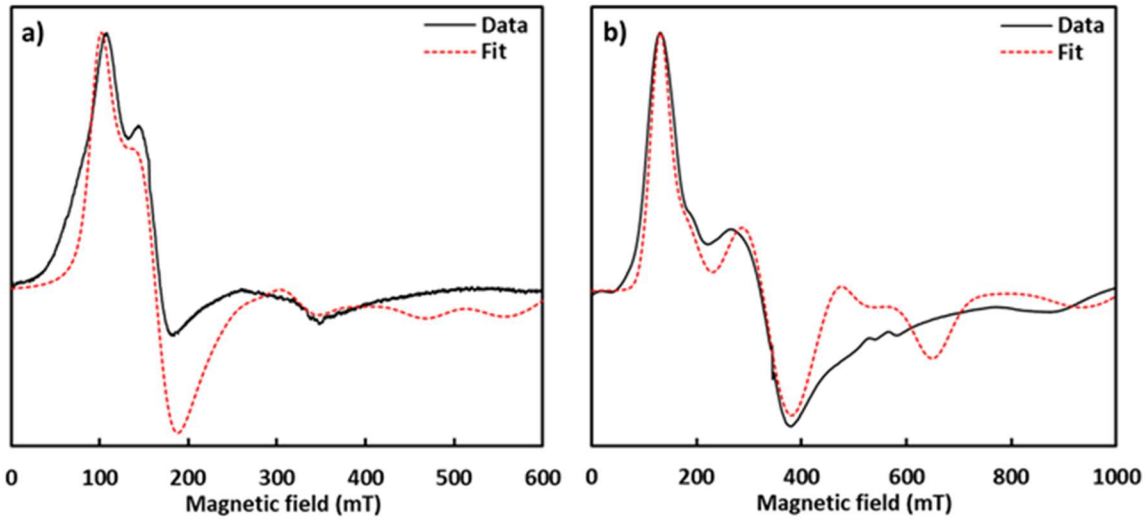

Figure 12. X-band CW EPR spectra collected at T = 5 K (black traces) and simulations (dashed red traces). **(a) 2-Ca**, $S = 5/2$, $g = 1.96$, $D = 0.3$ cm^{-1}, $E/D = 0.06$, fwhm distribution 0.03. Acquisition parameters: frequency = 9.3663 MHz, power = 20 mW, conversion time = 82 ms, modulation amplitude = 8 G. **(b) 3-Ca**, $S = 3/2$, $g = 1.98$, $D = 0.28$ cm^{-1}, $E/D = 0.33$. Acquisition parameters: frequency = 9.6399 MHZ, power = 8 mW, conversion time = 10 ms, modulation amplitude = 8 G.

2.5) Discussion

In conclusion, a series of $CaMn^{IV}_3O_4$ cuboidal complexes have been synthesized and characterized by sc-XRD/MicroED, magnetometry, and EPR spectroscopy, representing the first set of experimental studies that directly addresses the effect of systematic changes in cluster geometry and bridging oxo protonation on the spin state structure of $CaMn^{IV}_3O_4$

cubane models of the OEC. Our results demonstrate that the electronic structure of the $CaMn^{IV}_3$ unit is highly sensitive to small changes in geometric parameters in the metal-oxo core, nature of the bridging ligands, and protonation state of bridging oxo moieties. Complexes with *pseudo-C*$_3$ symmetric metal-oxo cores demonstrate a $S_G = 9/2$, reflecting the predicted behavior of the cuboidal $CaMn^{IV}_3$ subsite of the closed cubane isomer for the S_2 state of the OEC as well as computational predictions for synthetic complexes. However, it is important that desymmetrization of the cluster core, as seen in complexes **2-Ca** and **3-Ca**, results in complexes with spin ground states such as $S_G = 3/2$ and 5/2. Our results show that different relative ratio of J values can lead to different ground states, contrasting with the idea that the ground state of $CaMn^{IV}_3O_n(OH)_{(4-n)}$ ($n = 0 – 4$) complexes must necessarily be $S_G = 9/2$ as previously proposed. Nevertheless, while the present results demonstrate that closed $CaMn^{IV}_3O_n(OH)_{(4-n)}$ cubane motifs can have spin states other than $S = 9/2$, they do not rule out such an interpretation for the $CaMn^{IV}_3$ subunit of the OEC.

2.6) Experimental

General Considerations

Reactions were performed in an N_2-filled glovebox unless noted otherwise. Glassware was oven dried at 150 ºC for at least 2 hours prior to use and allowed to cool under vacuum. All reagents were used as received unless otherwise stated. Anhydrous tetrahydrofuran (THF) was purchased from Aldrich in 18 L Pure-Pac^{TM} containers. Anhydrous CH_3CN and THF were purified by sparging with nitrogen for 15 minutes and then passing under nitrogen pressure through a column of activated A2 alumina. $CDCl_3$ and C_6D_6 were purchased from Cambridge Isotope Laboratories. C_6D_6 was dried over Na/benzophenone, degassed by three freeze-pump-thaw cycles and vacuum-transferred prior

to use. ^{1}H NMR spectra were recorded on a Varian 300 or 500 MHz instrument, with shifts reported relative to the residual solvent peak. Complexes **1-Ca**, **2-Ca**, **3-Ca**, and **2-Y** were synthesized according to published procedures.

Synthesis of H_2diam:

Under ambient atmosphere, a stirring CH_2Cl_2 solution of 2,2'-(ethylenedioxy)bis(ethylamine) (1 mL, 6.8 mmol, 1 equiv) and triethylamine (4 mL, 28.7 mmol, 4.2 equiv) was cooled to 0 °C in an ice-water bath and was treated with 2,4,6-trimethylbenzoyl chloride (2.32 mL, 13.9 mmol, 2.04 equiv) dropwise, resulting in an exothermic reaction and immediate precipitation of a colorless solid. After the addition was complete, the reaction mixture was warmed to room temperature and allowed to stir for 16 hours. Water was added, and the organic layer was separated, washed with saturated aqueous $NaHCO_3$, washed with brine, dried over anhydrous $MgSO_4$, and filtered. Volatiles were removed under reduced pressure, and the residue was washed with copious amounts of hexanes and Et_2O to yield the desired compound as a colorless powder. Yield: (2.49 g, 83 %). ^{1}H NMR (500 MHz, $CDCl_3$): δ 6.80 (s, 4H), 5.98 (bs, 2H), 3.64−3.60 (overlapping m and s, 8H), 3.56 (m, 4H), 2.25−2.24 (overlapping s, 18H) ppm. ^{13}C NMR (125.7 MHz, $CDCl_3$): δ 170.65, 138.60, 135.01, 134.22, 128.30, 70.35, 69.98, 39.38, 21.20, 19.15 ppm. HRMS (FAB+): calculated for $C_{26}H_{36}N_2O_4$: 440.5840; found: 441.2746 [M+H]

Synthesis of $LCaMn_3O_4$(diam)(OAc) (**4-Ca**):

To a stirred suspension of **1-Ca** (252 mg, 0.18 mmol, 1 equiv) in THF (10 mL) was added H_2diam (89 mg, 0.20 mmol, 1.1 equiv). After stirring the reaction mixture at room temperature for 5 minutes, sodium *tert*-butoxide (43 mg, 0.45 mmol, 2.5 equiv) was added and additional THF was added to adjust the volume of the reaction to 20 mL. After stirring

the reaction at room temperature for 16 hours, the reaction mixture became homogenous. All volatiles were removed under reduced pressure, and the solid residue was triturated with pentane (3 mL). The solid was collected on a pad of Celite, rinsed with more pentane, and extracted with benzene. All volatiles were removed from the filtrate under reduced pressure, yielding **4-Ca** as a red-brown powder. Yield: 182 mg, 62%. Crystals suitable for X-ray crystallography were obtained from a slow vapor diffusion of Et_2O into a concentrated solution of **4-Ca** in benzene. ^{1}H NMR (300 MHz, C_6D_6): δ 94.4, 81.2, 20.3, 13.7, −14.7, −16.2, −16.7 ppm. Analysis calculated for $C_{88}H_{79}CaMn_3N_8O_{13}$ (**4-Ca**·$0.5C_6H_6$): C 63.61, H 4.79, N 6.74; found: C 63.71, H 5.02, N 6.50.

Synthesis of $LCaMn_3O_4(OBz^{Ph2})_3$ (**5-Ca**):

To an acetonitrile solution of $LMn_3O_4(py)_3(OTf)$ (50 mg, 0.034 mmol, 1 equiv), $Ca(OTf)_2$ (12.6 mg, 0.037 mmol, 1.1 equiv) and $NaOBz^{Ph2}$ (21.2 mg, 0.072 mmol, 2.1 equiv) were added as THF solutions. The reaction mixture was stirred at room temperature for 16 hrs. The red-brown precipitate was collected over Celite, washed with acetonitrile and Et_2O, and extracted with benzene. All volatiles were removed under reduced pressure, yielding **5-Ca** as a red-brown powder. Crystals suitable for X-ray crystallography were obtained from slow vapor diffusion of Et_2O into a concentrated pyridine solution of **5-Ca**. ^{1}H NMR (300 MHz, C_6D_6): δ 23.7, −17.9 ppm.

NMR spectroscopy

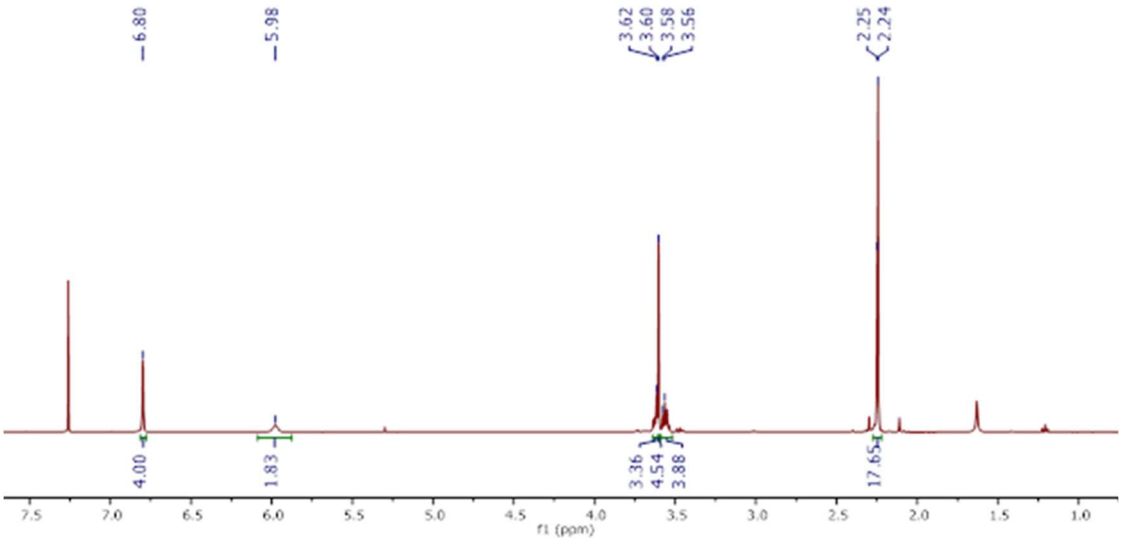

Figure 13. ^{1}H NMR of H_2diam in $CDCl_3$.

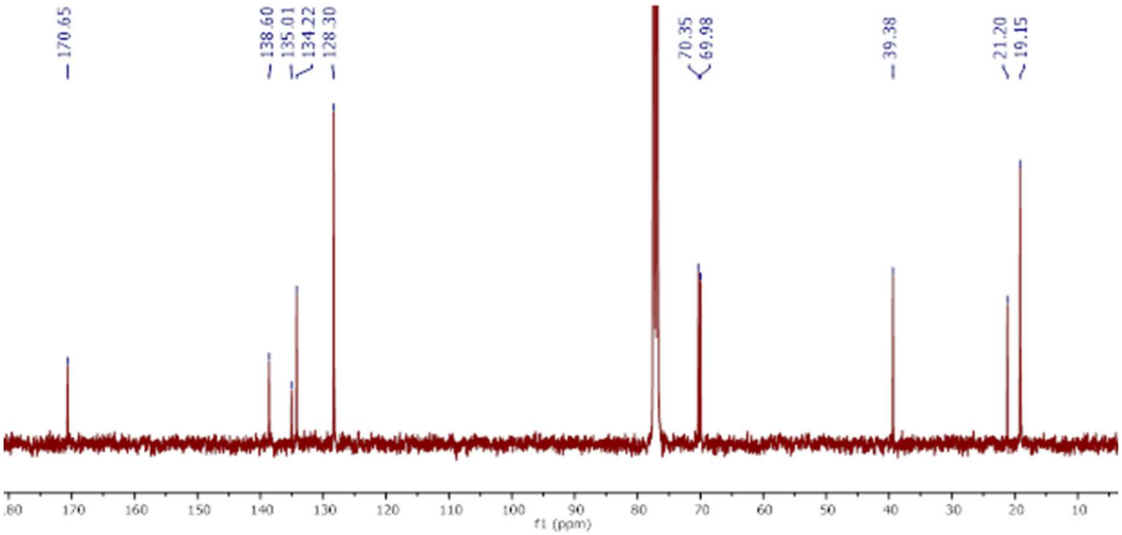

Figure 14. ^{13}C NMR of H_2diam in $CDCl_3$.

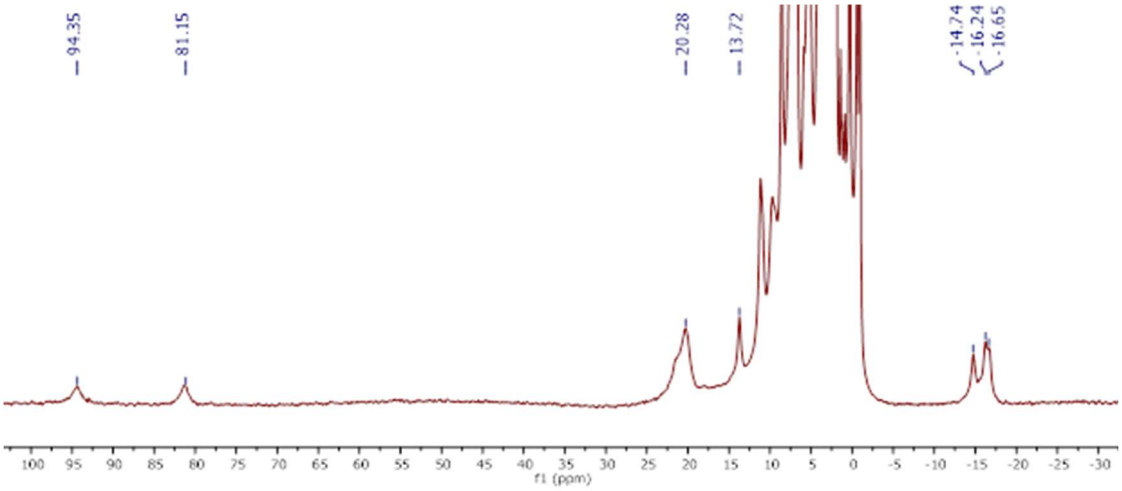

Figure 15. ^{1}H NMR of **4-Ca** in C_6D_6.

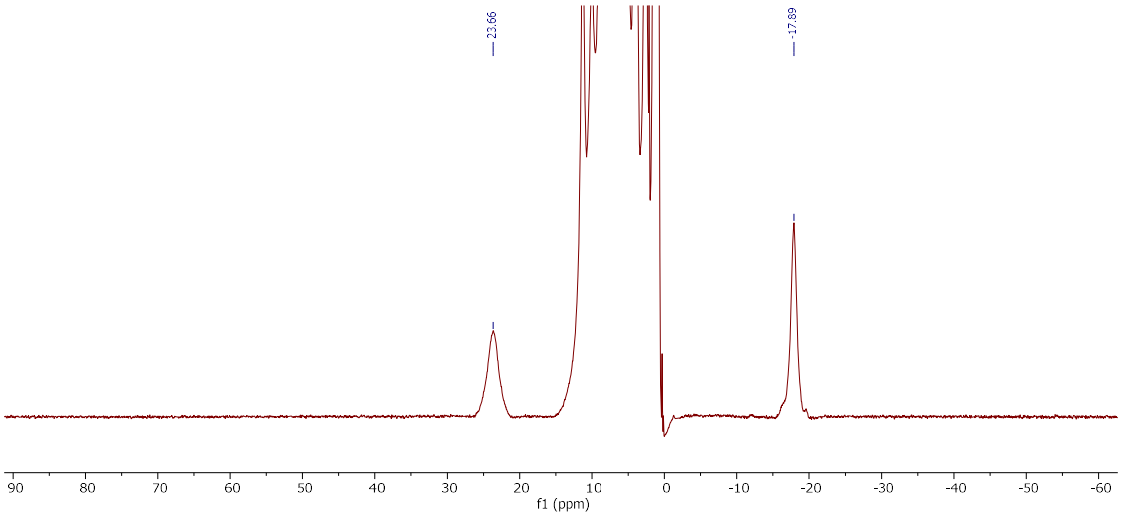

Figure 16. ^{1}H NMR of **5-Ca** in C_6D_6.

ESI-MS spectrometry

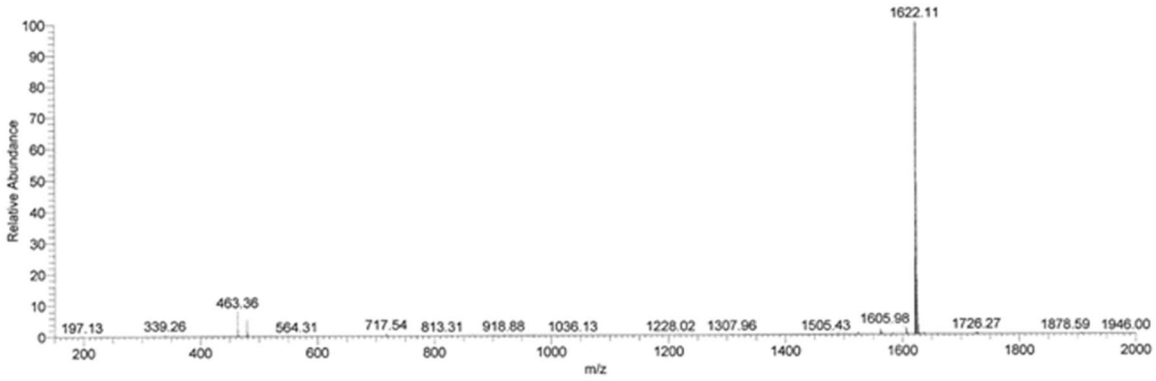

Figure 17. ESI-MS of **4-Ca**. Peak assignment: $[LCaMn_3O_4(diam)(OAc)]^+$ (m/z = 1622).

Electrochemistry

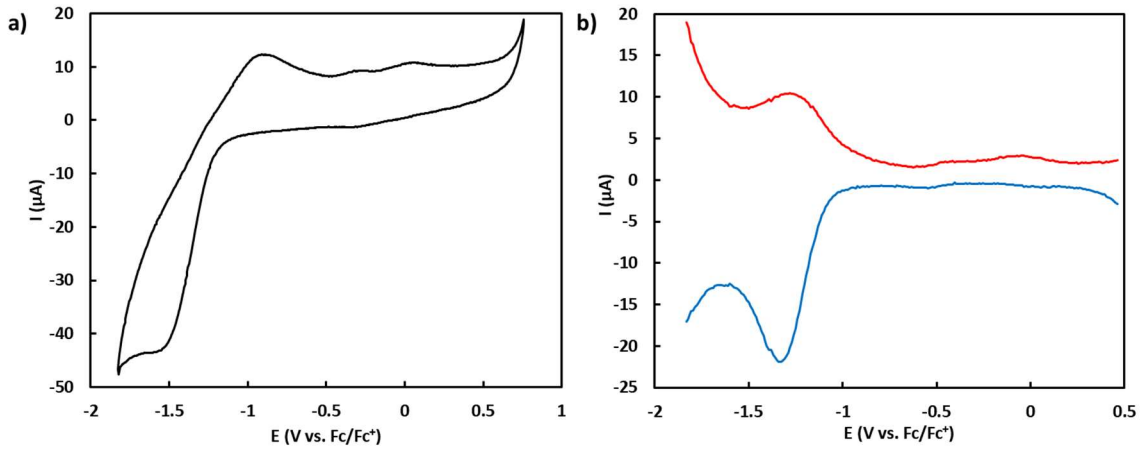

Figure 18. a) CV of **4-Ca** in CH_2Cl_2. $E_{1/2} = -1.3$ V vs Fc/Fc^+ assigned to ($Mn^{III}Mn^{IV}{}_2/Mn^{IV}{}_3$) redox couple. Redox couple is shifted ~ 400 mV more negative in comparison to that of **1-Ca** due to increased basicity of amidates versus acetates. **b)** Square wave voltammogram of **4-Ca**.

Table 2. Crystal and refinement data for complex **4-Ca**.

Compound	**4-Ca**
CCDC	2058414
Empirical formula	$C_{93}H_{96}CaMn_3N_8O_{15}$
Formula weight	1770.67
Temperature/K	100.0
Crystal system	triclinic
Space group	P-1
a/Å	16.032(2)
b/Å	16.081(2)
c/Å	19.756(3)
α/°	84.987(7)
β/°	84.858(7)
γ/°	62.604(7)
Volume/Å^3	4497.8(12)
Z	2
ρ_{calc}g/cm^3	1.307
μ/mm^{-1}	4.423
F(000)	1850.0
Crystal size/mm^3	0.8 × 0.5 × 0.4
Radiation	CuKα (λ = 1.54178)
2Θ range for data collection/°	6.198 to 160.604
Index ranges	$-19 \leq h \leq 20$, $-20 \leq k \leq 19$, $-24 \leq l \leq 22$
Reflections collected	131888
Independent reflections	18310 [R_{int} = 0.0631, R_{sigma} = 0.0376]
Data/restraints/parameters	18310/12/1052
Goodness-of-fit on F^2	1.029
Final R indexes [I>=2σ (I)]	R_1 = 0.0697, wR_2 = 0.1756
Final R indexes [all data]	R_1 = 0.0805, wR_2 = 0.1834
Largest diff. peak/hole / e Å^{-3}	1.10/-0.90

SQUID Magnetometry

Magnetic susceptibility measurements were carried on a Quantum Design MPMS 3 instrument running MPMS Multivu software. Crystalline samples were powdered and suspended in clear plastic straws in polycarbonate capsules. Data were recorded at 0.2 T from 2−300 K. Fitting simulations were performed using PHI.[54]

D-band EPR spectroscopy

High-frequency (130 GHz) experiments were performed at the CalEPR facility in the Britt lab at the University of California, Davis using a recently redesigned home-built 130 GHz EPR spectrometer equipped with an Oxford Instruments CF-935 liquid helium cryostat and an ITC-503 temperature controller.[50] The spectrometer is equipped with an 8 T cryogen-free magnet (Cryogenic Limited, UK). All data were acquired using a TE011 mode cylindrical resonant cavity designed and manufactured by HF EPR Instruments, Inc. (V. Krymov, New York).[51] Spectrometer control is achieved using the SpecMan software.[52] Electron-spin echo (ESE) detected field-swept spectra were collected using a Hahn echo sequence: $\pi/2 - \tau - \pi - \tau -$ echo. The length of the microwave pulse π was set to 40 ns and the interpulse delay τ was set to 240 ns. The ESE-EPR spectrum represents 1000 averages (1000 shots per point, 1 scan).

2.7) References

(1) Yano, J.; Yachandra, V., Mn_4Ca Cluster in Photosynthesis: Where and How Water is Oxidized to Dioxygen. *Chem. Rev.* **2014,** *114* (8), 4175-4205.

(2) Shen, J.-R., The Structure of Photosystem II and the Mechanism of Water Oxidation in Photosynthesis. *Annu. Rev. Plant Biol.* **2015,** *66* (1), 23-48.

(3) Pantazis, D. A., Missing Pieces in the Puzzle of Biological Water Oxidation. *ACS Catalysis* **2018,** *8* (10), 9477-9507.

(4) Umena, Y.; Kawakami, K.; Shen, J.-R.; Kamiya, N., Crystal structure of oxygen-evolving photosystem II at a resolution of 1.9 Å. *Nature* **2011,** *473*, 55.

(5) Suga, M.; Akita, F.; Hirata, K.; Ueno, G.; Murakami, H.; Nakajima, Y.; Shimizu, T.; Yamashita, K.; Yamamoto, M.; Ago, H.; Shen, J.-R., Native structure of photosystem II at 1.95 Å resolution viewed by femtosecond X-ray pulses. *Nature* **2014,** *517*, 99.

(6) Kern, J.; Chatterjee, R.; Young, I. D.; Fuller, F. D.; Lassalle, L.; Ibrahim, M.; Gul, S.; Fransson, T.; Brewster, A. S.; Alonso-Mori, R.; Hussein, R.; Zhang, M.; Douthit, L.; de Lichtenberg, C.; Cheah, M. H.; Shevela, D.; Wersig, J.; Seuffert, I.; Sokaras, D.; Pastor, E.; Weninger, C.; Kroll, T.; Sierra, R. G.; Aller, P.; Butryn, A.; Orville, A. M.; Liang, M.; Batyuk, A.; Koglin, J. E.; Carbajo, S.; Boutet, S.; Moriarty, N. W.; Holton, J. M.; Dobbek, H.; Adams, P. D.; Bergmann, U.; Sauter, N. K.; Zouni, A.; Messinger, J.; Yano, J.; Yachandra, V. K., Structures of the intermediates of Kok's photosynthetic water oxidation clock. *Nature* **2018,** *563* (7731), 421-425.

(7) Su, J.-H.; Cox, N.; Ames, W.; Pantazis, D. A.; Rapatskiy, L.; Lohmiller, T.; Kulik, L. V.; Dorlet, P.; Rutherford, A. W.; Neese, F.; Boussac, A.; Lubitz, W.; Messinger, J., The electronic structures of the S_2 states of the oxygen-evolving complexes of photosystem II in plants and cyanobacteria in the presence and absence of methanol. *Biochim. Biophys. Acta, Bioenerg.* **2011,** *1807* (7), 829-840.

(8) Cox, N.; Rapatskiy, L.; Su, J.-H.; Pantazis, D. A.; Sugiura, M.; Kulik, L.; Dorlet, P.; Rutherford, A. W.; Neese, F.; Boussac, A.; Lubitz, W.; Messinger, J., Effect of Ca^{2+}/Sr^{2+} Substitution on the Electronic Structure of the Oxygen-Evolving Complex of Photosystem II: A Combined Multifrequency EPR, ^{55}Mn-ENDOR, and DFT Study of the S_2 State. *J. Am. Chem. Soc.* **2011,** *133* (10), 3635-3648.

(9) Rapatskiy, L.; Cox, N.; Savitsky, A.; Ames, W. M.; Sander, J.; Nowaczyk, M. M.; Rögner, M.; Boussac, A.; Neese, F.; Messinger, J.; Lubitz, W., Detection of the Water-Binding Sites of the Oxygen-Evolving Complex of Photosystem II Using W-Band ^{17}O Electron–Electron Double Resonance-Detected NMR Spectroscopy. *J. Am. Chem. Soc.* **2012,** *134* (40), 16619-16634.

(10) Pantazis, D. A.; Ames, W.; Cox, N.; Lubitz, W.; Neese, F., Two Interconvertible Structures that Explain the Spectroscopic Properties of the Oxygen-Evolving Complex of Photosystem II in the S_2 State. *Angew. Chem. Int. Ed.* **2012,** *51* (39), 9935-9940.

(11) Bovi, D.; Narzi, D.; Guidoni, L., The S_2 State of the Oxygen-Evolving Complex of Photosystem II Explored by QM/MM Dynamics: Spin Surfaces and Metastable States Suggest a Reaction Path Towards the S3 State. *Angew. Chem. Int. Ed.* **2013,** *52* (45), 11744-11749.

(12) Cox, N.; Retegan, M.; Neese, F.; Pantazis, D. A.; Boussac, A.; Lubitz, W., Electronic structure of the oxygen-evolving complex in photosystem II prior to O-O bond formation. *Science* **2014,** *345* (6198), 804.
(13) Oyala, P. H.; Stich, T. A.; Stull, J. A.; Yu, F.; Pecoraro, V. L.; Britt, R. D., Pulse Electron Paramagnetic Resonance Studies of the Interaction of Methanol with the S_2 State of the Mn_4O_5Ca Cluster of Photosystem II. *Biochemistry* **2014,** *53* (50), 7914-7928.
(14) Oyala, P. H.; Stich, T. A.; Debus, R. J.; Britt, R. D., Ammonia Binds to the Dangler Manganese of the Photosystem II Oxygen-Evolving Complex. *J. Am. Chem. Soc.* **2015,** *137* (27), 8829-8837.
(15) Chatterjee, R.; Han, G.; Kern, J.; Gul, S.; Fuller, F. D.; Garachtchenko, A.; Young, I. D.; Weng, T.-C.; Nordlund, D.; Alonso-Mori, R.; Bergmann, U.; Sokaras, D.; Hatakeyama, M.; Yachandra, V. K.; Yano, J., Structural changes correlated with magnetic spin state isomorphism in the S_2 state of the Mn_4CaO_5 cluster in the oxygen-evolving complex of photosystem II. *Chem. Sci.* **2016,** *7* (8), 5236-5248.
(16) Lohmiller, T.; Krewald, V.; Sedoud, A.; Rutherford, A. W.; Neese, F.; Lubitz, W.; Pantazis, D. A.; Cox, N., The First State in the Catalytic Cycle of the Water-Oxidizing Enzyme: Identification of a Water-Derived μ-Hydroxo Bridge. *J. Am. Chem. Soc.* **2017,** *139* (41), 14412-14424.
(17) Siegbahn, P. E. M., Structures and Energetics for O_2 Formation in Photosystem II. *Acc. Chem. Res.* **2009,** *42* (12), 1871-1880.
(18) Pérez Navarro, M.; Ames, W. M.; Nilsson, H.; Lohmiller, T.; Pantazis, D. A.; Rapatskiy, L.; Nowaczyk, M. M.; Neese, F.; Boussac, A.; Messinger, J.; Lubitz, W.; Cox, N., Ammonia binding to the oxygen-evolving complex of photosystem II identifies the solvent-exchangeable oxygen bridge (μ-oxo) of the manganese tetramer. *Proc. Natl. Acad. Sci. U. S. A.* **2013,** *110* (39), 15561-15566.
(19) Gupta, R.; Taguchi, T.; Lassalle-Kaiser, B.; Bominaar, E. L.; Yano, J.; Hendrich, M. P.; Borovik, A. S., High-spin Mn–oxo complexes and their relevance to the oxygen-evolving complex within photosystem II. *Proc. Natl. Acad. Sci. U. S. A.* **2015,** *112* (17), 5319.
(20) Corry, T. A.; O'Malley, P. J., Molecular Identification of a High-Spin Deprotonated Intermediate during the S_2 to S_3 Transition of Nature's Water-Oxidizing Complex. *J. Am. Chem. Soc.* **2020,** *142* (23), 10240-10243.
(21) Krewald, V.; Retegan, M.; Neese, F.; Lubitz, W.; Pantazis, D. A.; Cox, N., Spin State as a Marker for the Structural Evolution of Nature's Water-Splitting Catalyst. *Inorg. Chem.* **2016,** *55* (2), 488-501.
(22) Kulik, L. V.; Epel, B.; Lubitz, W.; Messinger, J., Electronic Structure of the Mn4OxCa Cluster in the S_0 and S_2 States of the Oxygen-Evolving Complex of Photosystem II Based on Pulse 55Mn-ENDOR and EPR Spectroscopy. *J. Am. Chem. Soc.* **2007,** *129* (44), 13421-13435.
(23) Yamauchi, T.; Mino, H.; Matsukawa, T.; Kawamori, A.; Ono, T.-a., Parallel Polarization Electron Paramagnetic Resonance Studies of the S_1-State Manganese Cluster in the Photosynthetic Oxygen-Evolving System. *Biochemistry* **1997,** *36* (24), 7520-7526.
(24) Boussac, A.; Un, S.; Horner, O.; Rutherford, A. W., High-Spin States ($S \geq 5/2$) of the Photosystem II Manganese Complex. *Biochemistry* **1998,** *37* (12), 4001-4007.

(25) Boussac, A.; Rutherford, A. W., Comparative study of the g=4.1 EPR signals in the S_2 state of photosystem II. *Biochim. Biophys. Acta, Bioenerg.* **2000,** *1457* (3), 145-156.
(26) Haddy, A.; Lakshmi, K. V.; Brudvig, G. W.; Frank, H. A., Q-Band EPR of the S_2 State of Photosystem II Confirms an S=5/2 Origin of the X-Band g=4.1 Signal. *Biophys. J.* **2004,** *87* (4), 2885-2896.
(27) Marchiori, D. A.; Debus, R. J.; Britt, R. D., Pulse EPR Spectroscopic Characterization of the S_3 State of the Oxygen-Evolving Complex of Photosystem II Isolated from Synechocystis. *Biochemistry* **2020,** *59* (51), 4864-4872.
(28) Matsukawa, T.; Mino, H.; Yoneda, D.; Kawamori, A., Dual-Mode EPR Study of New Signals from the S_3-State of Oxygen-Evolving Complex in Photosystem II. *Biochemistry* **1999,** *38* (13), 4072-4077.
(29) Simon, P. S.; Makita, H.; Bogacz, I.; Fuller, F.; Bhowmick, A.; Hussein, R.; Ibrahim, M.; Zhang, M.; Chatterjee, R.; Cheah, M. H.; Chernev, P.; Doyle, M. D.; Brewster, A. S.; Alonso-Mori, R.; Sauter, N. K.; Bergmann, U.; Dobbek, H.; Zouni, A.; Messinger, J.; Kern, J.; Yachandra, V. K.; Yano, J., Capturing the sequence of events during the water oxidation reaction in photosynthesis using XFELs. *FEBS Lett.* **2023,** *597* (1), 30-37.
(30) Boussac, A.; Ugur, I.; Marion, A.; Sugiura, M.; Kaila, V. R. I.; Rutherford, A. W., The low spin - high spin equilibrium in the S_2-state of the water oxidizing enzyme. *Biochim. Biophys. Acta, Bioenerg.* **2018,** *1859* (5), 342-356.
(31) Isobe, H.; Shoji, M.; Yamanaka, S.; Mino, H.; Umena, Y.; Kawakami, K.; Kamiya, N.; Shen, J. R.; Yamaguchi, K., Generalized approximate spin projection calculations of effective exchange integrals of the $CaMn_4O_5$ cluster in the S1 and S3 states of the oxygen evolving complex of photosystem II. *PCCP* **2014,** *16* (24), 11911-11923.
(32) Lee, H. B.; Shiau, A. A.; Oyala, P. H.; Marchiori, D. A.; Gul, S.; Chatterjee, R.; Yano, J.; Britt, R. D.; Agapie, T., Tetranuclear $[Mn^{III}Mn_3^{IV}O_4]$ Complexes as Spectroscopic Models of the S_2 State of the Oxygen Evolving Complex in Photosystem II. *J. Am. Chem. Soc.* **2018,** *140* (49), 17175-17187.
(33) Lee, H. B.; Marchiori, D. A.; Chatterjee, R.; Oyala, P. H.; Yano, J.; Britt, R. D.; Agapie, T., S = 3 Ground State for a Tetranuclear $Mn^{IV4}O_4$ Complex Mimicking the S_3 State of the Oxygen-Evolving Complex. *J. Am. Chem. Soc.* **2020,** *142* (8), 3753-3761.
(34) Hagen, K. S.; Westmoreland, T. D.; Scott, M. J.; Armstrong, W. H., Structural and electronic consequences of protonation in $\{Mn_4O_6\}^{4+}$ cores: pH dependent properties of oxo-bridged manganese complexes. *J. Am. Chem. Soc.* **1989,** *111* (5), 1907-1909.
(35) Krewald, V.; Lassalle-Kaiser, B.; Boron, T. T.; Pollock, C. J.; Kern, J.; Beckwith, M. A.; Yachandra, V. K.; Pecoraro, V. L.; Yano, J.; Neese, F.; DeBeer, S., The Protonation States of Oxo-Bridged Mn^{IV} Dimers Resolved by Experimental and Computational Mn K Pre-Edge X-ray Absorption Spectroscopy. *Inorganic Chemistry* **2013,** *52* (22), 12904-12914.
(36) Mathe, Z.; Pantazis, D. A.; Lee, H. B.; Gnewkow, R.; Van Kuiken, B. E.; Agapie, T.; DeBeer, S., Calcium Valence-to-Core X-ray Emission Spectroscopy: A Sensitive

Probe of Oxo Protonation in Structural Models of the Oxygen-Evolving Complex. *Inorg. Chem.* **2019,** *58* (23), 16292-16301.

(37) Baldwin, M. J.; Stemmler, T. L.; Riggs-Gelasco, P. J.; Kirk, M. L.; Penner-Hahn, J. E.; Pecoraro, V. L., Structural and Magnetic Effects of Successive Protonations of Oxo Bridges in High-Valent Manganese Dimers. *J. Am. Chem. Soc.* **1994,** *116* (25), 11349-11356.

(38) Mukherjee, S.; Stull, J. A.; Yano, J.; Stamatatos, T. C.; Pringouri, K.; Stich, T. A.; Abboud, K. A.; Britt, R. D.; Yachandra, V. K.; Christou, G., Synthetic model of the asymmetric [Mn_3CaO_4] cubane core of the oxygen-evolving complex of photosystem II. *Proc. Natl. Acad. Sci. U. S. A.* **2012,** *109* (7), 2257.

(39) Zhang, C.; Chen, C.; Dong, H.; Shen, J.-R.; Dau, H.; Zhao, J., A synthetic Mn_4Ca-cluster mimicking the oxygen-evolving center of photosynthesis. *Science* **2015,** *348* (6235), 690.

(40) Kanady, J. S.; Tsui, E. Y.; Day, M. W.; Agapie, T., A Synthetic Model of the Mn_3Ca Subsite of the Oxygen-Evolving Complex in Photosystem II. *Science* **2011,** *333* (6043), 733.

(41) Krewald, V.; Neese, F.; Pantazis, D. A., On the Magnetic and Spectroscopic Properties of High-Valent Mn_3CaO_4 Cubanes as Structural Units of Natural and Artificial Water-Oxidizing Catalysts. *J. Am. Chem. Soc.* **2013,** *135* (15), 5726-5739.

(42) Kanady, J. S.; Lin, P.-H.; Carsch, K. M.; Nielsen, R. J.; Takase, M. K.; Goddard, W. A.; Agapie, T., Toward Models for the Full Oxygen-Evolving Complex of Photosystem II by Ligand Coordination To Lower the Symmetry of the Mn_3CaO_4 Cubane: Demonstration That Electronic Effects Facilitate Binding of a Fifth Metal. *J. Am. Chem. Soc.* **2014,** *136* (41), 14373-14376.

(43) Zhou, J.; Hu, Z.; Münck, E.; Holm, R. H., The Cuboidal Fe_3S_4 Cluster: Synthesis, Stability, and Geometric and Electronic Structures in a Non-Protein Environment. *J. Am. Chem. Soc.* **1996,** *118* (8), 1966-1980.

(44) Zhou, J.; Raebiger, J. W.; Crawford, C. A.; Holm, R. H., Metal Ion Incorporation Reactions of the Cluster $[Fe_3S_4(LS_3)]^{3-}$, Containing the Cuboidal $[Fe_3S_4]^0$ Core. *J. Am. Chem. Soc.* **1997,** *119* (27), 6242-6250.

(45) Zhou, J.; Holm, R. H., Synthesis and Metal Ion Incorporation Reactions of the Cuboidal Fe3S4 Cluster. *J. Am. Chem. Soc.* **1995,** *117* (45), 11353-11354.

(46) Panda, R.; Berlinguette, C. P.; Zhang, Y.; Holm, R. H., Synthesis of MFe3S4 Clusters Containing a Planar M^{II} Site (M = Ni, Pd, Pt), a Structural Element in the C-Cluster of Carbon Monoxide Dehydrogenase. *J. Am. Chem. Soc.* **2005,** *127* (31), 11092-11101.

(47) Lin, P.-H.; Tsui, E. Y.; Habib, F.; Murugesu, M.; Agapie, T., Effect of the Mn Oxidation State on Single-Molecule-Magnet Properties: Mn^{III} vs Mn^{IV} in Biologically Inspired $DyMn_3O_4$ Cubanes. *Inorg. Chem.* **2016,** *55* (12), 6095-6099.

(48) Tsui, E. Y.; Agapie, T., Reduction potentials of heterometallic manganese–oxido cubane complexes modulated by redox-inactive metals. *Proc. Natl. Acad. Sci. U. S. A.* **2013,** *110* (25), 10084.

(49) Baffert, C.; Orio, M.; Pantazis, D. A.; Duboc, C.; Blackman, A. G.; Blondin, G.; Neese, F.; Deronzier, A.; Collomb, M.-N., Trinuclear Terpyridine Frustrated Spin System with a $Mn^{IV}{}_3O_4$ Core: Synthesis, Physical Characterization, and Quantum

Chemical Modeling of Its Magnetic Properties. *Inorg. Chem.* **2009,** *48* (21), 10281-10288.

(50) Oyala, P. H.; Ravichandran, K. R.; Funk, M. A.; Stucky, P. A.; Stich, T. A.; Drennan, C. L.; Britt, R. D.; Stubbe, J., Biophysical Characterization of Fluorotyrosine Probes Site-Specifically Incorporated into Enzymes: E. coli Ribonucleotide Reductase As an Example. *J. Am. Chem. Soc.* **2016,** *138* (25), 7951-7964.

(51) Dorlet, P.; Seibold, S. A.; Babcock, G. T.; Gerfen, G. J.; Smith, W. L.; Tsai, A.-l.; Un, S., High-Field EPR Study of Tyrosyl Radicals in Prostaglandin H_2 Synthase-1. *Biochemistry* **2002,** *41* (19), 6107-6114.

(52) Epel, B.; Gromov, I.; Stoll, S.; Schweiger, A.; Goldfarb, D., Spectrometer manager: A versatile control software for pulse EPR spectrometers. *Concepts in Magnetic Resonance Part B-Magnetic Resonance Engineering* **2005,** *26B* (1), 36-45.

(53) Lee, H. B. Electronic Structure and Spectroscopy of Tetranuclear Mn_4O_4 and $CaMn_3O_4$ Complexes as Models of the Oxygen Evolving Complex in Photosystem II. California Institute of Technology, 2019.

(54) Chilton, N. F.; Anderson, R. P.; Turner, L. D.; Soncini, A.; Murray, K. S., PHI: A powerful new program for the analysis of anisotropic monomeric and exchange-coupled polynuclear d - and f -block complexes. *Journal of Computational Chemistry*, **2013**, *34*, 1164.

CHAPTER 3

Tetranuclear $[Mn^{III}Mn_3{}^{IV}O_4]$ Complexes as Spectroscopic Models of the S_2 State of the Oxygen Evolving Complex in Photosystem II

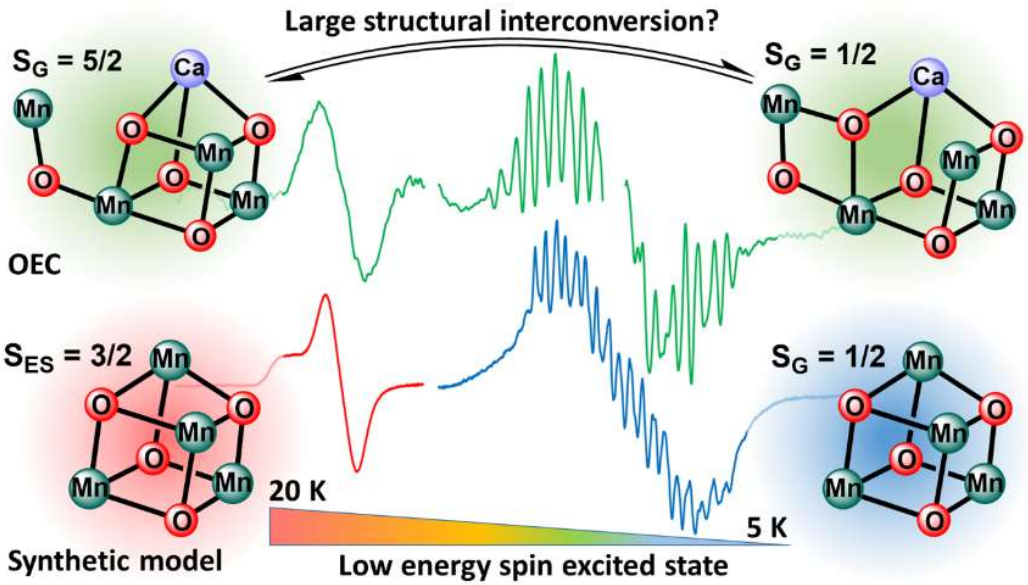

The text for this chapter was reproduced in part from:

Lee, H. B.; Shiau, A. A.; Oyala, P. H.; Marchiori, D. A.; Gul, S.; Chatterjee, R.; Yano, J.; Britt, R. D.; Agapie, T. *J. Am. Chem. Soc.*, **2018**, *140*, 17175-17187.

Abstract

Despite extensive biochemical, spectroscopic, and computational efforts in elucidating the mechanism of water oxidation in the oxygen evolving complex (OEC) found in Photosystem II (PSII), questions remain regarding the (electronic) structures of S_n-state intermediates. Model complexes of relevant nuclearity and Mn oxidation states for benchmarking spectroscopic studies are rare. Herein, the synthesis, crystal structure, electrochemistry, XAS, magnetic susceptibility, and variable temperature X-band CW-EPR of a $[Mn^{III}Mn^{IV}_3O_4]$ cuboidal complex is described. As a spectroscopic model of the S_2 state of the OEC, this species exhibits a low-spin multiline signal reminiscent to that of the biological system. Comparisons to literature compounds and structurally related $[Mn^{III}Mn^{IV}_3O_4]$ cuboidal complexes with different bridging ligands show that the electronic structures of these tetranuclear Mn complexes are highly sensitive to small geometric and ligand environment changes.

3.1) Introduction

The Oxygen Evolving Complex (OEC) of Photosystem II (PSII) is a low-symmetry $CaMn_4O_5$ cluster that catalyzes biological water oxidation.[1-6] While extensive collaborative studies from biochemical, crystallographic, spectroscopic, and computational disciplines have advanced our knowledge of this metallocofactor, details regarding the structure, electronic structure, and progression to through the S-state intermediates are debated. Interpretations from structural studies and spectroscopic characterization of observable lower-oxidation state intermediates heavily influence mechanistic proposals of O−O bond formation.[7] Thus, thorough determination of the (electronic) structure and unambiguous interpretation of spectroscopy for these lower S-state intermediates are crucial for advancing mechanistic understanding of the OEC.

In the S_2 state, two signals are observed by EPR spectroscopy, with the high spin (HS) $g = 4.1$ signal computationally attributed to a "closed-cubane" structure and the low spin (LS) $g = 2$ feature assigned to an "open-cubane" structure of similar energy.[8] Ferromagnetic coupling within the $CaMn^{IV}_3$ subunit and antiferromagnetic coupling to the fourth Mn results in a $S_G = 5/2$ for the closed cubane whereas a valence redistribution in the open-cubane form results in an overall $S_G = 1/2$ ground state (Figure 1). Interconvertibility of the two signals is a widely studied topic, as growing evidence suggests the conversion of the LS to HS species as an intermediate step within the progression from the S_2 to the S_3 state.[9] IR radiation of the LS form at low temperature (120 – 150 K) results in conversion to the HS form; annealing samples at 200 K causes the HS form to revert to the LS species.[10] pH dependence studies suggest conversion of the LS form to the HS form upon deprotonation, although atomistic details are unknown.[11-12]

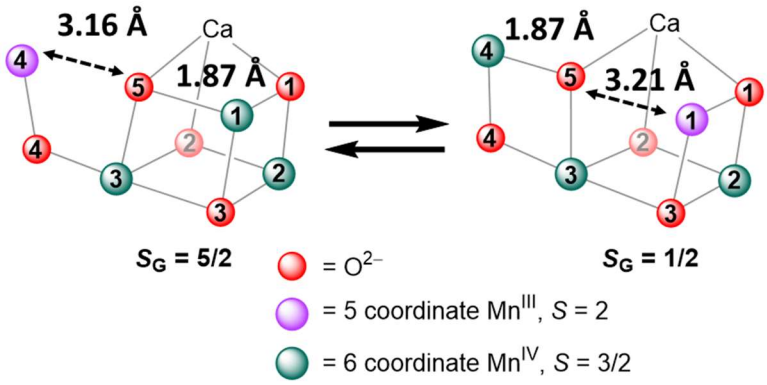

Figure 1. Open-closed cubane model proposed to account for the presence of and interconvertibility between the HS and LS signals observed in the EPR spectra of the S_2 state. Bond distances between Mn(4)−O(5) and Mn(1)−O(5) highlighted for each isomer.[8]

In comparison to the extensive structural and spectroscopic focus on the S_2 state of the OEC,[13-21] analogous studies on tetranuclear $Mn^{III}Mn^{IV}_3$-oxo model complexes are rare.[22-24] To summarize, (1) putative linear-chain complex $[Mn_4O_6(bpy)_6]^{3+}$ displays a multiline signal centered about $g = 2$ consistent with a $S_G = 1/2$ ground state,[25] (2) cuboidal $[L_6Mn_4O_4]^+$ (L = O_2PPh_2, $O_2P(p\text{-}OMePh)_2$) complexes feature a broad EPR spectrum suggesting $S \geq 3/2$,[26-27] (3) adamantane-shaped complex $[Mn_4O_6(bpea)_4]^{3+}$ (bpea = *N,N*-bis(2-pyridylmethyl)ethylamine) shows an intense signal at $g = 4.1$ attributed to the first excited Kramers doublet of a $S_G = 5/2$ ground state as determined by magnetic susceptibility,[28] and (4) OEC close structural mimic $CaMn_4O_4(OPiv)_8$ can be oxidized *in situ* to generate an EPR spectrum displaying both LS and HS signals.[29] However, further characterization of this species is not presented, and independent computational studies disagree on the assignment of these features.[22, 30]

The above examples highlight the relationship between cluster geometry and ground spin-state. However, it is important that in the open-closed cubane model, the geometries of the two isomers essentially differ only in the location of a particular O(5) bridging oxo ligand, a moiety notably implicated in the O−O bond forming step.[17, 31-32] Thus, systematic studies

on a series of complexes with smaller variations in the cluster core and environment could be well suited to establish structure-function and structure-electronic structure relationships.

Herein, we report the synthesis, crystal structure, electrochemistry, XAS, SQUID magnetometry, and EPR spectroscopy of a cuboidal $[Mn^{III}Mn^{IV}_3O_4]$ complex. Comparisons to a series of related compounds as well as homoleptic $[L_6Mn_4O_4]^+$ (L = O_2PPh_2, $O_2P(p\text{-}OMePh)_2$) complexes suggest that the spectroscopic properties of tetranuclear Mn_4O_4 complexes are highly sensitive to minute changes in structure as well as ligand environment.

3.2) Synthesis and X-ray crystallography

Addition of 3 equivalents of Ph_2PO_2H to **1** yields trisphosphinate $[Mn_4O_4]$ cluster **2** via a protonolysis pathway (Figure 2). ESI-MS of **2** shows a major *m*/*z* peak of 1792, consistent with the mass of $[LMn_4O_4(Ph_2PO_2)_3]^+$. The ^1H NMR spectrum in CD_2Cl_2 exhibits two broad, paramagnetically shifted peaks, characteristic of *pseudo* C_3-symmetric MMn_3O_4 clusters supported by L^{3-}.[33-36] The $LMn_4O_4(O_2PPh_2)_3$ formulation can be confirmed by X-ray diffraction. From the metal-oxo bond lengths determined from the X-ray structure of **2**, oxidation states of each manganese center can be assigned. Notably, axial elongation of Mn-oxo bonds due to population of dz^2 σ-antibonding orbitals are observed at 2.177(2) Å for Mn(3) and 2.187(2) for Mn(4). Thus, Mn(1) and Mn(2) are assigned as Mn^{IV} centers, where Mn(3) and Mn(4) are assigned as Mn^{III} centers.

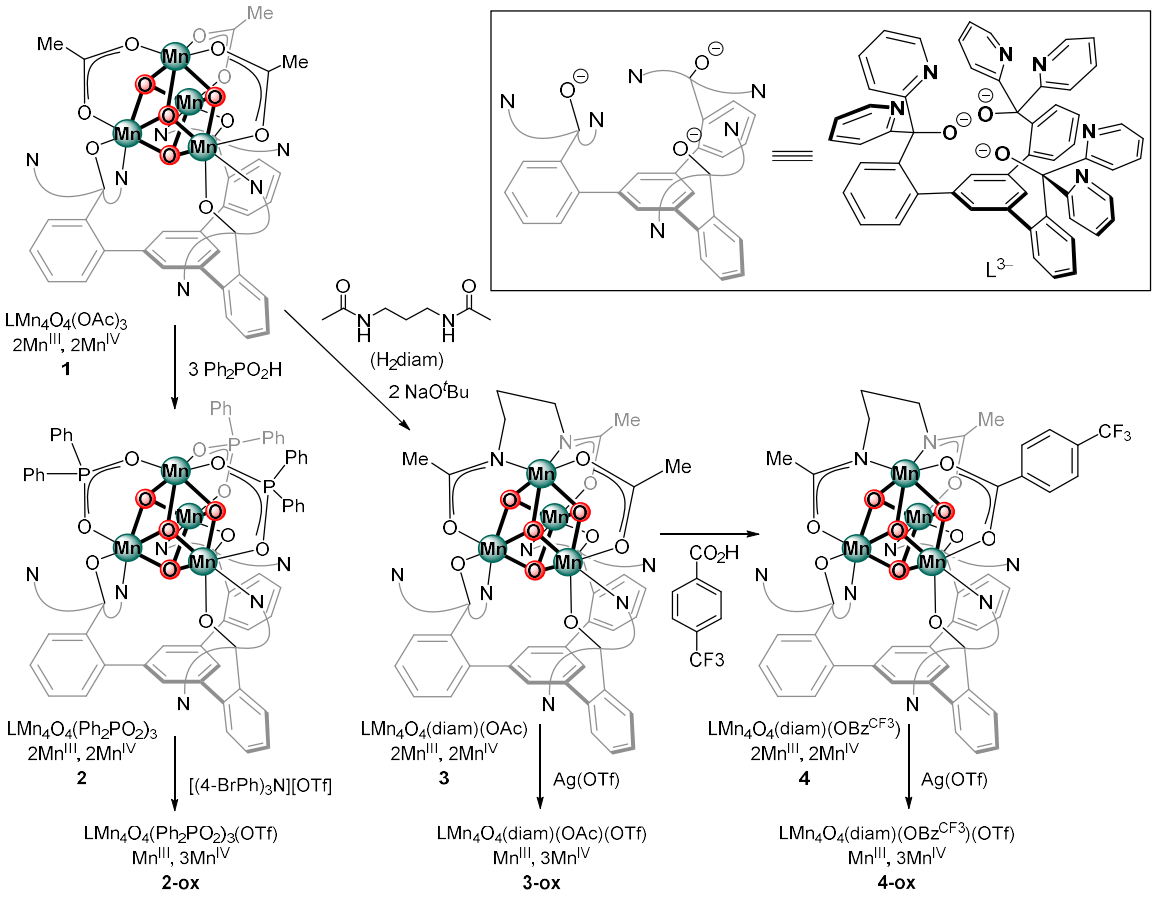

Figure 2. Synthesis of complexes discussed in this work. Complex **1** is previously reported.

Based on the reduction potential (+680 mV vs Fc/Fc^{+}) of the $[Mn_4O_4(O_2PPh_2)_6]^{+}$ complex,[26-27] we targeted a $Mn^{III}Mn^{IV}_3$ oxidation state cluster supported by bridging phosphinate ligands. The one-electron oxidized species **2-ox** can be accessed by addition of 1 equivalent of [(4-BrPh)$_3$N][OTf] to **2**. The ESI-MS peak of m/z = 1792 is consistent with the $[LMn_4O_4(O_2PPh_2)_3]^{+}$ formulation. Mn-oxo bond distances in the cluster core, determined from the X-ray structure (Figure 3), indicate a $Mn^{III}Mn^{IV}_3$ oxidation state with one elongated Mn(4)−O(4) distance at 2.241(1) Å. The spread of Mn-oxo distances is consistent with that of related species **3-ox** and **4-ox**.

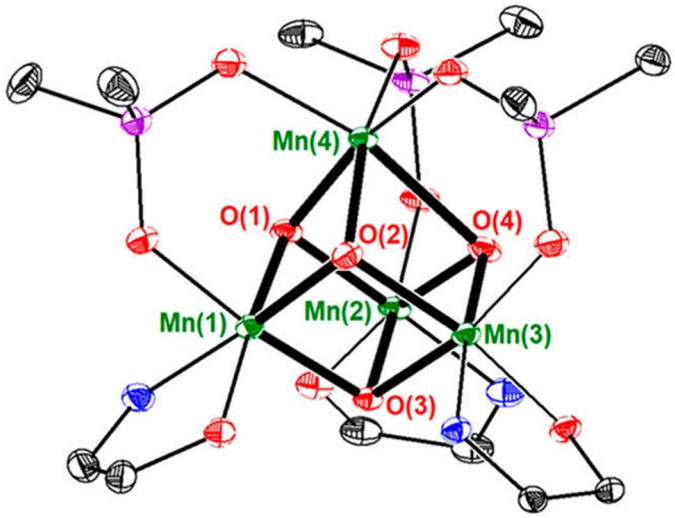

Figure 3. Truncated crystal structure of **2-ox**. Mn (green), O (red), N (blue), P (purple), C (black). Bolded bonds highlight metal-oxo bonds.

3.3) Electrochemistry

The electrochemistry of complexes **2**, **3**, and **4** were studied by cyclic voltammetry (CV). The CV of complex **2** exhibits two redox events, assigned as a reductive ($Mn^{III}_3Mn^{IV}/Mn^{III}_2Mn^{IV}_2$) couple and an oxidative ($Mn^{III}_2Mn^{IV}_2/Mn^{III}Mn^{IV}_3$) couple (Figure 4). The reduction potential of the ($Mn^{III}_2Mn^{IV}_2/Mn^{III}Mn^{IV}_3$) couple is observed at $E_{1/2}$ = +190 mV (vs Fc/Fc^+). Notably, this reduction potential is comparable to the estimated midpoint of the S_1/S_2 redox couple in the OEC (+900 mV vs SHE, approximately +250 mV vs Fc/Fc^+).[37]

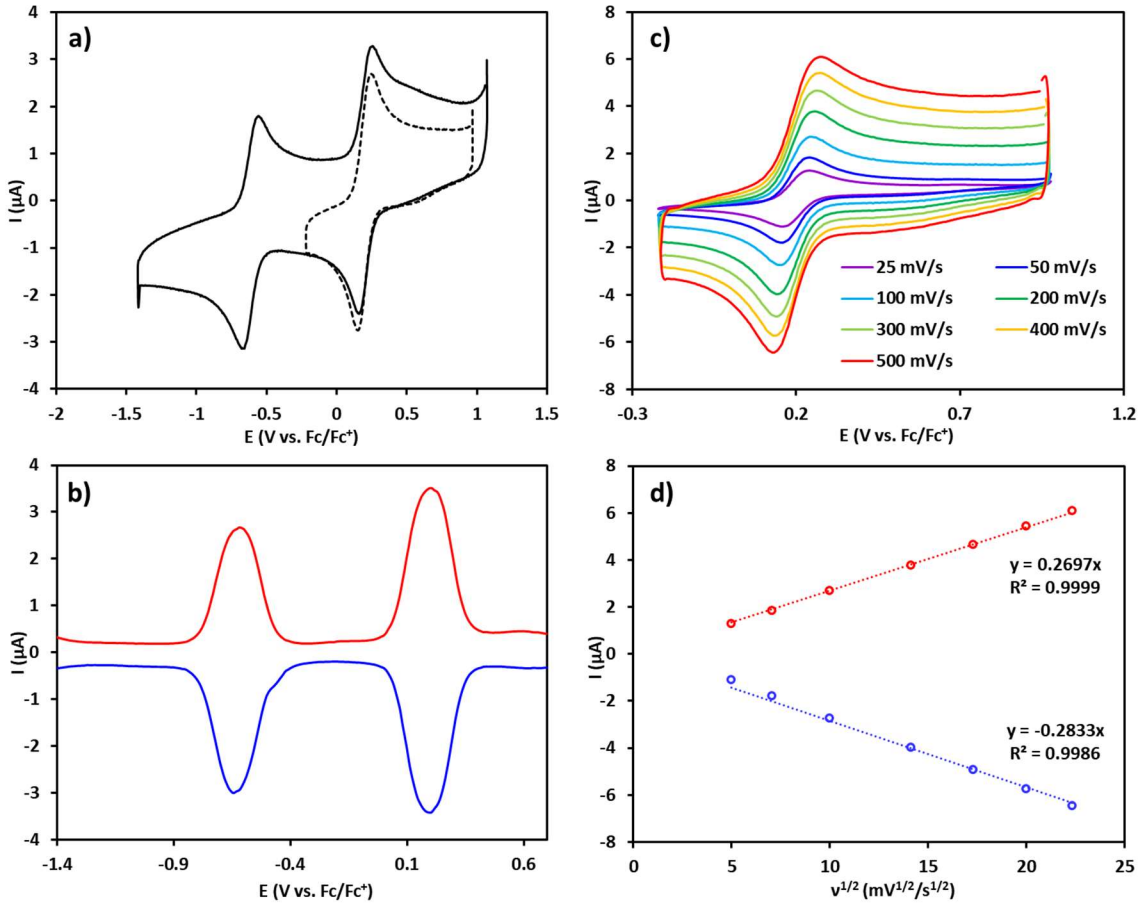

Figure 4. a) CV of **2**. Isolated redox couple shown in dotted lines. E = + 190 mV (vs. Fc/Fc^{+}). **b)** SWV of **2**. **c)** Isolated redox couple measured at various scan rates. **d)** Plot of peak current vs. square root of scan rate.

Reduction potentials of the ($Mn^{III}_2Mn^{IV}_2/Mn^{III}Mn^{IV}_3$) couples of complexes **1**, **3**, and **4** were also determined by CV ($E_{1/2}$ = +250 mV, −150 mV, and −15 mV vs Fc/Fc^{+}, respectively). Comparisons within this series reveal a linear relationship between ligand basicity and reduction potential,[38] similar to the phenomena observed for Co_4O_4 and $RuCo_3O_4$ complexes.[39-40]

3.4) XAS spectroscopy

Solution and solid-state Mn *K*-edge X-ray absorption near-edge spectroscopy (XANES) and extended X-ray absorption fine structure (EXAFS) data were collected (Figure 5). The absorption edge position of **2-ox**, determined from the second derivative

zero-crossings, was found to be 6553.3 eV. This value is comparable to that of the S_1 state (6553.1 eV) and S_2 state (6554.1 eV) of cyanobacteria PSII.[41] Importantly, EXAFS solution and solid-state data are indistinguishable from one another, with values in good agreement with those determined from XRD data, further supporting the structural integrity of **2-ox** in solution. Similar studies were performed on complexes **3-ox** and **4-ox**, resulting in the same conclusion regarding the structural integrity of these complexes in solution.

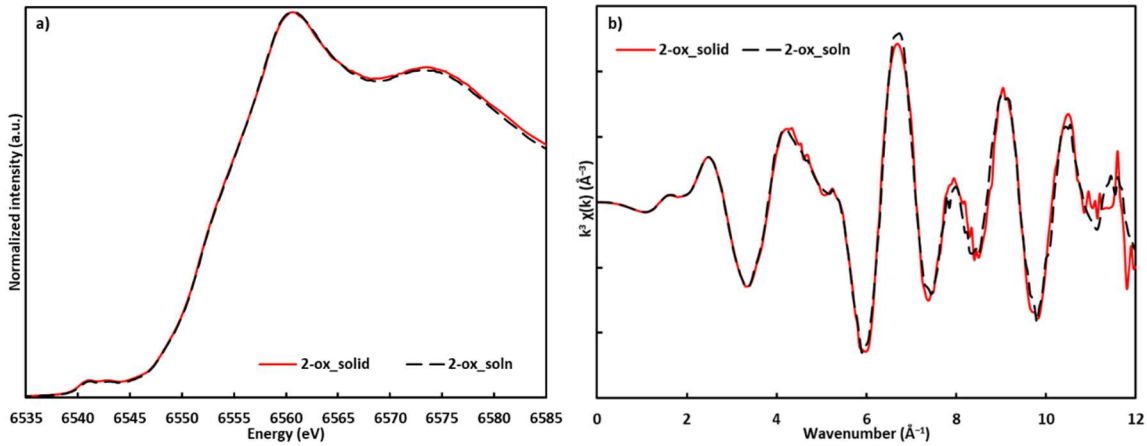

Figure 5. a) Normalized XANES data for solution and solid samples of **2-ox** at Mn *K*-edge. b) k^3-weighted *k*-space EXAFS at Mn *K*-edge of solution and solid samples of **2-ox**.

3.5) Magnetometry

Complex **2-ox** was studied by SQUID magnetometry to gain insight into the magnetic exchange coupling between Mn centers. In the temperature range from 1.8 – 300 K, magnetic susceptibility measurements were performed on powdered crystalline samples at a nonsaturating field of 0.4 T. At 300 K, the magnetic susceptibility of **2-ox** is 5.63 emu·K·mol^{-1}. This deviation from the expected spin-only value (8.62 emu·K·mol^{-1}) for uncoupled Mn^{III} (S = 2) and Mn^{IV} centers (S = 3/2) indicates overall antiferromagnetic coupling. Lowering the temperature results in a decrease in the measured χT value. At 1.8 K, the χT value of 0.383 emu·K·mol^{-1} is in good agreement with the χT value of 0.375

emu·K·mol^{-1} expected for a S = 1/2 (g = 2) system. Variable field and variable temperature data were also collected. Calculating the magnetization, a non-dimensional representation of unpaired electrons, shows saturation at M = 1 at high fields. Importantly, this behavior observed between 1.8 and 10 K suggests the lack of thermally accessible spin excited states within this temperature range.

This susceptibility data was fitted using software that utilizes an exact solution to the isotropic spin exchange Hamiltonian (Equation 1).[42] As the Mn^{III}(4)–O(4) distance is uniquely elongated (2.241(1) Å), the [Mn_4O_4] core of **2-ox** can be assumed to have *pseudo*-C_s symmetry with a mirror plane containing vectors Mn(4)–O(4) and Mn(4)–Mn(1) while bisecting the Mn(2)–Mn(3) vector (Figure 6). The susceptibility data was fit using the following values: $J_{12} = J_{13} = -8.8$ cm^{-1}, $J_{14} = -21.0$ cm^{-1}, $J_{24} = J_{34} = -3.2$ cm^{-1}, and $g = 2.00$. Notably, the small values for J_{24} and J_{34} are expected, considering the elongated Mn(4)–O(4) bond distance, as well as longer Mn(2)–Mn(4) and Mn(3)–Mn(4) distances of 2.9288(6) and 2.9585(7) Å, respectively.

$$\hat{\mathrm{H}} = -2 \sum_{i \neq j}^{i,j \in N} J_{ij} \hat{\mathrm{S}}_i \cdot \hat{\mathrm{S}}_j \quad (1)$$

Typically, six-coordinate Mn^{IV} centers exhibit $|D| \approx 0.2$ cm^{-1} and Mn^{III} centers exhibit $|D| \approx \sim 1 - 5$ cm^{-1}. Assuming zero field splitting (ZFS) parameters of $D(Mn^{IV}) = 0$ cm^{-1} and varying $D(Mn^{III}) = 0, -2, -4$ cm^{-1} did not significantly affect the values of J (Figure 13).[43] Simulation of the Zeeman field splitting diagram was carried out using $D(Mn^{IV}, Mn^{III}) = 0$ cm^{-1}, and a quartet first excited state approximately 28 cm^{-1} higher in energy than the doublet ground state is predicted. As with the values of J, variation of D (–2 or –4 cm^{-1}) also did not result in significant changes in the calculated energy gap between

the ground and first excited state (Figure 13). In the case assuming D = 0 cm^{-1}, the separation of 28 cm^{-1} is comparable to a temperature of 40 K, suggesting no significant population of the quartet state below 40 K (Figure 7). Interestingly, this value is also comparable to the estimated energy difference between ground and excited state of methanol treated PSII (primarily S = 1/2).[44] In comparison, a smaller energy separation of 3 – 6 cm^{-1} has been reported for untreated higher plant OEC in the S_2 state.[44-45]

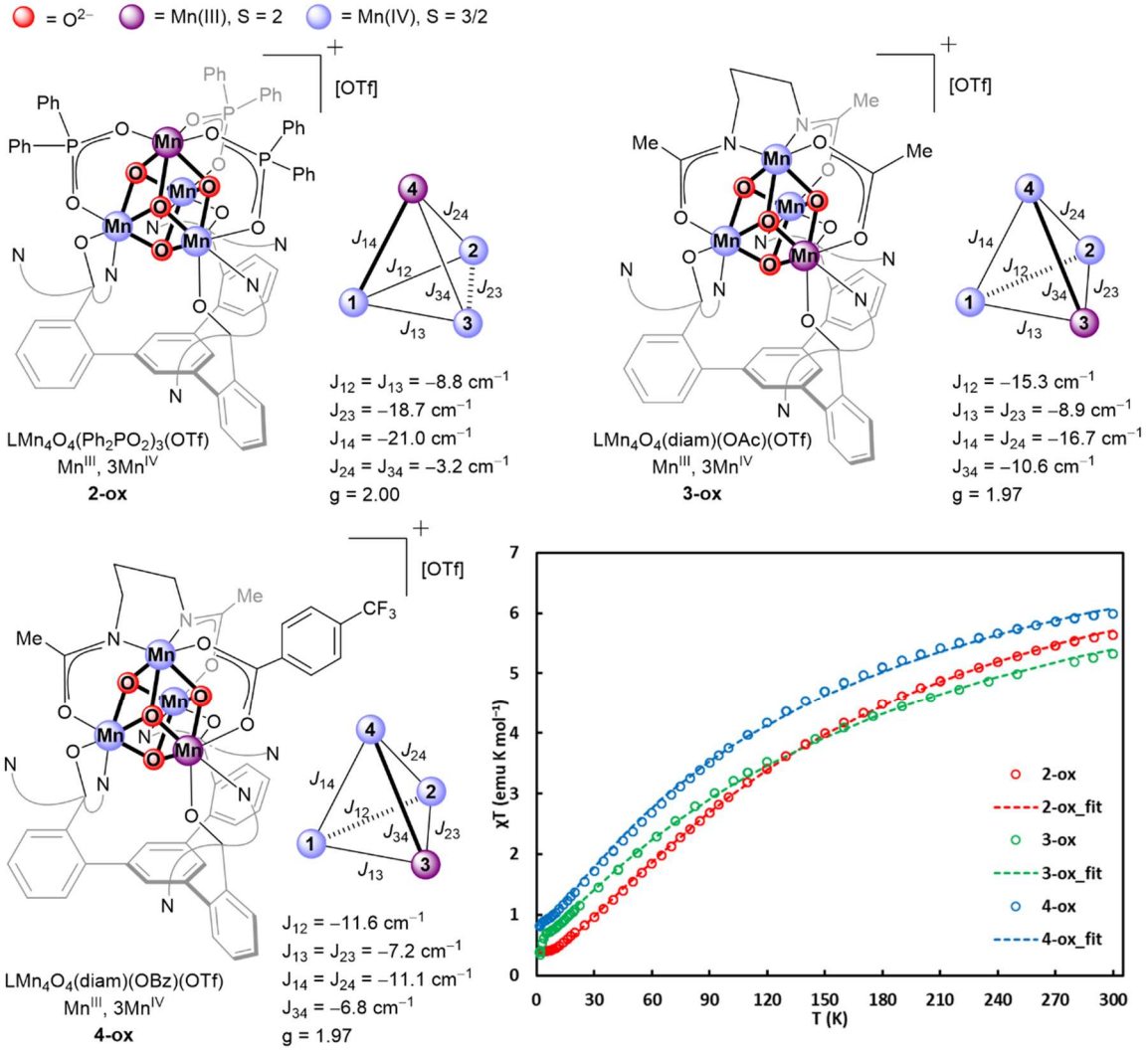

Figure 6. Exchange coupling model, fit parameters, and χT vs T plot of complexes **2-ox**, **3-ox**, and **4-ox**. For exchange coupling models, the mirror plane of the *pseudo-Cs* symmetry contains the bold vector and bisects the dashed vector.

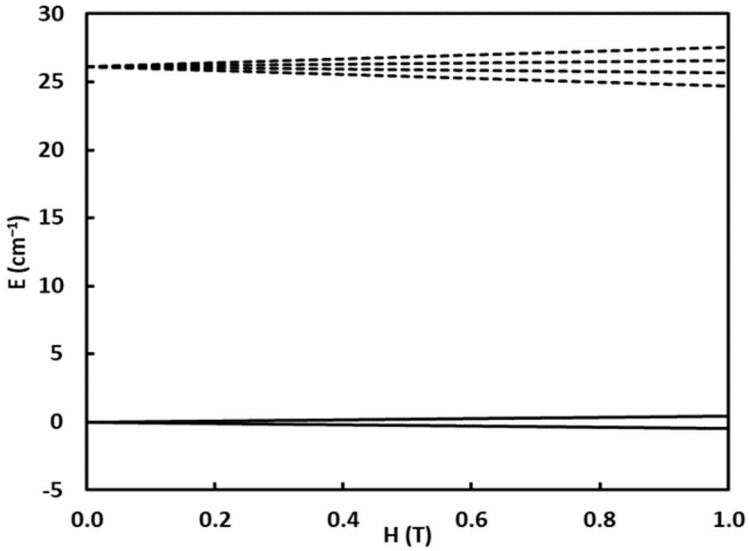

Figure 7. Calculated energy level diagram for **2-ox** using $D = 0$ cm^{-1}. A $S = 3/2$ excited state is predicted to be ~28 cm^{-1} higher in energy.

Although the magnetic susceptibility data of complexes **3-ox** and **4-ox** also indicate $S = 1/2$ ground states, the temperature dependence of χT values vary significantly throughout this series of $Mn^{III}Mn^{IV}_3$ complexes (Figure 6). Based on Mn-oxo and Mn-Mn distances in the cubane core determined from X-ray structures, similar C_S-symmetric coupling schemes differing in the location of the unique Mn^{III} can be used to describe the exchange coupling in complexes **3-ox** and **4-ox**; this analysis yielded the following parameters for **3-ox**: $J_{12} = -15.3$ cm^{-1}, $J_{13} = J_{23} = -8.9$ cm^{-1}, $J_{14} = J_{24} = -16.7$ cm^{-1}, $J_{34} = -10.6$ cm^{-1}, $g = 1.97$, and for **4-ox**: $J_{12} = -11.6$ cm^{-1}, $J_{13} = J_{23} = -7.2$ cm^{-1}, $J_{14} = J_{24} = -11.1$ cm^{-1}, $J_{34} = -6.8$ cm^{-1}, $g = 1.97$ (Figure 6). Notably, the smaller variation of exchange coupling constants in both complexes **3-ox** and **4-ox** relative to that of **2-ox** is consistent with the smaller spread in Mn-oxo bond distances.

Importantly, these differences in exchange coupling parameters with respect to those for **2-ox** result in significantly different calculated energy level diagrams. Whereas the magnetic susceptibility data for **2-ox** indicates a well isolated $S = 1/2$ ground state with

the first excited state 28 cm^{-1} higher in energy, the data for **3-ox** and **4-ox** suggests lower-lying excited states. For **3-ox**, a quartet excited state is predicted to be 3−5 cm^{-1} (equivalent temperature of 4.3−7.2 K) above the doublet ground state. This holds true for variations in $|D|(Mn^{III})$ = 0, 2, 4 cm^{-1}. Similarly, the calculated energy level diagram for **4-ox** indicates an even smaller energy separation (0−1 cm^{-1}, equivalent temperature 1.4 K) between the doublet ground state and quartet excited state. Overall, the magnetic susceptibility data of **2-ox**, **3-ox**, and **4-ox** indicate that energy spacings in the spin ladder of tetranuclear Mn complexes can be very sensitive to small changes in the cluster core and ligand environment.

3.6) EPR spectroscopy

Frozen solutions of complexes **2-ox**, **3-ox**, and **4-ox** were studied by CW X-band EPR spectroscopy. At 5 K, the EPR spectrum of **2-ox** features a broad low-field signal centered about g = 2 with ^{55}Mn hyperfine interactions (Figure 8). This is consistent with the S = 1/2 ground state predicted by the susceptibility data and represents the $|-1/2\rangle \rightarrow |1/2\rangle$ transition. Upon warming the sample, the g = 2 signal loses intensity. No signals were observed above 15 K. The lack of thermally populated spin excited states in this temperature range is consistent with the calculated energy splitting diagram determined from magnetic susceptibility studies. The spectrum can be approximated using the following parameters: g = [2.053, 2.003, 1.952] (g_{iso} = 2.00) and ^{55}Mn hyperfine interactions A_i, $(A_{iso})_i$: Mn_1 = [434, 434, 313], 394 MHz; Mn_2 = [293, 155, 245], 231 MHz; Mn_3 = [128, 146, 198], 157 MHz; Mn_4 = [134, 133, 72], 113 MHz. Notably, one set of ^{55}Mn hyperfine interactions is larger, consistent with the assignment of one Mn^{III} center in **2-ox**.[46]

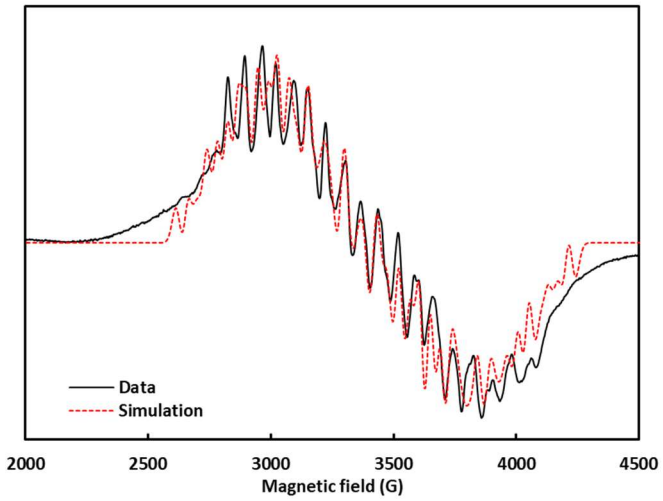

Figure 8. X-band EPR spectrum of **2-ox**. Acquisition parameters: frequency = 9.64 MHz, power = 8 mW, conversion time = 20.48 ms, modulation amplitude = 8 G. See text for simulation parameters.

This EPR spectrum of **2-ox** is in stark contrast with that of the homoleptic $[Mn_4O_4(Ph_2PO_2)_6]^+$ complex reported by Dismukes,[26-27] which only features higher spin ($S \geq 3/2$) signals. Further elaboration on the exchange-coupling scheme and interpretation of this data were not discussed.

Complexes **3-ox** and **4-ox** were also studied by EPR spectroscopy. At T = 5 K, the EPR spectrum of **3-ox** also displays a $S = 1/2$ signal centered at $g = 2$ featuring ^{55}Mn hyperfine interactions. Increasing the temperature results in a decrease in the intensity of this $S = 1/2$ signal along with an increase in intensity of a higher spin signal centered about $g = 4.2$. At ~17.5 K the two features are of roughly equal intensity, and above 20 K, both features start to lose intensity due to relaxation. This temperature dependence corroborates the calculated energy splitting diagram determined from magnetic susceptibility studies, as a quartet excited state is expected to be only 3−5 cm^{-1} higher in energy (Figure 9). Thus, the $g = 2$ and $g = 4.2$ features are assigned as the transitions within the $|\pm 1/2\rangle$ and $|\pm 3/2\rangle$ Kramers doublets, respectively. Similarly, the EPR spectrum of **4-ox** displays a major $S =$

1/2 feature at $g = 2$. However, even at T = 5 K, higher spin signals at $g = 7.5$ and $g = 5.5$ are observable. This result agrees with an even smaller energy separation between the doublet ground state and excited quartet states predicted by magnetic susceptibility.

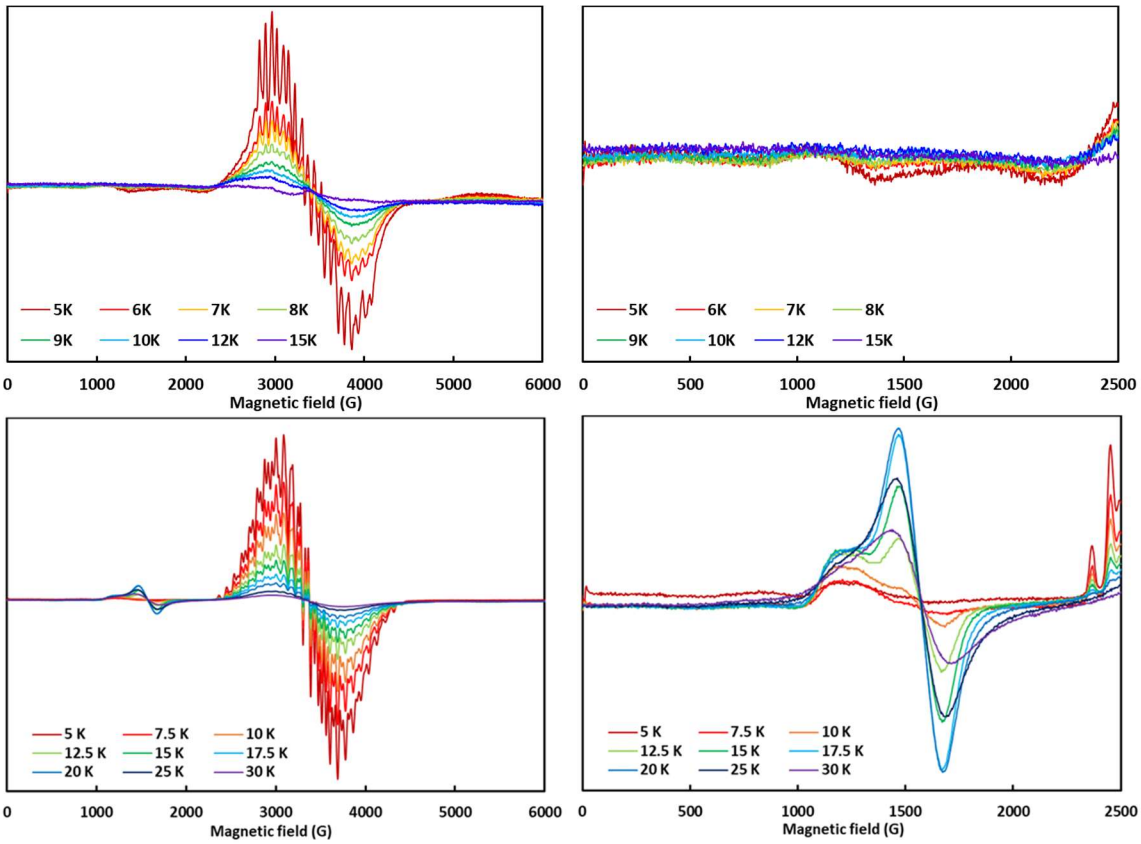

Figure 9. Variable temperature X-band CW EPR spectra of **2-ox** (top) and **3-ox** (bottom). Expanded view of the low-field region (right).

3.7) Discussion

Comparisons between **2-ox**, **3-ox**, and **4-ox** indicate that small changes in structure and nature of the bridging ligand(s) can have significant impact on observed magnetometry and spectroscopic properties. Specifically, the degree of thermal accessibility to excited spin states can be tuned by ligand substitution. These data contrast with the open-closed cubane hypothesis for the S_2 state of the OEC, where the high spin and low spin signals are attributed to structurally distinct isomers.

3.8) Experimental

General Considerations

All reactions were performed at room temperature in an N_2-filled glovebox or by using standard Schlenk techniques unless otherwise specified. Glassware was oven dried at 150 °C for at least 2h prior to use and allowed to cool under vacuum. All reagents were used as received unless otherwise stated. Diphenylphosphinic acid was recrystallized from 95% ethanol. Tris(4-bromophenyl)aminium triflate was synthesized according to literature.[47] Anhydrous tetrahydrofuran (THF) was purchased from Aldrich in 18 L Pure-Pac™ containers. Anhydrous CH_2Cl_2, CH_3CN, diethyl ether, benzene and THF were purified by sparging with nitrogen for 15 minutes and then passing under nitrogen pressure through a column of activated A2 alumina. NMR solvents (CD_2Cl_2) were purchased from Cambridge Isotope Laboratories, dried over calcium hydride, degassed by three freeze-pump-thaw cycles and vacuum-transferred prior to use. ^1H NMR spectra were recorded on a Varian 300 MHz instrument, with shifts reported relative to the residual solvent peak. Elemental analyses were performed at the California Institute of Technology.

Synthesis of $LMn_4O_4(O_2PPh_2)_3$ (**2**):

A solution of $LMn_4O_4(OAc)_3$ (600 mg, 0.46 mmol, 1 equiv) in CH_2Cl_2 (12 mL) was added to a stirring CH_2Cl_2 suspension of diphenylphosphinic acid (330 mg, 1.51 mmol, 3.3 equiv). After stirring the reaction at room temperature for 16 hours, a colorless precipitate formed and was filtered away. All volatiles were removed from the filtrate under reduced pressure. The solid residue was triturated with CH_2Cl_2 (15 mL) and Et_2O (15 mL). The brown powder was then suspended in 15 mL of THF, collected on a pad of Celite, dissolved in CH_2Cl_2, and filtered through Celite. All volatiles were removed from the filtrate under

reduced pressure, yielding compound **2** as a red-brown powder. Yield = 462 mg, 57 %. Crystals suitable for X-ray crystallography were grown from slow vapor diffusion of Et_2O into a concentrated solution of **2** in CH_2Cl_2. ^1H NMR (300 MHz, CD_2Cl_2): δ 16.3, 11.0, 9.7, 8.5, −14.3 ppm.

Synthesis of $[LMn_4O_4(O_2PPh_2)_3][OTf]$ (**2-ox**):

To a stirring solution of **2** (150 mg, 84 μmol, 1 equiv) in CH_2Cl_2 (5 mL), a blue CH_2Cl_2 solution (4 mL) of $[(4\text{-}BrPh)_3N][OTf]$ (53 mg, 84 μmol, 1 equiv) was added. After the brown solution was stirred at room temperature for 16 hours, all volatiles were removed under reduced pressure. The residue was washed with Et_2O (4 mL), washed with THF until the filtrate was no longer blue/green, dissolved in CH_2Cl_2, and filtered through Celite. Volatiles were removed from the filtrate under reduced pressure, yielding **2-ox** as a brown powder (112 mg, 69 %). Crystals suitable for X-ray crystallography were obtained from a slow vapor diffusion of Et_2O into a concentrated solution of **2-ox** in CH_2Cl_2. ^1H NMR (300 MHz, CD_2Cl_2): δ 10.9, 9.9, 8.9, 8.2, −14.8 ppm. Analysis calculated for $LMn_4O_4(O_2PPh_2)_3(OTf)$ $[C_{94}H_{69}F_3Mn_4N_6O_{16}P_3S]$: C 58.19, H 3.58, N 4.33; found: C 58.00, H 3.79, N 4.66.

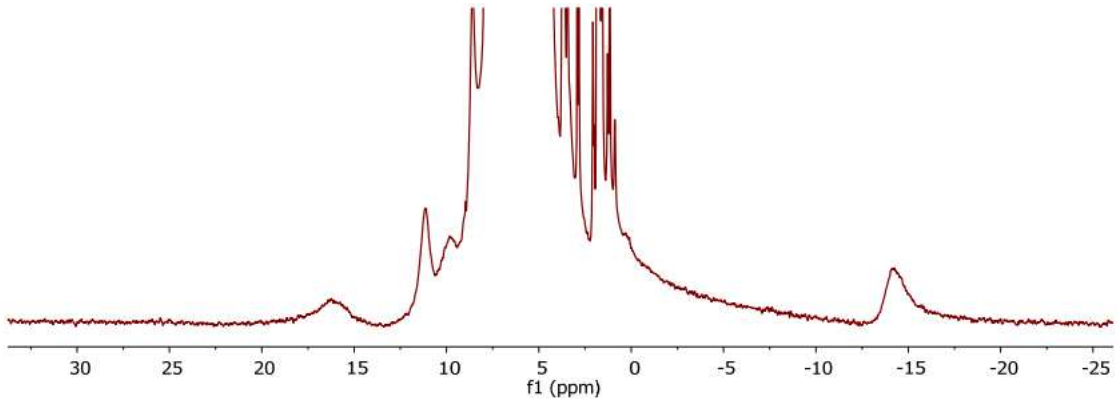

Figure 10. ^1H NMR of **2** in CD_2Cl_2.

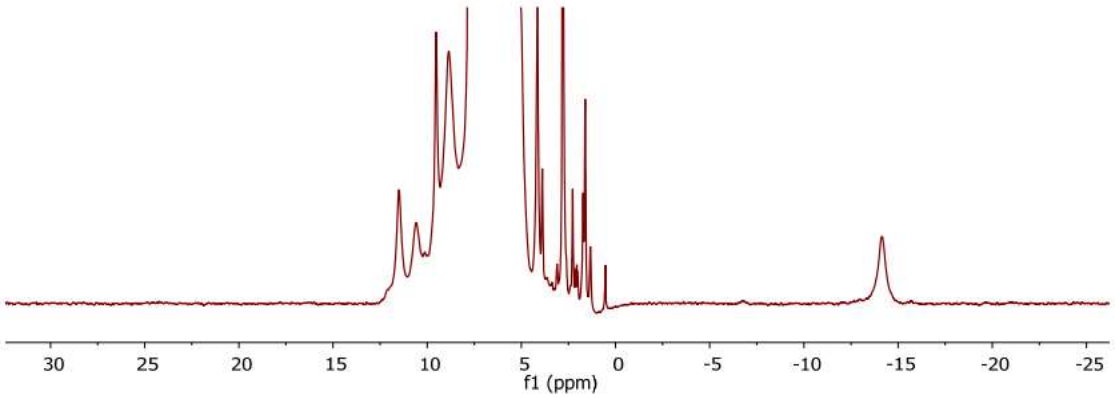

Figure 11. ^{1}H NMR of **2-ox** in CD_2Cl_2.

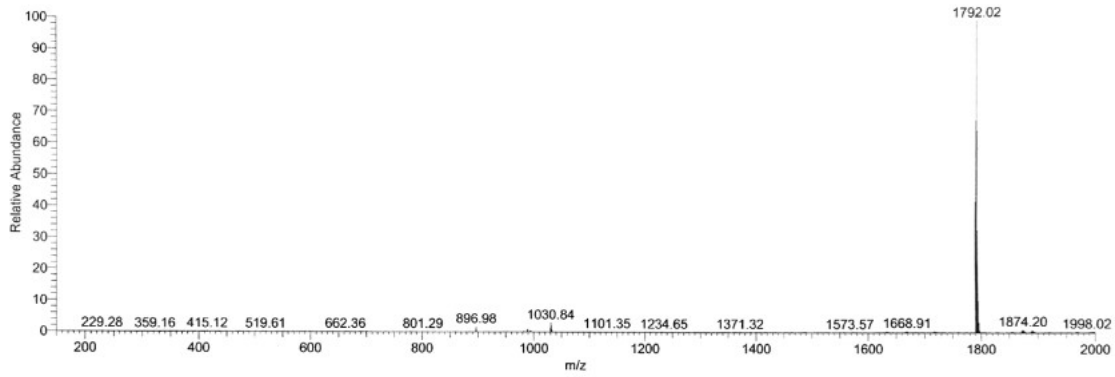

Figure 12. ESI-MS of **2**. *m*/*z* = 1792 is consistent with $[LMn_4O_4(O_2PPh_2)_3]^+$ formulation.

Table 1. Crystal and refinement data for complexes **2** and **2-ox**.

Compound	**2**	**2-ox**
CCDC	1863637	1863638
Empirical formula	$C_{94}H_{71}Cl_2Mn_4N_6O_{13}P_3$	$C_{95}H_{71}Cl_2F_3Mn_4N_6O_{16}P_3S$
Formula weight	1876.13	2025.20
Temperature/K	296.15	100.00
Crystal system	triclinic	monoclinic
Space group	P-1	$P2_1/n$
a/Å	14.2765(10)	14.3608(9)
b/Å	14.3034(8)	27.4932(17)
c/Å	23.7048(18)	23.6617(14)
α/°	72.614(2)	90
β/°	87.529(2)	101.255(2)
γ/°	67.645(2)	90
Volume/Å^3	4258.6(5)	9162.5(10)
Z	2	4
ρ_{calc}g/cm^3	1.463	1.468
μ/mm^{-1}	0.767	0.748
F(000)	1920.0	4132.0
Crystal size/mm^3	0.1 × 0.1 × 0.1	0.1 × 0.05 × 0.03
Radiation	MoKα (λ = 0.71073)	MoKα (λ = 0.71073)
2Θ range for data collection/°	3.094 to 61.002	3.67 to 59.818
Index ranges	$-20 \le h \le 19$, $-20 \le k \le 20$, $-33 \le l \le 33$	$-23 \le h \le 23$, $-45 \le k \le 45$, $-39 \le l \le 39$
Reflections collected	163138	4703347
Independent reflections	25775 [R_{int} = 0.0594, R_{sigma} = 0.0494]	43739 [R_{int} = 0.0541, R_{sigma} = 0.0346]
Data/restraints/parameters	25775/0/1099	43739/30/1211
Goodness-of-fit on F^2	1.012	1.049
Final R indexes [I>=2σ (I)]	R_1 = 0.0495, wR_2 = 0.1122	R_1 = 0.0590, wR_2 = 0.1539
Final R indexes [all data]	R_1 = 0.0780, wR_2 = 0.1244	R_1 = 0.0861, wR_2 = 0.1739
Largest diff. peak/hole / e Å^{-3}	0.90/-1.32	2.16/-2.32

SQUID Magnetometry

Magnetic susceptibility measurements were carried on a Quantum Design MPMS 3 instrument running MPMS Multivu software. Crystalline samples were powdered and suspended in clear plastic straws in polycarbonate capsules. Data were recorded at 0.4 T from 1.8−300 K. A diamagnetic correction of -970×10^{-6} cm^3 /mol was made for **2-ox**. Fitting simulations were performed using PHI.[42] Fitting simulations were performed assuming an on-site zero field splitting parameter D(MnIV) ≈ 0 cm^{-1} and D(MnIII) = 0, −2, or −4 cm^{-1}. The average J values are reported along with the standard deviation.

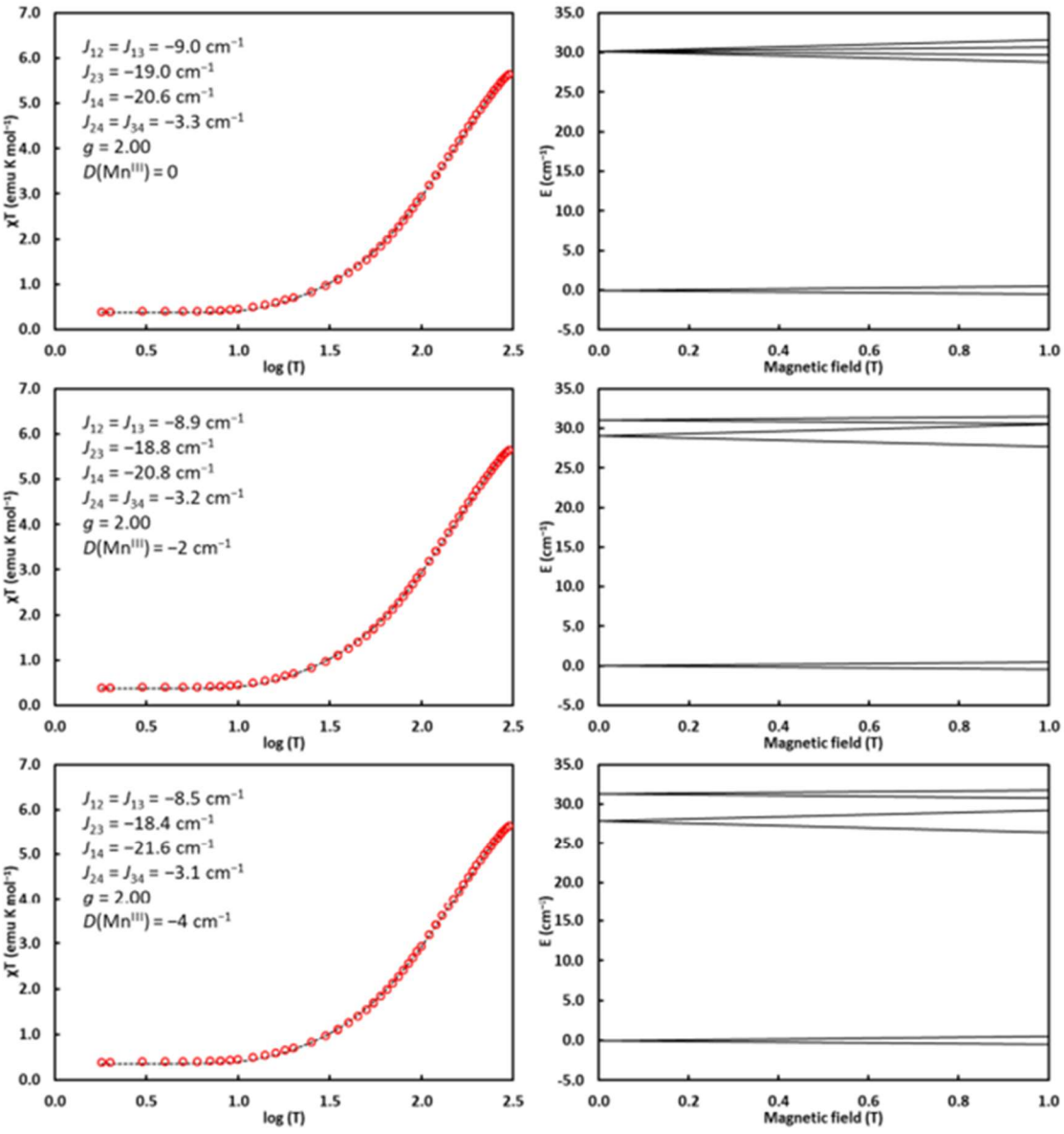

Figure 13. Fit parameters and corresponding χT vs. log(T) plots and Zeeman splitting diagrams for **2-ox**. Regardless of $D(Mn^{III})$ values within a reasonable range, a similarly large energy gap between ground and excited state is observed.

3.9) References

(1) Yano, J.; Yachandra, V., Mn_4Ca Cluster in Photosynthesis: Where and How Water is Oxidized to Dioxygen. *Chem. Rev.* **2014,** *114* (8), 4175-4205.

(2) Shen, J.-R., The Structure of Photosystem II and the Mechanism of Water Oxidation in Photosynthesis. *Annu. Rev. Plant Biol.* **2015,** *66* (1), 23-48.

(3) Cox, N.; Pantazis, D. A.; Neese, F.; Lubitz, W., Biological Water Oxidation. *Acc. Chem. Res.* **2013,** *46* (7), 1588-1596.

(4) Cox, N.; Pantazis, D. A.; Lubitz, W., Current Understanding of the Mechanism of Water Oxidation in Photosystem II and Its Relation to XFEL Data. *Annu. Rev. Biochem* **2020,** *89* (1), 795-820.

(5) Siegbahn, P. E. M., Structures and Energetics for O_2 Formation in Photosystem II. *Acc. Chem. Res.* **2009,** *42* (12), 1871-1880.

(6) Britt, R. D.; Marchiori, D. A., Photosystem II, poised for O_2 formation. *Science* **2019,** *366* (6463), 305.

(7) Cox, N.; Retegan, M.; Neese, F.; Pantazis, D. A.; Boussac, A.; Lubitz, W., Electronic structure of the oxygen-evolving complex in photosystem II prior to O-O bond formation. *Science* **2014,** *345* (6198), 804.

(8) Pantazis, D. A.; Ames, W.; Cox, N.; Lubitz, W.; Neese, F., Two Interconvertible Structures that Explain the Spectroscopic Properties of the Oxygen-Evolving Complex of Photosystem II in the S_2 State. *Angew. Chem. Int. Ed.* **2012,** *51* (39), 9935-9940.

(9) Boussac, A.; Rutherford, A. W.; Sugiura, M., Electron transfer pathways from the S_2-states to the S_3-states either after a Ca^{2+}/Sr^{2+} or a Cl^-/I^- exchange in Photosystem II from Thermosynechococcus elongatus. *Biochim. Biophys. Acta, Bioenerg.* **2015,** *1847* (6), 576-586.

(10) Boussac, A.; Un, S.; Horner, O.; Rutherford, A. W., High-Spin States ($S \geq 5/2$) of the Photosystem II Manganese Complex. *Biochemistry* **1998,** *37* (12), 4001-4007.

(11) Boussac, A.; Ugur, I.; Marion, A.; Sugiura, M.; Kaila, V. R. I.; Rutherford, A. W., The low spin - high spin equilibrium in the S_2-state of the water oxidizing enzyme. *Biochim. Biophys. Acta, Bioenerg.* **2018,** *1859* (5), 342-356.

(12) Ames, W.; Pantazis, D. A.; Krewald, V.; Cox, N.; Messinger, J.; Lubitz, W.; Neese, F., Theoretical Evaluation of Structural Models of the S_2 State in the Oxygen Evolving Complex of Photosystem II: Protonation States and Magnetic Interactions. *J. Am. Chem. Soc.* **2011,** *133* (49), 19743-19757.

(13) Oyala, P. H.; Stich, T. A.; Debus, R. J.; Britt, R. D., Ammonia Binds to the Dangler Manganese of the Photosystem II Oxygen-Evolving Complex. *J. Am. Chem. Soc.* **2015,** *137* (27), 8829-8837.

(14) Oyala, P. H.; Stich, T. A.; Stull, J. A.; Yu, F.; Pecoraro, V. L.; Britt, R. D., Pulse Electron Paramagnetic Resonance Studies of the Interaction of Methanol with the S_2 State of the Mn_4O_5Ca Cluster of Photosystem II. *Biochemistry* **2014,** *53* (50), 7914-7928.

(15) DeRose, V. J.; Latimer, M. J.; Zimmermann, J.-L.; Mukerji, I.; Yachandra, V. K.; Sauer, K.; Klein, M. P., Fluoride substitution in the Mn cluster from Photosystem II: EPR and X-ray absorption spectroscopy studies. *Chem. Phys.* **1995,** *194* (2), 443-459.

(16) Lohmiller, T.; Krewald, V.; Navarro, M. P.; Retegan, M.; Rapatskiy, L.; Nowaczyk, M. M.; Boussac, A.; Neese, F.; Lubitz, W.; Pantazis, D. A.; Cox, N., Structure, ligands and substrate coordination of the oxygen-evolving complex of photosystem II in the S_2 state: a combined EPR and DFT study. *PCCP* **2014,** *16* (24), 11877-11892.

(17) Vinyard, D. J.; Khan, S.; Askerka, M.; Batista, V. S.; Brudvig, G. W., Energetics of the S_2 State Spin Isomers of the Oxygen-Evolving Complex of Photosystem II. *J. Phys. Chem. B* **2017,** *121* (5), 1020-1025.

(18) Vinyard, D. J.; Brudvig, G. W., Insights into Substrate Binding to the Oxygen-Evolving Complex of Photosystem II from Ammonia Inhibition Studies. *Biochemistry* **2015,** *54* (2), 622-628.

(19) Boussac, A.; Rutherford, A. W., Comparative study of the g=4.1 EPR signals in the S_2 state of photosystem II. *Biochim. Biophys. Acta, Bioenerg.* **2000,** *1457* (3), 145-156.

(20) Britt, R. D.; Lorigan, G. A.; Sauer, K.; Klein, M. P.; Zimmermann, J.-L., The g = 2 multiline EPR signal of the S_2 state of the photosynthetic oxygen-evolving complex originates from a ground spin state. *Biochim. Biophys. Acta, Bioenerg.* **1992,** *1140* (1), 95-101.

(21) Horner, O.; Rivière, E.; Blondin, G.; Un, S.; Rutherford, A. W.; Girerd, J.-J.; Boussac, A., SQUID Magnetization Study of the Infrared-Induced Spin Transition in the S_2 State of Photosystem II: Spin Value Associated with the g = 4.1 EPR Signal. *J. Am. Chem. Soc.* **1998,** *120* (31), 7924-7928.

(22) Paul, S.; Neese, F.; Pantazis, D. A., Structural models of the biological oxygen-evolving complex: achievements, insights, and challenges for biomimicry. *Green Chemistry* **2017,** *19* (10), 2309-2325.

(23) Mukhopadhyay, S.; Mandal, S. K.; Bhaduri, S.; Armstrong, W. H., Manganese Clusters with Relevance to Photosystem II. *Chem. Rev.* **2004,** *104* (9), 3981-4026.

(24) Mullins, C. S.; Pecoraro, V. L., Reflections on small molecule manganese models that seek to mimic photosynthetic water oxidation chemistry. *Coord. Chem. Rev.* **2008,** *252* (3), 416-443.

(25) Blondin, G.; Davydov, R.; Philouze, C.; Charlot, M.-F.; Styring, t.; Åkermark, B.; Girerd, J.-J.; Boussac, A., Electron paramagnetic resonance study of the S =1/2 ground state of a radiolysis-generated manganese(III)–trimanganese(IV) form of $[Mn^{IV4}O_6(bipy)_6]^{4+}$ (bipy = 2,2′ -bipyridine). Comparison with the photosynthetic Oxygen Evolving Complex†. *J. Chem. Soc., Dalton Trans.* **1997,** (21), 4069-4074.

(26) Ruettinger, W. F.; Ho, D. M.; Dismukes, G. C., Protonation and Dehydration Reactions of the $Mn_4O_4L_6$ Cubane and Synthesis and Crystal Structure of the Oxidized Cubane $[Mn_4O_4L_6]^+$: A Model for the Photosynthetic Water Oxidizing Complex. *Inorg. Chem.* **1999,** *38* (6), 1036-1037.

(27) Ruettinger, W. F.; Campana, C.; Dismukes, G. C., Synthesis and Characterization of $Mn_4O_4L_6$ Complexes with Cubane-like Core Structure: A New Class of Models of the Active Site of the Photosynthetic Water Oxidase. *J. Am. Chem. Soc.* **1997,** *119* (28), 6670-6671.

(28) Dubé, C. E.; Sessoli, R.; Hendrich, M. P.; Gatteschi, D.; Armstrong, W. H., A Spin Topological Model for the g = 4.1 S_2 State Photosystem II Water Oxidase Manganese Aggregate. *J. Am. Chem. Soc.* **1999,** *121* (14), 3537-3538.

(29) Zhang, C.; Chen, C.; Dong, H.; Shen, J.-R.; Dau, H.; Zhao, J., A synthetic Mn_4Ca-cluster mimicking the oxygen-evolving center of photosynthesis. *Science* **2015,** *348* (6235), 690.

(30) Shoji, M.; Isobe, H.; Shen, J.-R.; Yamaguchi, K., Geometric and electronic structures of the synthetic Mn_4CaO_4 model compound mimicking the photosynthetic oxygen-evolving complex. *PCCP* **2016,** *18* (16), 11330-11340.

(31) Kern, J.; Chatterjee, R.; Young, I. D.; Fuller, F. D.; Lassalle, L.; Ibrahim, M.; Gul, S.; Fransson, T.; Brewster, A. S.; Alonso-Mori, R.; Hussein, R.; Zhang, M.; Douthit, L.; de Lichtenberg, C.; Cheah, M. H.; Shevela, D.; Wersig, J.; Seuffert, I.; Sokaras, D.; Pastor, E.; Weninger, C.; Kroll, T.; Sierra, R. G.; Aller, P.; Butryn, A.; Orville, A. M.; Liang, M.; Batyuk, A.; Koglin, J. E.; Carbajo, S.; Boutet, S.; Moriarty, N. W.; Holton, J. M.; Dobbek, H.; Adams, P. D.; Bergmann, U.; Sauter, N. K.; Zouni, A.; Messinger, J.; Yano, J.; Yachandra, V. K., Structures of the intermediates of Kok's photosynthetic water oxidation clock. *Nature* **2018,** *563* (7731), 421-425.

(32) Bovi, D.; Narzi, D.; Guidoni, L., The S_2 State of the Oxygen-Evolving Complex of Photosystem II Explored by QM/MM Dynamics: Spin Surfaces and Metastable States Suggest a Reaction Path Towards the S_3 State. *Angew. Chem. Int. Ed.* **2013,** *52* (45), 11744-11749.

(33) Lin, P.-H.; Tsui, E. Y.; Habib, F.; Murugesu, M.; Agapie, T., Effect of the Mn Oxidation State on Single-Molecule-Magnet Properties: MnIII vs MnIV in Biologically Inspired DyMn3O4 Cubanes. *Inorg. Chem.* **2016,** *55* (12), 6095-6099.

(34) Tsui, E. Y.; Agapie, T., Reduction potentials of heterometallic manganese–oxido cubane complexes modulated by redox-inactive metals. *Proc. Natl. Acad. Sci. U. S. A.* **2013,** *110* (25), 10084.

(35) Tsui, E. Y.; Kanady, J. S.; Agapie, T., Synthetic Cluster Models of Biological and Heterogeneous Manganese Catalysts for O_2 Evolution. *Inorg. Chem.* **2013,** *52* (24), 13833-13848.

(36) Kanady, J. S.; Tsui, E. Y.; Day, M. W.; Agapie, T., A Synthetic Model of the Mn_3Ca Subsite of the Oxygen-Evolving Complex in Photosystem II. *Science* **2011,** *333* (6043), 733.

(37) Rappaport, F.; Guergova-Kuras, M.; Nixon, P. J.; Diner, B. A.; Lavergne, J., Kinetics and Pathways of Charge Recombination in Photosystem II. *Biochemistry* **2002,** *41* (26), 8518-8527.

(38) Lee, H. B.; Agapie, T., Redox Tuning via Ligand-Induced Geometric Distortions at a YMn_3O_4 Cubane Model of the Biological Oxygen Evolving Complex. *Inorg. Chem.* **2019,** *58* (22), 14998-15003.

(39) Amtawong, J.; Balcells, D.; Wilcoxen, J.; Handford, R. C.; Biggins, N.; Nguyen, A. I.; Britt, R. D.; Tilley, T. D., Isolation and Study of Ruthenium–Cobalt Oxo Cubanes Bearing a High-Valent, Terminal Ru^V–Oxo with Significant Oxyl Radical Character. *J. Am. Chem. Soc.* **2019,** *141* (50), 19859-19869.

(40) Nguyen, A. I.; Wang, J.; Levine, D. S.; Ziegler, M. S.; Tilley, T. D., Synthetic control and empirical prediction of redox potentials for Co_4O_4 cubanes over a 1.4 V

range: implications for catalyst design and evaluation of high-valent intermediates in water oxidation. *Chem. Sci.* **2017,** *8* (6), 4274-4284.

(41) Glöckner, C.; Kern, J.; Broser, M.; Zouni, A.; Yachandra, V.; Yano, J., Structural Changes of the Oxygen-evolving Complex in Photosystem II during the Catalytic Cycle*. *J. Biol. Chem.* **2013,** *288* (31), 22607-22620.

(42) Chilton, N. F.; Anderson, R. P.; Turner, L. D.; Soncini, A.; Murray, K. S., PHI: A powerful new program for the analysis of anisotropic monomeric and exchange-coupled polynuclear d- and f-block complexes. *J. Comput. Chem.* **2013,** *34* (13), 1164-1175.

(43) Krzystek, J.; Ozarowski, A.; Telser, J., Multi-frequency, high-field EPR as a powerful tool to accurately determine zero-field splitting in high-spin transition metal coordination complexes. *Coord. Chem. Rev.* **2006,** *250* (17), 2308-2324.

(44) Su, J.-H.; Cox, N.; Ames, W.; Pantazis, D. A.; Rapatskiy, L.; Lohmiller, T.; Kulik, L. V.; Dorlet, P.; Rutherford, A. W.; Neese, F.; Boussac, A.; Lubitz, W.; Messinger, J., The electronic structures of the S2 states of the oxygen-evolving complexes of photosystem II in plants and cyanobacteria in the presence and absence of methanol. *Biochim. Biophys. Acta, Bioenerg.* **2011,** *1807* (7), 829-840.

(45) Pace, R. J.; Smith, P.; Bramley, R.; Stehlik, D., EPR saturation and temperature dependence studies on signals from the oxygen-evolving centre of photosystem II. *Biochim. Biophys. Acta, Bioenerg.* **1991,** *1058* (2), 161-170.

(46) Randall, D. W.; Sturgeon, B. E.; Ball, J. A.; Lorigan, G. A.; Chan, M. K.; Klein, M. P.; Armstrong, W. H.; Britt, R. D., ^{55}Mn ESE-ENDOR of a Mixed Valence Mn(III)Mn(IV) Complex: Comparison with the Mn Cluster of the Photosynthetic Oxygen-Evolving Complex. *J. Am. Chem. Soc.* **1995,** *117* (47), 11780-11789.

(47) Reed, C. J.; Agapie, T. Tetranuclear Fe Clusters with a Varied Interstitial Ligand: Effects on the Structure, Redox Properties, and Nitric Oxide Activation. *Inorg. Chem.*, **2017**, *56*, 13360-13367.

CHAPTER 4

Coordination Number Effect in High-spin Low-spin Equilibrium in Model Complexes of the S_2 state of the Oxygen Evolving Complex

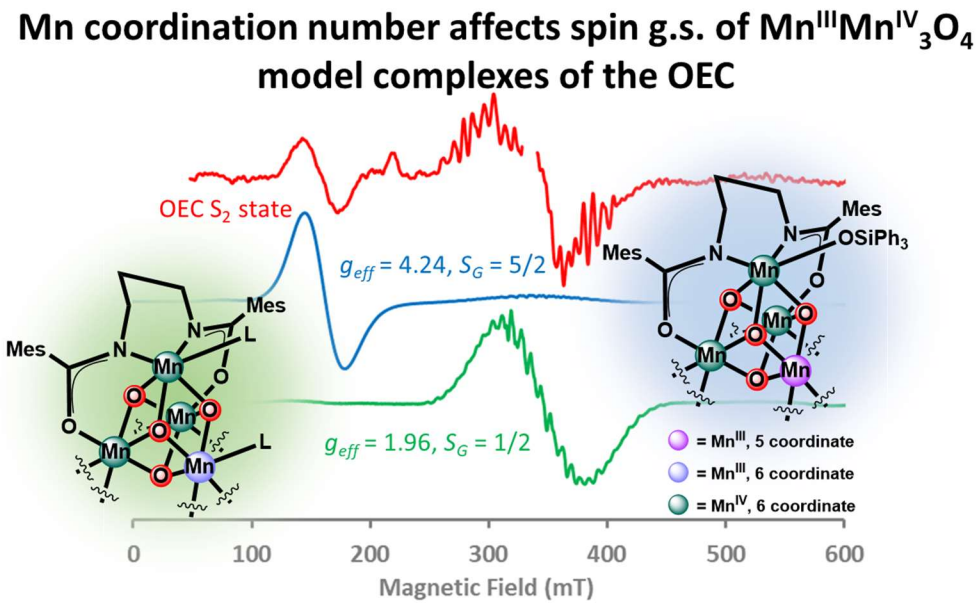

The text for this chapter was reproduced in part from:

Shiau, A. A.; Lee, H. B.; Oyala, P. H.; Agapie, T. *Submitted*.

Abstract

The S_2 state of the Oxygen Evolving Complex (OEC) of Photosystem II (PSII) shows high-spin (HS) and low-spin (LS) EPR signals computationally attributed to distinct structures. Conversion between the two is a crucial topic of study in the context of progression to higher S_n states; importantly, both isomers feature five-coordinate Mn^{III} centers, a characteristic absent in available spectroscopic model complexes. Herein, we report the synthesis, crystal structure, electrochemistry, SQUID magnetometry, and EPR spectroscopy of a $Mn^{III}Mn^{IV}{}_3O_4$ cuboidal complex featuring a five-coordinate Mn^{III}. Results demonstrate that coordination number has substantial effect on spectroscopy; a spin ground state of $S = 5/2$ is observed for the cluster with a five-coordinate Mn, and addition of water results in a spin state change of $S = 5/2 \rightarrow 1/2$, emphasizing the sensitivity of the spectroscopy of tetramanganese oxo clusters to changes in ligand environment, without dramatic changes in the Mn_4O_4 cluster core.

4.1) Introduction

The Oxygen Evolving Complex (OEC) in Photosystem II (PSII) performs the four-electron oxidation of water to dioxygen.[1-6] Upon photon absorption, the inorganic $CaMn_4O_x$ core sequentially advances to higher S_n (n = 0 – 4) states. Structural and spectroscopic characterization of these intermediates has been crucial for mechanistic proposals of the OEC. Although significant progress has been achieved through extensive biochemical, biophysical, spectroscopic, and structural studies, fundamental questions about this mechanism remain. Synthetic model complexes of appropriate metal oxidation states and cluster geometries for higher S_n states are rare but have been demonstrated to complement and benchmark studies on the OEC.[7-23]

For the S_2 state, two EPR signals are observed at g = 2 and g = 4.1, attributed to two structures of similar energy by computation (Figure 1).[24] Ferromagnetic coupling in the $CaMn^{IV}_3$ cuboidal subsite (S = 9/2) and antiferromagnetic coupling to the dangler Mn^{III} (S = 2) in the "closed-cubane" structure leads to a high-spin (HS) ground state of S_G = 5/2. In the "open-cubane" structure, the $CaMn^{III}Mn^{IV}_2$ subsite is proposed to be S = 1; antiferromagnetic coupling to the dangler Mn^{IV} (S = 3/2) leads to an overall low-spin (LS) ground state of S_G = 1/2. Effectively, the two structures differ in the location of O(5), an oxo proposed to be involved in O–O bond formation.[25-26] Notably, both Mn^{III} centers in these structures are five-coordinate, poised for binding an additional substrate water or hydroxide to give an all-octahedral Mn^{IV}_4 species in the S_3 state.[27-28]

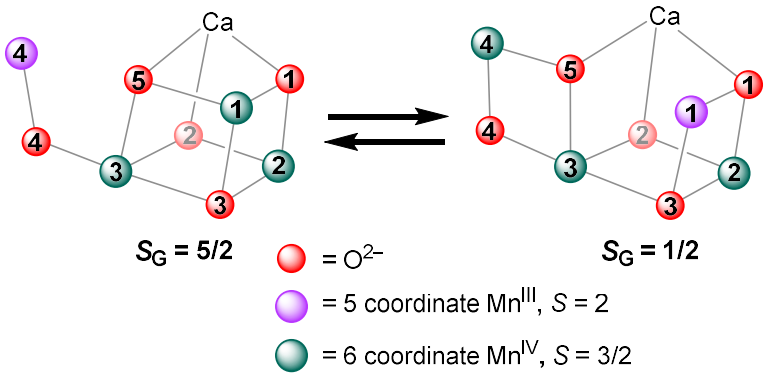

Figure 1. Proposed open-closed cubane structures of the inorganic $CaMn_4$ core of the OEC in the S_2 state.

Recent pH dependence studies on the S_2 state show that at high pH, the HS form is more prevalent.[29] Though atomistic details following deprotonation of the LS species are unknown, these results highlight the sensitivity of the OEC towards small changes in the ligand environment.[30-32] This observation is interesting as growing experimental data suggest that an intermediate step in the $S_2 \rightarrow S_3$ advancement is the conversion of the LS species to the HS species.[33]

In contrast to the wealth of literature in biochemical and biophysical studies, a relatively small number of synthetic $Mn^{III}Mn^{IV}_3$ compounds have been characterized by EPR spectroscopy. Crucially, available $Mn^{III}Mn^{IV}_3O_x$ model complexes of linear,[34] adamantane,[35] and cubane geometries all contain six-coordinate Mn centers.[15, 18, 36] OEC structural model compound $CaMn^{III}_2Mn^{IV}_2O_4(OPiv)_8$ contains a six-coordinate dangler Mn^{III}, crystallizing as the pyridine adduct.[37-38] *In situ* oxidation generates an EPR spectrum displaying two signals at g = 4.9 and g = 2 highly reminiscent of the biological system, though additional characterization was not reported. However, independent computational studies suggest these two signals arise from different structures.[7, 39]

A series of cuboidal $Mn^{III}Mn^{IV}_3O_4$ complexes reported by our laboratory[15, 40-41] show that tuning of ligand electronics affects cluster electronic structure and spectroscopy without significantly perturbing the cubane core. These results contrast with the large oxo movements and cluster core structural changes proposed as the origin of the HS and LS signals in the S_2 state of the OEC, highlighting the need for further systematic studies on a larger scope of model compounds to better understand the factors influencing the spectroscopy of tetramanganese-oxo clusters.[15]

Herein, we report on the sensitivity of the electronic structures of tetramanganese oxo clusters to changes in the Mn coordination number between five and six, as relevant to the OEC S_2 state.

The synthesis, crystal structure, electrochemistry, SQUID magnetometry, and EPR spectroscopy are described for a rare example of $Mn^{III}Mn^{IV}_3O_4$ cluster with a five-coordinate Mn center. The ground spin state of this cluster shifts from $S = 5/2$ to $S = 1/2$ upon the addition of water, suggesting coordination number has an important role in ground spin state of this family of tetramanganese complexes even in the absence of substantial structural changes within the Mn_4O_4 core.

4.2) Synthesis and crystal structure

To gain access to Mn_4O_4 cubane clusters with open coordination sites, we targeted acetate-free derivatives of complexes supported by L^{3-}. Treatment of **1** with three equivalents of pyridinium triflate yielded **2** via a protonolysis reaction (Scheme 1). The ESI-MS peaks at $m/z = 1242$ and 1321 are consistent with the masses of $[LMn_3O_4(py)_2]^+$ and $[LMn_3O_4(py)_3]^+$, respectively. Complex **2** is an incomplete cuboidal Mn_3O_4 complex, lacking a fourth metal,[70] a motif reminiscent of tris-thiolate supported $[Fe_3S_4]^0$ complex

reported by Holm,[42-43] and *N*-heterocyclic carbene supported $[Fe_3S_4]^{+/0}$ complexes reported by Suess.[44] Reconstitution of homometallic $[Fe_4S_4]$ and heterometallic $[MFe_3S_4]$ (M = Co, Ni, Cu, Mo, W, Pd, Pt, Tl, Ag) cubanes was achieved by addition of simple metal precursors,[43, 45-47] highlighting the synthetic utility of this approach for site-differentiated clusters challenging to prepare via self-assembly methods.

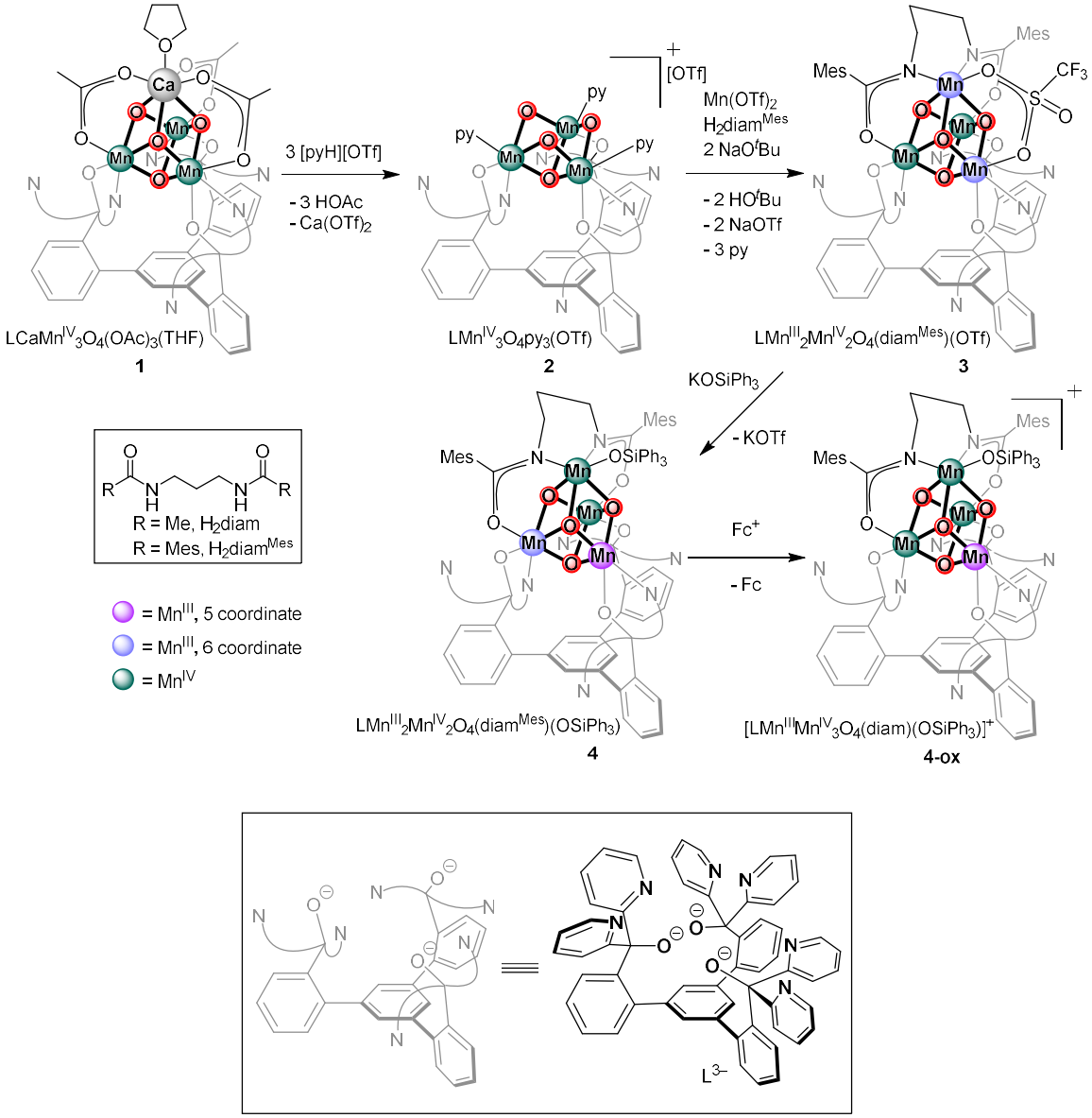

Figure 2. Synthesis of complexes studied in this work. Complex **1** is previously reported.

Inspired by this strategy, **2** was employed as a precursor to acetate-free Mn_4O_4 complexes with open coordination sites. Treatment of **2** with one equivalent of $Mn(OTf)_2 \cdot 2(MeCN)$, one equivalent of H_2diam^{Mes}, and two equivalents of base generated acetate-free cluster **3** (Figure 2). The X-ray crystal structure of **3** is consistent with the $LMn_4O_4(diam^{Mes})(OTf)$ formulation (Figure 4). Based on Mn–oxo bond lengths, individual manganese oxidation states of **3** can be assigned as follows: Mn(1) and Mn(2) as Mn^{IV}, Mn(3) and Mn(4) as Mn^{III}. Axial-elongation of Mn^{III}–oxo bond lengths due to population of σ-antibonding d_{z2} orbital can be observed for Mn(3) and Mn(4) (2.181(2) and 2.199(2) Å, respectively). The remaining Mn–oxo bond lengths vary between 1.823–1.925 Å, displaying a similar range to other $Mn^{III}_2Mn^{IV}_2O_4$ cubane complexes.[15, 40-41]

Addition of bulky siloxide $KOSiPh_3$ to **3** yields **4**. The crystal structure of **4** is consistent with the $LMn_4O_4(diam^{Mes})(OSiPh_3)$ formulation (Figure 4). In this structure, two axially elongated Mn^{III}–oxo bonds (Å) are observed (Mn(1)–O(2) 2.120(2), Mn(3)–O(4) 2.073(2)), confirming the $Mn^{III}_2Mn^{IV}_2$ oxidation state of **4**. In comparison to **3**, the position of one Mn^{III} ion in the cluster core is different; this internal redox reorganization is consistent with the ability of electron-donating siloxide ligands to act as both σ and π donors.[48] Similar behavior is observed for related disiloxide ligated Mn_4O_4 complexes.[41] Notably, addition of $KOSiPh_3$ to related acetate-ligated Mn_4O_4 clusters did not result in any reaction at ambient conditions, highlighting the utility of this synthetic strategy in accessing a five-coordinate Mn center for this series of complexes.

The cyclic voltammogram (CV) of **4** in THF shows a quasi-reversible redox process at –0.24 V versus Fc/Fc^+, assigned to the $(Mn^{III}_2Mn^{IV}_2)/(Mn^{III}Mn^{IV}_3)$ redox couple (Figure 3).

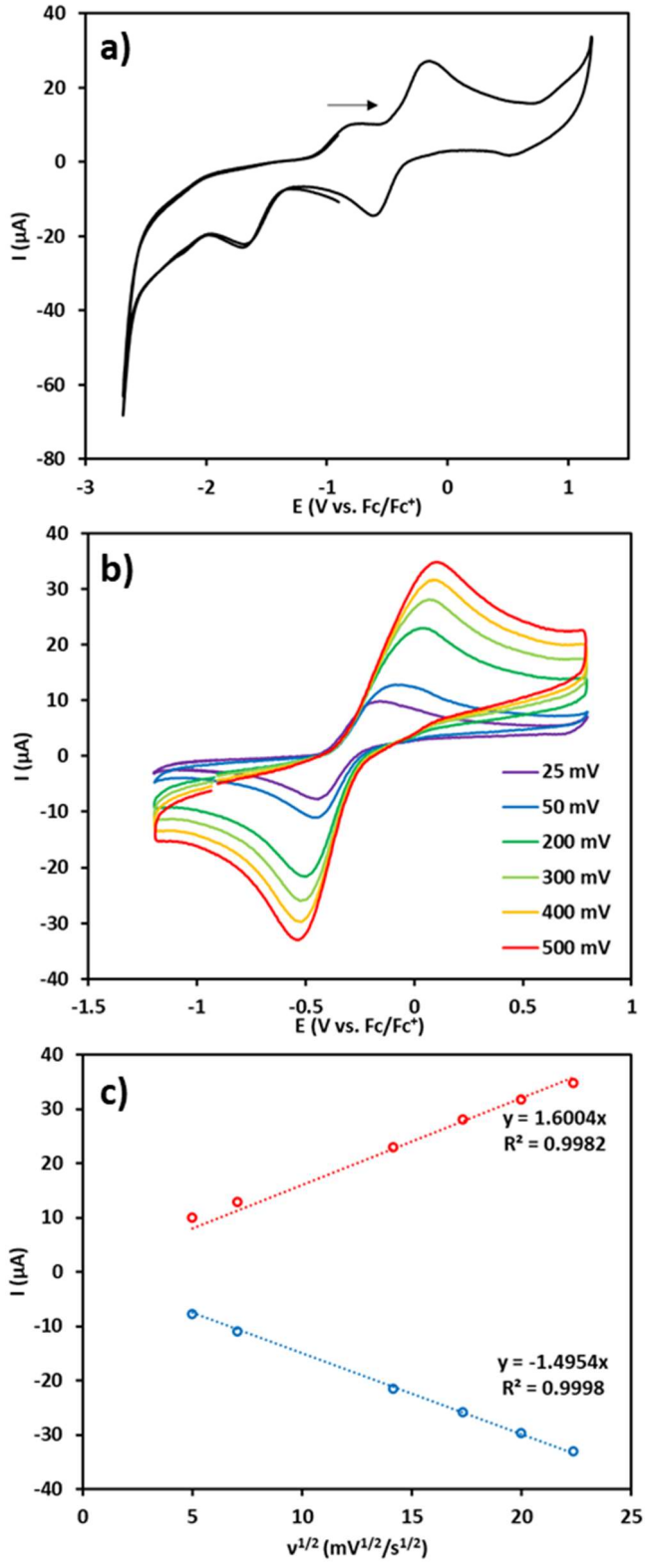

Figure 3. a) CV of **4**. E_{ox} = – 0.24 V vs. Fc/Fc^{+}. **b)** Isolated redox couple measured at various scan rates (mV/s) **c)** Plot of peak current vs. square root of scan rate.

Treatment of **4** with one equivalent of FcOTf generates the one-electron oxidized species **4-ox**. The crystal structure of **4-ox** is consistent with the $[LMn_4O_4(diam^{Mes})(OSiPh_3)][OTf]$ formulation (Figure 2). Axial-elongation of one Mn^{III}–oxo bond (2.093(3) Å *trans* to the open coordination site) due to population of σ-antibonding d_{z2} orbital is observed for Mn(3). To our knowledge, complex **4-ox** is the first structurally characterized $Mn^{III}Mn^{IV}_3O_x$ cluster featuring a Mn^{III} with an open coordination site. In the context of the isomerism proposed for the S_2 state of the OEC, and for comparison to previously studied model compounds, **4-ox** was further characterized to determine the effects of coordination number.

Table 1. Selected bond distances (Å) and angles (°) in complexes **3**, **4**, and **4-ox**. Bolded entries highlight elongated Mn-oxo bond lengths.

	3	**4**	**4-ox**
Mn(1) – O(2)	1.923(2)	**2.120(2)**	1.883(3)
Mn(1) – O(3)	1.823(2)	1.8927(19)	1.899(3)
Mn(1) – O(4)	1.878(2)	1.945(2)	1.879(3)
Mn(2) – O(1)	1.904(2)	1.922(2)	1.917(3)
Mn(2) – O(3)	1.867(2)	1.8831(19)	1.878(3)
Mn(2) – O(4)	1.866(2)	1.871(2)	1.891(3)
Mn(3) – O(1)	1.914(2)	1.9332(19)	1.938(3)
Mn(3) – O(2)	1.925(2)	1.8751(19)	1.917(3)
Mn(3) – O(4)	**2.181(2)**	**2.073(2)**	**2.093(3)**
Mn(4) – O(1)	1.923(2)	1.9243(19)	1.906(3)
Mn(4) – O(2)	1.902(2)	1.8748(19)	1.927(3)
Mn(4) – O(3)	**2.199(2)**	1.933(2)	1.928(3)
Mn(4) – O(5)	–	1.845(2)	1.810(3)
Mn(4)–O(5)–Si(1)	–	148.60(13)	154.7(2)

Table 2. Comparison of selected distances (Å) and bond angles (°) in complexes $[LMn_4O_4(diam)(OAc)]^{+}$ [15] and **4-ox**.

	$[LMn_4O_4(diam)(OAc)]^{+}$ [15]	**4-ox**
Mn(1) – Mn(2)	2.899(2)	2.847(1)
Mn(1) – Mn(3)	2.946(1)	2.878(1)
Mn(1) – Mn(4)	2.777(1)	2.786(1)
Mn(2) – Mn(3)	2.962(1)	2.936(2)
Mn(2) – Mn(4)	2.758(1)	2.782(1)
Mn(3) – Mn(4)	2.804(1)	2.847(1)
Mn(1) – O(3) – Mn(4)	93.7(2)	93.4(1)
Mn(1) – O(2) – Mn(4)	93.7(2)	94.0(1)
Mn(1) – O(3) – Mn(2)	99.4(2)	97.9(1)
Mn(1) – O(4) – Mn(2)	97.1(2)	98.0(1)
Mn(2) – O(3) – Mn(4)	93.4(2)	94.0(1)
Mn(2) – O(1) – Mn(4)	93.1(2)	93.4(1)
Mn(2) – O(1) – Mn(3)	101.5(2)	99.2(1)
Mn(2) – O(4) – Mn(3)	96.0(2)	94.8(1)
Mn(3) – O(2) – Mn(1)	101.4(2)	98.5(1)
Mn(3) – O(4) – Mn(1)	95.2(2)	92.7(1)
Mn(3) – O(1) – Mn(4)	94.3(2)	95.6(1)
Mn(3) – O(2) – Mn(4)	94.5(2)	95.6(1)

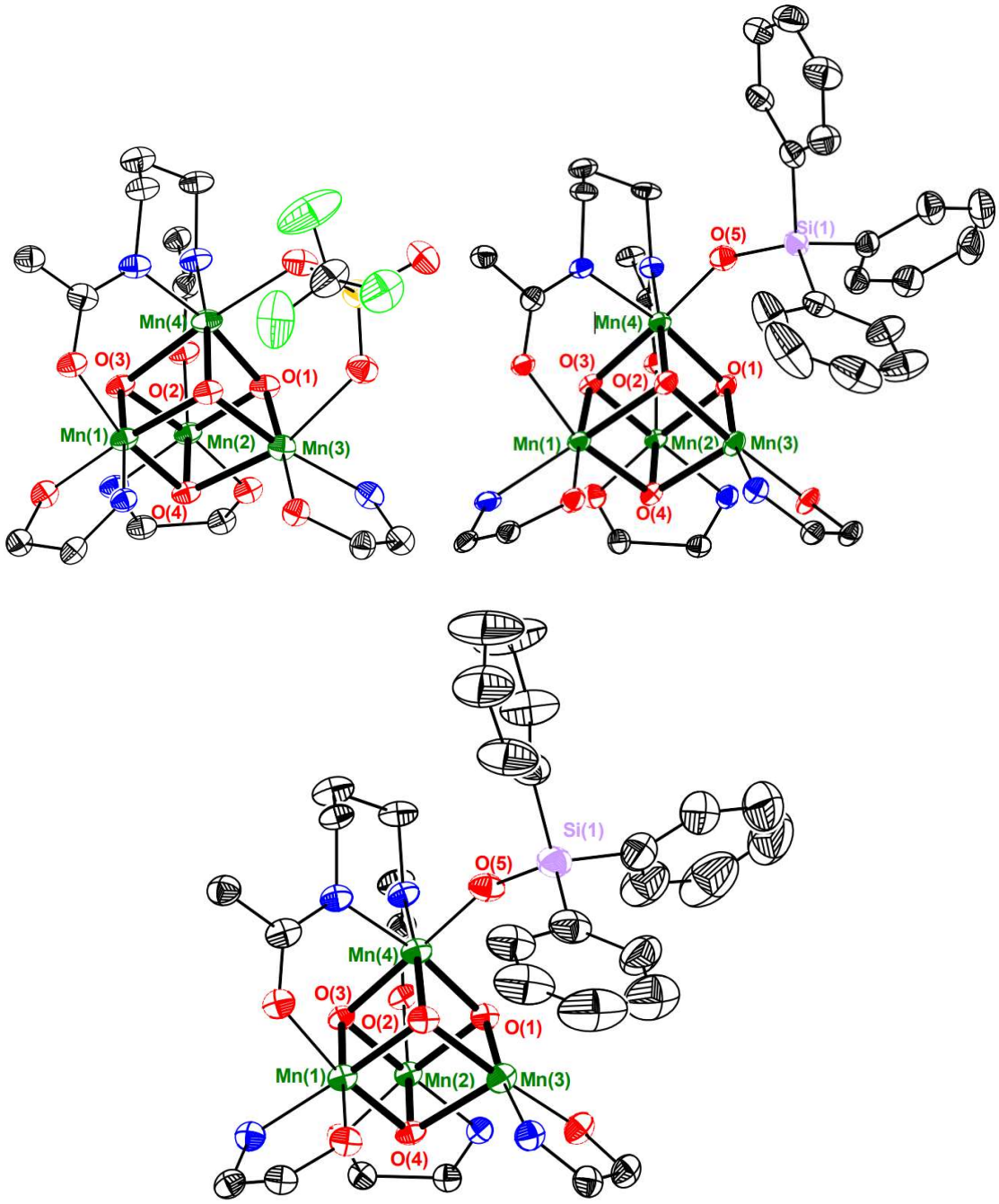

Figure 4. Truncated crystal structures of **3** (top, left), **4** (top, right), and **4-ox** (bottom). Mn(green), O (red), N (blue), C (black), F (light green), Si (light purple), S (yellow). Bolded bond highlight Mn-oxo bonds. Thermal ellipsoids are plotted at 50% probability.

4.3) Magnetometry

Complex **4-ox** was studied by SQUID magnetometry in the temperature range of 2–300 K at a nonsaturating field of 0.2 T (Figure 5). At 300 K, the χT value of 6.113 emu·K·mol^{-1} indicates antiferromagnetic coupling, as the expected spin-only value is 8.625 emu·K·mol^{-1} (g = 2) for an uncoupled Mn^{III} (S = 2) and three Mn^{IV} (S = 3/2) centers. χT decreases with temperature, reaching a minimum of 3.07 emu·K·mol^{-1} at 20 K. Further cooling shows an increase in χT until a value of 4.151 emu·K·mol^{-1} is observed at 2 K. This value is in good agreement with the expected χT value of 4.375 emu·K·mol^{-1} for a S_G = 5/2 (g = 2) ground state. The data can be modeled[49] with an isotropic spin exchange Hamiltonian (Eq. 1) with four unique magnetic interactions, assuming *pseudo*-C_S symmetry of the $[Mn_4O_4]$ core (Figure 3). Zero-field splitting (ZFS) parameters of $|D|$ = 0 cm^{-1} (Mn^{IV}) and 0.32 cm^{-1} (Mn^{III}) provided a good fit, consistent with EPR simulations, *vide infra*. ZFS values for octahedral Mn^{IV} complexes are expected to be small (~0.2 cm^{-1}) due to the near spherical symmetry of the $(t_{2g}^3 e_g^0)$ state.[50-52] While mononuclear Mn^{III} complexes of varying geometries tend to have larger ZFS values ($|D|$ = ~1–5 cm^{-1}),[53] smaller values ($|D|$ = ~0.3–0.4 cm^{-1}) have been observed for triangular Mn^{III}_3 and cuboidal $Mn^{III}_3Mn^{IV}O_3Cl$ complexes.[54-55] Overall, magnetic susceptibility studies indicate a S = 5/2 ground state for **4-ox**, contrasting directly with $[Mn_4O_4]^{7+}$ compounds supported by L^{3-}.

$$\widehat{H} = -2 \sum_{i \neq j}^{i,j \in N} J_{ij} \widehat{S}_i \cdot \widehat{S}_j \qquad (1)$$

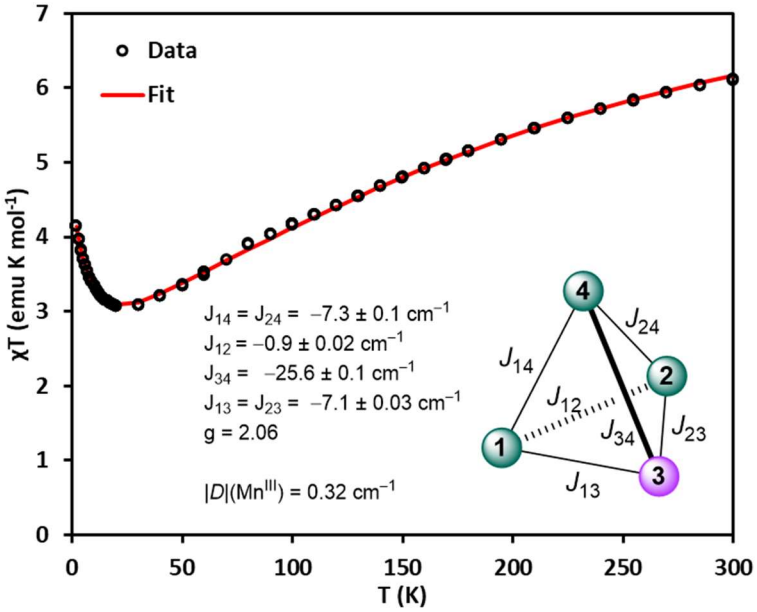

Figure 5. Magnetic susceptibility, exchange coupling model, and fit parameters for **4-ox**. For the exchange coupling model, the mirror plane of the *pseudo*-C_S symmetry contains the bolded vector and bisects the hashed vector. Numbering scheme is identical to that in Figure 4.

4.4) EPR spectroscopy

Frozen solution samples of **4-ox** were studied by X-band CW-EPR spectroscopy. At 5 K, the EPR spectrum of **4-ox** displays a broad, intense feature centered at ~160 mT (g = 4.24), with a small shoulder with maximum intensity at g ~ 8.9. A low-intensity signal centered at g = 2 with ^{55}Mn hyperfine interactions is also observed (Figure 6). All features display similar temperature dependence (Figure 6) and the spectrum can be simulated[56] using the following parameters: g = [2.074, 2.068, 2.045], g_{iso} = 2.062, $|D|$ = 0.32 cm^{-1}, E/D = 0.265 (Figure 7iv). This EPR spectrum is reminiscent of that of adamantane-shaped $[Mn_4O_6(bpea)_4]^{3+}$ (bpea = *N*, *N*-bis(2-pyridylmethyl)ethylamine).[35] An intense broad peak at g ~ 4.1 with a shoulder at g ~ 9.1 was assigned to a S_G = 5/2 with an E/D value of 0.2, with $|D|$ = 1.1 cm^{-1} determined from field-dependent magnetic susceptibility studies. A related complex **5-ox**, bearing different substituents on the siloxide moiety but also possessing a five-coordinate Mn^{III}, features a similar EPR spectrum (Figure 7).

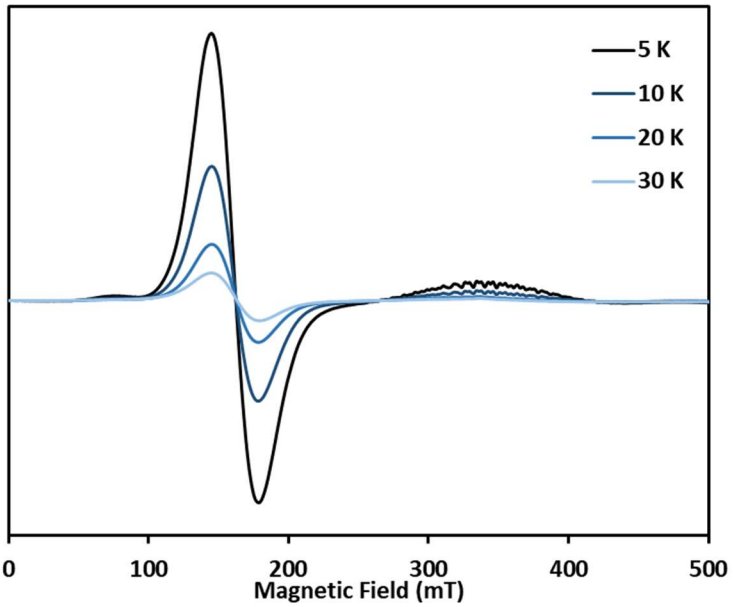

Figure 6. Variable temperature X-band EPR spectrum of **4-ox**. Acquisition parameters: frequency = 9.64 MHz, power = 8.7 mW, conversion time = 10.00 ms, and modulation amplitude = 8G.

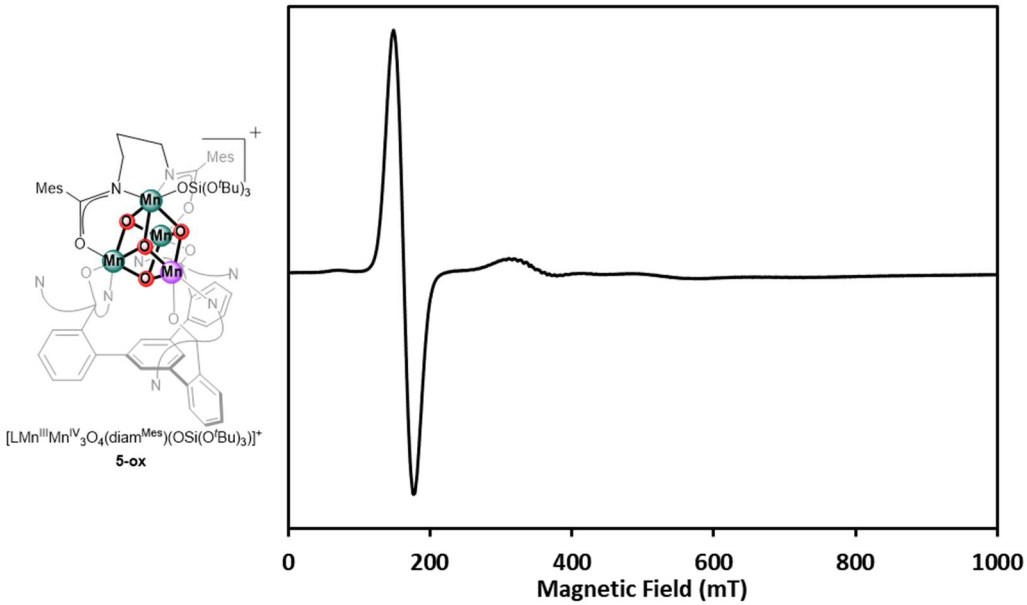

Figure 7. Scheme depicting complex **5-ox** (left). X-band CW EPR spectrum of **5-ox** at T = 5 K (right). Acquisition parameters: frequency = 9.64 MHz, power = 8.7 mW, conversion time = 10.00 ms, and modulation amplitude = 8G.

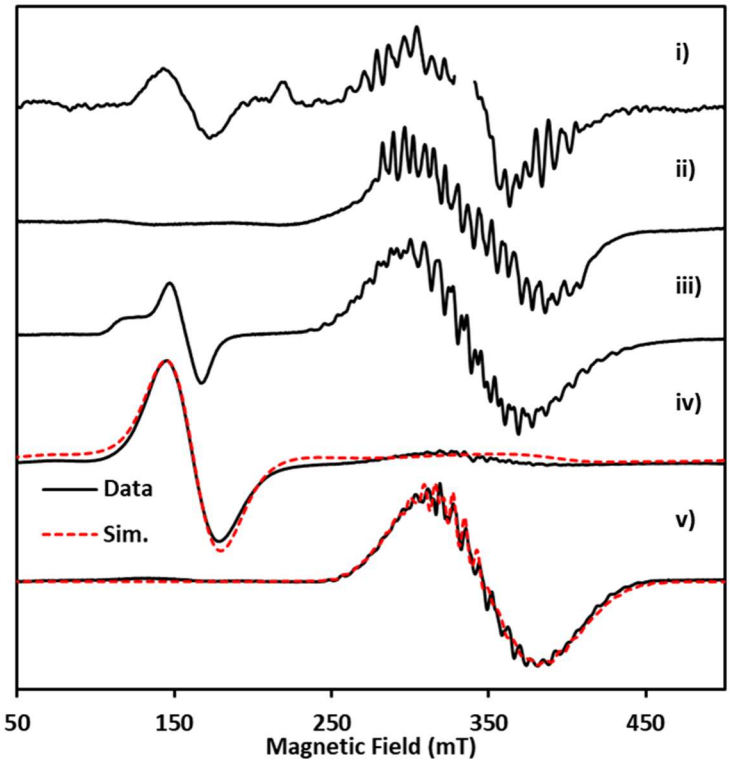

Figure 8. i) X-band EPR of the S_2 state of the OEC,[59] **ii)** $[LMn_4O_4(OPPh_2)_3][OTf]$ (5 K) $S_G = 1/2$,[15] **iii)** $[LMn_4O_4(diam)(OAc)][OTf]$ (17.5 K) $S_G = 1/2$, $S_{ES} = 3/2$,[15] **iv) 4-ox** (5 K), $S_G = 5/2$, **v)** addition of ~80 equiv. of H_2O to **4-ox**, (5 K) $S_G = 1/2$. Data (black traces) and simulation (dashed red traces). See text for simulation parameters and experimental section for acquisition parameters.

In contrast, other cuboidal Mn_4O_4 complexes supported by the same ancillary ligand L^{3-} exhibit $S_G = 1/2$.[15, 40] For tris-phosphinate cluster $[LMn_4O_4(O_2PPh_2)_3][OTf]$, a broad signal centered about $g = 2$ with ^{55}Mn hyperfine coupling interactions is observed, consistent with the well-isolated $S_G = 1/2$ ground state determined by magnetometry (Figure 8ii). Diamidate complex $[LMn_4O_4(diam)(OAc)][OTf]$ also possesses a ground state of $S = 1/2$, with a low-lying quartet excited state predicted to be 3 – 5 cm^{-1} (equivalent temperature 4.3–7.2 K) higher in energy. Consequently, the EPR spectrum of this species shows significant temperature dependence; at low temperatures (5 K) only a multiline signal at $g = 2$ is observed, but as the temperature is increased, population

of the quartet excited state gives rise to a broad signal at $g = 4.2$ concomitant with decreasing intensity of the LS signal (Figure 8iii). Despite high similarities in structural parameters of the cubane cores (Table 2), complex **4-ox** displays drastically different magnetic and spectroscopic properties from these examples.[15]

To further investigate the effect of Mn coordination number on the spectroscopy of Mn_4O_4 complexes, we monitored the reaction between **4-ox** and water by EPR spectroscopy. After addition of ~80 equivalents of water, a new species with a broad feature centered about $g = 2$ featuring ^{55}Mn hyperfine interactions is observed (Figure 8v). Assignment of this putative OH_x-bound species will be discussed.

To gain better understanding of the Mn hyperfine interactions (HFI) in this species, ^{55}Mn Davies electron nuclear double resonance (ENDOR) spectra were collected at Q-band (Figure 9b). The pulse sequence π-t_{RF}-π_{RF}-t_{RF}-$\pi/2$-τ–π–τ-echo was used. Spectra were collected at 1170, 1205, 1240, 1270, and 1300 mT along the envelope of the electron spin-echo detected EPR (ESE-EPR) spectrum (Figure 9a). The ESE-EPR spectrum, ENDOR spectra, and X-band CW spectrum can be approximated with the following parameters: g = [1.999, 1.946, 1.938], g_{iso} = 1.961, and ^{55}Mn hyperfine interactions A_i $(A_{iso})_i$ Mn_1 = [287, 311, 384] (327) MHz, Mn_2 = [203, 256, 292] (250) MHz, Mn_3 = [176, 204, 251] (209) MHz. Mn_4 = [130, 186, 221] (178) MHz. One unique Mn with larger HFI (A_{iso} = 327 MHz) is consistent with the presence of one Mn^{III} ion in this species.[57] This spread of HFI values is also comparable to those determined for $[LMn_4O_4(diam)(OAc)]^+$ and the S_2 state of *T. elongatus*, *Synechocystis*, and spinach PSII (Table 3).[15, 50, 58-59]

Table 3. Summary of the effective *g* and ^{55}Mn HFI tensors (isotropic) for **4-ox-H$_2$O**, [LMn$_4$O$_4$(diam)(OAc)]$^+$,[15] *T. elongatus*,[7] spinach PSII,[8] and *Synechocystis*.[59]

	g	A_1	A_2	A_3	A_4
4-ox-H$_2$O	1.961	327	250	209	178
[LMn$_4$O$_4$(diam)(OAc)]$^+$	1.970	315	230	228	198
T. elongatus	1.968	312	251	208	191
Spinach	1.977	298	248	205	193
Synechocystis	1.984	307	204	190	209

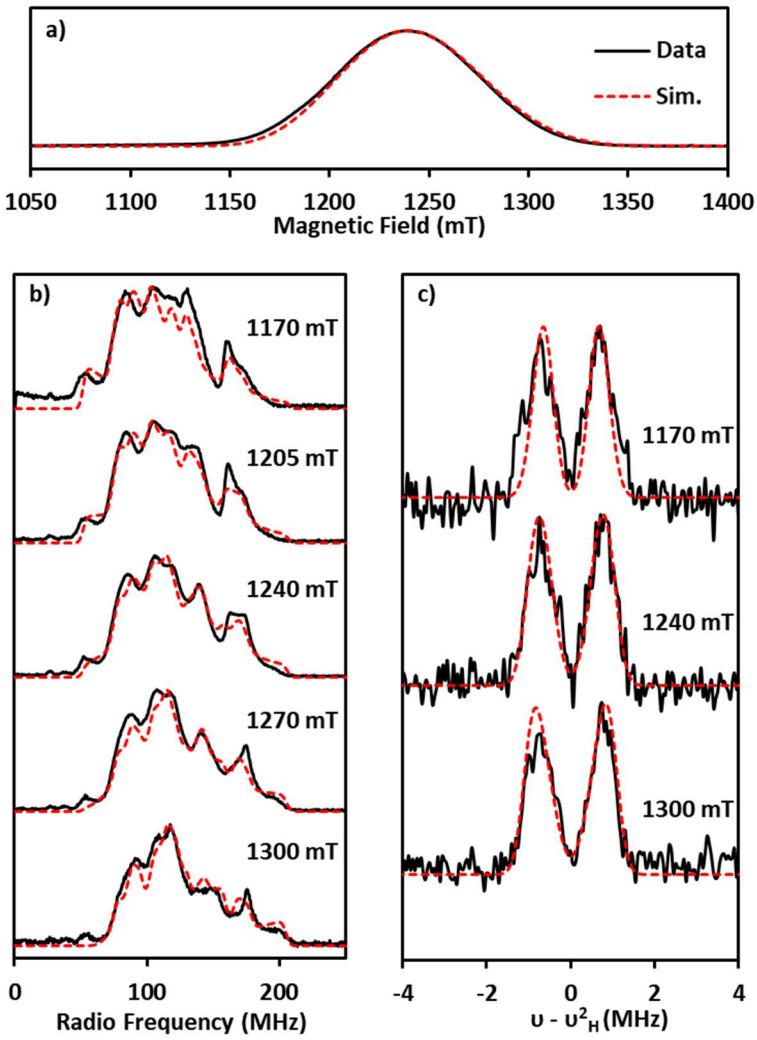

Figure 9. Experimental spectra of the reaction of **4-ox** and ~80 equiv. of H_2O (b) or D_2O (c) (black traces) and simulation (dashed red traces) **(a)** Q-band electron spin echo (ESE) EPR. **(b)** Q-band ^{55}Mn Davies ENDOR recorded at five magnetic field positions. **(c)** Q-band ^{2}H Mims ENDOR ^{2}H−^{1}H difference spectra centered at ^{2}H Larmor frequency collected at three magnetic field positions. See text for simulation parameters and experimental section for acquisition parameters.

Deuterium-labeled samples prepared analogously using $^{2}H_2O$ were further characterized via ^{2}H Mims ENDOR using the pulse sequence $\pi/2$-τ-$\pi/2$-t_{RF}-π_{RF}-t_{RF}-$\pi/2$-τ-echo (see Experimental section for further details). $^{2}H-^{1}H$ difference spectra (Figure 9c) centered about the Larmor frequency of ^{2}H show signals consistent with a single resolved class of weak coupling to deuterium of A (a_{iso}) = [−1.24, −2.06, −0.41] (−1.24) MHz, confirming the binding of $O^{2}H_x$ to the cluster. In the absence of definitive structural data confirming the location of the protons, assignment of this feature as a hydroxide or water bound to Mn^{III} or Mn^{IV} is difficult, and further detailed studies are in progress to evaluate and differentiate hydroxide versus water binding.[60-61]

Analogous samples prepared with $^{17}OH_2$ (70% enrichment) were also studied via ^{17}O Mims ENDOR at Q-band. Due to large overlap of the ^{17}O peaks with the ^{14}N signals from the ancillary ligands, one of the expected ^{17}O peaks is obscured. Based on the position of the observable ^{17}O peak relative to the ^{17}O Larmor frequency, a ^{17}O hyperfine coupling constant of A = ~ 3 MHz is estimated (Figure 10). Importantly, this study further confirms the binding of OH_x group(s) to the cluster. In addition to FTIR spectroscopy and mass spectrometry, W-band ^{17}O EPR studies on the S_0 and S_1 states have been utilized to determine different classes of exchangeable oxygen nuclei.[62-65] Hyperfine coupling constants of ~ 10 MHz, ~ 5 MHz, and < 2 MHz have been assigned to bridging oxos, terminal Mn-aquo(hydroxo) and Ca-aquo moieties, respectively.[66-67] Benchmarking from relevant ^{17}O-labelled Mn synthetic compounds is limited to mononuclear and dinuclear examples due to synthetic challenges.[68-69] In **4-ox-H_2O**, the estimated hyperfine coupling constant of ~ 3 MHz is within the expected regime for a terminal Mn-aquo/hydroxo moiety and represents a rare example of ^{17}O labeling in tetranuclear Mn_4 clusters.

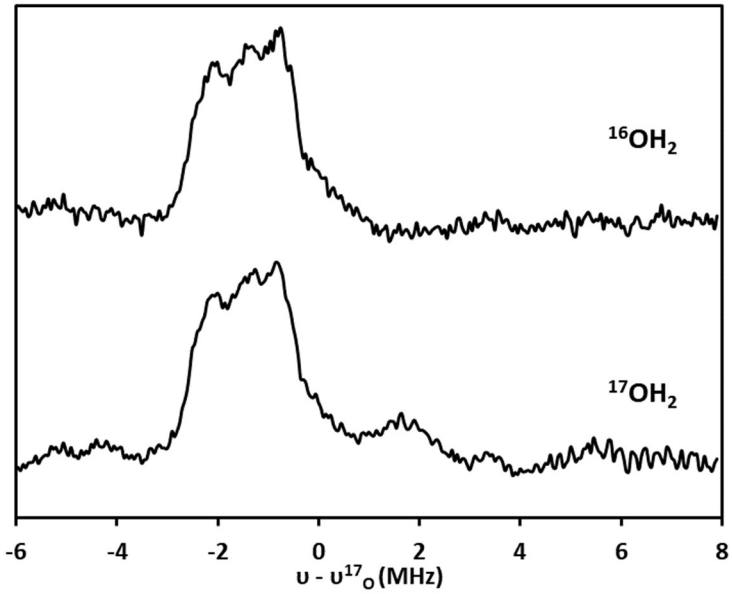

Figure 10. Q-band ^{17}O Mims ENDOR centered about ^{17}O Larmor frequency, collected at 1240 mT, T = 3.5 K. Comparison between samples prepared using natural abundance water (top) versus ^{17}O labeled water (bottom) confirm the binding of OH_x group(s) to the cluster. Peaks not centered about ^{17}O Larmor frequency present in both natural abundance and labeled samples are attributed to ^{14}N signals from ancillary ligands.

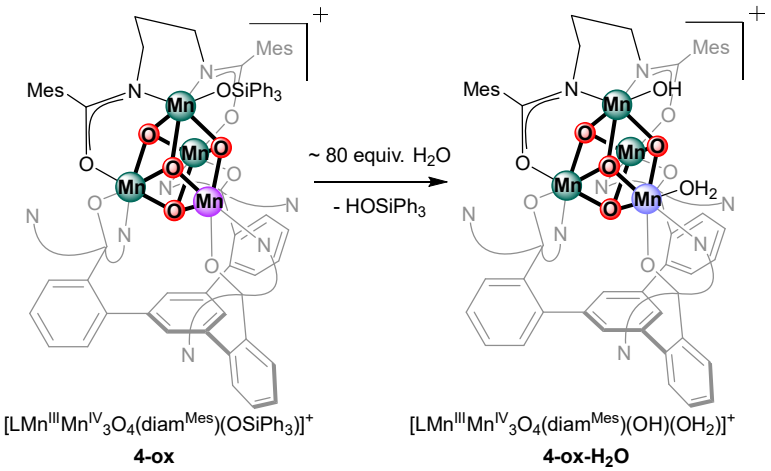

Figure 11. Addition of water to **4-ox** to generate **4-ox-H₂O**.

Given that an OH_x moiety is bound to the paramagnetic center, two scenarios are plausible. This new species can be the product of simple ligand binding to Mn^{III} or that of a more complex process involving hydrolysis of the siloxide to yield a hydroxide-bound

cluster and one equivalent of byproduct triphenylsilanol. Due to the large excess of water added, this putative hydroxide species is proposed to contain a water molecule coordinated to the original five-coordinate Mn^{III} site (Figure 11). Allowing pentane to diffuse into a THF solution of **4-ox** (with a different weakly-coordinating anion) treated with water also yielded crystals of lower quality, confirming an intact $[LMn_4O_4(diam^{Mes})(OH_x)(OH_y)]^+$ cluster core (Figure 12). Mn-oxo bond lengths in the core corroborate a $Mn^{III}Mn^{IV}_3$ oxidation state, with only one elongated Mn(3)−O(4) bond length of 2.186(9) Å (Table 4). The differences in the bond lengths of Mn(4)−O(5) (1.87(1) Å) and Mn(3)−O(6) (2.22(1) Å) suggest hydroxide and aquo ligands, respectively. Importantly, all Mn centers in both species are six-coordinate, with water-derived ligand(s) bound to the cluster, further demonstrating ground spin state conversion upon coordination number change at Mn. Notably, the X-band CW EPR spectrum of re-dissolved crystals in 1:1 CH_2Cl_2:2-MeTHF is nearly identical to that of the *in-situ* generated sample with ~ 80 equivalents of H_2O (Figure 13).

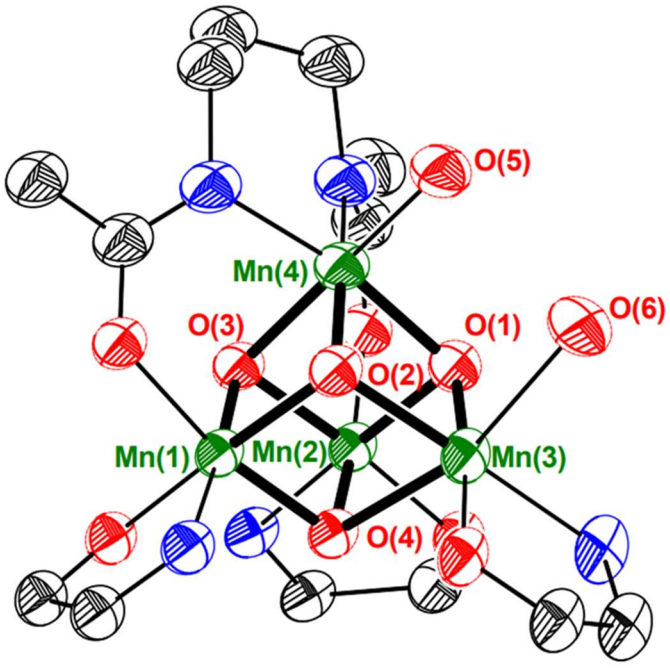

Figure 12. Truncated structures of **4-ox-H$_2$O**. Mn(green), O (red), N (blue), C (black), F (light green), Si (light purple), S (yellow). Bolded bond highlight Mn-oxo bonds. Thermal ellipsoids are plotted at 50% probability.

Table 4. Selected bond distances (Å) and angles (°) in complexes **4-ox-H$_2$O**. Bolded entries highlight elongated Mn-oxo bond lengths.

	4-ox-H$_2$O
Mn(1) – O(2)	1.919(1)
Mn(1) – O(3)	1.84(1)
Mn(1) – O(4)	1.89(1)
Mn(2) – O(1)	1.912(9)
Mn(2) – O(3)	1.89(1)
Mn(2) – O(4)	1.82(1)
Mn(3) – O(1)	1.89(2)
Mn(3) – O(2)	1.96(1)
Mn(3) – O(4)	**2.186(9)**
Mn(4) – O(1)	1.94(1)
Mn(4) – O(2)	1.92(2)
Mn(4) – O(3)	1.956(9)
Mn(4) – O(5)	1.87(1)
Mn(4) – O(6)	2.22(1)

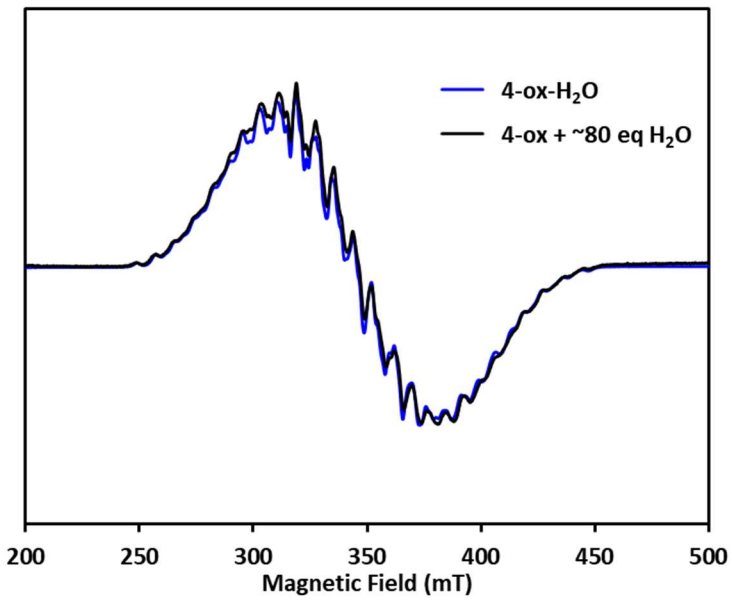

Figure 13. Comparison of the *in situ* generated water-bound species by addition of ~80 equiv. of H_2O to **4-ox** (black trace) and isolated crystals of **4-ox-H_2O**, dissolved in 1:1 CH_2Cl_2:2-MeTHF (blue trace). Both spectra collected at T = 5 K. Acquisition parameters: frequency = 9.64 MHz, power = 8.8 mW, conversion time = 10 ms, and modulation amplitude = 8 G.

4.5) Discussion

Comparisons in the series $[LMn_4O_4(O_2PPh_2)_3]^+$, $[LMn_4O_4(diam)(OAc)]^+$, **4-ox**, and **4-ox-H_2O** emphasize that large structural perturbations of the metal-oxo core are not required to observe HS and LS EPR signals in tetramanganese oxo complexes. Geometric changes much smaller than those proposed for the S_2 state of the OEC, including binding or dissociation of ligands, can have a significant impact on the electronic structure and spectroscopy.

In conclusion, a unique $Mn^{III}Mn^{IV}_3O_4$ cuboidal complex featuring a five-coordinate Mn center has been synthesized and characterized by XRD, electrochemistry, SQUID magnetometry, and EPR spectroscopy. Comparisons to a series of structurally similar complexes demonstrate the ability to change ground spin state without large perturbations of

the cluster core. Binding of OH_x group(s) was confirmed via presence of ^{2}H and ^{17}O coupling in Mims ENDOR spectra, and crystallography. For this series, coordination number plays an important role, as binding of additional ligands results in ground spin-state change from HS to LS.

4.6) Experimental

General considerations

All reactions were performed at room temperature in an N_2-filled glovebox or by using standard Schlenk techniques unless otherwise specified. Glassware was oven dried at 150 °C for at least 2h prior to use and allowed to cool under vacuum. All reagents were used as received unless otherwise stated. Compound **1** was prepared according to literature.[12] Ferrocenium triflate was synthesized according to literature. $KOSiPh_3$ was synthesized by addition of one equivalent of KH to $HOSiPh_3$ in THF. Anhydrous tetrahydrofuran (THF) was purchased from Aldrich in 18 L Pure-Pac^{TM} containers. Anhydrous CH_2Cl_2, diethyl ether, benzene, pentane, and THF were purified by sparging with nitrogen for 15 minutes and then passing under nitrogen pressure through a column of activated A2 alumina. NMR solvents were purchased from Cambridge Isotope Laboratories, dried over calcium hydride (CD_2Cl_2, CD_3CN) or over sodium/benzophenone (C_6D_6), degassed by three freeze-pump-thaw cycles and vacuum-transferred prior to use. $^{1}H_2O$ and $^{2}H_2O$ for EPR experiments were degassed by sparging with N_2 or three freeze-pump-thaw cycles, respectively. $^{17}OH_2$ (70% isotopic enrichment) was purchased from Sigma Aldrich. ^{1}H and ^{19}F NMR spectra were recorded on a Varian 300 MHz instrument, with shifts reported relative to the residual solvent peak. Elemental analyses were performed at the California Institute of Technology or at the University of Rochester.

Synthesis of N,N'-(propane-1,3-diyl)bis(2,4,6-trimethylbenzamide)

A 100 mL round bottom flask equipped with a magnetic stir bar was charged with a solution of 1,3-diaminopropane (1 mL, 0.888 g, 0.012 mmol, 1 equiv) in CH_2Cl_2 (20 mL) and cooled in an ice-water bath. To this stirring solution was added excess triethylamine (4 mL, 0.029 mmol). Two equivalents of 2,4,6-trimethylbenzoyl chloride (4.08 mL, 0.024 mmol, 2.04 equiv) was added dropwise via syringe and a white precipitate formed immediately. The reaction mixture was warmed up to room temperature and allowed to stir for 16 hours. Water (10 mL) was added to the reaction, followed by a saturated aqueous solution of $NaHCO_3$ (30 mL). The organic layer was collected, and the aqueous layer extracted with additional CH_2Cl_2 (15 mL x 3). The organic fractions were combined, dried over $MgSO_4$, and filtered. Volatiles were removed under reduced pressure and the residue was washed with copious amounts of Et_2O and hexanes to yield a white powder. (3 g, 69.7%). ^{1}H NMR (500 MHz, $CDCl_3$): d 6.83 (s, 4H), 6.30 (t, 2H), 3.56 (q, 4H), 2.29 (s, 12 H), 2.26 (s, 6H), 1.87 (p, 2H) ppm. ^{13}C NMR (125.7 MHz, $CDCl_3$): d 171.43, 138.58, 134.88, 134.11, 128.41, 36.37. 30.48, 21.21, 19.37 ppm.

Synthesis of $LMn_4O_4(diam^{Mes})(OTf)$ (**3**)

Compound **2** (750 mg, 0.51 mmol, 1 equiv) was dissolved in a 3:1 mixture of THF-pyridine (5 mL) and stirred. A THF solution of $Mn(OTf)_2 \cdot (MeCN)_2$ (244 mg, 0.56 mmol, 1.1 equiv) and a pyridine solution of H_2diam^{Mes} (206 mg, 0.56 mmol, 1.1 equiv) were added sequentially to the reaction mixture. After 5 minutes, sodium *tert*-butoxide (109 mg, 1.13 mmol, 2.2 equiv) was dissolved in THF and added dropwise, and the reaction mixture was stirred for 16 hours. Volatiles were removed under reduced pressure and the residue was triturated with Et_2O. The residue was suspended in Et_2O, collected over a pad of Celite, and

washed thoroughly with more Et_2O. The solid was extracted with a generous amount of benzene and all volatiles were removed from the filtrate under reduced pressure to yield compound **3** as a brown powder (300 mg, 35.6%). Crystals suitable for X-ray crystallography were obtained from slow vapor diffusion of Et_2O into a concentrated solution of **3** in benzene. ^{1}H NMR (300 MHz, C_6D_6): δ 55.5, 48.2, 25.3, 20.9, 17.9, 16.1, 14.2, −9.9, −13.3, −15.1, −49.4, −65.2 ppm. ^{19}F NMR (300 MHz, C_6D_6): δ –41 ppm. Analysis calculated for $LMn_4O_4(diam^{Mes})(OTf)$ [$C_{81}H_{67}F_3Mn_4N_8O_{12}S$]: C 58.85, H 4.08, N 6.78; found: C 58.52, H 3.99, N 6.69.

Synthesis of $LMn_4O_4(diam^{Mes})(OSiPh_3)$ (**4**)

To a stirring benzene suspension of compound **3** (44 mg, 0.027 mmol, 1 equiv), a benzene solution of $KOSiPh_3$ (10 mg, 0.032 mmol, 1.18 equiv) was added slowly. The reaction mixture was stirred at room temperature for 5 hours and filtered over a pad of Celite. All volatiles were removed under reduced pressure. Vapor diffusion of Et_2O into a concentrated THF solution of **4** shows co-crystallization of **4** and $KOSiPh_3$. This precipitate was collected and washed with Et_2O and cold benzene. Compound **4** was extracted with CH_2Cl_2. From this filtrate, all volatiles were removed under reduced pressure, yielding compound **4** as a brown powder (20 mg, 42%). Crystals suitable for X-ray crystallography were obtained from slow vapor-diffusion of Et_2O into a concentrated THF solution of **4**. ^{1}H NMR (300 MHz, C_6D_6): δ 38.8, 22.5, 20.4, 18.7, 15.0, 14.0, −2.1, −5.0, −15.5, −23.5, −36.7 ppm. Analysis calculated for $LMn_4O_4(diam^{Mes})(OSiPh_3) \cdot Et_2O$ [$C_{102}H_{92}Mn_4N_8O_{11}Si$]: C 66.09, H 5.00, N 6.04; found C 66.67, H 4.86, N 6.08.

Synthesis of [$LMn_4O_4(diam^{Mes})(OSiPh_3)$][OTf] (**4-ox**)

To a stirring CH_2Cl_2 solution of **4** (87.2 mg, 0.049 mmol, 1 equiv), a CH_2Cl_2 solution of FcOTf (17.2 mg, 0.051 mmol, 1.04 equiv) was added dropwise. The reaction was stirred for 30 minutes, and all volatiles were removed under reduced pressure. The residue was suspended in pentane, collected over a pad of Celite, washed with Et_2O and THF. The solid residue was dissolved in CH_2Cl_2 and filtered through the pad of Celite. Volatiles were removed from this filtrate, yielding compound **4-ox** as a brown powder (82.8 mg, 88%). Crystals suitable for X-ray crystallography were obtained from a slow vapor-diffusion of Et_2O into a concentrated CH_2Cl_2/fluorobenzene solution of **4-ox**. ^{1}H NMR (300 MHz, CD_2Cl_2): δ 51.0, 15.8, 12.5, 10.7, −11.4, −11.9, −27.6 ppm. ^{19}F NMR (300 MHz, CD_2Cl_2): δ −78 ppm. Analysis calculated for [$LMn_4O_4(diam^{Mes})(OSiPh_3)$][OTf]·$CH_2Cl_2$ [$C_{100}H_{84}Cl_2F_3Mn_4N_8O_{13}SSi$]: C 59.65, H 4.20, N 5.56; found: C 60.37, H 4.14, N 5.51.

Synthesis of $LMn_4O_4(diam^{Mes})(OSi(O^tBu)_3)$ (**5**)

To a stirring benzene suspension of compound **3** (20.1 mg, 0.012 mmol, 1 equiv), a benzene solution of $KOSi(O^tBu)_3$ (4.2 mg, 0.014 mmol, 1.16 equiv) was added. The reaction mixture was stirred at room temperature for 16 hours and filtered over a pad of Celite. All volatiles were removed under reduced pressure. This precipitate was collected and washed with Et_2O and cold benzene. Compound **5** was extracted with CH_2Cl_2. From this filtrate, all volatiles were removed under reduced pressure, yielding compound **5** as a brown powder (12 mg, 42%). Crystals suitable for X-ray crystallography were obtained from slow vapor-diffusion of Et_2O into a concentrated CH_2Cl_2 solution of **5**. ^{1}H NMR (300 MHz, C_6D_6): δ 47.2 (br), 26.0 (br), 19.5, 17.9, 16.6, 15.4, 13.7, 12.3, −4.6, −9.5, −17.5 ppm.

Synthesis of [$LMn_4O_4(diam^{Mes})(OSi(O^tBu)_3)$][OTf] (**5-ox**)

To a stirring CH_2Cl_2 solution of **5** (30.3 mg, 0.017 mmol, 1 equiv), a CH_2Cl_2 solution of FcOTf (6.1 mg, 0.018 mmol, 1.05 equiv) was added dropwise. The reaction was stirred for 1 hour, and all volatiles were removed under reduced pressure. The residue was suspended in pentane, collected over a pad of Celite, washed with Et_2O and THF. The solid residue was dissolved in CH_2Cl_2 and filtered through the pad of Celite. Volatiles were removed from this filtrate, yielding compound **5-ox** as a brown powder (15 mg, 88%). Crystals suitable for X-ray crystallography were obtained from a slow vapor-diffusion of Et_2O into a concentrated CH_2Cl_2 solution of **5-ox**. ^{1}H NMR (300 MHz, CD_2Cl_2): δ 55.7, 40.3, −9.0, −12.5, −14.5, −17.8, −29.3 ppm. ^{19}F NMR (300 MHz, CD_2Cl_2): δ −78 ppm.

Synthesis of [$LMn_4O_4(diam^{Mes})(OH)(OH)_2$][^{Me}SiF] (**4-ox-$H_2O$**)

To a stirring CH_2Cl_2 solution of **4** (21 mg, 0.012 mmol, 1 equiv), a CH_2Cl_2 solution of $Fc^{Me}SiF$[3] (10.4 mg, 0.013 mmol, 1.05 equiv) was added dropwise. The reaction was stirred for 1 hour, and all volatiles were removed under reduced pressure. The residue was suspended in pentane, collected over a pad of Celite, and washed with more pentane. The solid residue was dissolved in Et_2O and filtered through the pad of Celite. Volatiles were removed from this filtrate, yielding [$LMn_4O_4(diam^{Mes})(OSiPh_3)$][^{Me}SiF] as a brown powder (20 mg, 54%). ^{1}H NMR (300 MHz, C_6D_6): δ 50.7, −12.1, −13.1, −28.5 ppm. ^{19}F NMR (300 MHz, C_6D_6): δ −68 ppm. This compound was used without further purification. A drop of degassed water was added to a concentrated THF solution of this compound. Crystals suitable for X-ray crystallography were obtained from a slow vapor-diffusion of pentane into this THF solution.

NMR Spectroscopy

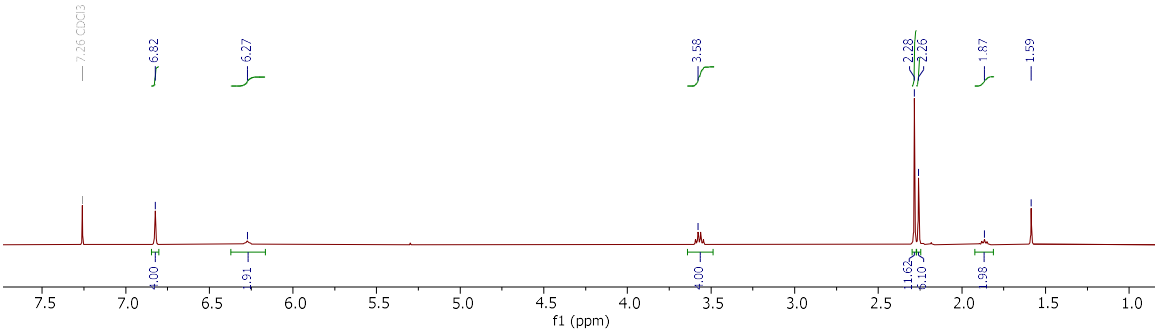

Figure 14. ^{1}H NMR of H_2diam^{Mes} in $CDCl_3$.

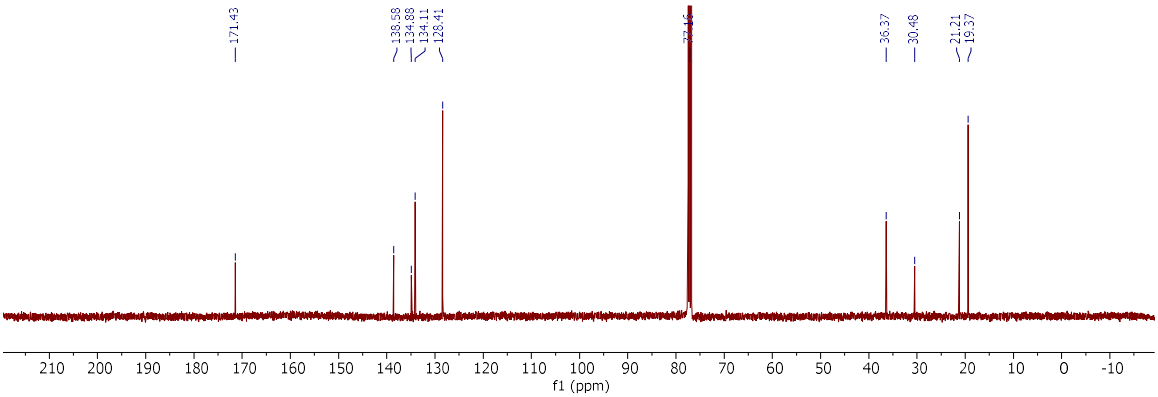

Figure 15. ^{13}C NMR of H_2diam^{Mes} in $CDCl_3$.

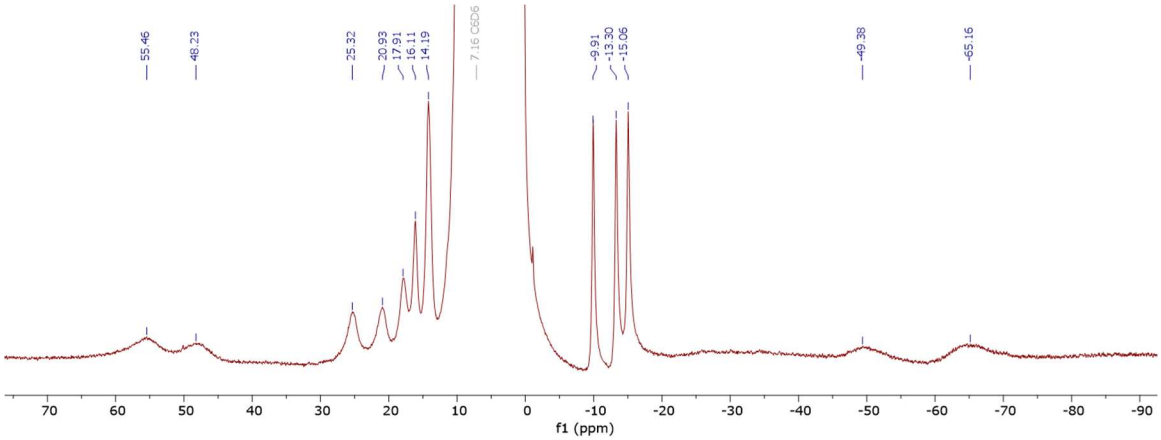

Figure 16. ^{1}H NMR of **3** in C_6D_6.

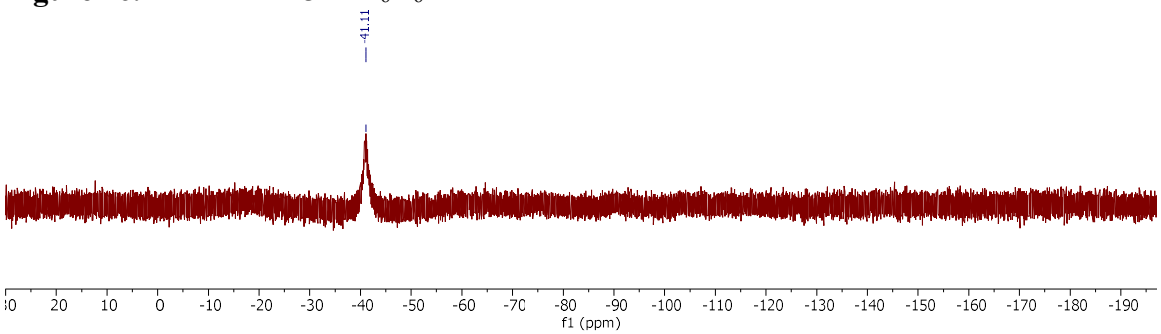

Figure 17. ^{19}F NMR of **3** in C_6D_6.

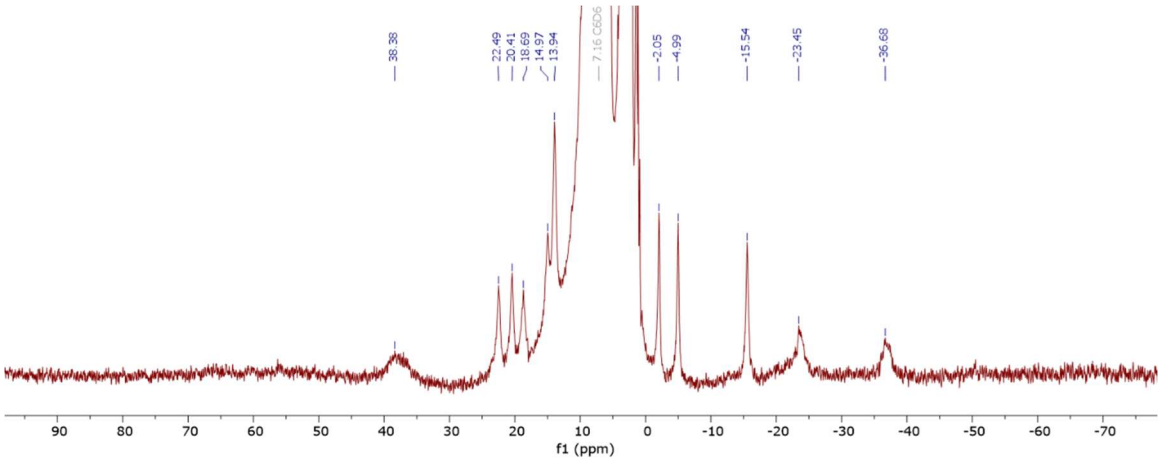

Figure 18. ^{1}H NMR of **4** in C_6D_6.

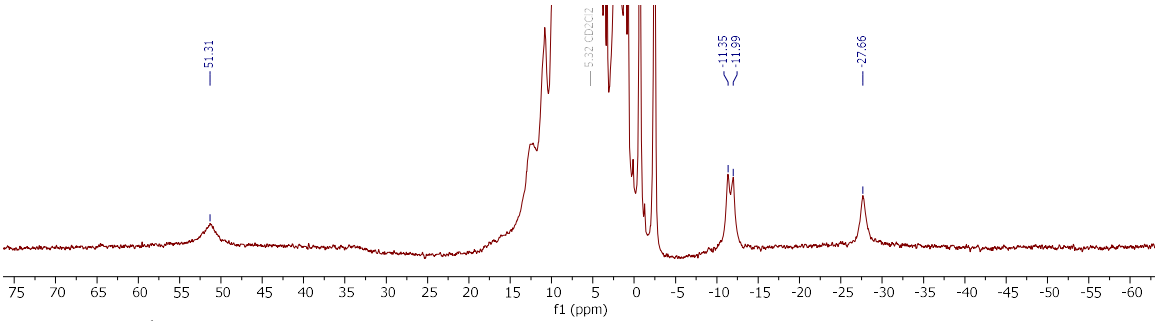

Figure 19. ^{1}H NMR of **4-ox** in CD_2Cl_2.

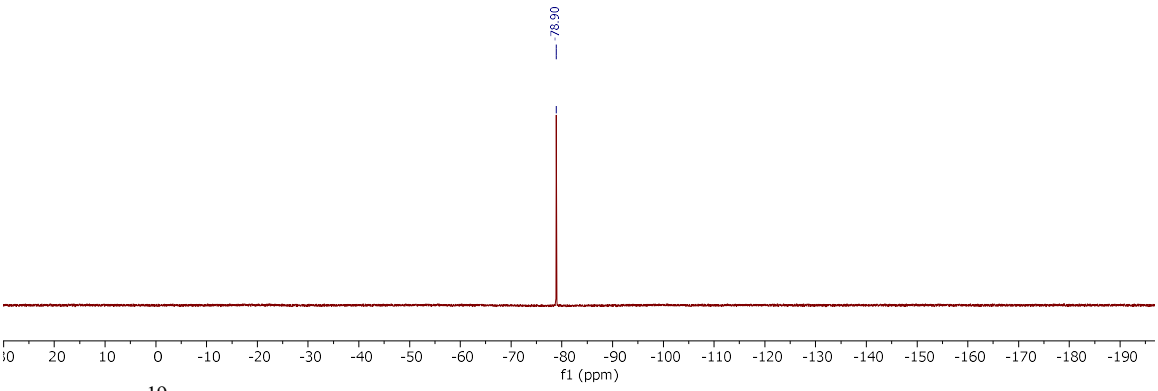

Figure 20. ^{19}F NMR of **4-ox** in CD_2Cl_2.

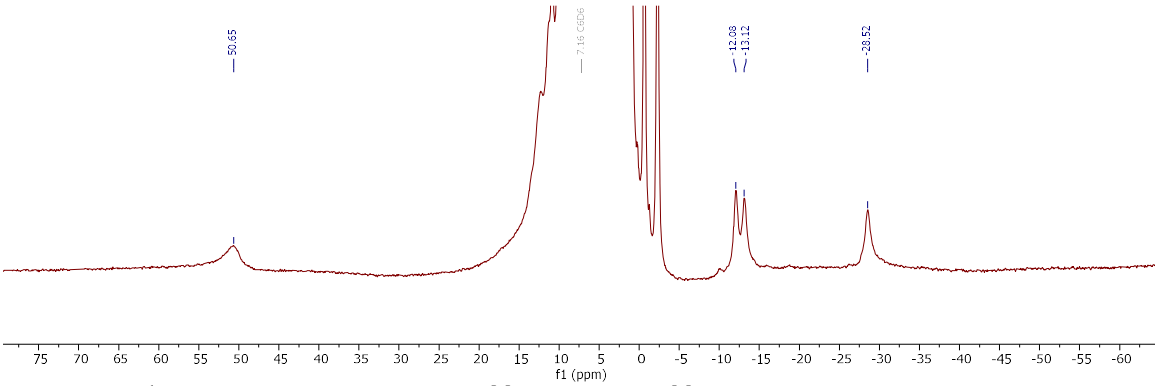

Figure 21. ^{1}H NMR of $[LMn_4O_4(diam^{Mes})(OSiPh_3)][^{Me}SiF]$ in C_6D_6.

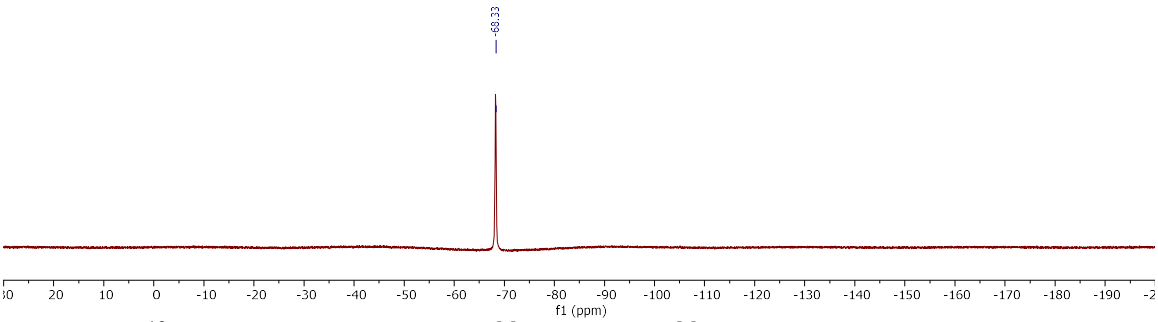

Figure 22. ^{19}F NMR of $[LMn_4O_4(diam^{Mes})(OSiPh_3)][^{Me}SiF]$ in C_6D_6.

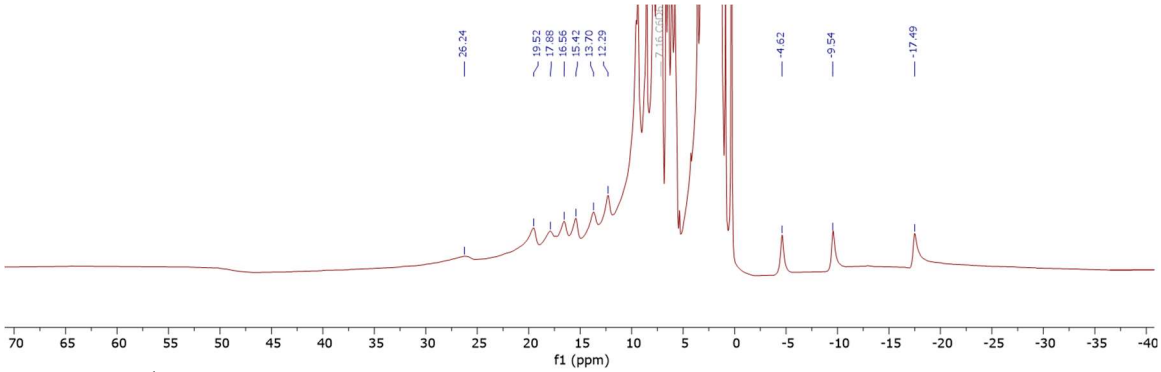

Figure 23. ^{1}H NMR of **5** in C_6D_6.

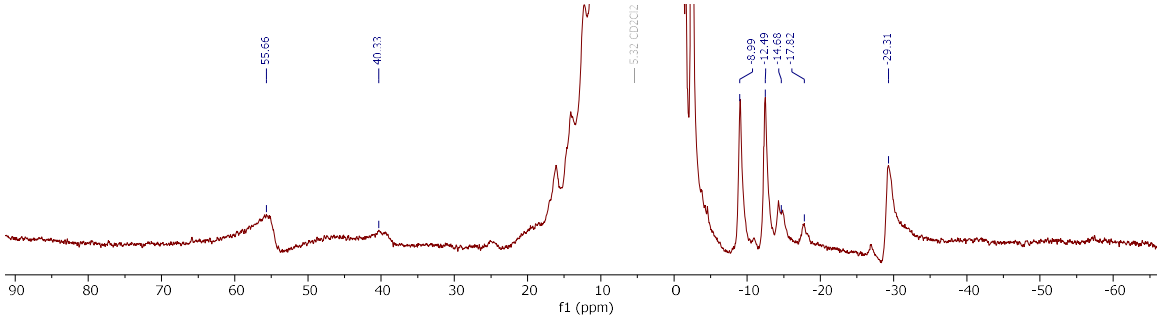

Figure 24. ^{1}H NMR of **5-ox** in CD_2Cl_2.

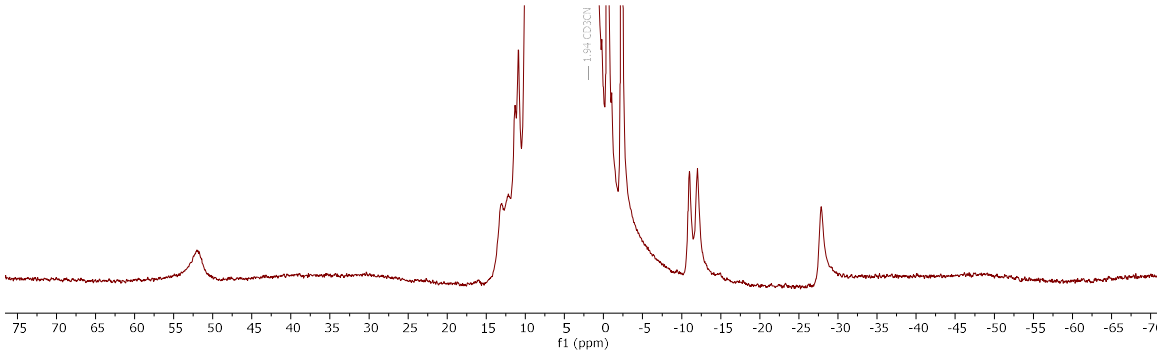

Figure 25. ^{1}H NMR of **4-ox** in CD_3CN.

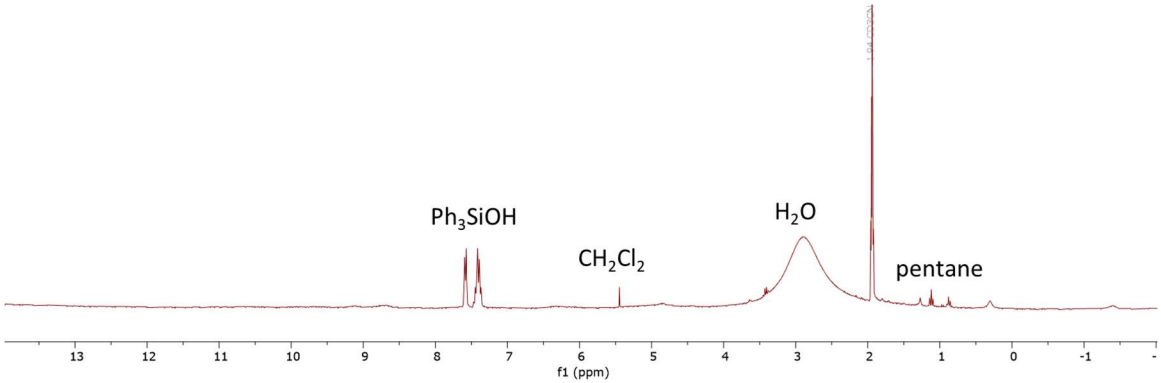

Figure 26. ^{1}H NMR of addition of ~80 equivalents of H_2O to **4-ox** in CD_3CN, using standard acquisition parameters for diamagnetic compounds. Spectrum acquired ~5 min after addition of H_2O. Presence of Ph_3SiOH suggests protonolysis of siloxide moiety.

Table 4. Crystal and refinement data for complexes **3** and **4**.

Compound	**3**	**4**
CCDC	2259279	2259280
Empirical formula	$C_{85}H_{77}F_3Mn_4N_8O_{13}S$	$C_{98}H_{82}Mn_4N_8O_{10}Si$
Formula weight	1727.36	1779.56
Temperature/K	100.00	99.99
Crystal system	monoclinic	monoclinic
Space group	$P2_1/n$	$P2_1/n$
a/Å	21.794(5)	16.085(2)
b/Å	15.9356(19)	25.868(3)
c/Å	23.734(4)	23.032(4)
α/°	90	90
β/°	109.230(8)	101.938(13)
γ/°	90	90
Volume/Å^3	7783(2)	9376(2)
Z	4	4
ρ_{calc}g/cm^3	1.474	1.261
μ/mm^{-1}	6.059	4.892
F(000)	3560.0	3680.0
Crystal size/mm^3	0.12 × 0.06 × 0.03	0.02 × 0.19 × 0.29
Radiation	CuKα (λ = 1.54178)	CuKα (λ = 1.54178)
2Θ range for data collection/°	6.806 to 145.686	5.2 to 159.494
Index ranges	-26 ≤ h ≤ 26, -19 ≤ k ≤ 19, -25 ≤ l ≤ 29	-19 ≤ h ≤ 19, -31 ≤ k ≤ 32, -28 ≤ l ≤ 28
Reflections collected	105798	81727
Independent reflections	15169 [R_{int} = 0.0613, R_{sigma} = 0.0411]	18915 [R_{int} = 0.0764, R_{sigma} = 0.0623]
Data/restraints/parameters	15169/0/1035	18915/0/1096
Goodness-of-fit on F^2	1.025	1.057
Final R indexes [I>=2σ (I)]	R_1 = 0.0507, wR_2 = 0.1225	R_1 = 0.0516, wR_2 = 0.1131
Final R indexes [all data]	R_1 = 0.0650, wR_2 = 0.1303	R_1 = 0.0742, wR_2 = 0.1230
Largest diff. peak/hole / e Å^{-3}	1.62/-0.68	0.66/-0.59

Table 5. Crystal and refinement data for complexes **4-ox** and **4-ox-H_2O**.

Compound	**4-ox**	**4-ox-H_2O**
CCDC	2259281	2259282
Empirical formula	$C_{99}H_{83}F_3Mn_4N_8O_{13}SSi$	$C_{112.92}H_{112.56}F_{24}Mn_4N_8O_{17.57}Si$
Formula weight	1929.64	2566.81
Temperature/K	100.00	100.15
Crystal system	monoclinic	triclinic
Space group	$P2_1/n$	P-1
a/Å	15.274(7)	15.9477(10)
b/Å	29.224(12)	19.5508(12)
c/Å	24.016(6)	21.5860(12)
α/°	90	89.277(3)
β/°	92.815(14)	73.810(4)
γ/°	90	66.035(4)
Volume/$Å^3$	10707(7)	5867.2(6)
Z	4	2
$\rho_{calc}g/cm^3$	1.197	1.453
μ/mm^{-1}	0.555	4.441
F(000)	3976.0	2633.0
Crystal size/mm^3	0.4 × 0.4 × 0.15	0.3 × 0.15 × 0.05
Radiation	MoKα (λ = 0.71073)	CuKα (λ = 1.54178)
2Θ range for data collection/°	3.67 to 59.818	4.29 to 133.188
Index ranges	$-16 \le h \le 21$, $-34 \le k \le 40$, $-33 \le l \le 33$	$-18 \le h \le 18$, $-23 \le k \le 23$, $-25 \le l \le 25$
Reflections collected	116207	198003
Independent reflections	30750 [R_{int} = 0.0532, R_{sigma} = 0.0652]	20259 [R_{int} = 0.1576, R_{sigma} = 0.0792]
Data/restraints/parameters	30750/78/1172	20259/4277/1836
Goodness-of-fit on F^2	1.055	1.066
Final R indexes [I>=2σ (I)]	R_1 = 0.1009, wR_2 = 0.2497	R_1 = 0.2224, wR_2 = 0.4719
Final R indexes [all data]	R_1 = 0.1290, wR_2 = 0.2674	R_1 = 0.2546, wR_2 = 0.4873
Largest diff. peak/hole / e $Å^{-3}$	1.75/-1.84	0.50/-0.38

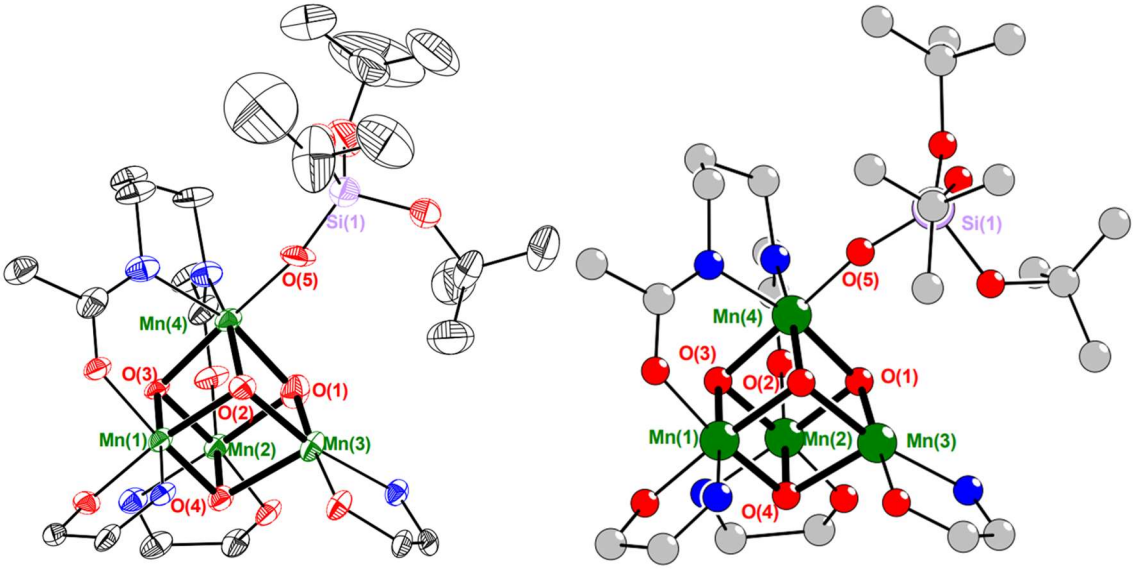

Figure 27. Truncated X-ray crystal structures of **5** (left) and **5-ox** (right). Mn(green), O (red), N (blue), C (black/gray), F (light green), Si (light purple), S (yellow). Bolded bond highlight Mn-oxo bonds. Thermal ellipsoids are plotted at 50% probability. **5-ox** represented as isotropic ball-and-stick model due to low-quality dataset.

SQUID magnetometry

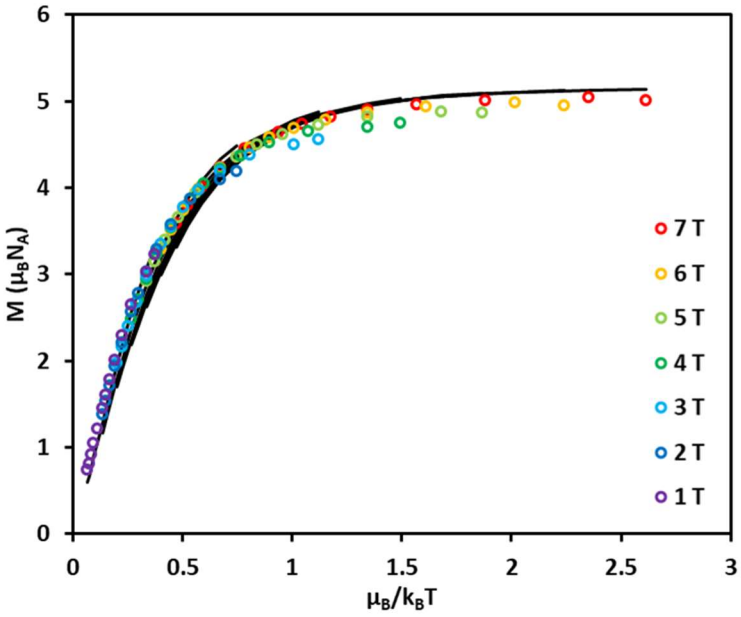

Figure 28. Reduced magnetization plot of complex **4-ox**. Black line represents simulation of data using parameters in text.

EPR Spectroscopy

Samples were prepared as solutions (c.a. 2 mM) in 1:1 CH_2Cl_2:2-MeTHF and rapidly cooled in liquid nitrogen to form a frozen glass. For ligand binding studies, a stock solution of complex **4-ox** in 1:1 CH_2Cl_2:2-MeTHF (2 mM) was prepared, and the desired equivalents of water (0.4 M in THF) were delivered via syringe. Samples were mixed by pipet, transferred to X-band or Q-band tubes, respectively, and frozen in LN_2 within 5-10 minutes of reagent addition. All X-band and Q-band EPR experiments presented in this study were acquired at the Caltech EPR facility. X-band CW EPR spectra were acquired on a Bruker (Billerica, MA) EMX spectrometer using Bruker Xenon software (ver. 1.2). Temperature control was achieved using liquid helium and an Oxford Instruments (Oxford, UK) ESR-900 cryogen flow cryostat and an ITC-503 temperature controller. Pulse EPR and electron nuclear double resonance (ENDOR) experiments were acquired using a Bruker ELEXSYS E580 pulse EPR spectrometer using a Bruker D2 pulse ENDOR resonator for Q-band experiments. Temperature control was achieved using an Oxford Instruments CF-935 helium flow cryostat and a Mercury ITC temperature controller. Spectra were simulated using EasySpin5 (release 5.2.35)[56] with Matlab R2020b. Acquisition parameters for Q-band Davies ENDOR: pulse sequence π-t_{RF}-π_{RF}-t_{RF}-$\pi/2$-τ–π–τ-echo; where π = 40 ns, $\pi/2$ = 20 ns, t_{RF} = RF pulse delay = 2 μs, π_{RF} = RF pulse length = 3 μs; and τ = 140 ns; MW frequency = 34.120 GHz, Temperature = 3.8 K, shot repetition time (srt) = 15 ms. The frequency of the RF pulse was randomly sampled to minimize nuclear spin saturation. Acquisition parameters for Q-band ^{2}H Mims ENDOR: pulse sequence $\pi/2$-τ-$\pi/2$-t_{RF}-π_{RF}-t_{RF}-$\pi/2$-τ-echo; where $\pi/2$ = 20 ns, t_{RF} = RF pulse delay = 2 μs, π_{RF} = RF pulse length = 40 μs; and τ = 140 ns; MW

frequency = 34.120 GHz, Temperature = 3.5 K, shot repetition time (srt) = 50 ms. The frequency of the RF pulse was randomly sampled to minimize nuclear spin saturation.

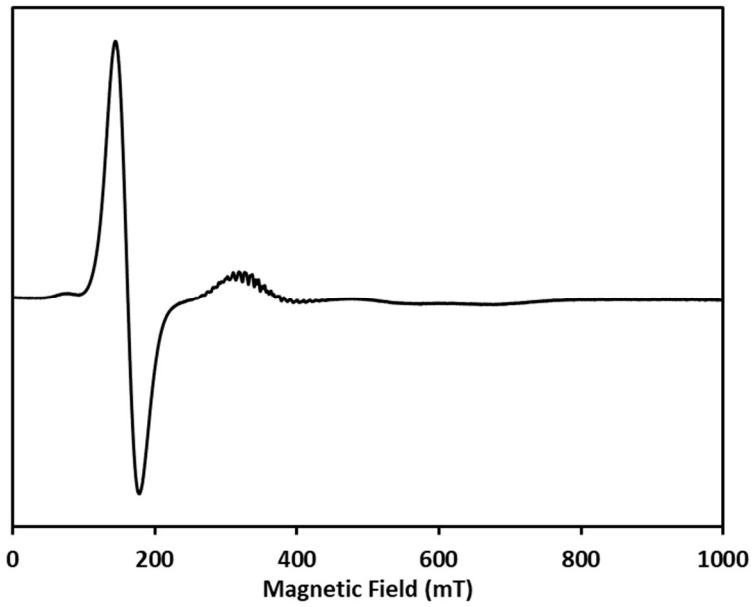

Figure 29. X-band EPR spectrum **4-ox** with addition of excess THF, collected at T = 5 K. Acquisition parameters: frequency = 9.64 MHz, power = 8.7 mW, conversion time = 10 ms, and modulation amplitude = 8 G.

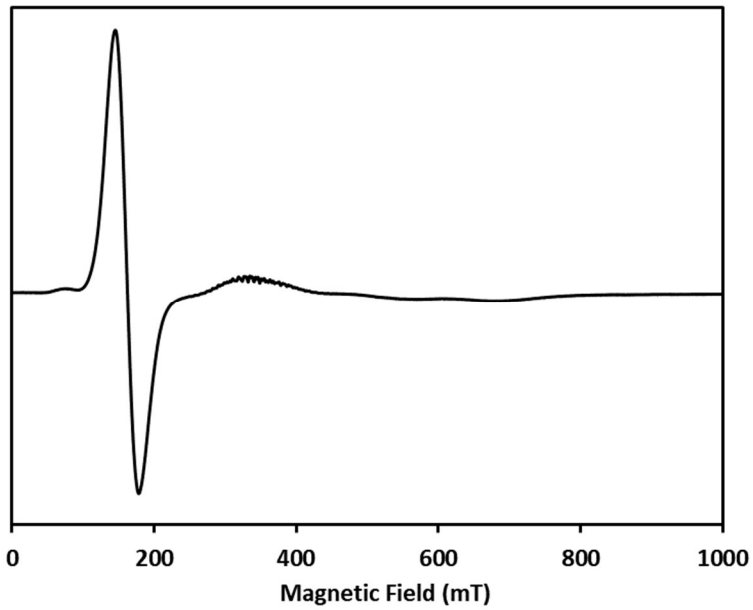

Figure 30. X-band CW-EPR of $[LMn_4O_4(diam^{Mes})(OSiPh_3)][^{Me}SiF]$, collected at T = 5 K. Acquisition parameters: frequency: 9.64 MHz, power = 8.8 mW, conversion time = 10 ms, and modulation amplitude = 8 G.

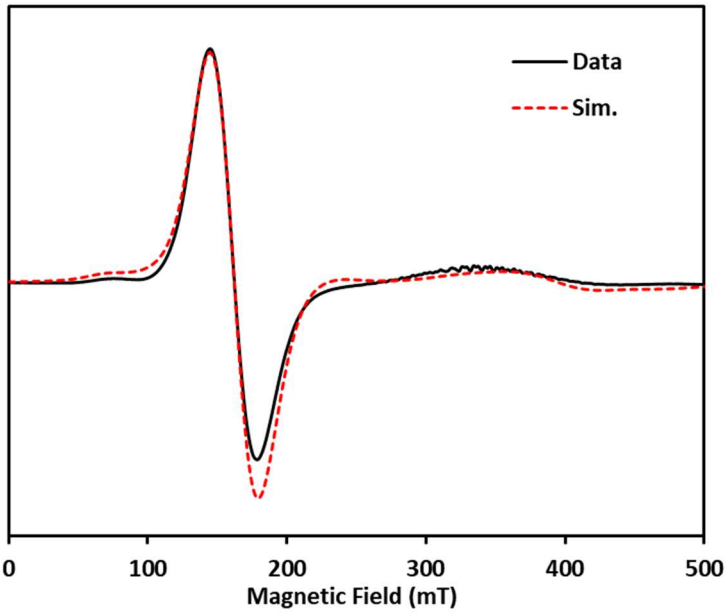

Figure 31. Closeup of X-band CW-EPR data (black trace) and simulation (dashed red trace) for **4-ox**, collected at T = 5 K. Acquisition parameters: frequency = 9.64 MHz, power = 8.7 mW, conversion time = 10 ms, and modulation amplitude = 8 G. See main text for simulation parameters.

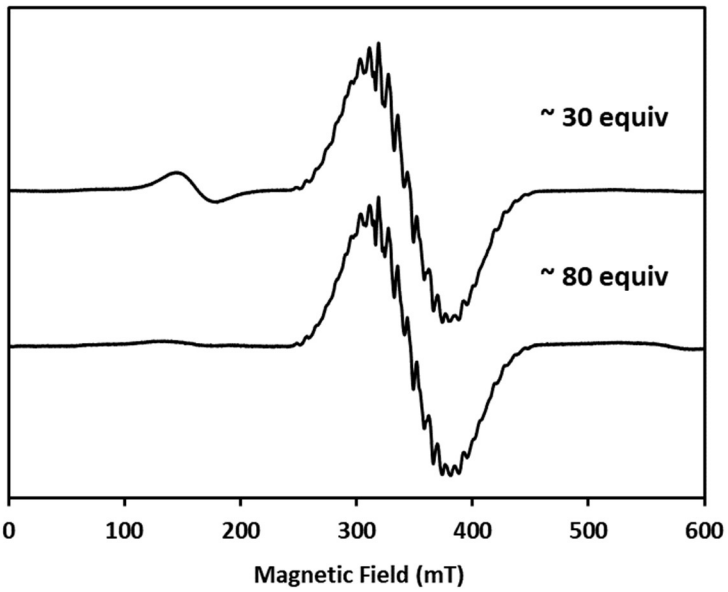

Figure 32. X-band CW EPR spectrum of addition of ~30 and ~80 equivalents of water. Full conversion observed at ~ 80 equivalents. Acquisition parameters: frequency = 9.64 MHz, power = 8.8 mW, conversion time = 10 ms, and modulation amplitude = 8 G.

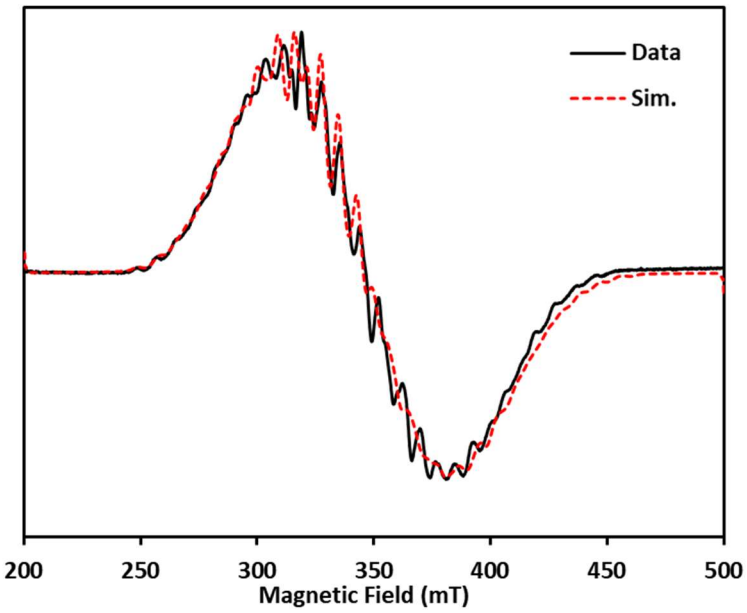

Figure 33. Closeup of X-band CW-EPR data (black trace) and simulation (dashed red trace) for the addition of ~80 equiv H_2O to **4-ox**, collected at T = 5 K. Acquisition parameters: frequency = 9.64 MHz, power = 8.8 mW, conversion time = 10 ms, and modulation amplitude = 8 G. See main text for simulation parameters.

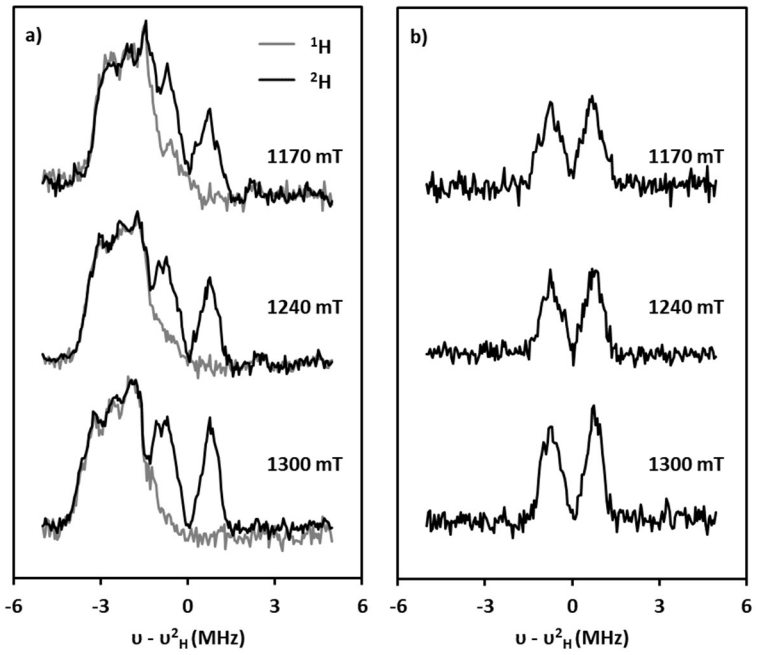

Figure 34. Q-band Mims ENDOR spectra of **4-ox-H_2O** at various fields, **(a)** data for natural abundance sample (gray), data for deuterium enriched sample (black), **(b)** ^{2}H – ^{1}H difference spectrum. Peaks not centered about ^{2}H Larmor frequency which are present in spectra of both ^{2}H and ^{1}H samples correspond to ^{14}N signals from the ancillary ligands.

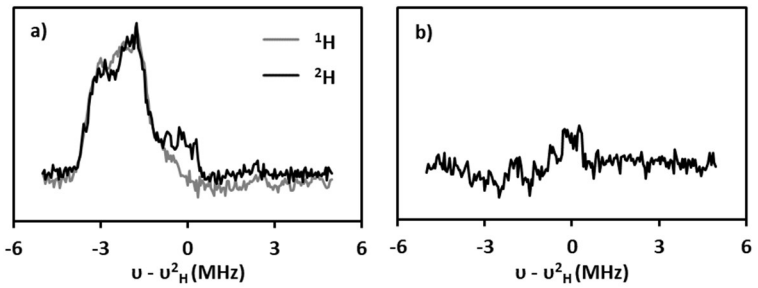

Figure 35. Q-band Mims ENDOR spectra collected at 1240 mT of **4-ox**, dissolved in 1:1 CD_2Cl_2:2-MeTHF, **(a)** data for natural abundance sample (gray), data for deuterated solvent sample (black), **(b)** ^2H – ^1H difference spectrum. Control experiment confirms ^2H signals seen for water addition experiment are not from matrix deuterium.

4.7) References

(1) Shen, J.-R., The Structure of Photosystem II and the Mechanism of Water Oxidation in Photosynthesis. *Annu. Rev. Plant Biol.* **2015**, *66* (1), 23-48.

(2) Yano, J.; Yachandra, V., Mn4Ca Cluster in Photosynthesis: Where and How Water is Oxidized to Dioxygen. *Chem. Rev.* **2014**, *114* (8), 4175-4205.

(3) Cox, N.; Pantazis, D. A.; Neese, F.; Lubitz, W., Biological Water Oxidation. *Acc. Chem. Res.* **2013**, *46* (7), 1588-1596.

(4) Cox, N.; Pantazis, D. A.; Lubitz, W., Current Understanding of the Mechanism of Water Oxidation in Photosystem II and Its Relation to XFEL Data. *Annu. Rev. Biochem.* **2020**, *89* (1), 795-820.

(5) Siegbahn, P. E. M., Structures and Energetics for O2 Formation in Photosystem II. *Acc. Chem. Res.* **2009**, *42* (12), 1871-1880.

(6) Britt, R. D.; Marchiori, D. A., Photosystem II, poised for O_2 formation. *Science* **2019**, *366* (6463), 305.

(7) Paul, S.; Cox, N.; Pantazis, D. A., What Can We Learn from a Biomimetic Model of Nature's Oxygen-Evolving Complex? *Inorg. Chem.* **2017**, *56* (7), 3875-3888.

(8) Young, K. J.; Brennan, B. J.; Tagore, R.; Brudvig, G. W., Photosynthetic Water Oxidation: Insights from Manganese Model Chemistry. *Acc. Chem. Res.* **2015**, *48* (3), 567-574.

(9) Blakemore, J. D.; Crabtree, R. H.; Brudvig, G. W., Molecular Catalysts for Water Oxidation. *Chem. Rev.* **2015**, *115* (23), 12974-13005.

(10) Tsui, E. Y.; Kanady, J. S.; Agapie, T., Synthetic Cluster Models of Biological and Heterogeneous Manganese Catalysts for O_2 Evolution. *Inorg. Chem.* **2013**, *52* (24), 13833-13848.

(11) Mukherjee, S.; Stull, J. A.; Yano, J.; Stamatatos, T. C.; Pringouri, K.; Stich, T. A.; Abboud, K. A.; Britt, R. D.; Yachandra, V. K.; Christou, G., Synthetic model of the asymmetric $[Mn_3CaO_4]$ cubane core of the oxygen-evolving complex of photosystem II. *Proceedings of the National Academy of Sciences* **2012**, *109* (7), 2257-2262.

(12) Kanady, J. S.; Tsui, E. Y.; Day, M. W.; Agapie, T., A Synthetic Model of the Mn_3Ca Subsite of the Oxygen-Evolving Complex in Photosystem II. *Science* **2011**, *333* (6043), 733.

(13) Kanady, J. S.; Mendoza-Cortes, J. L.; Tsui, E. Y.; Nielsen, R. J.; Goddard, W. A.; Agapie, T., Oxygen Atom Transfer and Oxidative Water Incorporation in Cuboidal Mn_3MO_n Complexes Based on Synthetic, Isotopic Labeling, and Computational Studies. *J. Am. Chem. Soc.* **2013**, *135* (3), 1073-1082.

(14) Kanady, J. S.; Lin, P.-H.; Carsch, K. M.; Nielsen, R. J.; Takase, M. K.; Goddard, W. A.; Agapie, T., Toward Models for the Full Oxygen-Evolving Complex of Photosystem II by Ligand Coordination To Lower the Symmetry of the Mn_3CaO_4 Cubane: Demonstration That Electronic Effects Facilitate Binding of a Fifth Metal. *J. Am. Chem. Soc.* **2014**, *136* (41), 14373-14376.

(15) Lee, H. B.; Shiau, A. A.; Oyala, P. H.; Marchiori, D. A.; Gul, S.; Chatterjee, R.; Yano, J.; Britt, R. D.; Agapie, T., Tetranuclear $[Mn^{III}Mn_3^{IV}O_4]$ Complexes as Spectroscopic Models of the S_2 State of the Oxygen Evolving Complex in Photosystem II. *J. Am. Chem. Soc.* **2018**, *140* (49), 17175-17187.

(16) Lee, H. B.; Marchiori, D. A.; Chatterjee, R.; Oyala, P. H.; Yano, J.; Britt, R. D.; Agapie, T., S = 3 Ground State for a Tetranuclear $Mn^{IV}_4O_4$ Complex Mimicking the S_3 State of the Oxygen-Evolving Complex. *J. Am. Chem. Soc.* **2020**, *142* (8), 3753-3761.

(17) Lee, H. B.; Shiau, A. A.; Marchiori, D. A.; Oyala, P. H.; Yoo, B.-K.; Kaiser, J. T.; Rees, D. C.; Britt, R. D.; Agapie, T., $CaMn_3^{IV}O_4$ Cubane Models of the Oxygen-Evolving Complex: Spin Ground States S<9/2 and the Effect of Oxo Protonation. *Angew. Chem. Int. Ed.* **2021**, *60* (32), 17671-17679.

(18) Ruettinger, W. F.; Campana, C.; Dismukes, G. C., Synthesis and Characterization of $Mn_4O_4L_6$ Complexes with Cubane-like Core Structure: A New Class of Models of the Active Site of the Photosynthetic Water Oxidase. *J. Am. Chem. Soc.* **1997**, *119* (28), 6670-6671.

(19) Ruettinger, W. F.; Ho, D. M.; Dismukes, G. C., Protonation and Dehydration Reactions of the $Mn_4O_4L_6$ Cubane and Synthesis and Crystal Structure of the Oxidized Cubane $[Mn_4O_4L_6]^+$: A Model for the Photosynthetic Water Oxidizing Complex. *Inorg. Chem.* **1999**, *38* (6), 1036-1037.

(20) Zhang, M.; Frei, H., Towards a Molecular Level Understanding of the Multi-Electron Catalysis of Water Oxidation on Metal Oxide Surfaces. *Catal. Lett.* **2015**, *145* (1), 420-435.

(21) Yao, R.; Li, Y.; Chen, Y.; Xu, B.; Chen, C.; Zhang, C., Rare-Earth Elements Can Structurally and Energetically Replace the Calcium in a Synthetic Mn_4CaO_4-Cluster Mimicking the Oxygen-Evolving Center in Photosynthesis. *J. Am. Chem. Soc.* **2021**, *143* (42), 17360-17365.

(22) Vaddypally, S.; Kondaveeti, S. K.; Karki, S.; Van Vliet, M. M.; Levis, R. J.; Zdilla, M. J., Reactive Pendant Mn═O in a Synthetic Structural Model of a Proposed S_4 State in the Photosynthetic Oxygen Evolving Complex. *J. Am. Chem. Soc.* **2017**, *139* (13), 4675-4681.

(23) Nguyen, A. I.; Darago, L. E.; Balcells, D.; Tilley, T. D., Influence of a "Dangling" Co(II) Ion Bound to a $[MnCo_3O_4]$ Oxo Cubane. *J. Am. Chem. Soc.* **2018**, *140* (29), 9030-9033.

(24) Pantazis, D. A.; Ames, W.; Cox, N.; Lubitz, W.; Neese, F., Two Interconvertible Structures that Explain the Spectroscopic Properties of the Oxygen-Evolving Complex of Photosystem II in the S_2 State. *Angew. Chem. Int. Ed.* **2012**, *51* (39), 9935-9940.

(25) Bovi, D.; Narzi, D.; Guidoni, L., The S_2 State of the Oxygen-Evolving Complex of Photosystem II Explored by QM/MM Dynamics: Spin Surfaces and Metastable States Suggest a Reaction Path Towards the S_3 State. *Angew. Chem. Int. Ed.* **2013**, *52* (45), 11744-11749.

(26) Vinyard, D. J.; Khan, S.; Askerka, M.; Batista, V. S.; Brudvig, G. W., Energetics of the S_2 State Spin Isomers of the Oxygen-Evolving Complex of Photosystem II. *J. Phys. Chem. B* **2017**, *121* (5), 1020-1025.

(27) Cox, N.; Retegan, M.; Neese, F.; Pantazis, D. A.; Boussac, A.; Lubitz, W., Electronic structure of the oxygen-evolving complex in photosystem II prior to O-O bond formation. *Science* **2014**, *345* (6198), 804.

(28) Kern, J.; Chatterjee, R.; Young, I. D.; Fuller, F. D.; Lassalle, L.; Ibrahim, M.; Gul, S.; Fransson, T.; Brewster, A. S.; Alonso-Mori, R.; Hussein, R.; Zhang, M.;

Douthit, L.; de Lichtenberg, C.; Cheah, M. H.; Shevela, D.; Wersig, J.; Seuffert, I.; Sokaras, D.; Pastor, E.; Weninger, C.; Kroll, T.; Sierra, R. G.; Aller, P.; Butryn, A.; Orville, A. M.; Liang, M.; Batyuk, A.; Koglin, J. E.; Carbajo, S.; Boutet, S.; Moriarty, N. W.; Holton, J. M.; Dobbek, H.; Adams, P. D.; Bergmann, U.; Sauter, N. K.; Zouni, A.; Messinger, J.; Yano, J.; Yachandra, V. K., Structures of the intermediates of Kok's photosynthetic water oxidation clock. *Nature* **2018**, *563* (7731), 421-425.

(29) Boussac, A.; Ugur, I.; Marion, A.; Sugiura, M.; Kaila, V. R. I.; Rutherford, A. W., The low spin - high spin equilibrium in the S_2-state of the water oxidizing enzyme. *Biochim. Biophys. Acta, Bioenerg.* **2018**, *1859* (5), 342-356.

(30) Ames, W.; Pantazis, D. A.; Krewald, V.; Cox, N.; Messinger, J.; Lubitz, W.; Neese, F., Theoretical Evaluation of Structural Models of the S_2 State in the Oxygen Evolving Complex of Photosystem II: Protonation States and Magnetic Interactions. *J. Am. Chem. Soc.* **2011**, *133* (49), 19743-19757.

(31) Liang, W.; Latimer, M. J.; Dau, H.; Roelofs, T. A.; Yachandra, V. K.; Sauer, K.; Klein, M. P., Correlation between Structure and Magnetic Spin State of the Manganese Cluster in the Oxygen-Evolving Complex of Photosystem II in the S_2 State: Determination by X-ray Absorption Spectroscopy. *Biochemistry* **1994**, *33* (16), 4923-4932.

(32) Chatterjee, R.; Han, G.; Kern, J.; Gul, S.; Fuller, F. D.; Garachtchenko, A.; Young, I. D.; Weng, T.-C.; Nordlund, D.; Alonso-Mori, R.; Bergmann, U.; Sokaras, D.; Hatakeyama, M.; Yachandra, V. K.; Yano, J., Structural changes correlated with magnetic spin state isomorphism in the S_2 state of the Mn_4CaO_5 cluster in the oxygen-evolving complex of photosystem II. *Chem. Sci.* **2016**, *7* (8), 5236-5248.

(33) Boussac, A.; Rutherford, A. W.; Sugiura, M., Electron transfer pathways from the S_2-states to the S_3-states either after a Ca^{2+}/Sr^{2+} or a Cl^-/I^- exchange in Photosystem II from Thermosynechococcus elongatus. *Biochim. Biophys. Acta, Bioenerg.* **2015**, *1847* (6), 576-586.

(34) Blondin, G.; Davydov, R.; Philouze, C.; Charlot, M.-F.; Styring, t.; Åkermark, B.; Girerd, J.-J.; Boussac, A., Electron paramagnetic resonance study of the S =1/2 ground state of a radiolysis-generated manganese(III)–trimanganese(IV) form of $[Mn^{IV}_4O_6(bipy)_6]^{4+}$ (bipy = 2,2′ -bipyridine). Comparison with the photosynthetic Oxygen Evolving Complex. *J. Chem. Soc., Dalton Trans.* **1997**, (21), 4069-4074.

(35) Dubé, C. E.; Sessoli, R.; Hendrich, M. P.; Gatteschi, D.; Armstrong, W. H., A Spin Topological Model for the g = 4.1 S_2 State Photosystem II Water Oxidase Manganese Aggregate. *J. Am. Chem. Soc.* **1999**, *121* (14), 3537-3538.

(36) Wu, J.-Z.; De Angelis, F.; Carrell, T. G.; Yap, G. P. A.; Sheats, J.; Car, R.; Dismukes, G. C., Tuning the Photoinduced O_2-Evolving Reactivity of $Mn_4O_4^{7+}$, $Mn_4O_4^{6+}$, and $Mn_4O_3(OH)^{6+}$ Manganese−Oxo Cubane Complexes. *Inorg. Chem.* **2006**, *45* (1), 189-195.

(37) Zhang, C.; Chen, C.; Dong, H.; Shen, J.-R.; Dau, H.; Zhao, J., A synthetic Mn_4Ca-cluster mimicking the oxygen-evolving center of photosynthesis. *Science* **2015**, *348* (6235), 690-693.

(38) Chen, C.; Chen, Y.; Yao, R.; Li, Y.; Zhang, C., Artificial Mn_4Ca Clusters with Exchangeable Solvent Molecules Mimicking the Oxygen-Evolving Center in Photosynthesis. *Angew. Chem. Int. Ed.* **2019**, *58* (12), 3939-3942.

(39) Shoji, M.; Isobe, H.; Shen, J.-R.; Yamaguchi, K., Geometric and electronic structures of the synthetic Mn_4CaO_4 model compound mimicking the photosynthetic oxygen-evolving complex. *PCCP* **2016**, *18* (16), 11330-11340.

(40) Lee, H. B.; Agapie, T., Redox Tuning via Ligand-Induced Geometric Distortions at a YMn_3O_4 Cubane Model of the Biological Oxygen Evolving Complex. *Inorg. Chem.* **2019**, *58* (22), 14998-15003.

(41) Shiau, A. A.; Lee, H. B.; Oyala, P. H.; Agapie, T., $Mn^{IV}_4O_4$ Model of the S_3 Intermediate of the Oxygen-Evolving Complex: Effect of the Dianionic Disiloxide Ligand. *Inorg. Chem.*, **2023**, *53*, 6832−6835.

(42) Zhou, J.; Hu, Z.; Münck, E.; Holm, R. H., The Cuboidal Fe_3S_4 Cluster: Synthesis, Stability, and Geometric and Electronic Structures in a Non-Protein Environment. *J. Am. Chem. Soc.* **1996**, *118* (8), 1966-1980.

(43) Zhou, J.; Holm, R. H., Synthesis and Metal Ion Incorporation Reactions of the Cuboidal Fe_3S_4 Cluster. *J. Am. Chem. Soc.* **1995**, *117* (45), 11353-11354.

(44) Brown, A. C.; Suess, D. L. M., An Open-Cuboidal $[Fe_3S_4]$ Cluster Characterized in Both Biologically Relevant Redox States. *J. Am. Chem. Soc.* **2023**, *145* (4), 2075-2080.

(45) Zhou, J.; Raebiger, J. W.; Crawford, C. A.; Holm, R. H., Metal Ion Incorporation Reactions of the Cluster $[Fe_3S_4(LS_3)]^{3-}$, Containing the Cuboidal $[Fe_3S_4]^0$ Core. *J. Am. Chem. Soc.* **1997**, *119* (27), 6242-6250.

(46) Sun, J.; Tessier, C.; Holm, R. H., Sulfur Ligand Substitution at the Nickel(II) Sites of Cubane-Type and Cubanoid $NiFe_3S_4$ Clusters Relevant to the C-Clusters of Carbon Monoxide Dehydrogenase. *Inorg. Chem.* **2007**, *46* (7), 2691-2699.

(47) Panda, R.; Berlinguette, C. P.; Zhang, Y.; Holm, R. H., Synthesis of MFe3S4 Clusters Containing a Planar M^{II} Site (M = Ni, Pd, Pt), a Structural Element in the C-Cluster of Carbon Monoxide Dehydrogenase. *J. Am. Chem. Soc.* **2005**, *127* (31), 11092-11101.

(48) Camp, C.; Pécaut, J.; Mazzanti, M., Tuning Uranium–Nitrogen Multiple Bond Formation with Ancillary Siloxide Ligands. *J. Am. Chem. Soc.* **2013**, *135* (32), 12101-12111.

(49) Chilton, N. F.; Anderson, R. P.; Turner, L. D.; Soncini, A.; Murray, K. S., PHI: A powerful new program for the analysis of anisotropic monomeric and exchange-coupled polynuclear d- and f-block complexes. *J. Comput. Chem.* **2013**, *34* (13), 1164-1175.

(50) Cox, N.; Rapatskiy, L.; Su, J.-H.; Pantazis, D. A.; Sugiura, M.; Kulik, L.; Dorlet, P.; Rutherford, A. W.; Neese, F.; Boussac, A.; Lubitz, W.; Messinger, J., Effect of Ca^{2+}/Sr^{2+} Substitution on the Electronic Structure of the Oxygen-Evolving Complex of Photosystem II: A Combined Multifrequency EPR, ^{55}Mn-ENDOR, and DFT Study of the S_2 State. *J. Am. Chem. Soc.* **2011**, *133* (10), 3635-3648.

(51) Zheng, M.; Khangulov, S. V.; Dismukes, G. C.; Barynin, V. V., Electronic structure of dimanganese(II,III) and dimanganese(III,IV) complexes and dimanganese catalase enzyme: a general EPR spectral simulation approach. *Inorg. Chem.* **1994**, *33* (2), 382-387.

(52) Duboc, C.; Collomb, M.-N., Multifrequency high-field EPR investigation of a mononuclear manganese(IV) complex. *Chem. Commun.* **2009**, (19), 2715-2717.

(53) Krzystek, J.; Ozarowski, A.; Telser, J., Multi-frequency, high-field EPR as a powerful tool to accurately determine zero-field splitting in high-spin transition metal coordination complexes. *Coord. Chem. Rev.* **2006**, *250* (17), 2308-2324.

(54) Stamatatos, T. C.; Foguet-Albiol, D.; Lee, S.-C.; Stoumpos, C. C.; Raptopoulou, C. P.; Terzis, A.; Wernsdorfer, W.; Hill, S. O.; Perlepes, S. P.; Christou, G., "Switching On" the Properties of Single-Molecule Magnetism in Triangular Manganese(III) Complexes. *J. Am. Chem. Soc.* **2007**, *129* (30), 9484-9499.

(55) Aubin, S. M. J.; Dilley, N. R.; Pardi, L.; Krzystek, J.; Wemple, M. W.; Brunel, L.-C.; Maple, M. B.; Christou, G.; Hendrickson, D. N., Resonant Magnetization Tunneling in the Trigonal Pyramidal $Mn^{IV}Mn^{III}_3$ Complex $[Mn_4O_3Cl(O_2CCH_3)_3(dbm)_3]$. *J. Am. Chem. Soc.* **1998**, *120* (20), 4991-5004.

(56) Stoll, S.; Schweiger, A., EasySpin, a comprehensive software package for spectral simulation and analysis in EPR. *J. Magn. Res.* **2006**, *178* (1), 42-55.

(57) Randall, D. W.; Sturgeon, B. E.; Ball, J. A.; Lorigan, G. A.; Chan, M. K.; Klein, M. P.; Armstrong, W. H.; Britt, R. D., ^{55}Mn ESE-ENDOR of a Mixed Valence Mn(III)Mn(IV) Complex: Comparison with the Mn Cluster of the Photosynthetic Oxygen-Evolving Complex. *J. Am. Chem. Soc.* **1995**, *117* (47), 11780-11789.

(58) Su, J.-H.; Cox, N.; Ames, W.; Pantazis, D. A.; Rapatskiy, L.; Lohmiller, T.; Kulik, L. V.; Dorlet, P.; Rutherford, A. W.; Neese, F.; Boussac, A.; Lubitz, W.; Messinger, J., The electronic structures of the S_2 states of the oxygen-evolving complexes of photosystem II in plants and cyanobacteria in the presence and absence of methanol. *Biochim. Biophys. Acta, Bioenerg.* **2011**, *1807* (7), 829-840.

(59) Marchiori, D. A.; Oyala, P. H.; Debus, R. J.; Stich, T. A.; Britt, R. D., Structural Effects of Ammonia Binding to the Mn_4CaO_5 Cluster of Photosystem II. *J. Phys. Chem. B* **2018**, *122* (5), 1588-1599.

(60) Martinie, R. J.; Blaesi, E. J.; Krebs, C.; Bollinger, J. M., Jr.; Silakov, A.; Pollock, C. J., Evidence for a Di-μ-oxo Diamond Core in the Mn(IV)/Fe(IV) Activation Intermediate of Ribonucleotide Reductase from Chlamydia trachomatis. *J. Am. Chem. Soc.* **2017**, *139* (5), 1950-1957.

(61) Beal, N. J.; O'Malley, P. J., Manganese Oxidation State Assignment for Manganese Catalase. *J. Am. Chem. Soc.* **2016**, *138* (13), 4358-4361.

(62) Hillier, W.; Wydrzynski, T., ^{18}O-Water exchange in photosystem II: Substrate binding and intermediates of the water splitting cycle. *Coord. Chem. Rev.* **2008**, *252* (3), 306-317.

(63) Nilsson, H.; Rappaport, F.; Boussac, A.; Messinger, J., Substrate–water exchange in photosystem II is arrested before dioxygen formation. *Nature Commun.*, **2014** *5* (1), 4305.

(64) Noguchi, T.; Sugiura, M., FTIR Detection of Water Reactions during the Flash-Induced S-State Cycle of the Photosynthetic Water-Oxidizing Complex. *Biochemistry* **2002**, *41* (52), 15706-15712.

(65) Noguchi, T., Fourier transform infrared analysis of the photosynthetic oxygen-evolving center. *Coord. Chem. Rev.* **2008**, *252* (3), 336-346.

(66) Lohmiller, T.; Krewald, V.; Sedoud, A.; Rutherford, A. W.; Neese, F.; Lubitz, W.; Pantazis, D. A.; Cox, N., The First State in the Catalytic Cycle of the Water-Oxidizing Enzyme: Identification of a Water-Derived μ-Hydroxo Bridge. *J. Am. Chem. Soc.* **2017**, *139* (41), 14412-14424.

(67) Rapatskiy, L.; Cox, N.; Savitsky, A.; Ames, W. M.; Sander, J.; Nowaczyk, M. M.; Rögner, M.; Boussac, A.; Neese, F.; Messinger, J.; Lubitz, W., Detection of the Water-Binding Sites of the Oxygen-Evolving Complex of Photosystem II Using W-Band ^{17}O Electron–Electron Double Resonance-Detected NMR Spectroscopy. *J. Am. Chem. Soc.* **2012**, *134* (40), 16619-16634.

(68) Rapatskiy, L.; Ames, W. M.; Pérez-Navarro, M.; Savitsky, A.; Griese, J. J.; Weyhermüller, T.; Shafaat, H. S.; Högbom, M.; Neese, F.; Pantazis, D. A.; Cox, N., Characterization of Oxygen Bridged Manganese Model Complexes Using Multifrequency ^{17}O-Hyperfine EPR Spectroscopies and Density Functional Theory. *J. Phys. Chem. B* **2015**, *119* (43), 13904-13921.

(69) Usov, O. M.; Grigoryants, V. M.; Tagore, R.; Brudvig, G. W.; Scholes, C. P., Hyperfine Coupling to the Bridging ^{17}O in the Di-μ-oxo Core of a Mn^{III}–Mn^{IV} Model Significant to the Core Electronic Structure of the O_2-Evolving Complex in Photosystem II. *J. Am. Chem. Soc.* **2007**, *129* (39), 11886-11887.

(70) Lee, H. B. Electronic Structure and Spectroscopy of Tetranuclear Mn_4O_4 and $CaMn_3O_4$ Complexes as Models of the Oxygen Evolving Complex in Photosystem II. California Institute of Technology, 2019.

CHAPTER 5

$Mn^{IV}_4O_4$ Model of the S_3 Intermediate of the Oxygen-Evolving Complex: Effect of the Dianionic Disiloxide Ligand

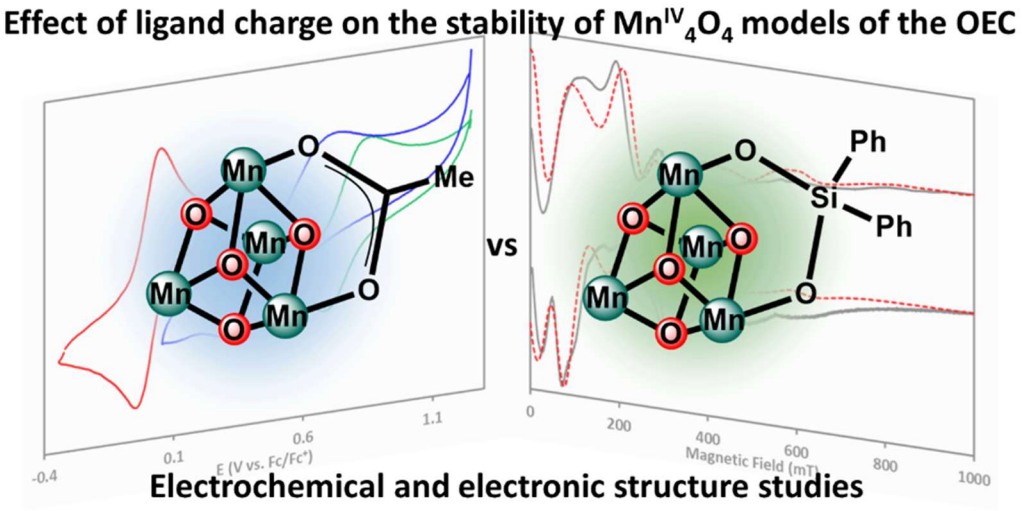

The text for this chapter was reproduced in part from:

Shiau, A. A.; Lee, H. B.; Oyala, P. H.; Agapie, T. *Inorg. Chem.*, **2023**, *53*, 6832−6835.

Abstract

Synthetic complexes provide useful models to study the interplay between the structure and spectroscopy of the different S_n-state intermediates of the oxygen-evolving complex (OEC) of photosystem II (PSII). Complexes containing the Mn^{IV}_4 core corresponding to the S_3 state, the last observable intermediate prior to dioxygen formation, remain very rare. Toward the development of synthetic strategies to stabilize highly oxidized tetranuclear complexes, ligands with increased anion charge were pursued. Herein, we report the synthesis, electrochemistry, SQUID magnetometry, and electron paramagnetic resonance spectroscopy of a stable $Mn^{IV}_4O_4$ cuboidal complex supported by a disiloxide ligand. The substitution of an anionic acetate or amidate ligand with a dianionic disiloxide ligand shifts the reduction potential of the $Mn^{III}Mn^{IV}_3/Mn^{IV}_4$ redox couple by up to ~760 mV, improving stability. The $S = 3$ spin ground state of the siloxide-ligated $Mn^{IV}_4O_4$ complex matches the acetate and amidate variants, in corroboration with the Mn^{IV}_4 assignment of the S_3 state of the OEC.

5.1) Introduction

Biological water oxidation to dioxygen is catalyzed at the oxygen evolving complex (OEC) of Photosystem II (PSII).[1-9] The proposed mechanism is described in the context of the Kok cycle of S_n (n = 0−4) states. The S_3 state is the last observable intermediate prior to dioxygen formation. Despite extensive biochemical, biophysical, computational, and structural studies to understand the advanced S-states, few multimetallic synthetic examples with relevant metal oxidation states and cluster geometries are available to complement and benchmark these studies.[10-24]

Due to synthetic challenges, relatively few Mn^{IV}_4 clusters have been reported, which belong to three classes: (1) linear[25-27] and (2) adamantane-shaped[28-31] complexes featuring $[Mn_4O_6]^{4+}$ cores, and (3) a recently reported cubane-shaped complex featuring a $[Mn_4O_4]^{8+}$ core.[17] Notably, all three types demonstrate different spin ground states, indicating that the electronic structure of cluster complexes is intimately tied to their geometry. For example, the linear $[Mn^{IV}_4O_6(bpy)_6]^{4+}$ complex features strong pairwise antiferromagnetic coupling that leads to a S = 0 ground state.[25] In contrast, the adamantane-shaped $[Mn^{IV}_4O_6(tacn)_4]^{4+}$ complex and its ligand-substituted derivatives display ferromagnetic interactions that lead to an S = 6 ground state, determined by magnetic susceptibility studies.[28, 31]

Recently, our group reported the synthesis and characterization of Mn_4O_4 cuboidal complexes supported by a bridging diamidate ligand. Specifically, complex $LMn^{III}_2Mn^{IV}_2(diam)(OAc)$ (**1**) supported by a tris-alkoxide ligand, a multinucleating diamidate, and an acetate serves as a precursor for the one- and two-electron oxidized complexes as models of the S_2 and S_3 states of the OEC.[17-18] (Figure 1).

Upon oxidation of the $Mn^{III}Mn^{IV}_3O_4$ cluster to the $Mn^{IV}_4O_4$ cluster (**1-ox)**, the spin ground state changes from S = 1/2 to S = 3, mimicking the spin state change observed for the S2→S3 transition in the OEC. Importantly, the electron-rich diamidate was crucial in accessing this high oxidation state cluster. Despite this ligand choice, **1-ox** is unstable even as a solid at –40 ºC, thwarting its isolation. To stabilize such a highly oxidized cluster, we targeted exchange of the acetate with a more electron donating ligand. Herein, we report the synthesis and characterization of an isolable and room temperature stable $[Mn^{IV}_4O_4]^{8+}$ cuboidal complex supported by a disiloxide ligand. Results highlight the ability of the disiloxide ligand to support highly oxidized metal clusters. Electronic structure studies confirm an $S = 3$ spin ground state consistent with the acetate and amidate variants, further supporting the Mn^{IV}_4 assignment of the S_3 state of the OEC.

Siloxides such as tris(tertbutoxy)siloxide and triphenylsiloxide have been used as supporting ligands for a variety of high oxidation state transition metal and *f*-element complexes.[32-37] Silsesquioxane-derived ligands have also been demonstrated to support manganese clusters.[38-40] In comparison, silanediol-derived ($R_2Si(OH)_2$) ligands have not been as widely explored, especially for multinuclear systems.[41-50] Diphenylsilanediol reacts with (*p*-halophenyl)stibonic acids to yield Sb_4O_4 complexes where four disiloxides bridge Sb-atoms at alternating corners of a cubane.[47] With the precedent of disiloxides supporting similar cluster motifs to the desired Mn complexes and the ability of siloxides to support high-valent metal centers, Mn clusters were targeted with the hypothesis that replacing a monoanionic bridging ligand with a dianionic one will improve the stability of the more highly oxidized variants.

5.2) Synthesis

Treatment of **1** with diphenylsilanediol generates **2** via a protonolysis reaction (Scheme 1). The ESI-MS peak (*m*/*z* = 1511) is consistent with the mass of $[LMn_4O_4(diam)(HO_2SiPh_2)]^+$. The single crystal X-ray diffraction (scXRD) structure of **2** is consistent with this formulation, although the H-atom of the silanol moiety has not been located (Figure 19). Axial elongations of Mn−oxo distances are observed for Mn(1) and Mn(2) (2.049(6), 2.172(7) Å, respectively). This structural feature is consistent with the high-spin Mn^{III} oxidation state where distortion results from partial occupation of the d_z^2-σ-antibonding orbital weakening the Mn–O interaction along z. Lacking such distortions, Mn(3) and Mn(4) are assigned as Mn^{IV}. Compared to **1**, **2** displays a redox reorganization within the cluster. In **1**, the Mn^{IV} centers are ligated by three amidate oxygen donors, but in **2** the Mn^{III} ions are ligated by the amidate O-atoms, and Mn^{IV} by siloxides, consistent with the more electron-donating nature of this moiety. Treatment of **2** with NaO^{t}Bu and FcOTf generated **3**. The ESI-MS peak (*m*/*z* = 1510) is consistent with the mass of $[LMn_4O_4(diam)(O_2SiPh_2)]^+$. The scXRD structure supports the $LMn_4O_4(diam)(O_2SiPh_2)$ formulation (Figure 2). The oxidation state of Mn(2) is assigned as Mn^{III}, as only one elongated Mn−oxo bond length is observed (Mn(2)–O(4): 2.106(7) Å). All other Mn-oxo distances are within 1.864(7)−1.942(7) Å, consistent with the $Mn^{III}Mn^{IV}_3$ oxidation state assignment of **3**. Additionally, the EPR spectrum of **3** shows a broad signal centered around $g = 2$ featuring ^{55}Mn hyperfine interactions, consistent with an $S = 1/2$ spin ground state reminiscent of related acetate, phosphinate, and amidate-supported $Mn^{III}Mn^{IV}_3O_4$ complexes (Figure 26).[18, 51]

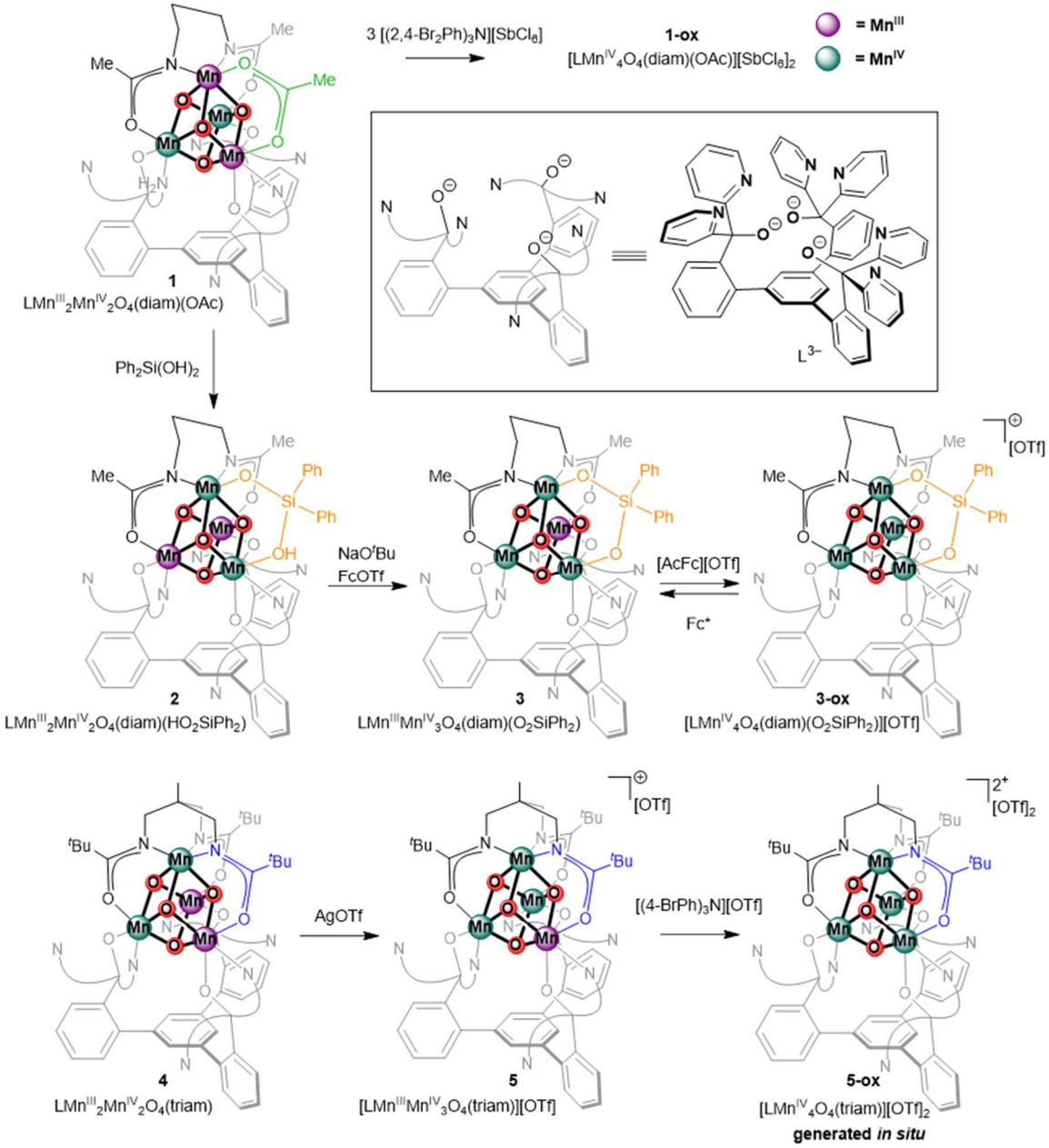

Figure 1. Synthesis of complexes studied in this work. **1**, **1-ox**, **4**, and **5** are previously reported.[40-41, 81]

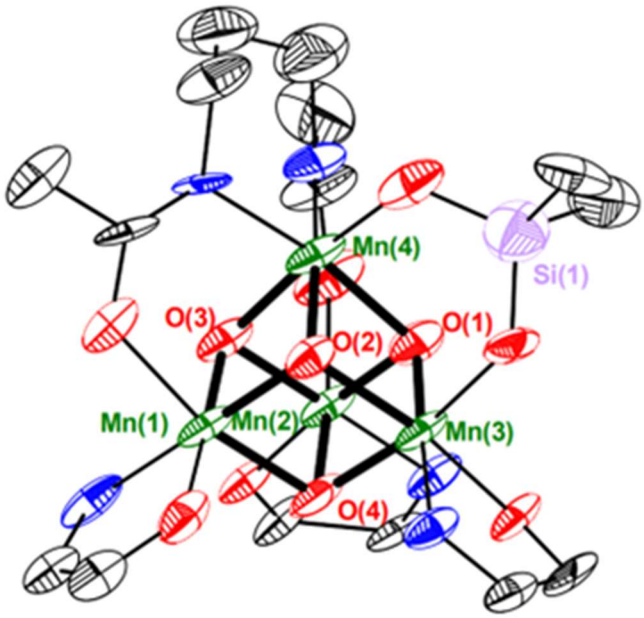

Figure 2. Truncated crystal structure of **3**. Mn (green), O (red), N (blue), Si (purple), C (black). Bolded bonds highlight Mn-oxo bonds. Ellipsoids at 50% probability.

5.3) Electrochemistry

The cyclic voltammograms (CV) of **2** and **3** show reversible $Mn^{III}_2Mn^{IV}_2/Mn^{III}Mn^{IV}_3$ redox couples at –10 and –750 mV versus Fc/Fc^+, respectively (Figure 20–21). The CV of **3** also shows a reversible feature at +15 mV assigned to the $Mn^{III}Mn^{IV}_3/Mn^{IV}_4$ couple (Figure 4a). Markedly, the dianionic disiloxide ligand decreases the reduction potential of the $Mn^{III}Mn^{IV}_3/Mn^{IV}_4$ couple by ~760 mV relative to that of **1**, and ~505 mV relative to that of **4**, which contains three electron-donating amidates (Figure 3). These are the only Mn_4O_4 cubanes that display a $Mn^{III}Mn^{IV}_3/Mn^{IV}_4$ redox event electrochemically. Compared to that of **1** and **4**, the reversibility of this redox couple for **3** is greatly increased suggesting improved stability (Figure 20).

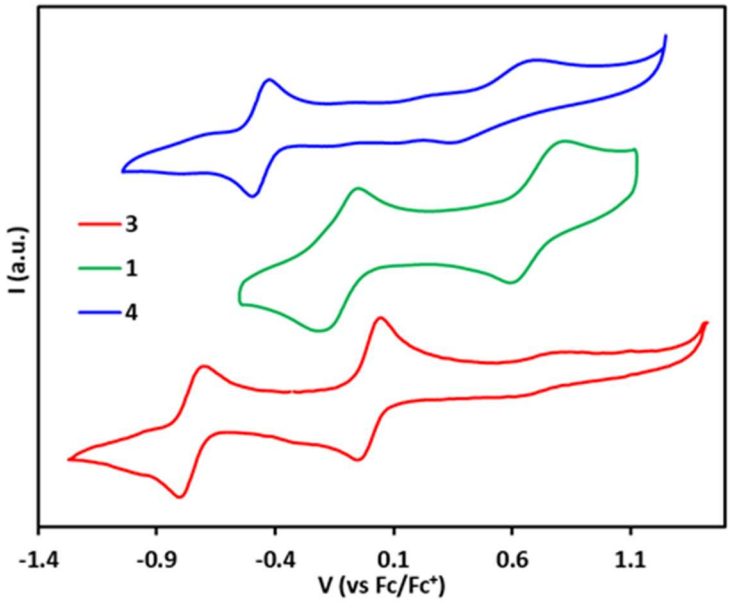

Figure 3. CV of complexes **1** (green), **3** (red), and **4** (blue) showing both $Mn^{III}_2Mn^{IV}_2/Mn^{III}Mn^{IV}_3$ and $Mn^{III}Mn^{IV}_3/Mn^{IV}_4$ redox events.

As in the case of Co_4O_4 and $RuCo_3O_5$ complexes,[52-55] the redox properties of the MMn_3O_4 (M = Mn, Y) complexes can be tuned by the nature of the supporting ligands, exhibiting a linear correlation between cluster reduction potential and effective ligand basicity (Figure 4b).[51] Comparing the series of Mn_4O_4 clusters with different ligands on only three faces of the cubane,[18, 51] a substantial shift in the reduction potential (~1 V) is observed (Figure 3). In comparison, changing ligands on all six faces of the cubane in Co_4O_4 complexes results in a reduction potential range of 1.4 V.[52] For the Mn_4O_4 series, **3** features the lowest reduction potential owing to the combined effect of an additional negative ligand charge and higher ligand basicity compared to the previously studied monoanionic ligands. This behavior highlights the utility of the disiloxide ligand in facilitating access to high oxidation state clusters. Using both the $Mn^{III}_2Mn^{IV}_2/Mn^{III}Mn^{IV}_3$ and $Mn^{III}Mn^{IV}_3/Mn^{IV}_4$ reduction potentials of **3** (–750, +15 mV, respectively), an effective basicity of ~25 was predicted based on the intersection with trendlines developed from the series of related

complexes (Figure 4b). Notably, the $Mn^{III}_2Mn^{IV}_2/Mn^{III}Mn^{IV}_3$ potential for **2** and the $Mn^{III}Mn^{IV}_3/Mn^{IV}_4$ potential for **3** (–10, +15 mV, respectively) are close, exemplifying the reduction potential levelling effect of combining proton and electron removal (to convert **2** to **3-ox**) as proposed for the OEC catalytic cycle.[56]

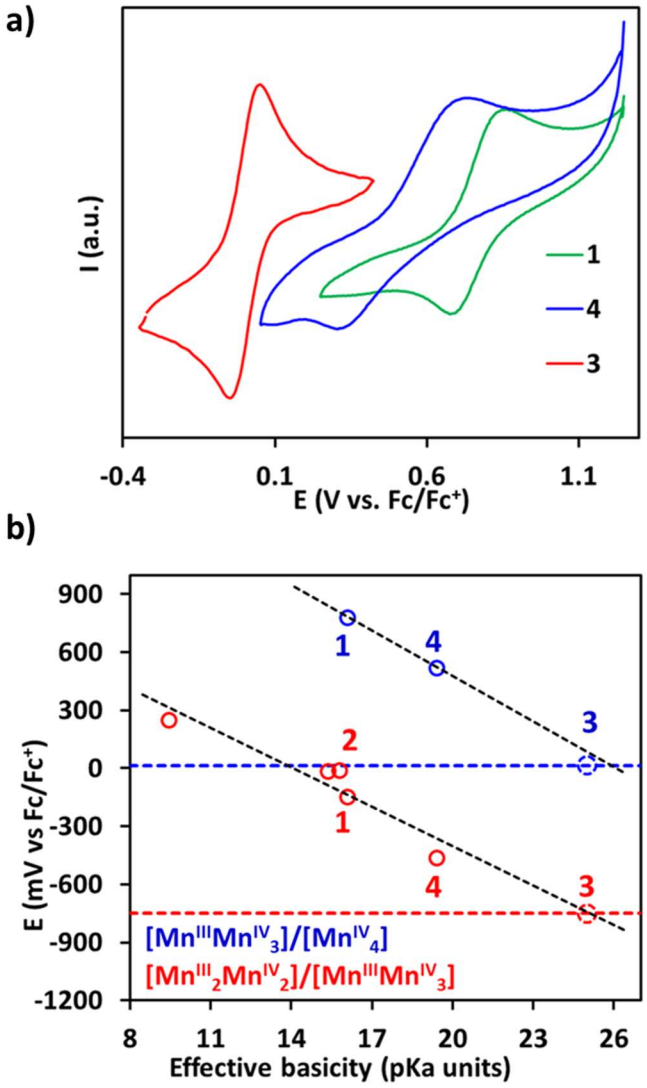

Figure 4. a) CV of **1**, **3**, and **4**. Isolated waves correspond to $Mn^{III}Mn^{IV}_3/Mn^{IV}_4$ redox couple. Measured $E_{1/2}$ (mV): +780 (**1**), +15 (**3**), +520 (**4**). **b)** Linear correlation between redox potential and effective ligand basicity in $[Mn_4O_4]$ complexes. Red and blue circles correspond to $Mn^{III}_2Mn^{IV}_2/Mn^{III}Mn^{IV}_3$ and $Mn^{III}Mn^{IV}_3/Mn^{IV}_4$ values, respectively. Red and blue dotted lines correspond to the respective redox couples for complex **3**. Black dotted lines are linear fits.

5.4) Magnetism and EPR spectroscopy

As there is a single reported cuboidal $Mn^{IV}_4O_4$,[17] isolation of the one-electron oxidation product of **3** was targeted. Treatment of **3** with [AcFc][OTf] ($E_{1/2}$ = +270 mV vs Fc/Fc^+, CH_2Cl_2)[57] results in the formation of $Mn^{IV}_4O_4$ species **3-ox**. Although oxidants with varying counter-anions were utilized, conditions for growing single crystals of **3-ox** suitable for X-ray characterization remain elusive. The ESI-MS peak (*m*/*z* = 1510) is consistent with the mass of $[LMn_4O_4(diam)(O_2SiPh_2)]^+$. Anion exchange of **3-ox** with $LiB(C_6F_6)_4$ shows the same ^1H NMR spectrum, while in the ^{19}F NMR spectrum the triflate peak is replaced with three peaks of the tetrakis(pentafluorophenyl)borate anion (Figures 11−12). This supports the assignment of an outer-sphere triflate for **3-ox**. Furthermore, treatment of **3-ox** with $FeCp^*_2$ ($E_{1/2}$ = −590 mV vs Fc/Fc^+, CH_2Cl_2)[57] results in the formation of $[FeCp^*_2][OTf]$ and **3** (Figure 13). Together, these data corroborate **3-ox** as the one-electron oxidized analogue of **3**, with an intact Mn_4O_4 cuboidal core and metal coordination sphere. **3-ox** is room temperature stable as a solid and can thus be characterized via methods unamenable for studying the related complex **1-ox**.

To gain insight into the magnetic exchange coupling between the Mn^{IV} centers, magnetic susceptibility experiments were performed on powdered samples of **3-ox** in a non-saturating field of 0.2 T (Figure 5a). At 300 K, a χT value of 7.55 emu·K·mol^{-1} is close to the expected value of 7.5 emu·K·mol^{-1} (*g* = 2) for four uncoupled Mn^{IV} centers. At 1.8 K, the χT value of 5.45 emu·K·mol^{-1} at 1.8 K is slightly lower than the value expected for an *S* = 3 (g = 2) ground-state (6 emu·K·mol^{-1}). An isotropic spin exchange Hamiltonian (eq. 1) with four distinct magnetic interactions can be employed to model the data, assuming *pseudo-*C_S symmetry. From EPR simulations, the axial zero-field splitting (ZFS) value of

$D(Mn^{IV})$ = +0.151 cm^{-1} was estimated. The coupling scheme, ZFS value, and incorporation of a mean field model of intermolecular antiferromagnetic interaction *zJ* yielded reasonable fit of both the magnetic susceptibility and magnetization data (Figure 25). This ZFS parameter is smaller than the estimated value for **1-ox** (D = +0.4 cm^{-1}),[17] but comparable to those of a $CaMn^{IV}_3O_4$ cluster reported by Christou ($|D| \approx 0.068$ cm^{-1}),[12] and the S_3 state of *T. elongatus* ($|D|$ = 0.175 cm^{-1}) and chemically modified *T. elongatus* ($|D|$ = 0.281 cm^{-1}) of PSII.[5-6, 58] Comparably, the S_3 state of *Synechocystis* has been modeled as a mixture of four species with a range of $|D|$ = 0.163–0.33 cm^{-1}.[59] Small ZFS values (~0.2 cm^{-1}) are expected for Mn^{IV} complexes because of the near spherical symmetry of the (t_{2g}^3 e_g^0) state,[60-62] but a wider spread of values ($|D|$ = 0.17–2.3 cm^{-1}) has been reported for six-coordinate monometallic Mn^{IV} complexes.[63-65] Overall, this coupling scheme is consistent with the ααaβ spin topology approaching the trimer-monomer magnetic coupling model of pseudo-octahedral Mn^{IV} centers reported for **1-ox**.[17]

$$\widehat{H} = -2 \sum_{i \neq j}^{i,j \in N} J_{ij} \widehat{S}_i \cdot \widehat{S}_j \qquad (1)$$

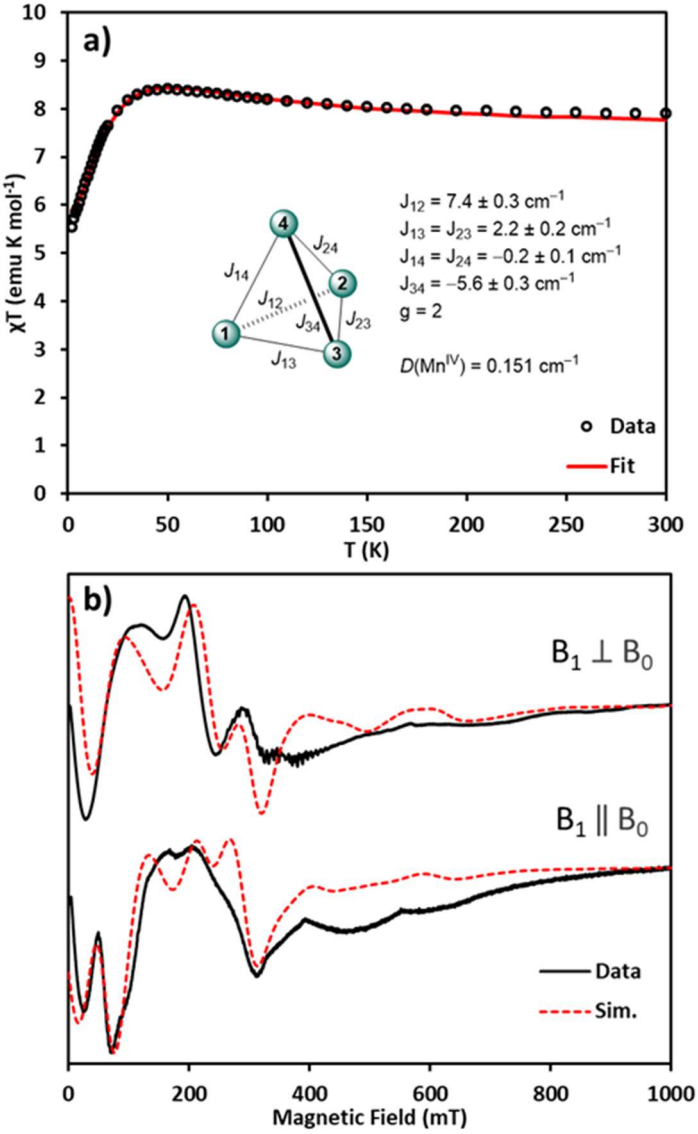

Figure 5. a) Exchange coupling model, fit parameters, and magnetic susceptibility for **3-ox**. For the exchange coupling model, the mirror plane of the *pseudo*-C_S symmetry contains the bold vector and bisects the hashed vector. Numbering scheme is identical to that in Figure 1. **b)** Perpendicular and parallel-mode X-band CW-EPR of **3-ox**.

To obtain further insight into the electronic structure of **3-ox**, X-band CW-EPR studies were conducted. The parallel-mode X-band CW-EPR of **3-ox** displays two main features at g = ~26 and ~9.8 (Figure 5b). The broad spectrum was modeled using $S = 3$, $g = 2$, a Gaussian distribution of D centered at 0.151 with a full width at half maximum of 0.035 (Figure 27), and E/D = 0.166. Expanding this series of cuboidal $Mn^{IV}_4O_4$ complexes,

triamidate-supported **5-ox** was generated in situ from oxidation of **5** with [(4-BrPh)$_3$N][OTf]. Like that of **1-ox**, the parallel-mode X-band EPR spectrum of **5-ox** features an intense signal at g ~12, consistent with an S = 3 spin ground state. A larger D of +0.55 cm^{-1} and E/D of 0.18 provided a satisfactory fit (Figure 6), in agreement with the observation that more covalent metal-ligand interactions result in larger ZFS parameters.[66]

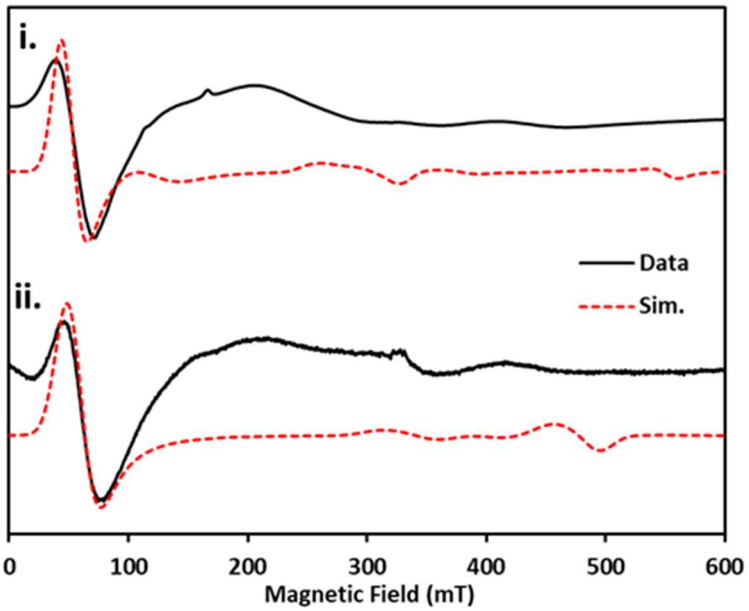

Figure 6. Parallel-mode X-band CW-EPR of **i. 1-ox**. Simulation parameters[41]: S = 3, g = 1.97, D = 0.4 cm^{-1}, E/D = 0.1. **ii. 5-ox**. Simulation parameters: S = 3, g = 2, D = 0.55 cm^{-1}, E/D = 0.18.

5.5) Discussion

In summary, highly oxidized Mn_4O_4 complexes featuring bridging disiloxide ligands were synthesized and characterized. Effects of exchanging an acetate or amidate for a disiloxide on a metal-oxo cluster include a large negative shift in reduction potential, making the previously unstable $Mn^{IV}{}_4O_4$ species derived from **1** readily accessible by relatively weak oxidants like acetylferrocenium. Complexes **3-ox** and **5-ox** expand the series of $Mn^{IV}{}_4O_4$ cubane models of the S_3 state. Characterization via SQUID magnetometry and EPR spectroscopy corroborate an $S = 3$ ground state. Despite structural differences with the biological system, these cuboidal tetra-manganese-oxo clusters serve as spectroscopic models for studies of the impact of ligand changes, as they all demonstrate a spin change of $S = 1/2 \rightarrow S = 3$ upon oxidation from $Mn^{III}Mn^{IV}{}_3$ to $Mn^{IV}{}_4$, mimicking the $S_2 \rightarrow S_3$ transition in the OEC.

5.6) Experimental section

General considerations

All reactions were performed at room temperature in an N_2-filled glovebox or by using standard Schlenk techniques unless otherwise specified. Glassware was oven dried at 150 °C for at least 2h prior to use and allowed to cool under vacuum. All reagents were used as received unless otherwise stated. Diphenylsilanediol was recrystallized from chloroform. Ferrocenium triflate and tris(4-bromophenyl)aminium triflate were synthesized according to literature. Anhydrous tetrahydrofuran (THF) was purchased from Aldrich in 18 L Pure-Pac^{TM} containers. Anhydrous CH_2Cl_2, diethyl ether, benzene, and THF were purified by sparging with nitrogen for 15 minutes and then passing under nitrogen pressure through a column of activated A2 alumina. NMR solvents were purchased from Cambridge Isotope

Laboratories, dried over calcium hydride (CD_2Cl_2) or sodium/benzophenone (C_6D_6), degassed by three freeze-pump-thaw cycles and vacuum-transferred prior to use. ^{1}H NMR spectra were recorded on a Varian 300 MHz instrument, with shifts reported relative to the residual solvent peak. Elemental analyses were performed at the California Institute of Technology or at the University of Rochester.

All compounds are mildly air-sensitive and decompose over the course of hours in air.

Synthesis of $LMn_4O_4(diam)(HO_2SiPh_2)$ (**2**)

A solution of diphenylsilanediol (54 mg, 0.25 mmol, 1.1 equiv) in THF (5 mL) was added to a stirring CH_2Cl_2 solution of $LMn_4O_4(diam)(OAc)$ (**1**) (300 mg, 0.22 mmol, 1 equiv). After stirring the reaction mixture at room temperature for 16 hours, all volatiles were removed under reduced pressure. The solid residue was triturated with CH_2Cl_2 (5 mL) twice and with pentane (3 mL) once. The brown powder was suspended in 5 mL of pentane, collected on a pad of Celite, and washed thoroughly with pentane and Et_2O. The product was dissolved in benzene and filtered through Celite. All volatiles were removed from the filtrate under reduced pressure, yielding **2** as a brown powder. Yield: 293.2 mg, 88%. Analysis calculated for $LMn_4O_4(diam)(HO_2SiPh_2)$ [$C_{76}H_{62}Mn_4N_8O_{11}Si$]: C 60.40, H 4.14, N 7.41; found: C 60.36, H 4.21, N 7.17.

Synthesis of $LMn_4O_4(diam)(O_2SiPh_2)$ (**3**)

A solution of sodium *tert*-butoxide (5.0 mg, 0.052 mmol, 1.05 equiv) in THF (2 mL) was added to a stirring THF solution of **2** (75 mg, 0.049 mmol, 1 equiv). After 5-10 minutes of stirring, the reaction mixture was transferred to a stirring suspension of FcOTf (17.4 mg, 0.052 mmol, 1.05 equiv) in THF (5 mL). The reaction mixture was stirred at room

temperature for 16 hours and became homogeneous. All volatiles were removed under reduced pressure. The solid residue was suspended in pentane, collected on a pad of Celite, and washed with pentane until all the Fc byproduct was removed. The brown solid was further washed with Et_2O (3 mL, x3), dissolved in benzene, and filtered through Celite. All volatiles were removed from the filtrate under reduced pressure, yielding **3** as a brown powder. Yield: 58.3 mg (79%). Crystals suitable for X-ray crystallography were grown from slow vapor diffusion of Et_2O into a concentrated solution of **3** in benzene. Analysis calculated for $LMn_4O_4(diam)(O_2SiPh_2)\cdot Et_2O$ [$C_{80}H_{71}Mn_4N_8O_{12}Si$]: C 60.65, H 4.52, N 7.07; found: C 60.16, H 4.15, N 6.92.

Synthesis of [$LMn_4O_4(diam)(O_2SiPh_2)$][OTf] (**3-ox**)

To a stirring solution of **3** (35 mg, 0.023 mmol) in THF (5 mL), a blue THF solution (4 mL) of $[(4\text{-}BrPh)_3N]$[OTf] (15.4 mg, 0.024 mmol, 1.05 equiv) was added. After the brown solution was stirred at room temperature for 15 minutes, all volatiles were removed under reduced pressure. (A weaker oxidant such as acetylferrocenium triflate can also be utilized but including a 16-hour reaction time, with the same workup procedure as described below.) The residue was washed with Et_2O (4 mL), dissolved in benzene, and filtered through Celite. The precipitate from a slow vapor diffusion of Et_2O into a concentrated solution of **3-ox** in benzene was collected, washed with Et_2O, and minimal benzene. The resulting brown solid was dissolved in CH_2Cl_2 and filtered. Volatiles were removed from the filtrate under reduced pressure to yield **3-ox**. Yield: 19 mg (49%). Analysis calculated for $[LMn_4O_4(diam)(O_2SiPh_2)][OTf]\cdot CH_2Cl_2$ [$C_{78}H_{63}Cl_2F_3Mn_4N_8O_{14}SSi$]: C 53.71, H 3.64, N 6.42; found: C 54.20, H 3.63, N 6.18.

In-situ generation of **5-ox** for EPR

[LMn_4O_4(triam)][OTf] (**5**) was prepared according to literature[51] by oxidation of **4** with AgOTf. Dissolve [LMn_4O_4(triam)][OTf] (88 mg, 0.053 mmol) in CH_2Cl_2. An optimal amount of [$(4\text{-BrPh})_3N$][OTf] (35 mg, 0.055 mmol, 1.05 equiv) was dissolved in CH_2Cl_2 and added dropwise. The mixture was stirred for 30 minutes and then all volatiles were removed under reduced pressure. The residue was washed with Et_2O (3 x 2 mL), benzene (3 x 2 mL), dissolved in CH_2Cl_2 and filtered through Celite. A c.a. 1 mM solution of this red-brown solid in MeCN can be filtered into an EPR tube and frozen in liquid nitrogen.

NMR spectroscopy

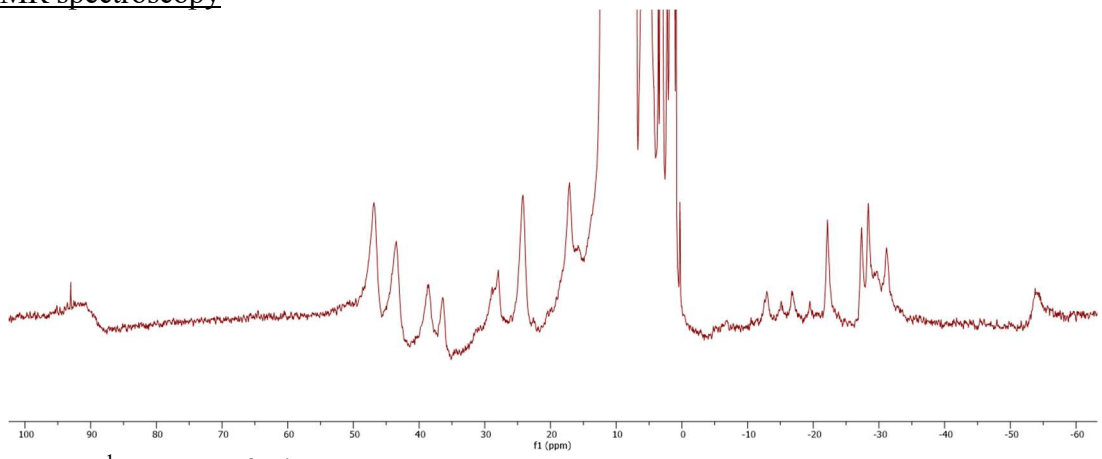

Figure 7. ^{1}H NMR of **2** in C_6D_6.

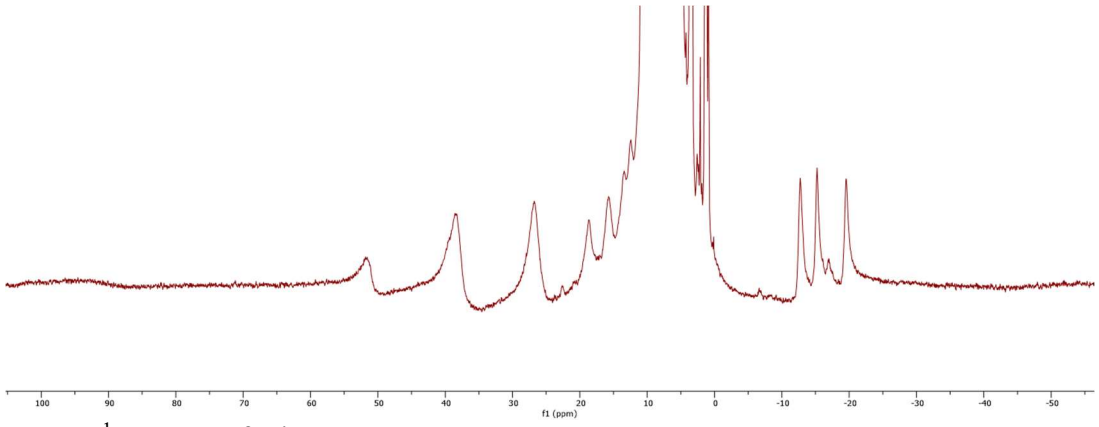

Figure 8. ^{1}H NMR of **3** in C_6D_6.

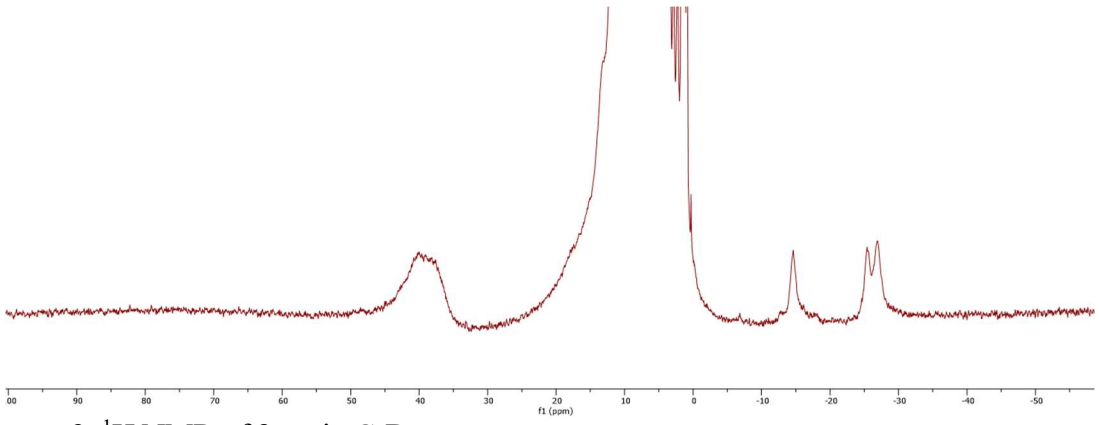

Figure 9. ^{1}H NMR of **3-ox** in C_6D_6.

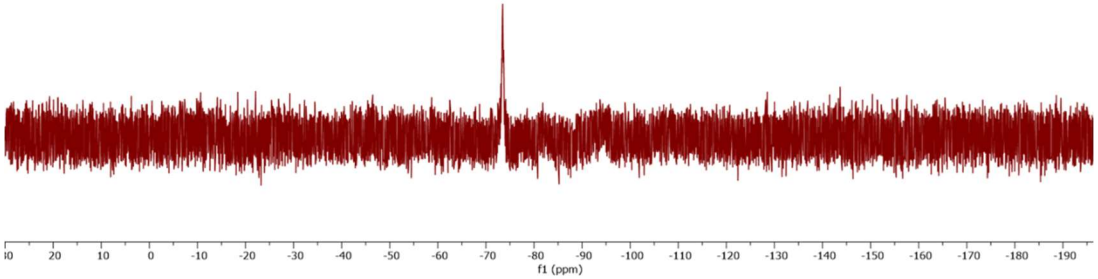

Figure 10. ^{19}F NMR of **3-ox** in C_6D_6.

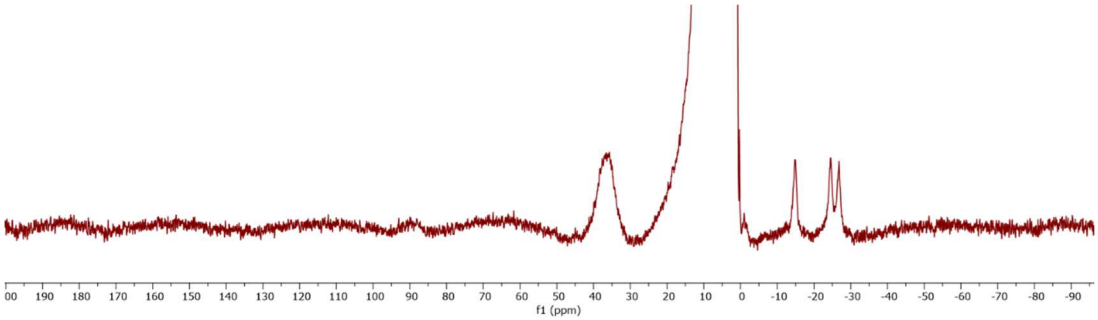

Figure 11. ^{1}H NMR of anion exchange reaction of **3-ox** with one equivalent of $LiB(C_6F_5)_4$, after workup, in C_6D_6.

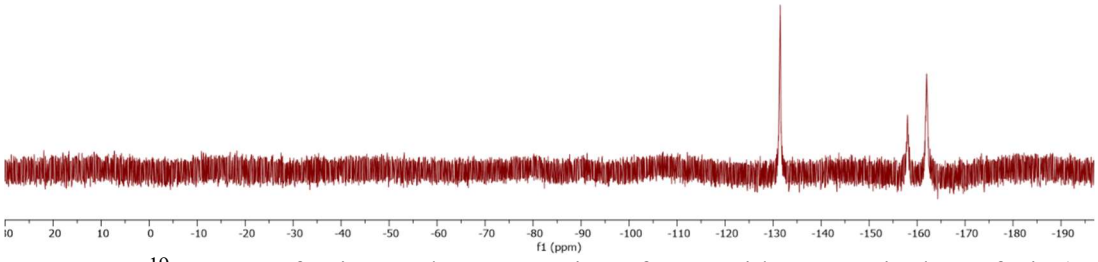

Figure 12. ^{19}F NMR of anion exchange reaction of **3-ox** with one equivalent of $LiB(C_6F_5)_4$, after workup, in C_6D_6.

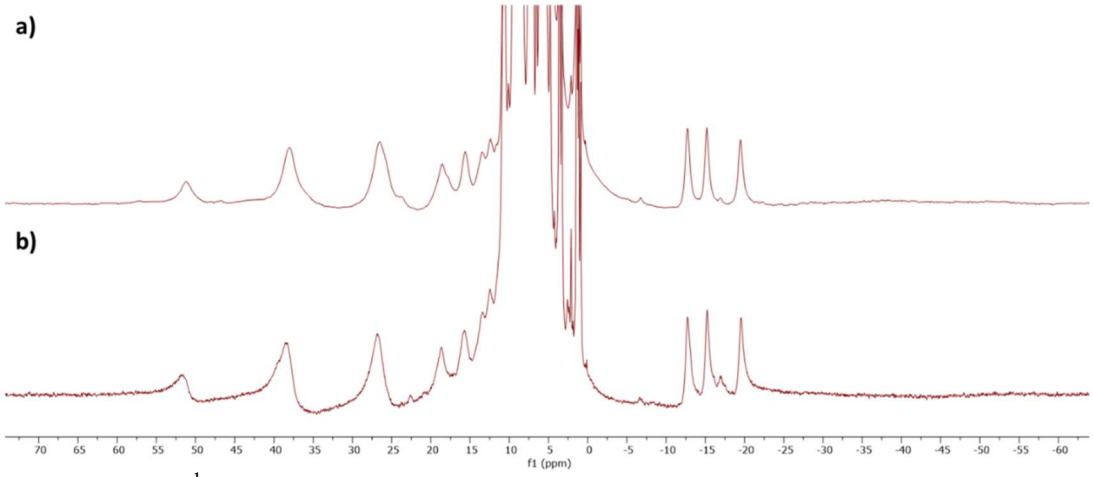

Figure 13. a) ^{1}H NMR (C_6D_6) of reaction between **3-ox** and 1 equivalent of Fc*, after extraction away from byproduct Fc*$^{+}$. **b)** ^{1}H NMR (C_6D_6) of **3**, synthesized and purified according to the procedures described *vide supra*.

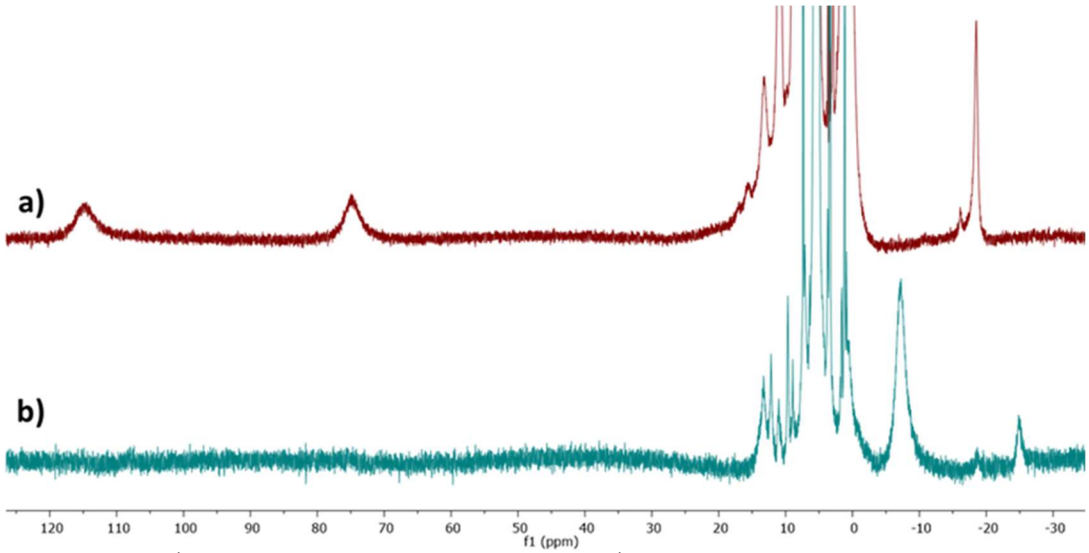

Figure 14. a) ^{1}H NMR (CD_2Cl_2) spectra of **5**. **b)** ^{1}H NMR (CD_2Cl_2) spectra of **5-ox**.

ESI-MS spectrometry

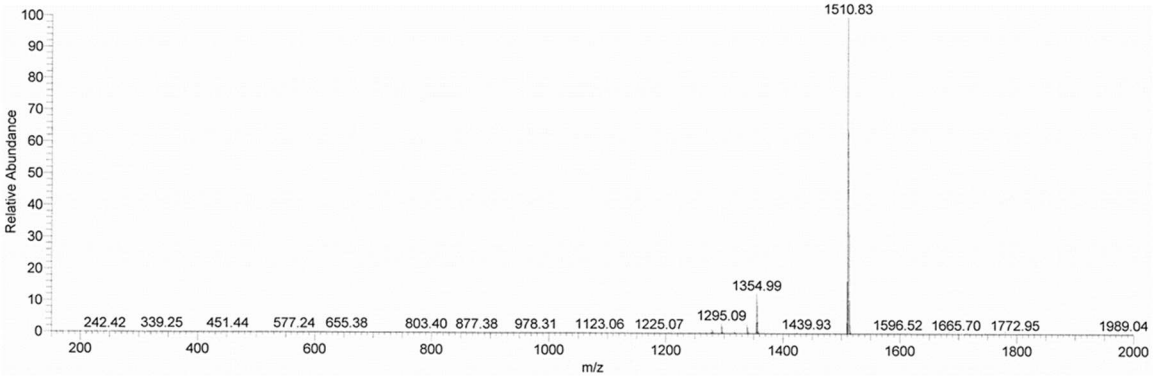

Figure 15. ESI-MS of **2**. m/z = 1511 consistent with $[LMn_4O_4(diam)(HO_2SiPh_2)]^+$. m/z = 1355 consistent with $[LMn_4O_4(diam)(OAc)]^+$.

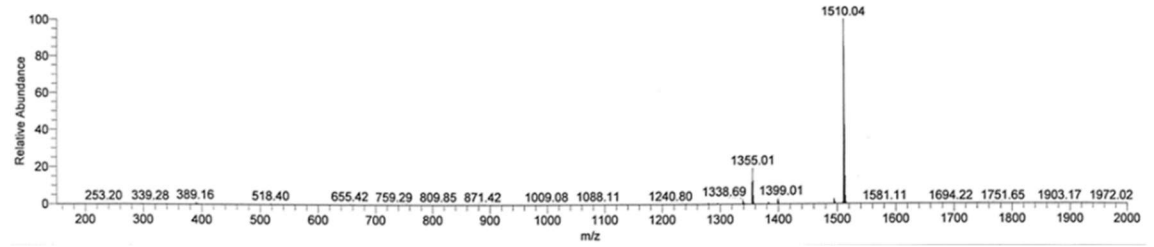

Figure 16. ESI-MS of **3**. m/z = 1510 consistent with $[LMn_4O_4(diam)(O_2SiPh_2)]^+$. m/z = 1355 consistent with $[LMn_4O_4(diam)(OAc)]^+$.

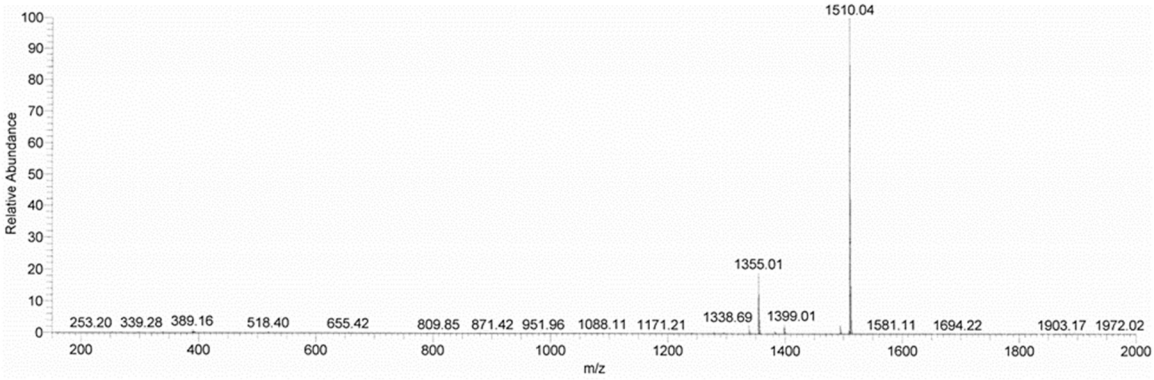

Figure 17. ESI-MS of **3-ox**. m/z = 1510 consistent with $[LMn_4O_4(diam)(O_2SiPh_2)]^+$. m/z = 1355 consistent with $[LMn_4O_4(diam)(OAc)]^+$.

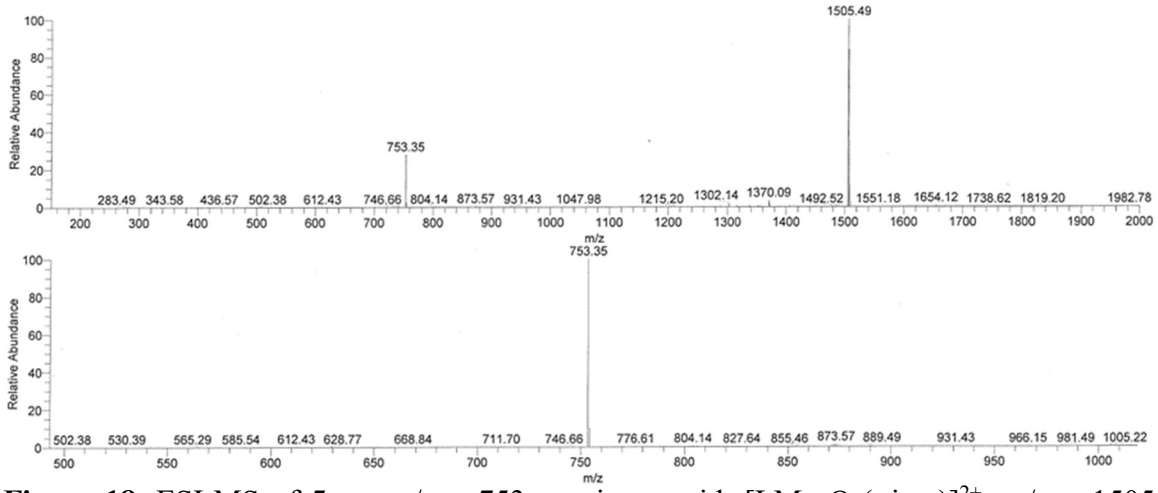

Figure 18. ESI-MS of **5-ox**. m/z = 753 consistent with $[LMn_4O_4(triam)]^{2+}$. m/z = 1505 consistent with $[LMn_4O_4(triam)]^{+}$.

Table 1. Crystal and refinement data for complexes **2** and **3**.

Compound	**2**	**3**
CCDC	2171723	2171724
Empirical formula	$C_{76}H_{61}Mn_4N_8O_{11}Si$	$C_{76}H_{61}Mn_4N_8O_{11}Si$
Formula weight	1510.17	1510.17
Temperature/K	99.99	100.0
Crystal system	triclinic	triclinic
Space group	P-1	P-1
a/Å	15.232(5)	15.149(8)
b/Å	15.802(6)	15.752(6)
c/Å	17.585(6)	17.589(6)
α/°	90.39(3)	90.17(3)
β/°	101.55(2)	102.05(4)
γ/°	106.965(18)	106.960(19)
Volume/Å^3	3957(2)	3917(3)
Z	2	2
ρ_{calc}g/cm^3	1.268	1.280
μ/mm^{-1}	5.710	5.768
F(000)	1550.0	1550.0
Crystal size/mm^3	0.05 × 0.05 × 0.05	0.05 x 0.05 x 0.05
Radiation	CuKα (λ = 1.54178)	CuKα (λ = 1.54178)
2Θ range for data collection/°	5.142 to 101.496	5.88 to 89.308
Index ranges	$-15 \le h \le 15$, $-15 \le k \le 15$, $-17 \le l \le 17$	$-13 \le h \le 13$, $-14 \le k \le 14$, $-16 \le l \le 16$
Reflections collected	18442	15525
Independent reflections	8178 [R_{int} = 0.0681, R_{sigma} = 0.1029]	6080 [R_{int} = 0.0661, R_{sigma} = 0.0796]
Data/restraints/parameters	8178/2290/735	6080/2302/705
Goodness-of-fit on F^2	1.074	1.089
Final R indexes [I>=2σ (I)]	R_1 = 0.0893, wR_2 = 0.2502	R_1 = 0.0903, wR_2 = 0.2530
Final R indexes [all data]	R_1 = 0.1244, wR_2 = 0.2713	R_1 = 0.1136, wR_2 = 0.2743
Largest diff. peak/hole / e Å^{-3}	0.75/-0.62	0.74/-0.86

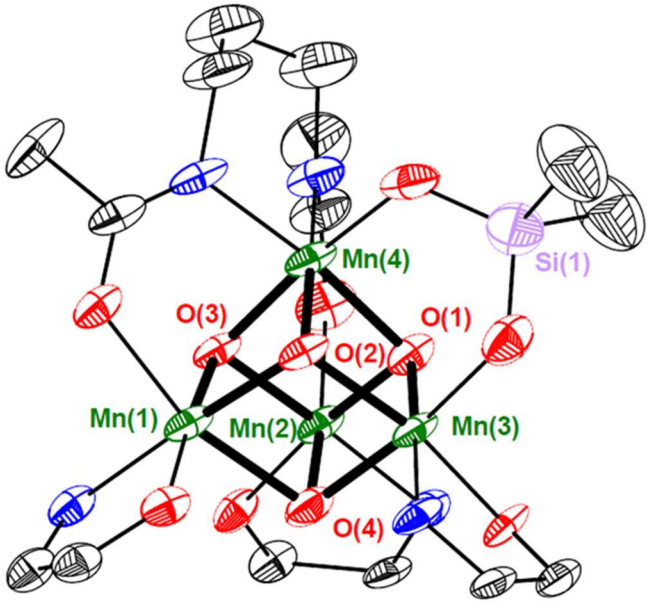

Figure 19. Truncated crystal structure of **2**. Mn (green), O (red), N (blue), Si (purple), C (black). Bolded bonds high-light Mn-oxo bonds. Ellipsoids at 50% probability.

Table 2. Mn-oxo bond distances (Å) of complexes **2** and **3**. Bolded entries highlight elongated Mn-oxo bond lengths.

	2	**3**
Mn(1) – O(2)	1.966(6)	1.873(8)
Mn(1) – O(3)	1.868(6)	1.864(7)
Mn(1) – O(4)	**2.049(6)**	1.899(6)
Mn(2) – O(1)	1.893(6)	1.891(8)
Mn(2) – O(3)	1.942(6)	1.938(7)
Mn(2) – O(4)	**2.172(7)**	**2.106(7)**
Mn(3) – O(1)	1.902(6)	1.871(7)
Mn(3) – O(2)	1.882(6)	1.901(6)
Mn(3) – O(4)	1.948(7)	1.896(9)
Mn(4) – O(1)	1.957(6)	1.942(7)
Mn(4) – O(2)	1.925(6)	1.930(7)
Mn(4) – O(3)	1.937(7)	1.93(1)

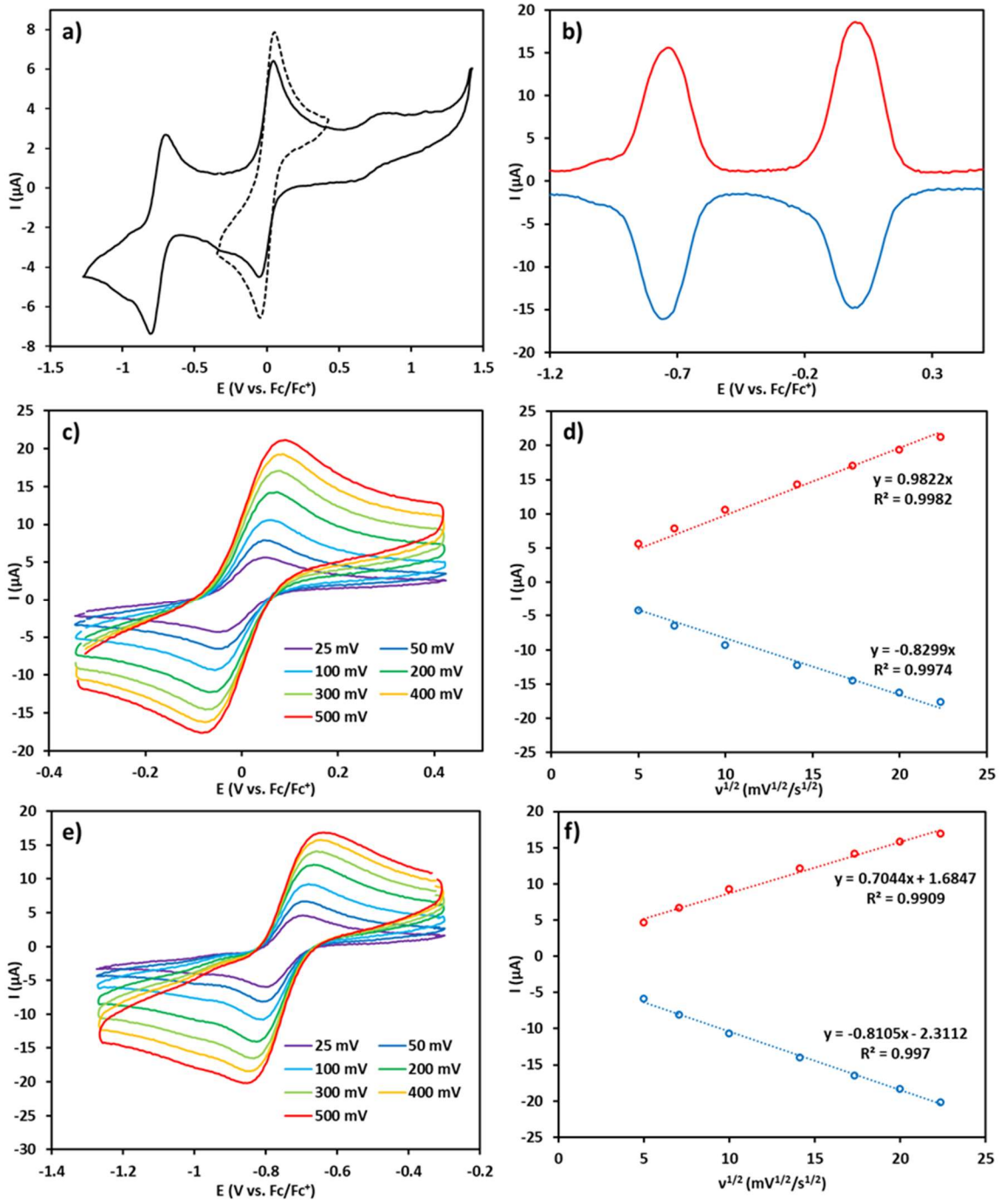

Figure 20. a) CV of **3**. Isolated $Mn^{III}Mn^{IV}_3/Mn^{IV}_4$ redox couple shown in dotted lines. E = + 15 mV vs. Fc/Fc^+. Small feature around ~780 mV vs Fc/Fc^+ corresponds to small impurity of **1**. **b)** SWV of **3**. **c)** Isolated $Mn^{III}Mn^{IV}_3/Mn^{IV}_4$ redox couple measured at various scan rates. **d)** Plot of peak current vs. square root of scan rate. **e)** Isolated $Mn^{III}_2Mn^{IV}_2/Mn^{III}Mn^{IV}_3$ redox couple measured at various scan rates. E = – 750 mV vs. Fc/Fc^+. **f)** Plot of peak current vs. square root of scan rate.

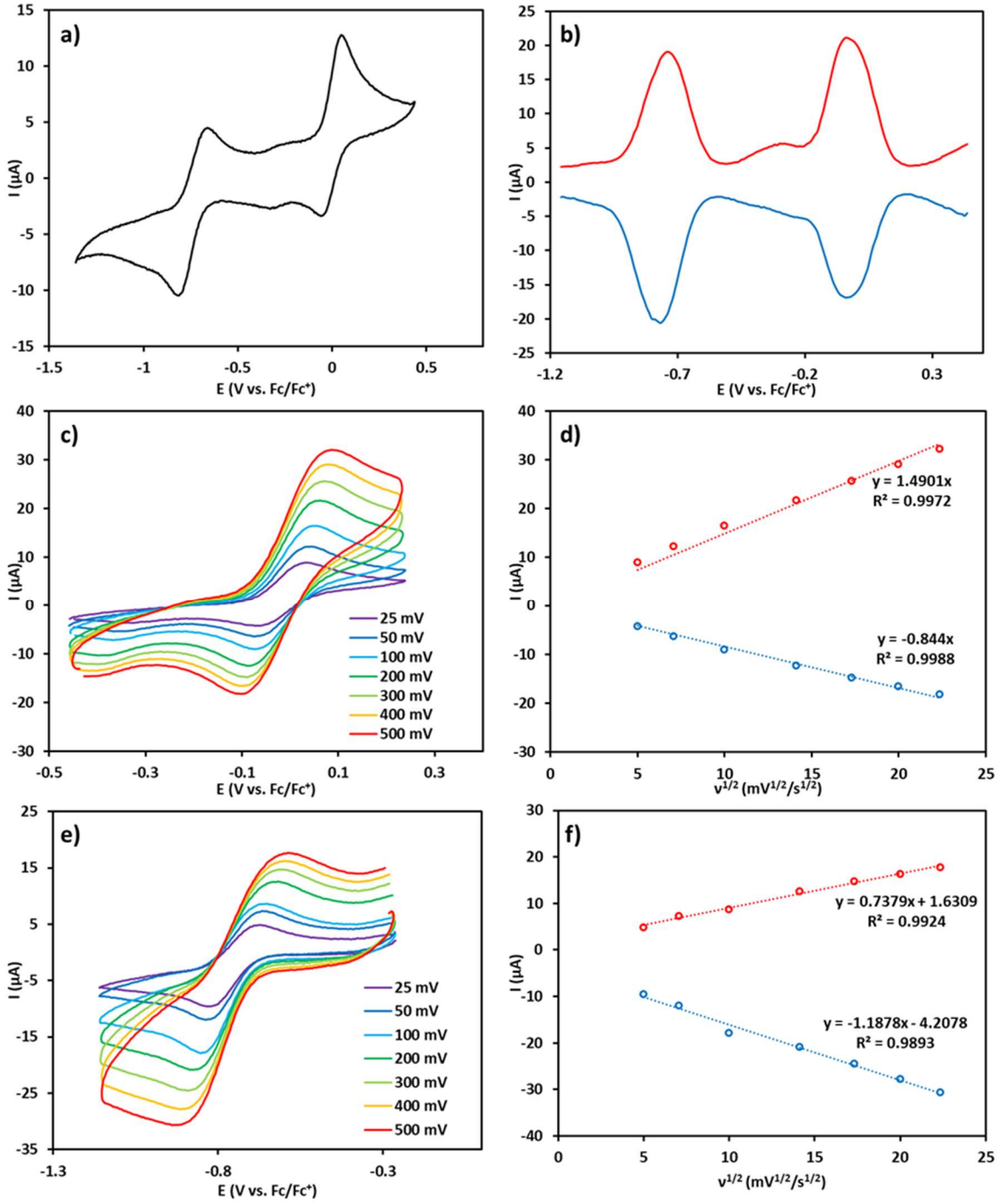

Figure 21. a) CV of **2**. Small impurity at –250 mV vs Fc/Fc^{+}. **b)** SWV of **2**. **c)** $Mn^{III}_2Mn^{IV}_2/Mn^{III}Mn^{IV}_3$ redox couple E = − 10 mV vs. Fc/Fc^{+}. Isolated redox couple measured at various scan rates. **d)** Plot of peak current vs. square root of scan rate. **e)** $Mn^{III}_2Mn^{IV}_2/Mn^{III}_3Mn^{IV}$ redox couple E = – 750 mV vs. Fc/Fc^{+}. Isolated redox couple measured at various scan rates. **f)** Plot of peak current vs. square root of scan rate.

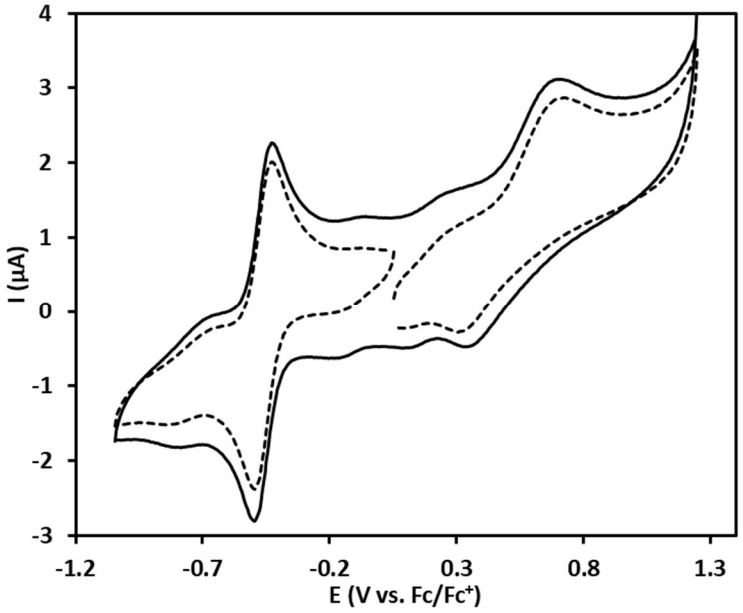

Figure 22. CV of **6**. Isolated $Mn^{III}_2Mn^{IV}_2$/$Mn^{III}Mn^{IV}_3$ and $Mn^{III}Mn^{IV}_3$/Mn^{IV}_4 redox couples shown in dotted lines, with E = – 465 mV and E = +520 mV vs. Fc/Fc^+, respectively.

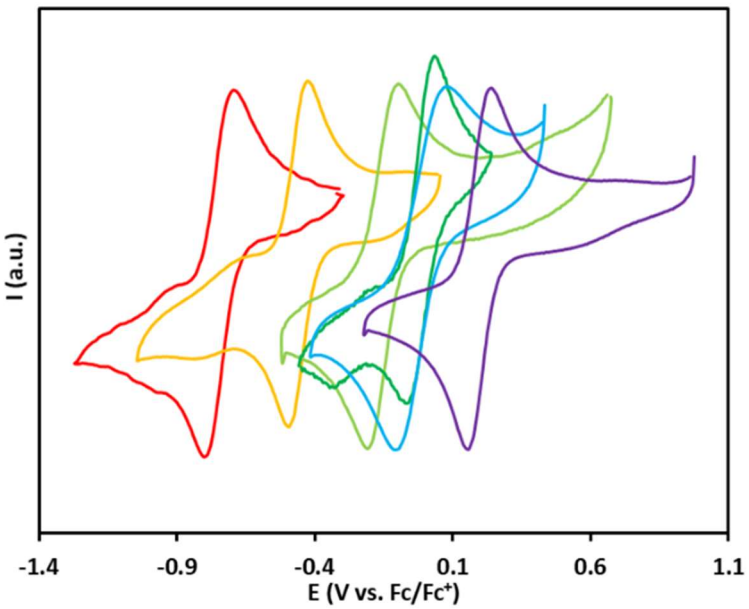

Figure 23. CV of $[Mn_4O_4]$ complexes. Isolated $Mn^{III}_2Mn^{IV}_2$/$Mn^{III}Mn^{IV}_3$ redox couples shown. Red = **3**, yellow = **4**, light green = **1**, green = **2**, blue = $LMn_4O_4(diam)(p\text{-}CF_3C_6H_4CO_2)$, purple = $LMn_4O_4(O_2PPh_2)_3$.[18]

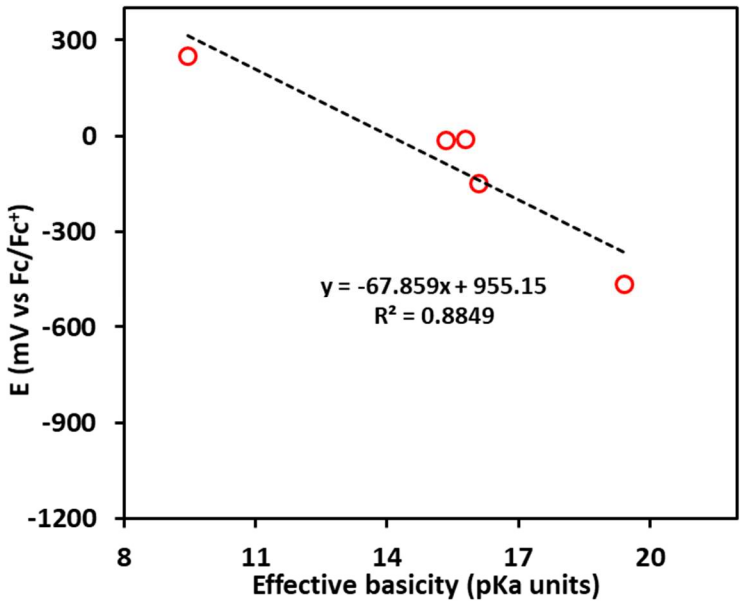

Figure 24. Linear correlation between $Mn^{III}_2Mn^{IV}_2/Mn^{III}Mn^{IV}_3$ redox potential and effective ligand basicity in $[Mn_4O_4]$ complexes **1**, **2**, **4**, $LMn_4O_4(diam)(p\text{-}CF_3C_6H_4CO_2)$, and $LMn_4O_4(OAc)_3$. Values for complexes **1**, **4**, $LMn_4O_4(diam)(p\text{-}CF_3C_6H_4CO_2)$, and $LMn_4O_4(OAc)_3$ are from Ref. 3. Calculated diphenylsilanediol pK_a (11.4) obtained from Ref. 67. Equation used to calculate effective ligand basicity adapted from Refs. 51 and 52.

SQUID magnetometry

Magnetic susceptibility measurements were carried on a Quantum Design MPMS 3 instrument running MPMS Multivu software. Crystalline samples were powdered and suspended in clear plastic straws in polycarbonate capsules. Data were recorded at 0.2 T from 1.8 − 300 K. Diamagnetic corrections (–840 × 10^{-6} cm^3/mol) were made for **3-ox**. Fitting simulations were performed using PHI.[68] Fitting simulations were performed assuming an on-site zero field splitting parameter D(Mn^{IV}) ≈ 0.151 cm^{-1}.

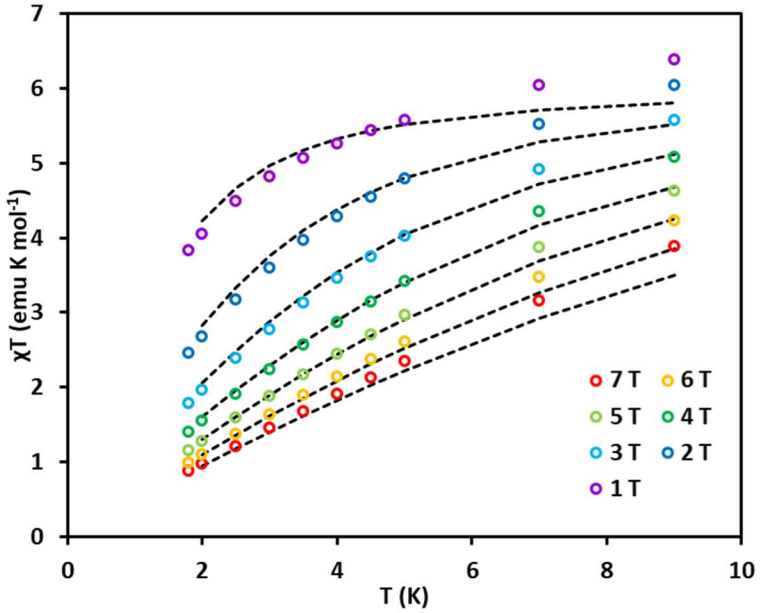

Figure 25. Magnetization data of **3** with fit using the value of $D = 0.151$ cm^{-1} determined by EPR and contributions from intermolecular interactions (mean field model): TIP = $5 \cdot 10^{-4}$ emu mol^{-1}, $zJ = -0.006$ cm^{-1}.

EPR spectroscopy

Samples were prepared as solutions (c.a. 1 mM) in 2-MeTHF unless specified otherwise and rapidly cooled in liquid nitrogen to form a frozen glass. All X-band CW-EPR experiments presented in this study were acquired at the Caltech EPR facility. X-band CW EPR spectra were acquired on a Bruker (Billerica, MA) EMX spectrometer using Bruker Win-EPR software (ver. 3.0). Temperature control was achieved using liquid helium and an Oxford Instruments (Oxford, UK) ESR-900 cryogen flow cryostat and an ITC-503 temperature controller. Data were collected at T = 5 K. Spectra were simulated using EasySpin[69] (release 5.2.33) with Matlab R2020b.

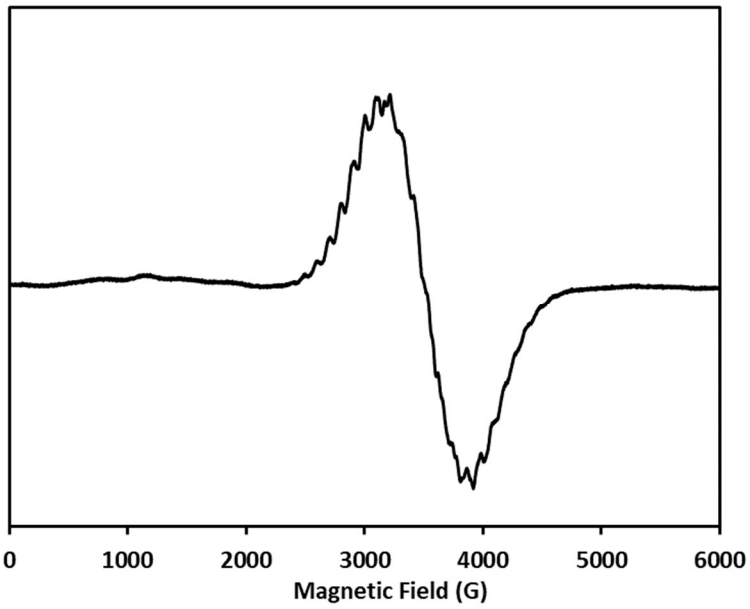

Figure 26. X-band CW-EPR spectra of **3** at 5 K. Data acquisition parameters: frequency = 9.6386 MHz, power = 8 mW, conversion time = 5 ms, modulation amplitude = 4 G.

Data acquisition parameters:
3-ox ($B_0 \perp h\nu$): frequency = 9.6389 MHz, power = 8 mW, conversion time = 5 ms, modulation amplitude = 4 G. T = 5 K.

3-ox ($B_0 \parallel h\nu$): frequency = 9.3881 MHz, power = 8 mW, conversion time = 10 ms, modulation amplitude = 8 G. T = 5 K.

7-ox (B_0 ‖ hν): frequency = 9.3760 MHz, power = 20 mW, conversion time = 82 ms, modulation amplitude = 8 G. T = 5 K.

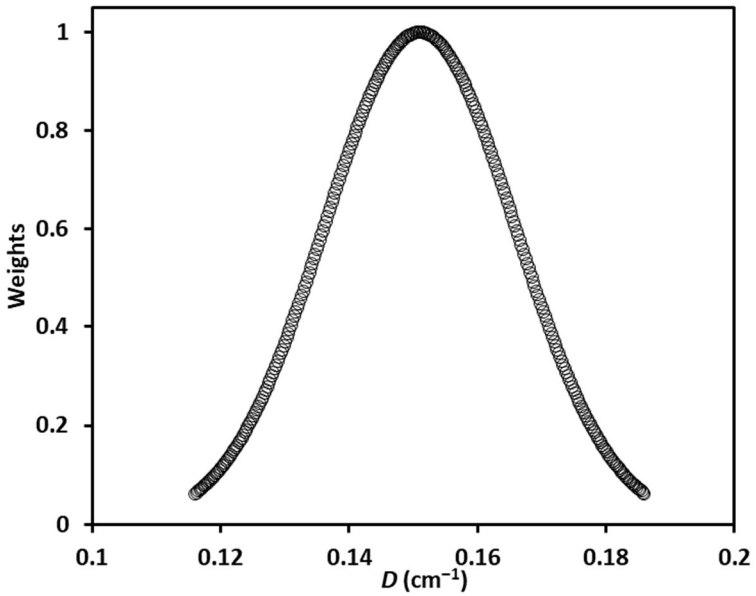

Figure 27. Gaussian distribution of *D* centered at 0.151 used for fitting spectra for **3-ox**. FWHM = 0.035.

UV-Vis spectroscopy

UV-Vis spectra were recorded on a Cary 50 spectrometer.

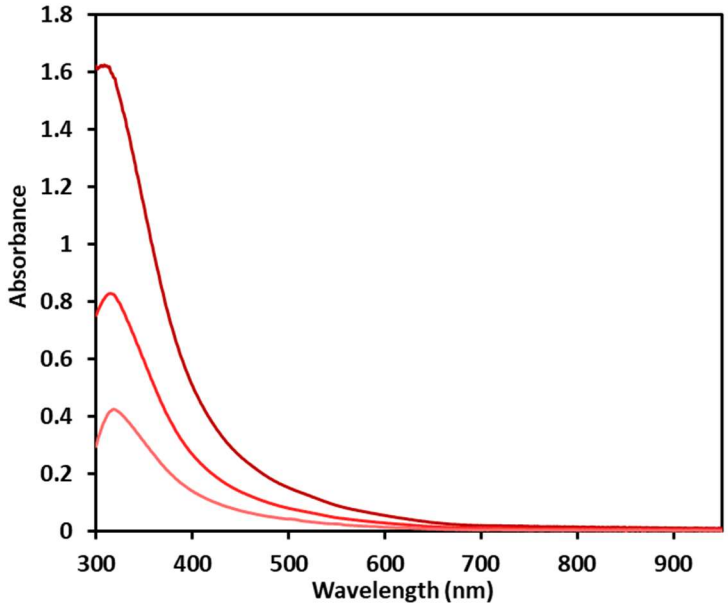

Figure 28. UV-Vis absorbance spectra of **2** (1 cm cuvette; 100, 50, 25 μM) in CH_2Cl_2. ε ($M^{-1} \cdot cm^{-1}$) = 1.64 x 10^4 (315 nm).

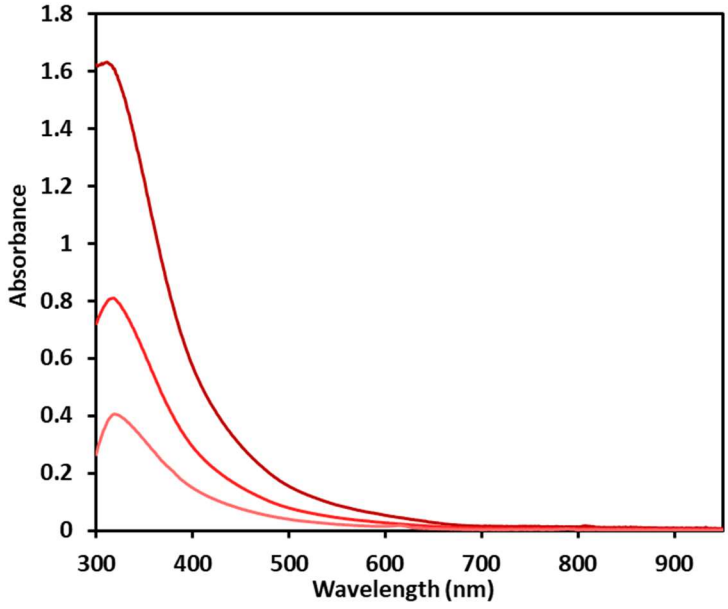

Figure 29. UV-Vis absorbance spectra of **3** (1 cm cuvette; 100, 50, 25 μM) in CH_2Cl_2. ε ($M^{-1} \cdot cm^{-1}$) = 1.60 x 10^4 (321 nm).

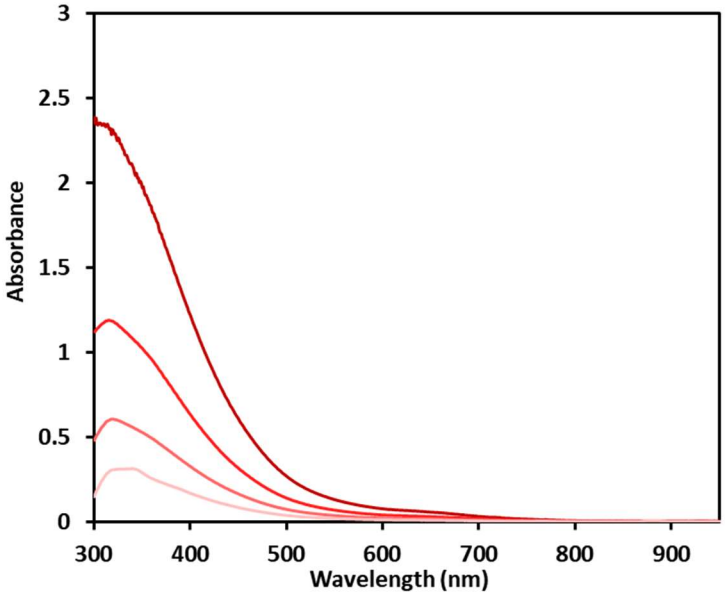

Figure 30. UV-Vis absorbance spectra of **3-ox** (1 cm cuvette; 100, 50, 25, 12.5 μM) in CH_2Cl_2. ε ($M^{-1} \cdot cm^{-1}$) = 2.40 x 10^4 (325 nm).

5.7) References

(1) Yano, J.; Yachandra, V., Mn_4Ca Cluster in Photosynthesis: Where and How Water is Oxidized to Dioxygen. *Chem. Rev.* **2014,** *114* (8), 4175-4205.

(2) Pantazis, D. A., Missing Pieces in the Puzzle of Biological Water Oxidation. *ACS Catalysis* **2018,** *8* (10), 9477-9507.

(3) Cox, N.; Pantazis, D. A.; Lubitz, W., Current Understanding of the Mechanism of Water Oxidation in Photosystem II and Its Relation to XFEL Data. *Annu. Rev. Biochem* **2020,** *89* (1), 795-820.

(4) Shen, J.-R., The Structure of Photosystem II and the Mechanism of Water Oxidation in Photosynthesis. *Annu. Rev. Plant Biol.* **2015,** *66* (1), 23-48.

(5) Cox, N.; Retegan, M.; Neese, F.; Pantazis, D. A.; Boussac, A.; Lubitz, W., Electronic structure of the oxygen-evolving complex in photosystem II prior to O-O bond formation. *Science* **2014,** *345* (6198), 804.

(6) Boussac, A.; Sugiura, M.; Rutherford, A. W.; Dorlet, P., Complete EPR Spectrum of the S_3-State of the Oxygen-Evolving Photosystem II. *J. Am. Chem. Soc.* **2009,** *131* (14), 5050-5051.

(7) Drosou, M.; Pantazis, D. A., Redox Isomerism in the S_3 State of the Oxygen-Evolving Complex Resolved by Coupled Cluster Theory. *Chem. Eur. J.* **2021,** *27* (50), 12815-12825.

(8) Zahariou, G.; Ioannidis, N.; Sanakis, Y.; Pantazis, D. A., Arrested Substrate Binding Resolves Catalytic Intermediates in Higher-Plant Water Oxidation. *Angew. Chem. Int. Ed.* **2021,** *60* (6), 3156-3162.

(9) Miyagawa, K.; Shoji, M.; Isobe, H.; Kawakami, T.; Nakajima, T.; Yamaguchi, K., Relative energies among S_3 intermediates in the photosystem II revealed by DLPNO coupled cluster and hybrid DFT calculations. Possible pathways of water insertion in the S_2 to S_3 transition. *Chem. Phys. Lett.* **2022,** *793*, 139439.

(10) Young, K. J.; Brennan, B. J.; Tagore, R.; Brudvig, G. W., Photosynthetic Water Oxidation: Insights from Manganese Model Chemistry. *Acc. Chem. Res.* **2015,** *48* (3), 567-574.

(11) Blakemore, J. D.; Crabtree, R. H.; Brudvig, G. W., Molecular Catalysts for Water Oxidation. *Chem. Rev.* **2015,** *115* (23), 12974-13005.

(12) Mukherjee, S.; Stull, J. A.; Yano, J.; Stamatatos, T. C.; Pringouri, K.; Stich, T. A.; Abboud, K. A.; Britt, R. D.; Yachandra, V. K.; Christou, G., Synthetic model of the asymmetric $[Mn_3CaO_4]$ cubane core of the oxygen-evolving complex of photosystem II. *Proc. Natl. Acad. Sci. U. S. A.* **2012,** *109* (7), 2257.

(13) Kanady, J. S.; Tran, R.; Stull, J. A.; Lu, L.; Stich, T. A.; Day, M. W.; Yano, J.; Britt, R. D.; Agapie, T., Role of oxido incorporation and ligand lability in expanding redox accessibility of structurally related Mn_4 clusters. *Chem. Sci.* **2013,** *4* (10), 3986-3996.

(14) Tsui, E. Y.; Kanady, J. S.; Agapie, T., Synthetic Cluster Models of Biological and Heterogeneous Manganese Catalysts for O_2 Evolution. *Inorg. Chem.* **2013,** *52* (24), 13833-13848.

(15) Kanady, J. S.; Lin, P.-H.; Carsch, K. M.; Nielsen, R. J.; Takase, M. K.; Goddard, W. A.; Agapie, T., Toward Models for the Full Oxygen-Evolving Complex of Photosystem II by Ligand Coordination To Lower the Symmetry of the Mn_3CaO_4

Cubane: Demonstration That Electronic Effects Facilitate Binding of a Fifth Metal. *J. Am. Chem. Soc.* **2014,** *136* (41), 14373-14376.

(16) Lee, H. B.; Shiau, A. A.; Marchiori, D. A.; Oyala, P. H.; Yoo, B.-K.; Kaiser, J. T.; Rees, D. C.; Britt, R. D.; Agapie, T., $CaMn_3^{IV}O_4$ Cubane Models of the Oxygen-Evolving Complex: Spin Ground States S<9/2 and the Effect of Oxo Protonation. *Angew. Chem. Int. Ed.* **2021,** *60* (32), 17671-17679.

(17) Lee, H. B.; Marchiori, D. A.; Chatterjee, R.; Oyala, P. H.; Yano, J.; Britt, R. D.; Agapie, T., S = 3 Ground State for a Tetranuclear $Mn^{IV4}O_4$ Complex Mimicking the S_3 State of the Oxygen-Evolving Complex. *J. Am. Chem. Soc.* **2020,** *142* (8), 3753-3761.

(18) Lee, H. B.; Shiau, A. A.; Oyala, P. H.; Marchiori, D. A.; Gul, S.; Chatterjee, R.; Yano, J.; Britt, R. D.; Agapie, T., Tetranuclear $[Mn^{III}Mn_3^{IV}O_4]$ Complexes as Spectroscopic Models of the S_2 State of the Oxygen Evolving Complex in Photosystem II. *J. Am. Chem. Soc.* **2018,** *140* (49), 17175-17187.

(19) Ruettinger, W. F.; Campana, C.; Dismukes, G. C., Synthesis and Characterization of $Mn_4O_4L_6$ Complexes with Cubane-like Core Structure: A New Class of Models of the Active Site of the Photosynthetic Water Oxidase. *J. Am. Chem. Soc.* **1997,** *119* (28), 6670-6671.

(20) Ruettinger, W. F.; Ho, D. M.; Dismukes, G. C., Protonation and Dehydration Reactions of the $Mn_4O_4L_6$ Cubane and Synthesis and Crystal Structure of the Oxidized Cubane $[Mn_4O_4L_6]^+$: A Model for the Photosynthetic Water Oxidizing Complex. *Inorg. Chem.* **1999,** *38* (6), 1036-1037.

(21) Zhang, C.; Chen, C.; Dong, H.; Shen, J.-R.; Dau, H.; Zhao, J., A synthetic Mn_4Ca-cluster mimicking the oxygen-evolving center of photosynthesis. *Science* **2015,** *348* (6235), 690.

(22) Yao, R.; Li, Y.; Chen, Y.; Xu, B.; Chen, C.; Zhang, C., Rare-Earth Elements Can Structurally and Energetically Replace the Calcium in a Synthetic Mn_4CaO_4-Cluster Mimicking the Oxygen-Evolving Center in Photosynthesis. *J. Am. Chem. Soc.* **2021,** *143* (42), 17360-17365.

(23) Vaddypally, S.; Kondaveeti, S. K.; Karki, S.; Van Vliet, M. M.; Levis, R. J.; Zdilla, M. J., Reactive Pendant Mn═O in a Synthetic Structural Model of a Proposed S_4 State in the Photosynthetic Oxygen Evolving Complex. *J. Am. Chem. Soc.* **2017,** *139* (13), 4675-4681.

(24) Nguyen, A. I.; Darago, L. E.; Balcells, D.; Tilley, T. D., Influence of a "Dangling" Co(II) Ion Bound to a [MnCo3O4] Oxo Cubane. *J. Am. Chem. Soc.* **2018,** *140* (29), 9030-9033.

(25) Philouze, C.; Blondin, G.; Girerd, J.-J.; Guilhem, J.; Pascard, C.; Lexa, D., Aqueous Chemistry of High-Valent Manganese. Structure, Magnetic, and Redox Properties of a New Type of Mn-Oxo Cluster, $[Mn_4^{IV}O_4(bpy)_6]^{4+}$: Relevance to the Oxygen Evolving Center in Plants. *J. Am. Chem. Soc.* **1994,** *116* (19), 8557-8565.

(26) Chen; Collomb, M.-N.; Duboc, C.; Blondin, G.; Rivière, E.; Faller, J. W.; Crabtree, R. H.; Brudvig, G. W., New Linear High-Valent Tetranuclear Manganese-Oxo Cluster Relevant to the Oxygen-Evolving Complex of Photosystem II with Oxo, Hydroxo, and Aqua Coordinated to a Single Mn(IV). *Inorg. Chem.* **2005,** *44* (25), 9567-9573.

(27) Chen, H.; Faller, J. W.; Crabtree, R. H.; Brudvig, G. W., Dimer-of-Dimers Model for the Oxygen-Evolving Complex of Photosystem II. Synthesis and Properties of $[Mn^{IV4}O_5(terpy)_4(H_2O)_2](ClO_4)_6$. *J. Am. Chem. Soc.* **2004,** *126* (23), 7345-7349.

(28) Dubé, C. E.; Mukhopadhyay, S.; Bonitatebus, P. J.; Staples, R. J.; Armstrong, W. H., Tuning Tetranuclear Manganese−Oxo Core Electronic Properties: Adamantane-Shaped Complexes Synthesized by Ligand Exchange. *Inorg. Chem.* **2005,** *44* (14), 5161-5175.

(29) Mukhopadhyay, S.; Staples, R. J.; Armstrong, W. H., Toward synthetic models for high oxidation state forms of the Photosystem II active site metal cluster: the first tetranuclear manganese cluster containing a $[Mn_4(\mu\text{-}O)_5]^{6+}$ core. *Chem. Commun.* **2002,** (8), 864-865.

(30) Dubé, C. E.; Wright, D. W.; Pal, S.; Bonitatebus, P. J.; Armstrong, W. H., Tetranuclear Manganese-Oxo Aggregates Relevant to the Photosynthetic Water Oxidation Center. Crystal Structure, Spectroscopic Properties and Reactivity of Adamantane-Shaped $[Mn_4O_6(bpea)_4]^{4+}$ and the Reduced Mixed-Valence Analog $[Mn_4O_6(bpea)_4]^{3+}$. *J. Am. Chem. Soc.* **1998,** *120* (15), 3704-3716.

(31) Hagen, K. S.; Westmoreland, T. D.; Scott, M. J.; Armstrong, W. H., Structural and electronic consequences of protonation in $\{Mn_4O_6\}^{4+}$ cores: pH dependent properties of oxo-bridged manganese complexes. *J. Am. Chem. Soc.* **1989,** *111* (5), 1907-1909.

(32) Krempner, C., Role of Siloxides in Transition Metal Chemistry and Homogeneous Catalysis. *Eur. J. Inorg. Chem.* **2011,** *2011* (11), 1689-1698.

(33) Camp, C.; Pécaut, J.; Mazzanti, M., Tuning Uranium–Nitrogen Multiple Bond Formation with Ancillary Siloxide Ligands. *J. Am. Chem. Soc.* **2013,** *135* (32), 12101-12111.

(34) Friedrich, J.; Qiao, Y.; Maichle-Mössmer, C.; Schelter, E. J.; Anwander, R., Redox-enhanced hemilability of a tris(tert-butoxy)siloxy ligand at cerium. *Dalton Trans.* **2018,** *47* (30), 10113-10123.

(35) Palumbo, C. T.; Zivkovic, I.; Scopelliti, R.; Mazzanti, M., Molecular Complex of Tb in the +4 Oxidation State. *J. Am. Chem. Soc.* **2019,** *141* (25), 9827-9831.

(36) Willauer, A. R.; Palumbo, C. T.; Scopelliti, R.; Zivkovic, I.; Douair, I.; Maron, L.; Mazzanti, M., Stabilization of the Oxidation State +IV in Siloxide-Supported Terbium Compounds. *Angew. Chem. Int. Ed.* **2020,** *59* (9), 3549-3553.

(37) Hirneise, L.; Langmann, J.; Zitzer, G.; Ude, L.; Maichle-Mössmer, C.; Scherer, W.; Speiser, B.; Anwander, R., Tuning Organocerium Electrochemical Potentials by Extending Tris(cyclopentadienyl) Scaffolds with Terminal Halogenido, Siloxy, and Alkoxy Ligands. *Organometallics* **2021,** *40* (11), 1786-1800.

(38) Gau, M. R.; Zdilla, M. J., Multinuclear Clusters of Manganese and Lithium with Silsesquioxane-Derived Ligands: Synthesis and Ligand Rearrangement by Dioxygen- and Base-Mediated Si–O Bond Cleavage. *Inorg. Chem.* **2021,** *60* (5), 2866-2871.

(39) Lorenz, V.; Blaurock, S.; Edelmann, F. T., The First Heterobimetallic Metallasilsesquioxane Derivatives of Manganese. *Z. Anorg. Allg. Chem.* **2008,** *634*, 2819-2824.

(40) Riollet, V.; Quadrelli, E. A.; Copéret, C.; Basset, J.-M.; Andersen, R. A.; Köhler, K.; Böttcher, R.-M.; Herdtweck, E., Grafting of $[Mn(CH_2{}^tBu)_2(tmeda)]$ on Silica

and Comparison with Its Reaction with a Silsesquioxane. *Chem. Eur. J.* **2005,** *11* (24), 7358-7365.

(41) King, L.; Sullivan, A. C., Main group and transition metal compounds with silanediolate $[R_2SiO_2]^{2-}$ and α,ω-siloxane diolate $[O(R_2SiO)_n]^{2-}$ ligands. *Coord. Chem. Rev.* **1999,** *189* (1), 19-57.

(42) Gosink, H.-J.; Roesky, H. W.; Schmidt, H.-G.; Noltemeyer, M.; Irmer, E.; Herbst-Irmer, R., Synthesis and Structures of Cyclic and Acyclic Metallasiloxanes of Groups 5-7. *Organometallics* **1994,** *13* (9), 3420-3426.

(43) Carbó, J. J.; González-del Moral, O.; Martín, A.; Mena, M.; Poblet, J.-M.; Santamaría, C., Construction of Titanasiloxanes by Incorporation of Silanols to the Metal Oxide Model $[\{Ti(\eta^5\text{-}C_5Me_5)(\mu\text{-}O)\}_3(\mu_3\text{-}CR)]$: DFT Elucidation of the Reaction Mechanism. *Chem. Eur. J.* **2008,** *14* (26), 7930-7938.

(44) D'Alfonso, G.; Formaggio, V.; Roberto, D.; Ugo, R.; Lucenti, E.; Carlucci, L., Surface Organometallic Chemistry: Synthesis and X-ray Characterization of Novel Silanolate Surface Models $[Re_2(CO)_8(\mu\text{-}H)(\mu\text{-}OSiR_2R')]$ and of the First Models with Two Homo and Hetero Metal Carbonyl Fragments Linked to Vicinal or Geminal Silanols. *Organometallics* **2003,** *22* (16), 3271-3278.

(45) Beckmann, J.; Jurkschat, K.; Pieper, N.; Schürmann, M., The first organoelement oxides containing three different metals; synthesis and structure of (Ph_2SiOR_2SnOMO) [R = $(CH_2)_3NMe_2$; M = But_2Sn, But_2Ge, PhB]† ‡. *Chem. Commun.* **1999,** (12), 1095-1096.

(46) Kishore, P. V. V. N.; Baskar, V., Hexa- and Trinuclear Organoantimony Oxo Clusters Stabilized by Organosilanols. *Inorg. Chem.* **2014,** *53* (13), 6737-6742.

(47) Prabhu, M. S. R.; Jami, A. K.; Baskar, V., Organoantimony(V) Oxido Cubane Cluster $[(p\text{-}X\text{-}C_6H_4Sb)_4(O)_4(Ph_2SiO_2)_4]$ (X = Cl, Br) Stabilized by Diphenyldisiloxides. *Organometallics* **2009,** *28* (13), 3953-3956.

(48) Pusztai, E.; Albright, H.; Cai, Y.; Hu, R.; West, R.; Tang, B. Z.; Guzei, I. A., Synthesis and Photophysical Properties of Two Strongly Fluorescent Bis(diquinaldinatoalumino)-9-silafluorenes. *Organometallics* **2013,** *32* (23), 6871-6874.

(49) Fandos, R.; Otero, A.; Rodríguez, A.; Ruiz, M. J.; Terreros, P., Molecular Models of Titania–Silica Systems and a Late Transition Metal Complex Grafted Thereon. *Angew. Chem. Int. Ed.* **2001,** *40* (15), 2884-2887.

(50) Marciniec, B.; Maciejewski, H., Transition metal-siloxide complexes; synthesis, structure and application to catalysis. *Coord. Chem. Rev.* **2001,** *223* (1), 301-335.

(51) Lee, H. B.; Agapie, T., Redox Tuning via Ligand-Induced Geometric Distortions at a YMn_3O_4 Cubane Model of the Biological Oxygen Evolving Complex. *Inorg. Chem.* **2019,** *58* (22), 14998-15003.

(52) Nguyen, A. I.; Wang, J.; Levine, D. S.; Ziegler, M. S.; Tilley, T. D., Synthetic control and empirical prediction of redox potentials for Co_4O_4 cubanes over a 1.4 V range: implications for catalyst design and evaluation of high-valent intermediates in water oxidation. *Chem. Sci.* **2017,** *8* (6), 4274-4284.

(53) Amtawong, J.; Balcells, D.; Wilcoxen, J.; Handford, R. C.; Biggins, N.; Nguyen, A. I.; Britt, R. D.; Tilley, T. D., Isolation and Study of Ruthenium–Cobalt Oxo Cubanes Bearing a High-Valent, Terminal Ru^V–Oxo with Significant Oxyl Radical Character. *J. Am. Chem. Soc.* **2019,** *141* (50), 19859-19869.

(54) Amtawong, J.; Skjelstad, B. B.; Handford, R. C.; Suslick, B. A.; Balcells, D.; Tilley, T. D., C–H Activation by $RuCo_3O_4$ Oxo Cubanes: Effects of Oxyl Radical Character and Metal–Metal Cooperativity. *J. Am. Chem. Soc.* **2021,** *143* (31), 12108-12119.

(55) Amtawong, J.; Nguyen, A. I.; Tilley, T. D., Mechanistic Aspects of Cobalt–Oxo Cubane Clusters in Oxidation Chemistry. *J. Am. Chem. Soc.* **2022,** *144* (4), 1475-1492.

(56) Klauss, A.; Haumann, M.; Dau, H., Alternating electron and proton transfer steps in photosynthetic water oxidation. *Proc. Natl. Acad. Sci. U. S. A.* **2012,** *109* (40), 16035-16040.

(57) Connelly, N. G.; Geiger, W. E., Chemical Redox Agents for Organometallic Chemistry. *Chem. Rev.* **1996,** *96* (2), 877-910.

(58) Chrysina, M.; Heyno, E.; Kutin, Y.; Reus, M.; Nilsson, H.; Nowaczyk Marc, M.; DeBeer, S.; Neese, F.; Messinger, J.; Lubitz, W.; Cox, N., Five-coordinate Mn^{IV} intermediate in the activation of nature's water splitting cofactor. *Proc. Natl. Acad. Sci. U. S. A.* **2019,** *116* (34), 16841-16846.

(59) Marchiori, D. A.; Debus, R. J.; Britt, R. D., Pulse EPR Spectroscopic Characterization of the S_3 State of the Oxygen-Evolving Complex of Photosystem II Isolated from Synechocystis. *Biochemistry* **2020,** *59* (51), 4864-4872.

(60) Cox, N.; Rapatskiy, L.; Su, J.-H.; Pantazis, D. A.; Sugiura, M.; Kulik, L.; Dorlet, P.; Rutherford, A. W.; Neese, F.; Boussac, A.; Lubitz, W.; Messinger, J., Effect of Ca^{2+}/Sr^{2+} Substitution on the Electronic Structure of the Oxygen-Evolving Complex of Photosystem II: A Combined Multifrequency EPR, ^{55}Mn-ENDOR, and DFT Study of the S_2 State. *J. Am. Chem. Soc.* **2011,** *133* (10), 3635-3648.

(61) Zheng, M.; Khangulov, S. V.; Dismukes, G. C.; Barynin, V. V., Electronic structure of dimanganese(II,III) and dimanganese(III,IV) complexes and dimanganese catalase enzyme: a general EPR spectral simulation approach. *Inorg. Chem.* **1994,** *33* (2), 382-387.

(62) Duboc, C.; Collomb, M.-N., Multifrequency high-field EPR investigation of a mononuclear manganese(IV) complex. *Chem. Commun.* **2009,** (19), 2715-2717.

(63) Dolai, M.; Amjad, A.; Debnath, M.; Tol, J. v.; Barco, E. d.; Ali, M., Water-Stable Manganese(IV) Complex of a N_2O_4-Donor Non-Schiff-Base Ligand: Synthesis, Structure, and Multifrequency High-Field Electron Paramagnetic Resonance Studies. *Inorg. Chem.* **2014,** *53* (11), 5423-5428.

(64) Leto, D. F.; Massie, A. A.; Colmer, H. E.; Jackson, T. A., X-Band Electron Paramagnetic Resonance Comparison of Mononuclear Mn^{IV}-oxo and Mn^{IV}-hydroxo Complexes and Quantum Chemical Investigation of Mn^{IV} Zero-Field Splitting. *Inorg. Chem.* **2016,** *55* (7), 3272-3282.

(65) Zlatar, M.; Gruden, M.; Vassilyeva, O. Y.; Buvaylo, E. A.; Ponomarev, A. N.; Zvyagin, S. A.; Wosnitza, J.; Krzystek, J.; Garcia-Fernandez, P.; Duboc, C., Origin of the Zero-Field Splitting in Mononuclear Octahedral Mn^{IV} Complexes: A Combined Experimental and Theoretical Investigation. *Inorg. Chem.* **2016,** *55* (3), 1192-1201.

(66) Zadrozny, J. M.; Telser, J.; Long, J. R., Slow magnetic relaxation in the tetrahedral cobalt(II) complexes $[Co(EPh)_4]^{2-}$ (EO, S, Se). *Polyhedron* **2013,** *64*, 209-217.

(67) Tran, N. T.; Wilson, S. O.; Franz, A. K., Cooperative Hydrogen-Bonding Effects in Silanediol Catalysis. *Org. Lett.*, **2012**, *14*, 186.

(68) Chilton, N. F.; Anderson, R. P.; Turner, L. D.; Soncini, A.; Murray, K. S., PHI: A powerful new program for the analysis of anisotropic monomeric and exchange-coupled polynuclear d - and f -block complexes. *Journal of Computational Chemistry*, **2013**, *34*, 1164.
(69) Stoll, S.; Schweiger, A., EasySpin, a comprehensive software package for spectral simulation and analysis in EPR. *Journal of Magnetic Resonance*, **2006**, *178*, 42.

APPENDIX 1

EPR Spectroscopic Characterization of $Mn^{III}Mn^{IV}_3O_4$ Model Complexes Bound to Biologically Relevant Substrates

Abstract

Mechanistic details of the Oxygen Evolving Complex (OEC) of Photosystem II (PSII) have been studied through a combination of biochemical, structural, spectroscopic, and computational methods. EPR spectroscopic characterization of intermediates with isotopically labeled biologically relevant molecules such as water, methanol, and ammonia have contributed to understanding the key aspects of the mechanism of the OEC. Analogous benchmarking studies for synthetic model complexes are rare due to synthetic challenges in accessing and stabilizing complexes bound to these substrate molecules. Herein, we report the reactivity of a $Mn^{III}Mn^{IV}_3O_4$ synthetic complex with water, hydroxide, ammonia, methanol, and methoxide and the EPR characterization of these species.

A1.1) Introduction

The Oxygen Evolving Complex (OEC) of Photosystem II (PSII) is nature's catalyst for water oxidation, consisting of a unique pentametallic $CaMn_4O_5$ cluster core which is proposed to undergo structural changes throughout the catalytic cycle.[1-7] The S_0 – S_3 intermediates have been subjects of extensive biochemical, structural, spectroscopic, and computational studies, with conclusions and results from these studies heavily influencing mechanistic proposals for the O–O bond forming step in the elusive S_4 state.[8-14] One critical question that remains debated is the site of substrate-water binding to the $CaMn_4$ cluster of the OEC,[15-16] complicated by the situation in which the substrate is also the solvent. Based on previous FTIR spectroscopy, mass spectrometry, and W-band ^{17}O EPR studies, several classes of solvent exchangeable oxygen nuclei have been observed and proposed as possible substrate binding sites (Figure 1).[17-20] In addition, biochemical studies utilizing small molecule analogues of water such as ammonia have greatly aided mechanistic interpretations by narrowing down possible substrate-water binding sites.[8-9, 11] Notably, chemical treatments with small molecules such as amines, alcohols, and halides affect the equilibrium between high-spin (HS) and low-spin (LS) signals of the S_2 state and influence progression to higher S_n states.

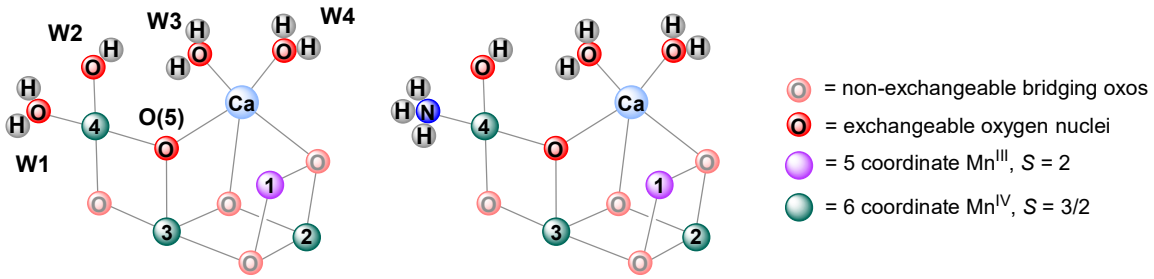

Figure 1. Proposed structure of the OEC in the S_2 state highlighting positions of proposed fast, solvent exchangeable oxygen nuclei (left): terminal Mn and Ca bound aquo or hydroxo moieties labelled W1 – W4 and bridging μ^3-O(5). Ammonia proposed to bind terminally to dangler Mn^{IV} (right).

In particular, ammonia has been studied as a substrate analogue because pf opportunities in probing specific nuclei (i.e., ^{14}N and ^{15}N) distinguishable from water. Ammonia has been demonstrated to be a non-competitive inhibitor which can also alter the multiline signal in the S_2 state.[9, 11] As determination of the ammonia binding site can rule out a potential substrate-water binding site, it is important to consider two competing proposals. Kinetic studies have been interpreted to favor the assignment of the ammonia derived ligand as a bridging nitrido ligand in place of O5,[21-22] while pulse EPR studies on ^{14}N and ^{15}N ammonia treated PSII from *Synechocystis* suggest terminal ammonia bound to the dangler Mn^{IV} (Figure 1).[8-9]

Methanol and other primary alcohols are also known to alter the S_2 state, favoring the population of the LS signal.[23-25] On the basis of multifrequency EPR and ENDOR spectroscopic analysis of ^{13}C-labeled methanol binding to the OEC and comparisons to methanol binding to a synthetic $Mn^{III}Mn^{IV}$ dimeric complex,[10] it was concluded that methanol likely does not bind to Mn in the S_2 state. Instead, it is proposed that methanol can be ligated to Ca by replacing W3 or is within the vicinity of the $CaMn_4$ core and affects the HS-LS equilibrium of the S_2 state via hydrogen bonding interactions.

Systematic studies on the effects of these specific substrate ligands on the spectroscopy of synthetic tetranuclear Mn_4 complexes are rare for several reasons. First, many multimetallic model complexes are synthesized via self-assembly methods, limiting the degree of synthetic control over aspects such as cluster geometry and ligand environment.[26-30] Secondly, reactivity with substrate molecules often requires accessible open coordination sites on Mn (or Ca). Multimetallic Mn complexes typically contain *pseudo*-octahedral Mn centers, with only a few rare examples containing a five-coordinate

Mn.[26, 31-32] Creating open coordination sites in a controlled fashion via ligand removal in complexes prepared by self-assembly methods is also difficult, as these methods tend to favor generation of homoleptic or high-symmetry complexes.

Recently, we have reported the synthesis and characterization of a site differentiated $Mn^{III}Mn^{IV}_3O_4$ complex (**1**) containing one five-coordinate Mn. This coordination number change was demonstrated to have significant effect on the ground spin state of this family of tetranuclear Mn-oxo clusters. It is hypothesized that this complex can serve as a precursor in reactivity with biologically relevant small molecules due to the presence of an open coordination site on Mn. Herein, the reactivity of complex **1** with water, hydroxide, ammonia, methanol, methoxide, alkylhydrogenperoxide, and hydrogen peroxide is explored and monitored by EPR spectroscopy.

A1.2) Water and Hydroxide

As previously demonstrated, addition of excess water (~80 equivalents) to **1** results in the conversion of the HS species to a new LS species. Following loss of silanol in a protonolysis reaction, $[LMn^{III}Mn^{IV}_3O_4(diam^{Mes})(OH_x)(OH_y)]^+$ (**1-H_2O-OH**) was isolated (Figure 2). Though the lower quality of these crystals does not allow for unambiguous assignment of protonation state of the water-derived ligands, Mn−O bond lengths suggest a Mn^{IV}–OH and Mn^{III}–OH_2 assignment. ^{2}H Mims ENDOR spectra of complex **1** show only one resolved class of deuterium atoms. In the context of the interplay between Mn oxidation state and substrate protonation state in the OEC, we targeted complexes with only one water-derived ligand in efforts to minimize ambiguity. In attempts to isolate the water-bound species without protonolysis of the siloxide moiety, crystals of **1** were subjected to water vapor for at least 48 hours, resulting in a single crystal to single crystal conversion to a water-

bound species (O-atom partial occupancy).[33] Due to the thin nature of the plate-like crystals and crystal cracking from unit cell changes, the quality of the XRD data is low, only allowing for confirmation of connectivity (Figure 3).

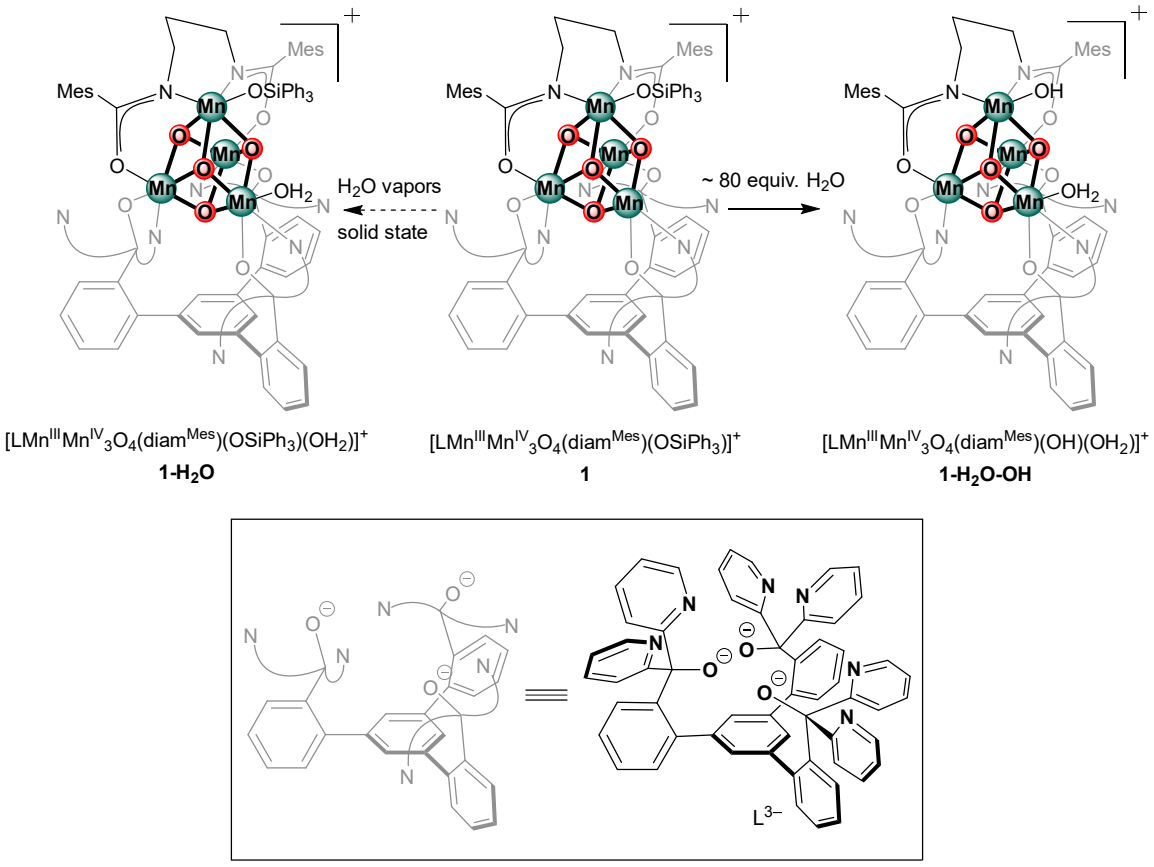

Figure 2. Solution-state versus solid-state reactivity of **1** with water.

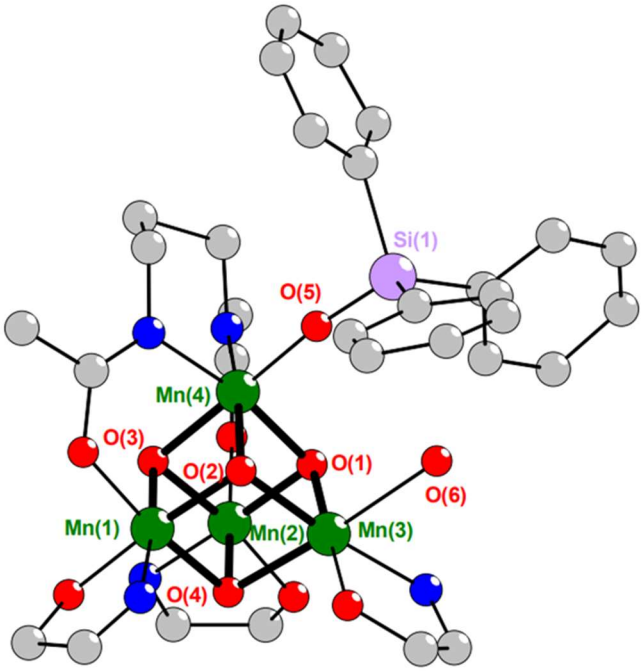

Figure 3. Truncated crystal structure of reaction product (**1-H_2O**) from subjecting crystals of **1** to water vapor for 48 hours. Occupancy of O(6) is ~30%. Due to low quality dataset, atoms depicted as ball-and-stick model. Mn (green), Si (light purple), O (red), N (blue), C (gray).

Addition of hydroxide to **1** was also investigated and monitored by EPR spectroscopy. Titration of different equivalents (0 – 1) of TBAOH (1 M in MeOH) (TBA = tetrabutylammonium) shows near stoichiometric conversion of **1** to a putative hydroxide bound species (Figure 4). Utilizing a 1:1 mixture of DBU: H_2O in THF (DBU = 1,8-diazabicyclo[5.4.0]undec-7-ene) (Figure 5), consumption of the HS complex **1** is also observed. Notably, it is hypothesized MeOH can also bind to the cluster, discussed *vide infra*. A control experiment with the addition of DBU to **1** in the absence of methanol and water does not result in significant reactivity with **1** (Figure 5). However, it is noted

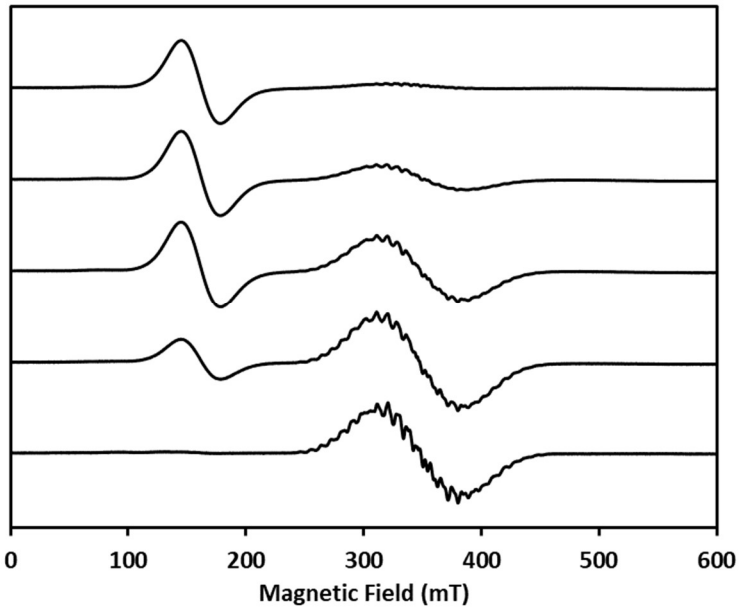

Figure 4. Addition of varying equivalents (from the top: 0, 0.13, 0.25, 0.5, 1 equivalents), of TBAOH (1 M in MeOH) to **1**, collected at T = 5 K. Acquisition parameters: frequency = 9.64 MHz, power = 8.8 mW, conversion time = 10 ms, and modulation amplitude = 8 G.

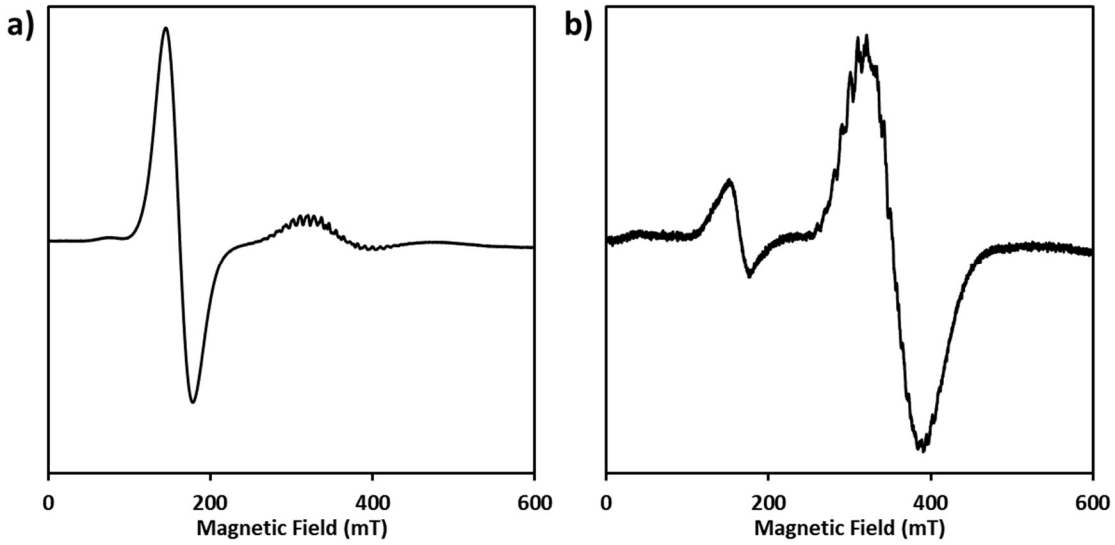

Figure 5. (a) Addition of DBU (1 equiv) to **1**. **(b)** Addition of 1 equivalent of a 1:1 DBU:H_2O mixture to **1**. Acquisition parameters: frequency = 9.64 MHz, power = 8.8 mW, conversion time = 10 ms, and modulation amplitude = 8 G.

Stoichiometric addition of H_2O to benzyl potassium results in the formation of an anhydrous suspension of KOH. Addition of 2 equivalents of this mixture to complex **1** results in near complete conversion of **1** to a new low-spin species, as monitored by EPR spectroscopy (Figure 7). Temperature dependence studies were also performed in the temperature range of T = 5 – 20 K (Figure 8), suggesting an accessible higher spin excited state. Analogous preparations of the hydroxide mixture utilizing $^{2}H_2O$ and $^{17}OH_2$ were performed and labelled samples of the putative hydroxide species were prepared. No significant differences of the hyperfine features in the CW-spectrum were observed in the labelled samples (Figure 9), and pulse-EPR studies are underway to confirm the binding of a hydroxide moiety to the Mn_4O_4 unit. Further characterization and attempts to isolate the product are also underway.

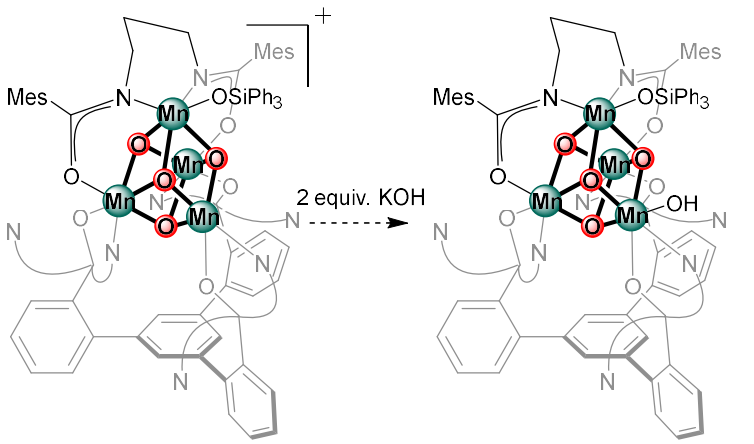

Figure 6. Proposed product of reaction between **1** and 2 equivalents of KOH, generated from KBn and H_2O.

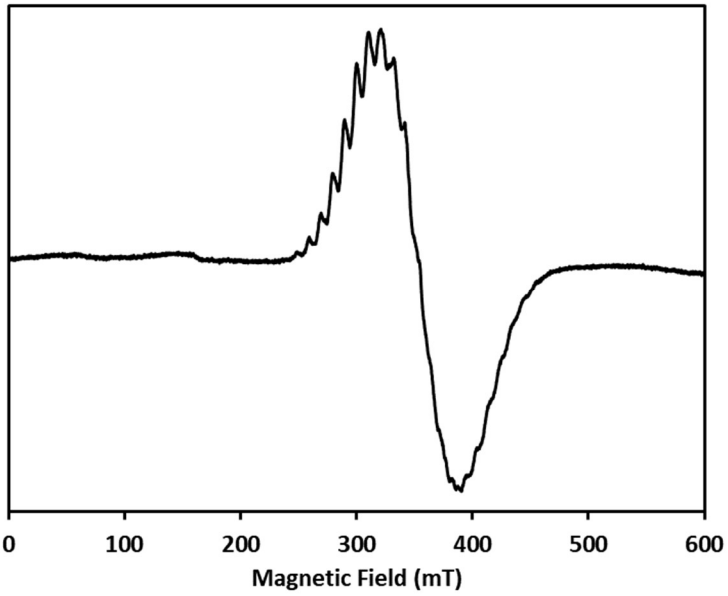

Figure 7. Addition of 2 equivalents of KOH to **1** in 1:1 2-MeTHF:CH_2Cl_2. Acquisition parameters: frequency = 9.64 MHz, power = 8.7 mW, conversion time = 10 ms, and modulation amplitude = 8 G.

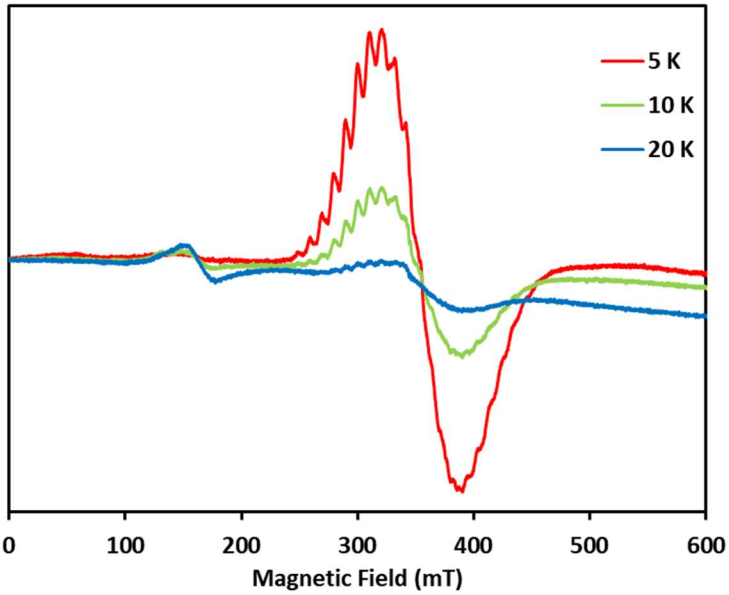

Figure 8. Temperature dependence studies (T = 5, 10, 20 K) on the addition of 2 equivalents of KOH to **1** in 1:1 2-MeTHF:CH_2Cl_2. Acquisition parameters: frequency = 9.64 MHz, power = 8.7 mW, conversion time = 10 ms, and modulation amplitude = 8 G.

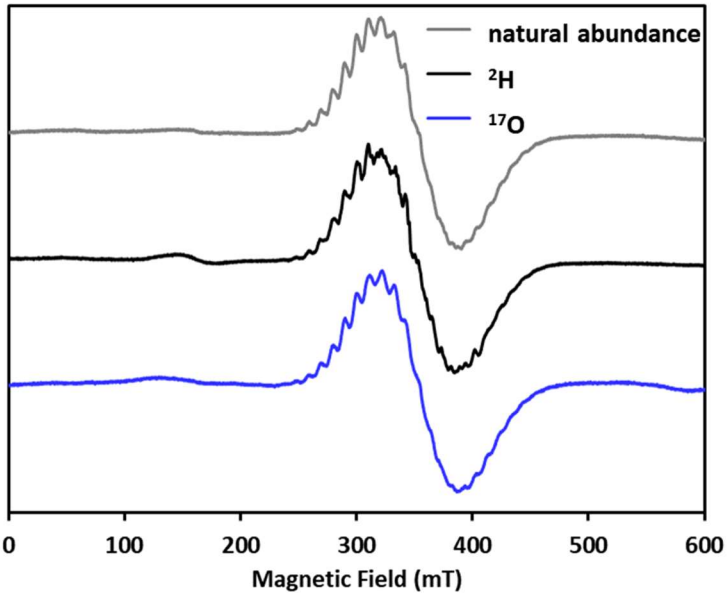

Figure 9. Comparisons of X-band CW EPR spectra of natural abundance, ^{2}H labelled, and ^{17}O labelled samples of the putative hydroxide complex. Acquisition parameters: frequency = 9.64 MHz, power = 8.7 mW, conversion time = 10 ms, and modulation amplitude = 8 G.

A1.3) Ammonia

Addition of varying equivalents of ammonia (0.4 M in THF) to **1** suggests that the conversion to a new LS species is complete upon the addition of ~100 equivalents (Figure 11). This contrasts with the studies with water and hydroxide. Due to the more basic nature of NH_3 versus H_2O, it is proposed that protonolysis of the siloxide moiety is not as feasible (Figure 10). Interestingly, removing all volatiles of an ammonia-treated sample of **1** and subsequent sample preparation of this residue by re-dissolving in 1:1 CH_2Cl_2:2-MeTHF shows the conversion of a mixture containing both HS and LS signals to one with predominantly the HS signal (Figure 12). This result suggests some degree of reversibility in the reaction with NH_3 and lability of the NH_3 ligand, lending support for the hypothesis that the new LS species is bound to both siloxide and NH_3.

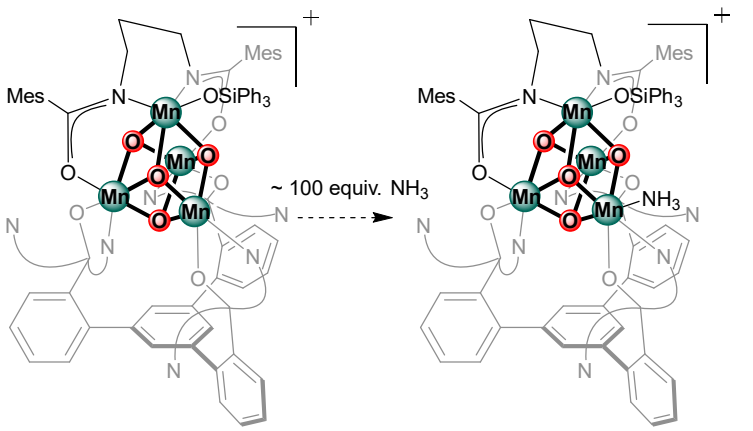

Figure 10. Proposed product of reaction between **1** and ~ 100 equivalents of NH_3.

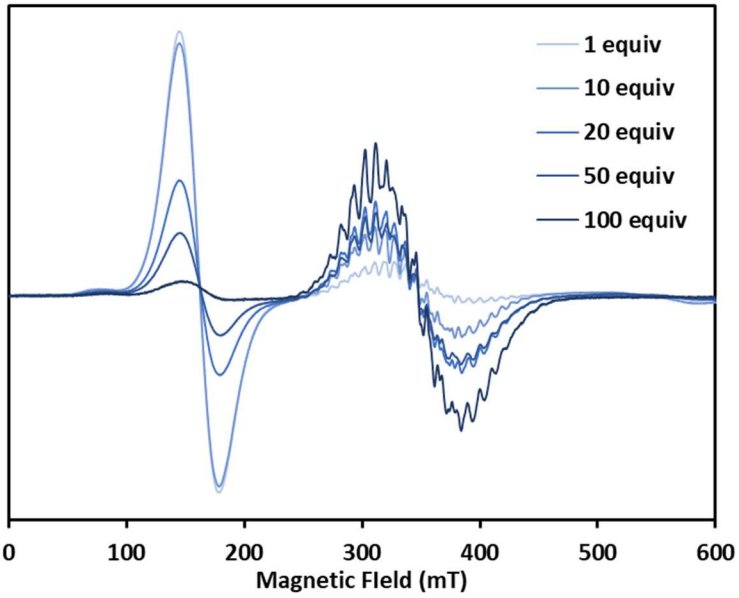

Figure 11. Addition of varying equivalents of NH_3 (0.4 M in THF) to **1**, with spectra collected at T = 5 K. Acquisition parameters: frequency = 9.64 MHz, power = 8.8 mW, conversion time = 10 ms, and modulation amplitude = 8 G.

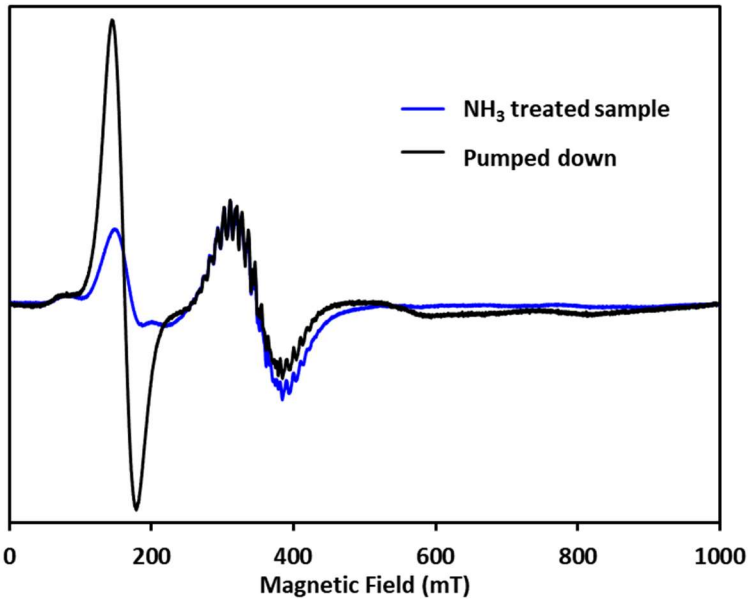

Figure 12. Comparison between NH_3 treated sample (blue) and same sample after subjecting to vacuum, then redissolving the resulting residue (black). Spectra scaled to roughly have same intensity of LS signal. Data collected at T = 5 K. Acquisition parameters: frequency = 9.64 MHz, power = 8.8 mW, conversion time = 10 ms, and modulation amplitude = 8 G.

Interestingly, even with the large excess of reagent added, some HS signal remains. X-band CW spectra collected at variable temperatures reveal different temperature dependent relaxation behavior of the HS and LS signals (Figure 13). One possible explanation is that ammonia binding tunes the energy gap between ground and higher-spin excited states. Notably, the nature of ligand environment has been previously demonstrated to have such an effect in related synthetic Mn_4O_4 complexes. Furthermore, the Q-band ESE-EPR spectrum of **1** displays broad features at low field in addition to features centered about $g = 2$ due to a small zero-field splitting value ($|D| = 0.32$ cm^{-1}) (Figure 14). These signals are not observed in the ammonia-treated samples, consistent with the tentative assignment of the HS signal resulting from a thermally accessible excited state as opposed to unreacted starting material **1**.

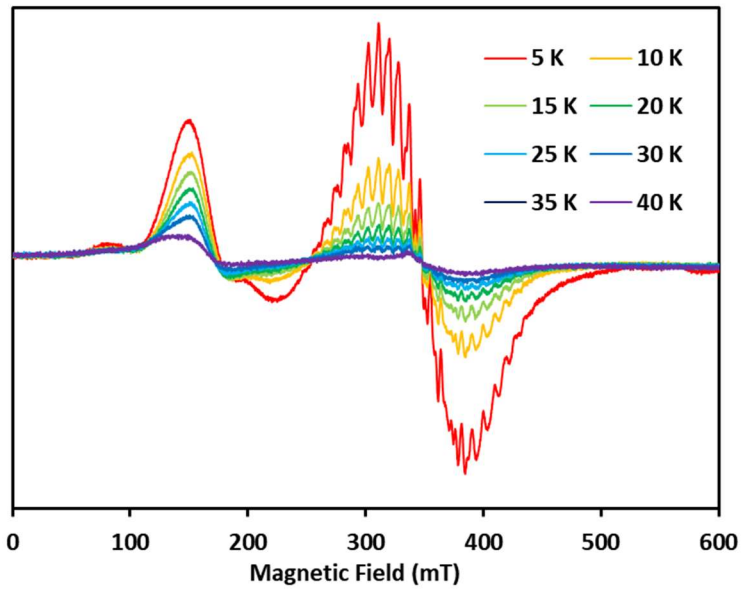

Figure 13. X-band CW EPR spectra of addition of ~ 100 equivalents of NH_3 to **1**, collected at various temperatures. Acquisition parameters: frequency = 9.64 MHz, power = 8.7 mW, conversion time = 10 ms, and modulation amplitude = 8 G.

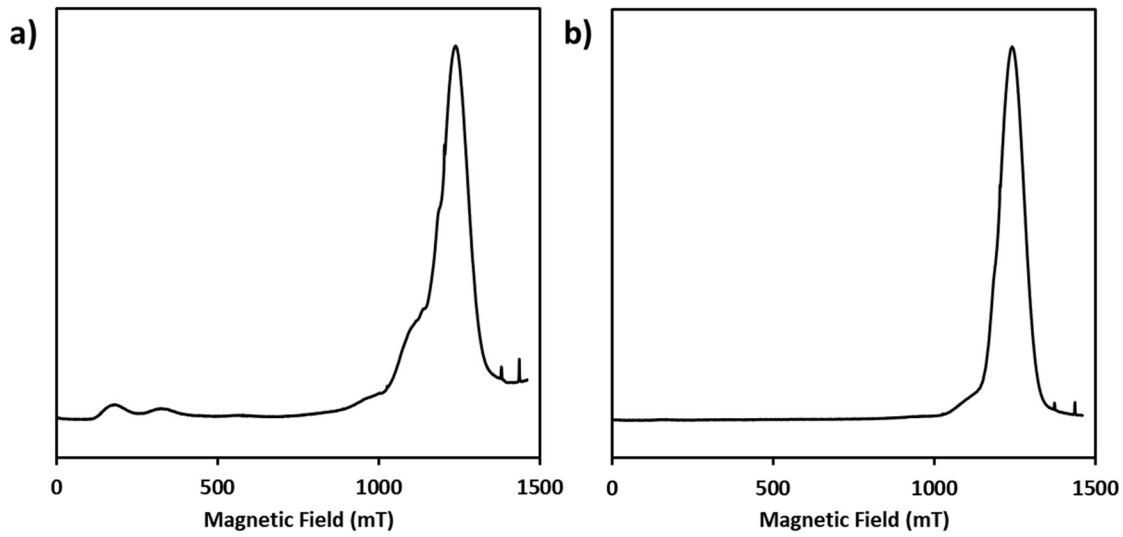

Figure 14. Q-band ESE-EPR spectra of **(a) 1** collected at T = 3.2 K and **(b) 1-NH_3**, collected at 3.5 K.

Comparisons between labelled $^{15}NH_3$ and natural abundance samples were attempted utilizing pulse techniques (ESEEM, HYSCORE, ENDOR) at both X and Q-bands. However, due to overlap with the ^{14}N signals originating from ancillary ligands, the ^{15}N signals could not be resolved. Samples prepared from addition of N^2H_3 were studied by ^2H Mims ENDOR spectroscopy. Signals centered about the ^2H Larmor frequency were observed and can be estimated to have a ^2H hyperfine interaction (HFI) of A = ~2 MHz (Figure 15). This magnitude is comparable to that observed for the related hydroxide and water bound species.

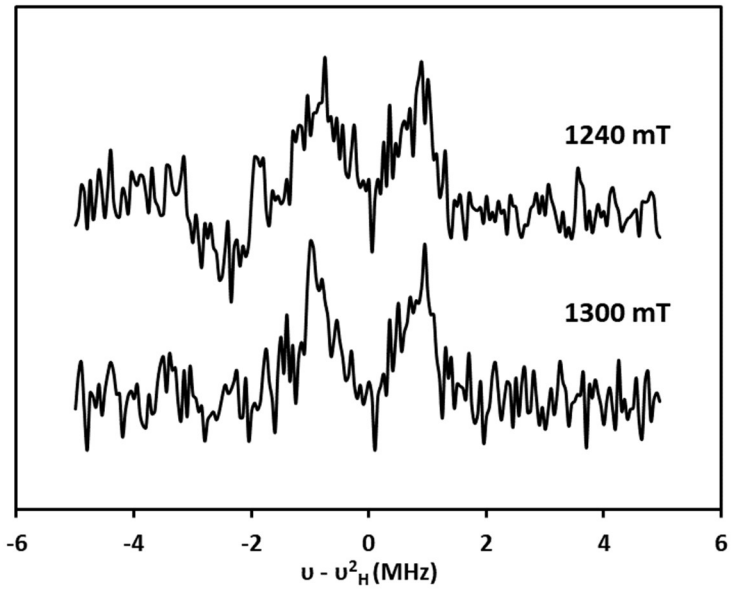

Figure 15. $^{2}H - {}^{1}H$ difference Mims ENDOR spectra of $N^{2}H_3$-treated samples of **1** collected at 1240 and 1300 mT.

A single crystal to single crystal reaction of complex **1** with ammonia was performed. Subjecting crystals of **1**, grown from vapor diffusion of Et_2O into a *o*-difluorobenzene solution, to an atmosphere of ammonia for 2 hours resulted in an observed change in the unit cell of the crystals. Importantly, this new unit cell is unique to the one obtained from subjecting crystals of **1** to water (vapor). Although the quality of the dataset is insufficient for determination of precise structural metrics, this result yields the connectivity of the reaction product (Figure 16). Likely due to disorder, the expected triflate counteranion is not located, though unaccounted electron density surrounding the cluster is present in this dataset.

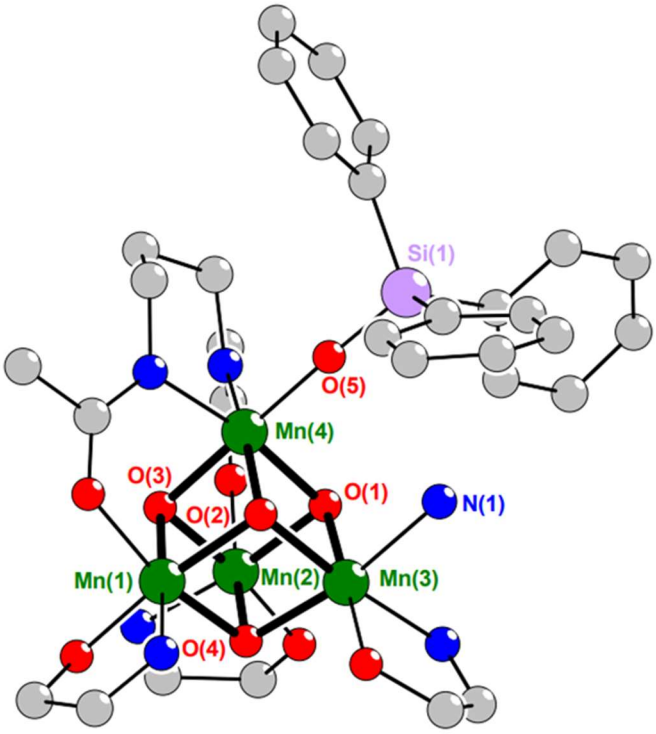

Figure 16. Truncated crystal structure of reaction product (**1-NH$_3$**) from subjecting crystals of **1** to ammonia for 2 hours. Due to low quality dataset, atoms depicted as ball-and-stick model. Mn (green), Si (light purple), O (red), N (blue), C (gray).

A1.4) Methanol, methoxide, and miscellaneous

Addition of excess methanol (~ 60 equivalents) likewise results in the conversion of **1** to a new LS species, as monitored by EPR spectroscopy (Figure 17). Addition of one equivalent of DBU in excess methanol results in the complete conversion to a new LS species, suggesting the formation of a methoxide bound complex. ^{2}H labeled samples can be prepared utilizing CD_3OD; signals centered about the ^{2}H Larmor frequency in the ^{2}H Mims ENDOR spectrum (Figure 18) have estimated ^{2}H hyperfine interactions of A = ~0.5 MHz. This value is significantly smaller than those observed for water/hydroxide and ammonia binding discussed previously, suggesting these signals arise from the methyl deuterons. Unfortunately, attempts at isolating a methoxide bound species have not been successful thus far.

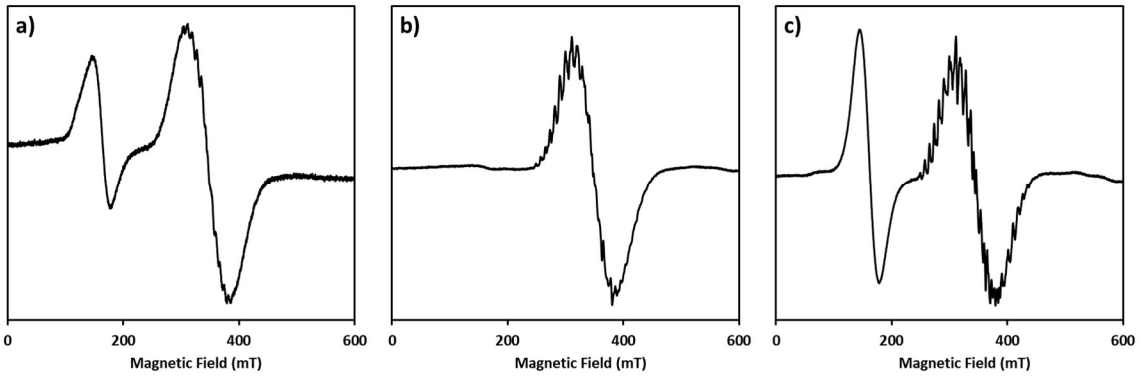

Figure 17. X-band CW EPR spectrum of the **(a)** addition of ~ 60 equiv of MeOH to **1**. **(b)** addition of 1 equivalent of DBU in excess MeOH (~ 60 equiv relative to **1**). **(c)** addition of 1 equivalent of DBU and 1 equivalent of MeOH to **1**. Spectra collected at T = 5 K. Acquisition parameters: frequency = 9.64 MHz, power = 8.7 mW, conversion time = 10 ms, and modulation amplitude = 8 G.

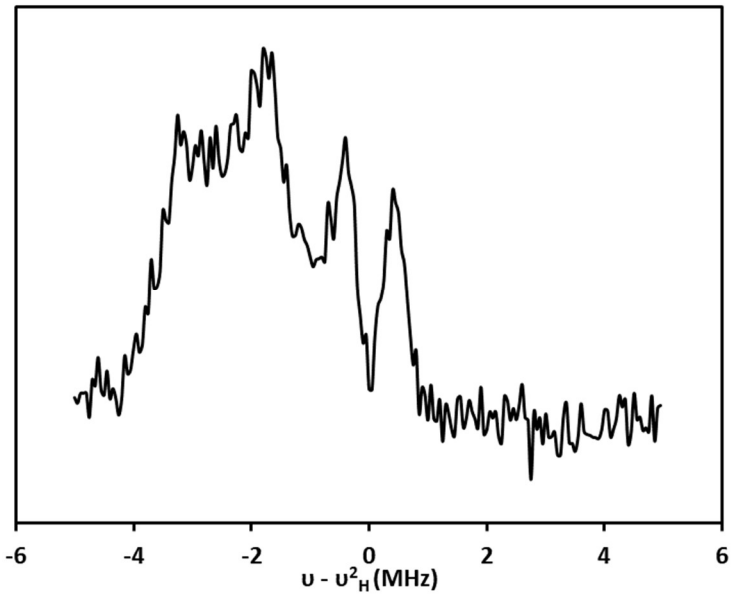

Figure 18. Q-band ^{2}H Mims ENDOR spectrum collected at 1240 mT of putative methoxide-bound cluster. Estimated ^{2}H hyperfine coupling constant A = ~0.5 MHz. Peaks not centered about ^{2}H Larmor frequency are attributed to ^{14}N signals from ancillary ligands.

Other substrates of interest include (hydro)peroxides and superoxide, as comparisons to the water/hydroxide species isolated previously (**1-H_2O-OH**). Preliminary studies on the addition of 10 equivalents of $HO_2{}^tBu$ (5.5 M in decane) to **1** shows incomplete consumption of the HS species and formation of a new LS species (Figure 19). It is hypothesized that the

reaction with $HO_2{}^tBu$ involves protonolysis of the siloxide moiety and results in an alkylperoxide bound in an η^2 fashion, although further characterization is needed to confirm this assignment.

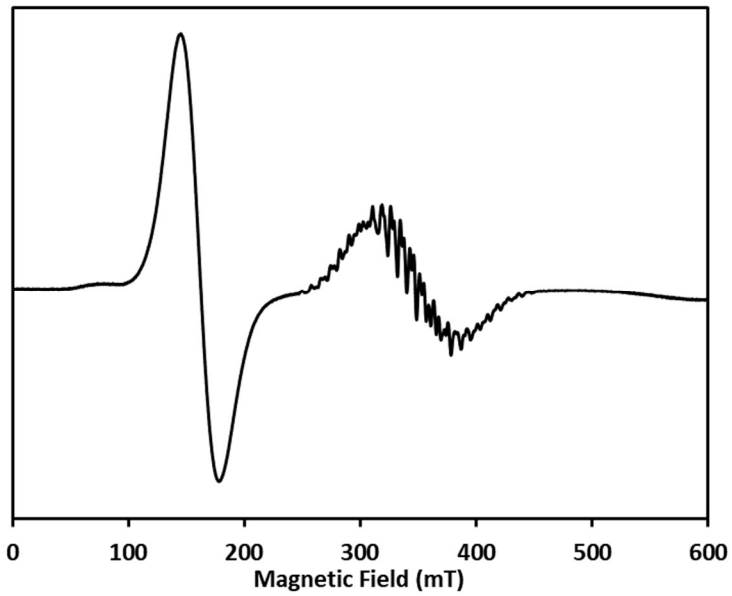

Figure 19. X-band CW EPR spectrum of the reaction between **1** and 10 equivalents of $HO_2{}^tBu$ (5.5 M in decane), collected at T = 5 K. Acquisition parameters: frequency = 9.64 MHz, power = 8.8 mW, conversion time = 10 ms, and modulation amplitude = 8 G.

Similarly, addition of anhydrous sources of hydrogen peroxide results in the conversion to a new low-spin species. Reactions with DABCO · $(H_2O_2)_2$ (DABCO = 1,4-diazabicyclo[2.2.2]octane) are incomplete likely due to the insolubility of this reagent. Utilizing 3 equivalents of a phosphine-oxide adduct of H_2O_2 ([(*o*-tol)$_3$P=O · H_2O_2]$_2$), soluble in common organic solvents such as tetrahydrofuran and methylene chloride,[34, 35] a new low-spin species is observed (Figure 20). X-band CW EPR spectra were also collected at T = 5 K, 10 K, 15 K, 20 K, and 30 K (Figure 21). Similar to previously reported [Mn_4O_4] complexes,[36] a new higher spin signal is observed as the temperature is increased, concomitant with decreasing intensity of the LS signal. This observation suggests the presence of a low-lying high spin excited state. Notably, a small amount of complex **1**

remains in this mixture, as determined based on the temperature dependence behavior, and is denoted with an asterisk (*) (Figure 22).

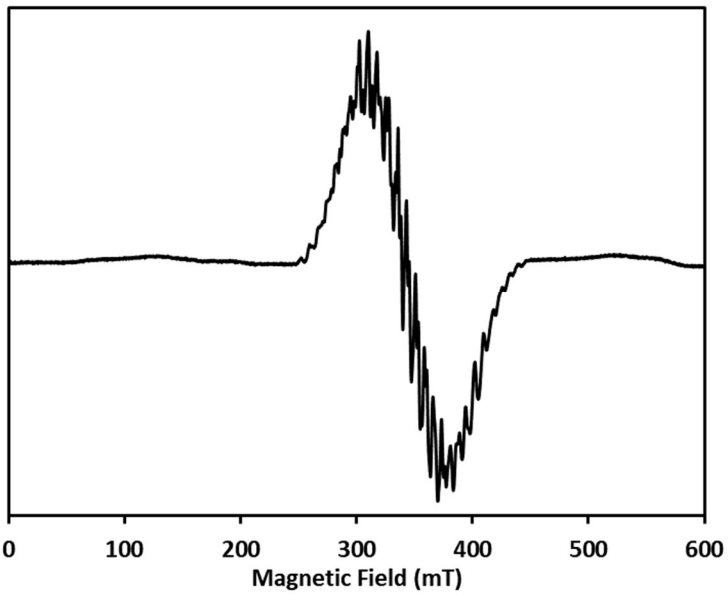

Figure 20. X-band CW EPR spectrum of the reaction between **1** and 3 equivalents of [(*o*-tol)$_3$PO(H$_2$O$_2$)]$_2$, collected at T = 5 K. Acquisition parameters: frequency = 9.64 MHz, power = 8.7 mW, conversion time = 10 ms, and modulation amplitude = 8 G.

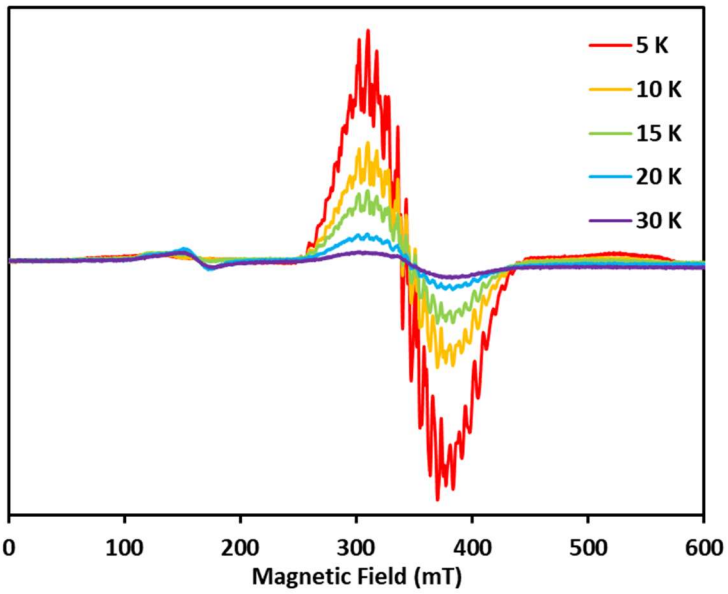

Figure 21. X-band CW EPR spectrum of the reaction between **1** and 3 equivalents of [(*o*-tol)$_3$PO(H$_2$O$_2$)]$_2$, collected at various temperatures. Acquisition parameters: frequency = 9.64 MHz, power = 8.7 mW, conversion time = 10 ms, and modulation amplitude = 8 G.

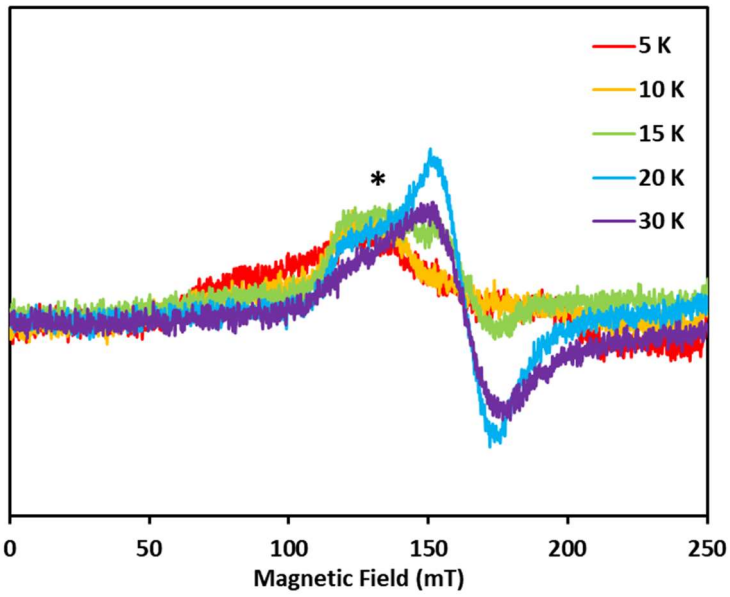

Figure 22. Expanded view of the low-field region of the X-band CW EPR spectrum of the reaction between **1** and 3 equivalents of $[(o\text{-tol})_3PO(H_2O_2)]_2$, collected at various temperatures. Presence of small amounts of complex **1** denoted with an asterisk (*). Acquisition parameters: frequency = 9.64 MHz, power = 8.7 mW, conversion time = 10 ms, and modulation amplitude = 8 G.

A1.5) Discussion

The reactivity of complex **1** with various biologically relevant small molecules was explored and studied via EPR spectroscopy. In general, these reactions are hypothesized to generate Mn_4O_4 clusters featuring all (pseudo)octahedral Mn centers, due to the observed spin state change from $S = 5/2$ of the starting complex **1** to $S = 1/2$ of new products. More detailed experiments and analysis of these reaction products to better understand how different substrates affect the *J*-coupling between Mn centers and thus the energy differences between ground and excited states are underway.

A1.6) Experimental

General considerations

All reactions were performed at room temperature in an N_2-filled glovebox or by using standard Schlenk techniques unless otherwise specified. Glassware was oven dried at 150 °C for at least 2h prior to use and allowed to cool under vacuum. All reagents were used as received unless otherwise stated. Compound **1** was prepared according to literature. Anhydrous tetrahydrofuran (THF) was purchased from Aldrich in 18 L Pure-Pac^{TM} containers. Anhydrous CH_2Cl_2, diethyl ether, benzene, pentane, and THF were purified by sparging with nitrogen for 15 minutes and then passing under nitrogen pressure through a column of activated A2 alumina. NMR solvents were purchased from Cambridge Isotope Laboratories, dried over calcium hydride (CD_2Cl_2, CD_3CN) or over sodium/benzophenone (C_6D_6), degassed by three freeze-pump-thaw cycles and vacuum-transferred prior to use. ^1H_2O and ^2H_2O for EPR experiments were degassed by sparging with N_2 or three freeze-pump-thaw cycles, respectively. $^{17}OH_2$ (70% isotopic enrichment) was purchased from Sigma Aldrich. NH_3 (0.4 M in THF) solutions was purchased from Sigma Aldrich and used

without further purification. Isotopically labeled N^2H_3 and $^{15}NH_3$ solutions were prepared by saturating 2 mL of anhydrous THF with the desired gas on the high-vacuum line. Isotopically labeled N^2H_3 and $^{15}NH_3$ gases were subjected to three freeze-pump-thaw cycles prior to use and transferred while submerged in a dry-ice/acetone bath (– 78 °C).

EPR spectroscopy

Samples were prepared as solutions (c.a. 2 mM) in 1:1 CH_2Cl_2:2-MeTHF and rapidly cooled in liquid nitrogen to form a frozen glass. For reactivity studies, a stock solution of complex **1** in 1:1 CH_2Cl_2:2-MeTHF (2 mM) was prepared, and the desired equivalents of substrate (prepared as 0.4 M solutions in THF unless specified otherwise) were added via syringe. Reaction mixtures were mixed by pipet, filtered, and transferred to X-band or Q-band tubes, respectively, and frozen in LN_2 within 5-10 minutes of reagent addition. All X-band and Q-band EPR experiments presented in this study were acquired at the Caltech EPR facility. X-band CW EPR spectra were acquired on a Bruker (Billerica, MA) EMX spectrometer using Bruker Xenon software (ver. 1.2). Temperature control was achieved using liquid helium and an Oxford Instruments (Oxford, UK) ESR-900 cryogen flow cryostat and an ITC-503 temperature controller. Pulse EPR and electron nuclear double resonance (ENDOR) experiments were acquired using a Bruker ELEXSYS E580 pulse EPR spectrometer using a Bruker D2 pulse ENDOR resonator for Q-band experiments. Temperature control was achieved using an Oxford Instruments CF-935 helium flow cryostat and a Mercury ITC temperature controller. Acquisition parameters for Q-band ^2H Mims ENDOR: pulse sequence $\pi/2$-τ-$\pi/2$-t_{RF}-π_{RF}-t_{RF}-$\pi/2$-τ-echo; where $\pi/2$ = 20 ns, t_{RF} = RF pulse delay = 2 μs, π_{RF} = RF pulse length = 40 μs; and τ = 140 ns; MW frequency = 34.120 GHz,

Temperature = 3.5 K, shot repetition time (srt) = 50 ms. The frequency of the RF pulse was randomly sampled to minimize nuclear spin saturation.

A1.7) References

(1) Yano, J.; Yachandra, V., Mn_4Ca Cluster in Photosynthesis: Where and How Water is Oxidized to Dioxygen. *Chem. Rev.* **2014,** *114* (8), 4175-4205.

(2) Shen, J.-R., The Structure of Photosystem II and the Mechanism of Water Oxidation in Photosynthesis. *Annu. Rev. Plant Biol.* **2015,** *66* (1), 23-48.

(3) Britt, R. D.; Marchiori, D. A., Photosystem II, poised for O_2 formation. *Science* **2019,** *366* (6463), 305.

(4) Cox, N.; Pantazis, D. A.; Lubitz, W., Current Understanding of the Mechanism of Water Oxidation in Photosystem II and Its Relation to XFEL Data. *Annu. Rev. Biochem* **2020,** *89* (1), 795-820.

(5) Cox, N.; Pantazis, D. A.; Neese, F.; Lubitz, W., Biological Water Oxidation. *Acc. Chem. Res.* **2013,** *46* (7), 1588-1596.

(6) Ibrahim, M.; Fransson, T.; Chatterjee, R.; Cheah, M. H.; Hussein, R.; Lassalle, L.; Sutherlin, K. D.; Young, I. D.; Fuller, F. D.; Gul, S.; Kim, I.-S.; Simon, P. S.; de Lichtenberg, C.; Chernev, P.; Bogacz, I.; Pham, C. C.; Orville, A. M.; Saichek, N.; Northen, T.; Batyuk, A.; Carbajo, S.; Alonso-Mori, R.; Tono, K.; Owada, S.; Bhowmick, A.; Bolotovsky, R.; Mendez, D.; Moriarty, N. W.; Holton, J. M.; Dobbek, H.; Brewster, A. S.; Adams, P. D.; Sauter, N. K.; Bergmann, U.; Zouni, A.; Messinger, J.; Kern, J.; Yachandra, V. K.; Yano, J., Untangling the sequence of events during the $S_2 \rightarrow S_3$ transition in photosystem II and implications for the water oxidation mechanism. *Proc. Natl. Acad. Sci. U. S. A.* **2020,** *117* (23), 12624-12635.

(7) Kern, J.; Chatterjee, R.; Young, I. D.; Fuller, F. D.; Lassalle, L.; Ibrahim, M.; Gul, S.; Fransson, T.; Brewster, A. S.; Alonso-Mori, R.; Hussein, R.; Zhang, M.; Douthit, L.; de Lichtenberg, C.; Cheah, M. H.; Shevela, D.; Wersig, J.; Seuffert, I.; Sokaras, D.; Pastor, E.; Weninger, C.; Kroll, T.; Sierra, R. G.; Aller, P.; Butryn, A.; Orville, A. M.; Liang, M.; Batyuk, A.; Koglin, J. E.; Carbajo, S.; Boutet, S.; Moriarty, N. W.; Holton, J. M.; Dobbek, H.; Adams, P. D.; Bergmann, U.; Sauter, N. K.; Zouni, A.; Messinger, J.; Yano, J.; Yachandra, V. K., Structures of the intermediates of Kok's photosynthetic water oxidation clock. *Nature* **2018,** *563* (7731), 421-425.

(8) Marchiori, D. A.; Oyala, P. H.; Debus, R. J.; Stich, T. A.; Britt, R. D., Structural Effects of Ammonia Binding to the Mn_4CaO_5 Cluster of Photosystem II. *J. Phys. Chem. B* **2018,** *122* (5), 1588-1599.

(9) Oyala, P. H.; Stich, T. A.; Debus, R. J.; Britt, R. D., Ammonia Binds to the Dangler Manganese of the Photosystem II Oxygen-Evolving Complex. *J. Am. Chem. Soc.* **2015,** *137* (27), 8829-8837.

(10) Oyala, P. H.; Stich, T. A.; Stull, J. A.; Yu, F.; Pecoraro, V. L.; Britt, R. D., Pulse Electron Paramagnetic Resonance Studies of the Interaction of Methanol with the S_2 State of the Mn_4O_5Ca Cluster of Photosystem II. *Biochemistry* **2014,** *53* (50), 7914-7928.

(11) Pérez Navarro, M.; Ames, W. M.; Nilsson, H.; Lohmiller, T.; Pantazis, D. A.; Rapatskiy, L.; Nowaczyk, M. M.; Neese, F.; Boussac, A.; Messinger, J.; Lubitz, W.; Cox, N., Ammonia binding to the oxygen-evolving complex of photosystem II

identifies the solvent-exchangeable oxygen bridge (μ-oxo) of the manganese tetramer. *Proc. Natl. Acad. Sci. U. S. A.* **2013,** *110* (39), 15561-15566.

(12) Cox, N.; Retegan, M.; Neese, F.; Pantazis, D. A.; Boussac, A.; Lubitz, W., Electronic structure of the oxygen-evolving complex in photosystem II prior to O-O bond formation. *Science* **2014,** *345* (6198), 804.

(13) Marchiori, D. A.; Debus, R. J.; Britt, R. D., Pulse EPR Spectroscopic Characterization of the S_3 State of the Oxygen-Evolving Complex of Photosystem II Isolated from Synechocystis. *Biochemistry* **2020,** *59* (51), 4864-4872.

(14) Suga, M.; Akita, F.; Sugahara, M.; Kubo, M.; Nakajima, Y.; Nakane, T.; Yamashita, K.; Umena, Y.; Nakabayashi, M.; Yamane, T.; Nakano, T.; Suzuki, M.; Masuda, T.; Inoue, S.; Kimura, T.; Nomura, T.; Yonekura, S.; Yu, L.-J.; Sakamoto, T.; Motomura, T.; Chen, J.-H.; Kato, Y.; Noguchi, T.; Tono, K.; Joti, Y.; Kameshima, T.; Hatsui, T.; Nango, E.; Tanaka, R.; Naitow, H.; Matsuura, Y.; Yamashita, A.; Yamamoto, M.; Nureki, O.; Yabashi, M.; Ishikawa, T.; Iwata, S.; Shen, J.-R., Light-induced structural changes and the site of O=O bond formation in PSII caught by XFEL. *Nature* **2017,** *543*, 131.

(15) Lohmiller, T.; Krewald, V.; Sedoud, A.; Rutherford, A. W.; Neese, F.; Lubitz, W.; Pantazis, D. A.; Cox, N., The First State in the Catalytic Cycle of the Water-Oxidizing Enzyme: Identification of a Water-Derived μ-Hydroxo Bridge. *J. Am. Chem. Soc.* **2017,** *139* (41), 14412-14424.

(16) Rapatskiy, L.; Cox, N.; Savitsky, A.; Ames, W. M.; Sander, J.; Nowaczyk, M. M.; Rögner, M.; Boussac, A.; Neese, F.; Messinger, J.; Lubitz, W., Detection of the Water-Binding Sites of the Oxygen-Evolving Complex of Photosystem II Using W-Band ^{17}O Electron–Electron Double Resonance-Detected NMR Spectroscopy. *J. Am. Chem. Soc.* **2012,** *134* (40), 16619-16634.

(17) Hillier, W.; Wydrzynski, T., ^{18}O-Water exchange in photosystem II: Substrate binding and intermediates of the water splitting cycle. *Coord. Chem. Rev.* **2008,** *252* (3), 306-317.

(18) Nilsson, H.; Rappaport, F.; Boussac, A.; Messinger, J., Substrate–water exchange in photosystem II is arrested before dioxygen formation. *Nature Communications* **2014,** *5* (1), 4305.

(19) Noguchi, T., Fourier transform infrared analysis of the photosynthetic oxygen-evolving center. *Coord. Chem. Rev.* **2008,** *252* (3), 336-346.

(20) Noguchi, T.; Sugiura, M., FTIR Detection of Water Reactions during the Flash-Induced S-State Cycle of the Photosynthetic Water-Oxidizing Complex. *Biochemistry* **2002,** *41* (52), 15706-15712.

(21) Vinyard, D. J.; Brudvig, G. W., Insights into Substrate Binding to the Oxygen-Evolving Complex of Photosystem II from Ammonia Inhibition Studies. *Biochemistry* **2015,** *54* (2), 622-628.

(22) Britt, R. D.; Zimmermann, J. L.; Sauer, K.; Klein, M. P., Ammonia binds to the catalytic manganese of the oxygen-evolving complex of photosystem II. Evidence by electron spin-echo envelope modulation spectroscopy. *J. Am. Chem. Soc.* **1989,** *111* (10), 3522-3532.

(23) Nöring, B.; Shevela, D.; Renger, G.; Messinger, J., Effects of methanol on the Si-state transitions in photosynthetic water-splitting. *Photosynth. Res.* **2008,** *98* (1), 251-260.

(24) Su, J.-H.; Cox, N.; Ames, W.; Pantazis, D. A.; Rapatskiy, L.; Lohmiller, T.; Kulik, L. V.; Dorlet, P.; Rutherford, A. W.; Neese, F.; Boussac, A.; Lubitz, W.; Messinger, J., The electronic structures of the S2 states of the oxygen-evolving complexes of photosystem II in plants and cyanobacteria in the presence and absence of methanol. *Biochim. Biophys. Acta, Bioenerg.* **2011,** *1807* (7), 829-840.

(25) Force, D. A.; Randall, D. W.; Lorigan, G. A.; Clemens, K. L.; Britt, R. D., ESEEM Studies of Alcohol Binding to the Manganese Cluster of the Oxygen Evolving Complex of Photosystem II. *J. Am. Chem. Soc.* **1998,** *120* (51), 13321-13333.

(26) Mukhopadhyay, S.; Mandal, S. K.; Bhaduri, S.; Armstrong, W. H., Manganese Clusters with Relevance to Photosystem II. *Chem. Rev.* **2004,** *104* (9), 3981-4026.

(27) Blakemore, J. D.; Crabtree, R. H.; Brudvig, G. W., Molecular Catalysts for Water Oxidation. *Chem. Rev.* **2015,** *115* (23), 12974-13005.

(28) Paul, S.; Neese, F.; Pantazis, D. A., Structural models of the biological oxygen-evolving complex: achievements, insights, and challenges for biomimicry. *Green Chemistry* **2017,** *19* (10), 2309-2325.

(29) Mukherjee, S.; Stull, J. A.; Yano, J.; Stamatatos, T. C.; Pringouri, K.; Stich, T. A.; Abboud, K. A.; Britt, R. D.; Yachandra, V. K.; Christou, G., Synthetic model of the asymmetric $[Mn_3CaO_4]$ cubane core of the oxygen-evolving complex of photosystem II. *Proc. Natl. Acad. Sci. U. S. A.* **2012,** *109* (7), 2257.

(30) Zhang, C.; Chen, C.; Dong, H.; Shen, J.-R.; Dau, H.; Zhao, J., A synthetic Mn_4Ca-cluster mimicking the oxygen-evolving center of photosynthesis. *Science* **2015,** *348* (6235), 690.

(31) Koellner, C. A.; Gau, M. R.; Polyak, A.; Bayana, M.; Zdilla, M. J., Hemicubane topological analogs of the oxygen-evolving complex of photosystem II mediating water-assisted propylene carbonate oxidation. *Chem. Commun.* **2022,** *58* (15), 2532-2535.

(32) Hamilton, C. R.; Baglia, R. A.; Gordon, A. D.; Zdilla, M. J., Synthesis of Tetranuclear, Four-Coordinate Manganese Clusters with "Pinned Butterfly" Geometry Formed by Metal-Mediated N−N Bond Cleavage in Diphenylhydrazine. *J. Am. Chem. Soc.* **2011,** *133* (12), 4208-4211.

(33) Supriya, S.; Das, S. K., Reversible Single Crystal to Single Crystal Transformation through Fe−O(H)Me/Fe−OH_2 Bond Formation/Bond Breaking in a Gas−Solid Reaction at an Ambient Condition. *J. Am. Chem. Soc.* **2007,** *129* (12), 3464-3465.

(34) Arp, F. F.; Bhuvanesh, N.; Blümel, J. Hydrogen peroxide adducts of triaylphosphine oxides. *Dalton Trans.*, **2019**, *48*, 14312-14325.

(35) Kim, B.; Brueggemeyer, M. T.; Transue, W. J.; Park, Y.; Cho, J.; Siegler, M. A.; Solomon, E. I.; Karlin, K. D. Fenton-like Chemistry by a Copper(I) Complex and H_2O_2 Relevant to Enzyme Peroxygenase C-H Hydroxylation. *J. Am. Chem. Soc.*, **2023**, *Article ASAP.*

(36) Lee, H. B.; Shiau, A. A.; Oyala, P. H.; Marchiori, D. A.; Gul, S.; Chatterjee, R.; Yano, J.; Britt, R. D.; Agapie, T. Tetranuclear $[Mn^{III}Mn_3{}^{IV}O_4]$ Complexes as Spectroscopic Models of the S_2 State of the Oxygen Evolving Complex in Photosystem II. *J. Am. Chem. Soc.*, **2018**, *140* (42), 17175-17187.

APPENDIX 2

Miscellaneous structures

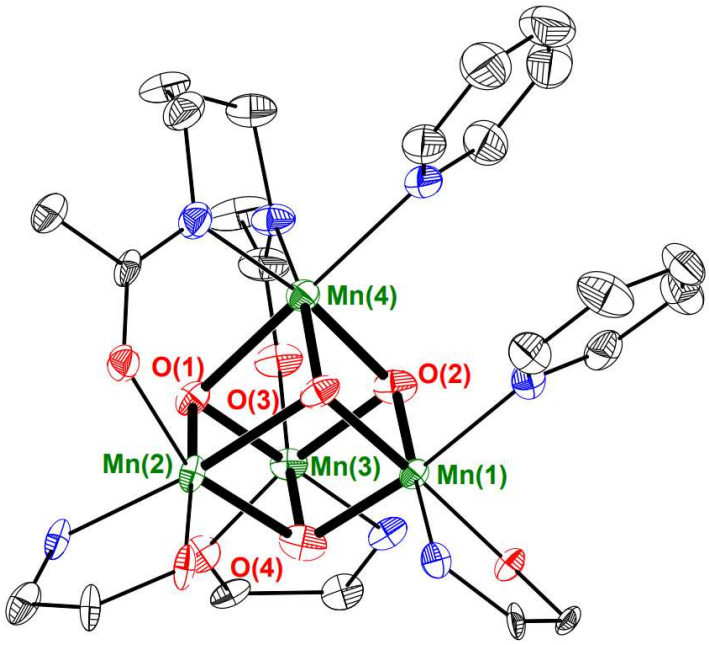

Figure 1. Truncated structure of $[LMn_4O_4(diam^{Mes})(py)_2][BAr^{F24}]$. Synthesized from anion exchange between $LMn_4O_4(diam^{Mes})(OTf)$ and $NaBAr^{F24}$ in the presence of pyridine. Bolded bonds highlight Mn-oxo bonds. Bond lengths in the Mn_4O_4 core suggest $Mn^{III}_2Mn^{IV}_2$ oxidation state as expected. Mn (green), O (red), N (blue), C (black).

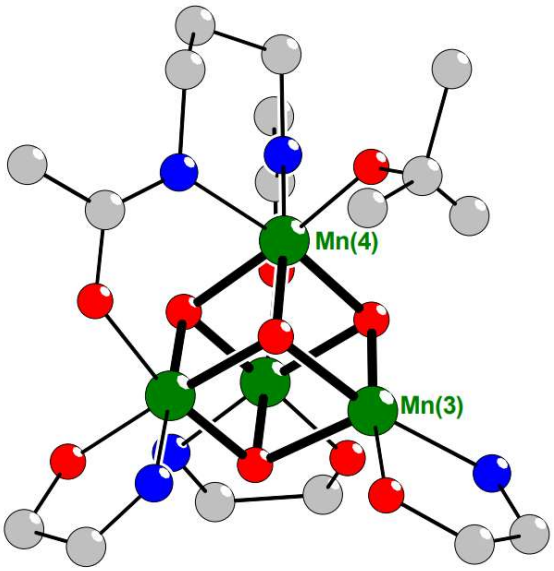

Figure 2. Truncated structure of $LMn_4O_4(diam^{Mes})(O^tBu)$. O^tBu group is disordered between Mn(4) and Mn(3) sites (not depicted above). Product formed from addition of excess (~ 6 equivalents) NaO^tBu to $LMn_3O_4(py)_3(OTf)$, $Mn(OTf)_2$, and H_2diam^{Mes}. Mn (green), O (red), N (blue), C (gray).

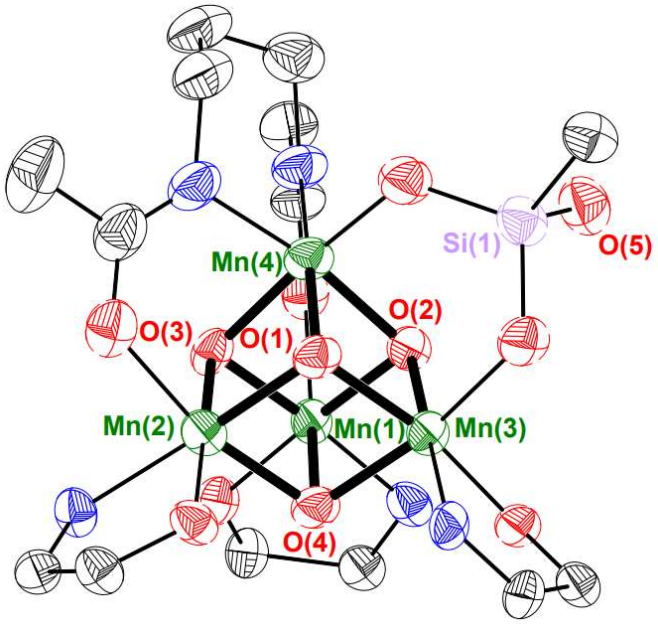

Figure 3. Truncated structure of $LMn_4O_4(diam)(O_3H_xSiAr)$ Ar = 1,3,5 triisopropylphenyl. Synthesized from protonolysis reaction of $LMn_4O_4(diam)(OAc)$ and $ArSi(OH)_3$. Bolded bonds highlight Mn-oxo bonds. Preliminary bond lengths suggest $Mn^{III}Mn^{IV}_3$ oxidation state, suggesting unidentified *in situ* oxidation and/or H-atom loss from trisilanol moiety. Mn (green), Si (light purple), O (red), N (blue), C (black).

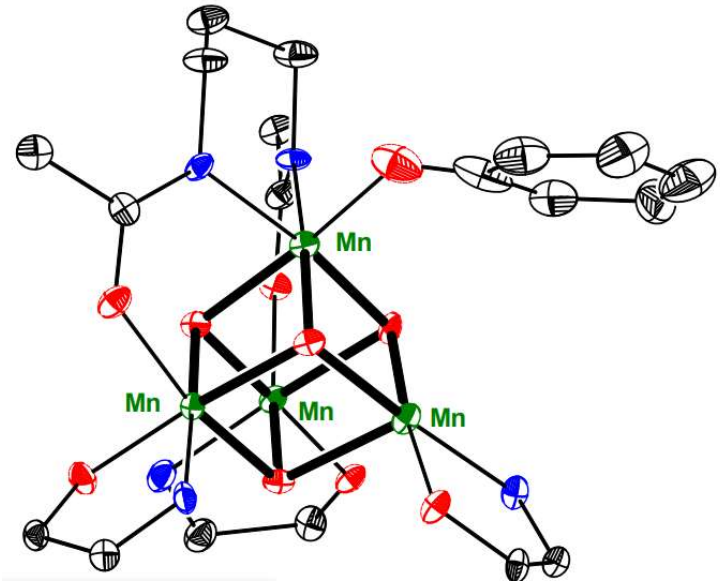

Figure 4. Truncated structure of $LMn_4O_4(diam^{Mes})(OAr)$, Ar = 3,5 di-tertbutylphenyl. Di-tertbutyl groups omitted for clarity; disorder is severe in these groups. Synthesized from salt metathesis of $LMn_4O_4(diam^{Mes})(OTf)$ and KOAr in benzene. Bolded bonds highlight Mn-oxo bonds. Mn (green), O (red), N (blue), C (black).

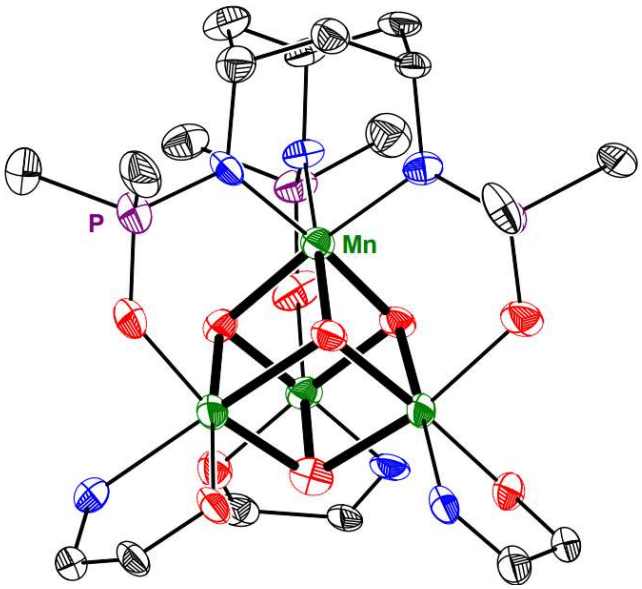

Figure 5. Truncated structure of LMn_4O_4(Cy-phosphinamide). Bolded bonds highlight Mn-oxo bonds. Mn(green), P (purple), O (red), N (blue), C (black).

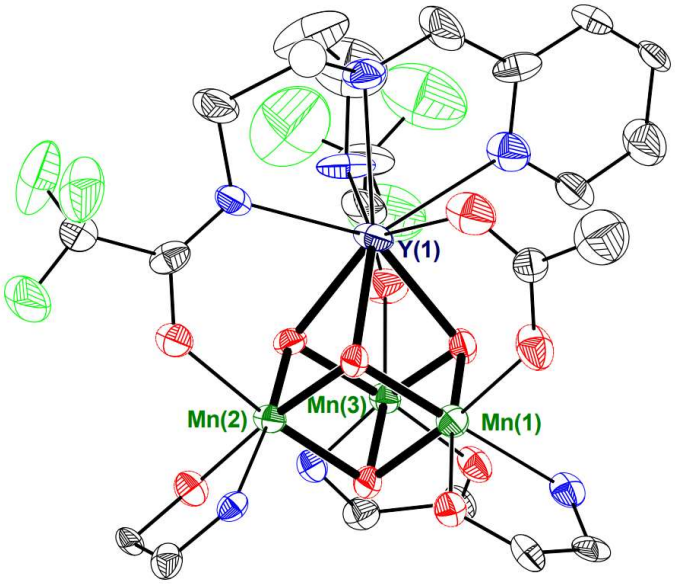

Figure 6. Truncated structure of $LYMn_3O_4(py\text{-}diam^{CF3})(OAc)$. Product of metalation of $[LYMn_3O_4(OAc)_3][OTf]$ with $H_2(py\text{-}diam^{CF3})$ and base. Note that isolated product is one electron reduced from starting material. Bolded bonds represent M-oxo bonds. Y (dark blue), Mn (green), F (light green), O (red), N (blue), C (black). Note one carbon depicted as ball and stick model.

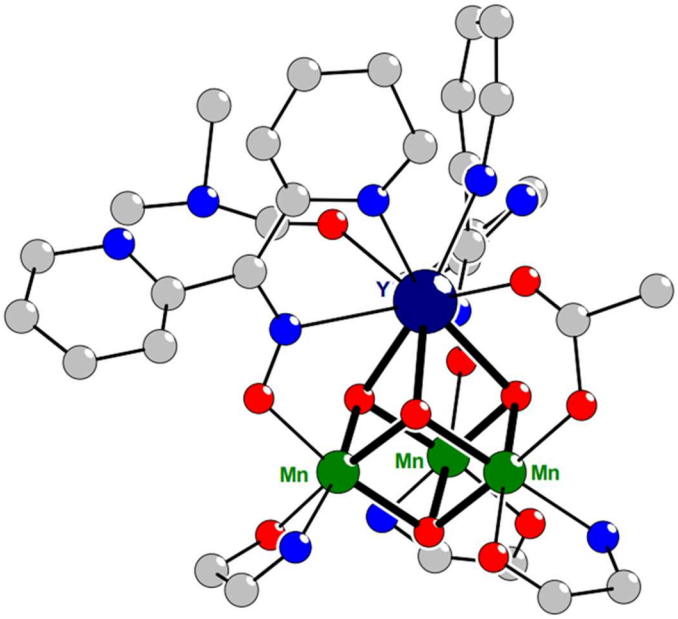

Figure 7. Truncated structure of $[LYMn_3O_4(py\text{-}ox)_2(OAc)(DMF)][OTf]$, py-ox = di-2-pyridyl ketone oximate. Product of protonolysis reaction of $[LYMn_3O_4(OAc)_3][OTf]$ and H(py-ox). Bolded bonds represent M-oxo bonds. Y (dark blue), Mn (green), O (red), N (blue), C (black).

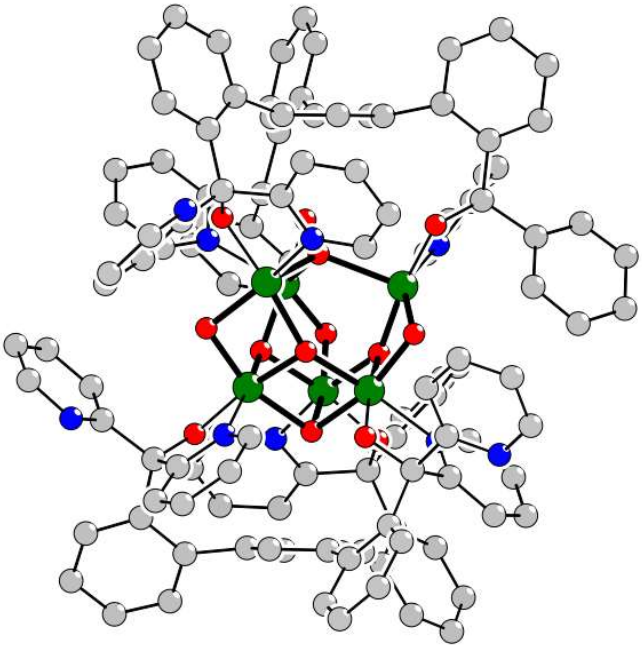

Figure 8. Structure of $L_2Mn_6O_8$. Unexpected decomposition product in unoptimized reaction conditions for LMn_4O_4(diam)(OTf). Bolded bonds represent Mn-oxo bonds. Mn (green), O (red), N (blue), C (gray).

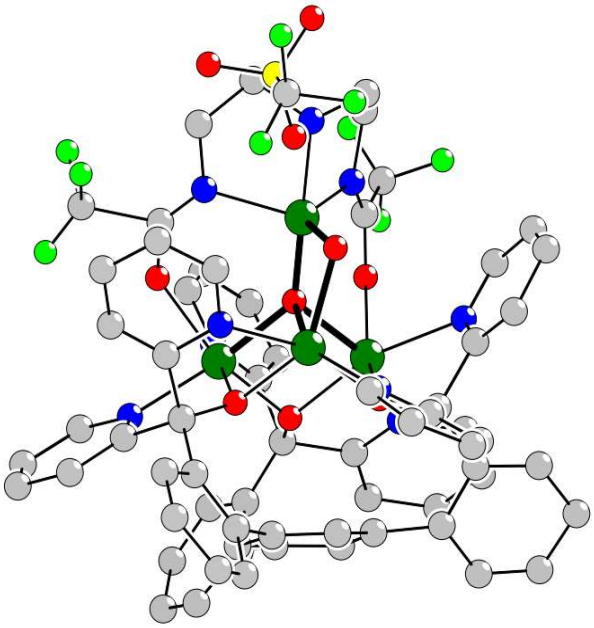

Figure 9. Structure of LMn_4O_2(N-diam^{CF3})(OTf). One unexpected product of $LMn_3O_4(py)_3$(OTf), $Mn(OTf)_2$, NH-H_2diam^{CF3}, and 3 equivalents of NaO^{t}Bu. Bolded bonds represent Mn-oxo bonds. See below for a second product. Mn green), S (yellow), F (light green), O (red), N (blue), C (gray).

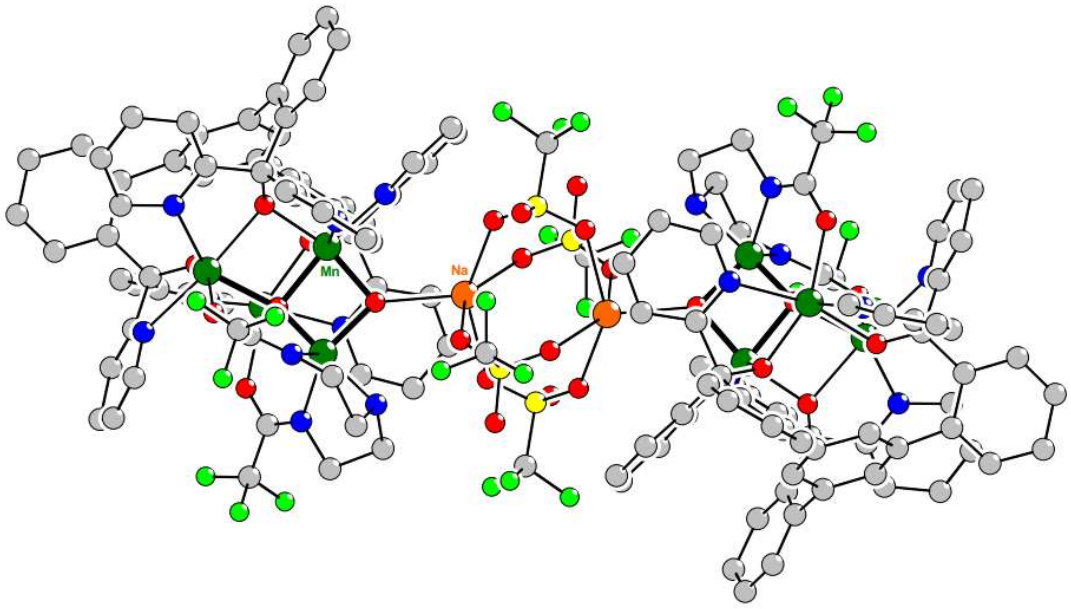

Figure 10. Structure of $[LMn_4O_2(N\text{-}diam^{CF3})Na(OTf)_2]_2$. One unexpected product of $LMn_3O_4(py)_3(OTf)$, $Mn(OTf)_2$, $NH\text{-}H_2diam^{CF3}$, and 3 equivalents of NaO^tBu. Bolded bonds represent Mn-oxo bonds. See above for another product. Mn green), Na (orange), S (yellow), F (light green), O (red), N (blue), C (gray).

ABOUT THE AUTHOR

Angela was born in the Bay Area in California, and grew up in Irvine, California. She attended UC Berkeley for her undergraduate studies, completing her degree in Chemistry. She discovered her love for inorganic synthesis while she was as an undergraduate researcher in Prof. John Arnold's laboratory studying the coordination chemistry of thorium and uranium guanidinate complexes. In 2017, she moved to Pasadena to begin her graduate studies here at Caltech in the laboratory of Prof. Theodor Agapie. Upon graduation, Angela will be beginning her post-doctoral studies at UC Davis in the laboratory of Prof. R. David Britt. Angela's family is tired of helping her move up and down the state. Outside of lab, Angela likes to discover new restaurants, play video games, and hang out with her cats, eV and JJ.